UNIVERSITY OF CAPE TOWN
IYUNIVESITHI YASEKAPA • UNIVERSITEIT VAN KAAPSTAD

Novel, Low-Cost, CFRP Pressure Vessel Design for Hydrogen Fuel Cell Applications

Nyasha Nigel Mawire

Dissertation presented for the Degree of

Master of Science in Engineering

in the Department of Mechanical Engineering

Faculty of Engineering and the Built Environment

University of Cape Town

24 June 2019

Plagiarism declaration

I, Nyasha Nigel Mawire, hereby:

a) grant the University of Cape Town free license to reproduce this dissertation in whole or in part, for research;
b) declare that:

"I know the meaning of plagiarism and declare that all the work in this document, save for that which is properly acknowledged, is my own. This dissertation has been submitted to the Turnitin module and I confirm that my supervisor has seen my report and any concerns revealed by such have been resolved with my supervisor."

I am now presenting the dissertation for examination for the degree of MSc (Eng) in Mechanical Engineering.

Signed by candidate

Nyasha Nigel Mawire

24 June 2019

Abstract

In 2015, the Ascension III water rocket shattered the previous long-standing world record of 633 m after reaching an altitude of 835 m. This feat was primarily attributed to the design of the Carbon Fibre Reinforced Plastic (CFRP) pressure vessel portion of the rocket. The pressure vessel was composed on a long, thin-walled commercial CFRP cylindrical tube that had two Poly Vinyl Chloride (PVC) end caps bonded onto either end with an adhesive. The inside wall of the CFRP tube was coated with a thin rubber liner to prevent leakage through the tube wall of the pressurised air-water mixture that provided the necessary thrust for the rocket. The outcome was that the CFRP pressure vessel design was thus, novel, low-cost and lightweight with the potential to be used in other gas storage applications for example in Hydrogen Fuel Cell (HFC) applications. This report details the research aimed at identifying the feasibility and suitability of the proposed CFRP pressure vessel concept for high pressure hydrogen gas storage for use in Hydrogen Fuel Cell Powered Vehicles (HFCPVs).

The primary component of the pressure vessel to be designed was the CFRP tube which was to be commercially filament wound using carbon fibre and epoxy resin. With an angle ply laminate structure for the CFRP tube, an optimal fibre winding angle of 50^{o} was initially chosen to maximise the burst pressure. The stress analysis and strain behaviour of the CFRP tube were modelled using the Classical Lamination Theory. Specimens were made using the same CFRP material as the tube and were tensile tested to give an initial set of approximate properties to be used in the design calculations. The distinct geometrical features of the end cap were designed, and Aluminium 6082-T6 was selected as a suitable material for its construction as it was easy to machine while it also possessed desirable mechanical properties. SpaBond 340 LV epoxy adhesive was used to bond the end caps onto the ends of the CFRP tube.

A number of specimen CFRP pressure vessels were constructed with the inclusion of the rubber liner. Hydrostatic burst tests were performed on specimen vessels with different wall thicknesses (2 mm and 4 mm) to determine the pressure at which each type of vessel would fail. However, only the 2 mm vessels experienced failure of the CFRP tube section as the predominant failure mode while most 4 mm vessels failed by shearing of the interface between the adhesive layer and end cap. According to the ASME Boiler and Pressure Code Section X, the maximum design pressures at which the CFRP pressure vessels could operate at were at most, 2.25 times smaller than the respective failure pressures. The maximum design pressures were thus determined to be 147 bar and 182 bar for the 2 mm and 4 mm CFRP pressure vessels respectively.

The specimen pressure vessels were also fitted with strain gauges on the external cylindrical surface of the CFRP tubes to measure the longitudinal and hoop strain during the burst tests. The strain measurements allowed the deformation behaviour of the CFRP tubes to be modelled which would prove useful for designing further CFRP tubes. For all specimen CFRP pressure vessels, it was observed that the deformation response of the CFRP tubes were linear up until a certain pressure. Beyond that point, a decrease in stiffness was observed which suggested that some form of irreparable damage had commenced. Other specimen CFRP pressure vessels were constructed and underwent hydraulic proof testing at 1.25 times the design pressure for 30 minutes and at the design pressure for a further 24 hours. The objective was to assess if the pressure vessels were durable and reliable of which all tested specimen vessels passed successfully. The hydraulic proof test results seemingly suggested that the rubber liner could adequately prevent leakage of water from the vessels at their design pressures.

The long-term gas leak test was performed at the design pressure using air (i.e. a compressible fluid) on the proof tested pressure vessels to detect and localize any leaks for a duration of up to 72 hours.

However, the leak rates were determined to be at least an order of magnitude larger than the recommended leak rate for hydrogen gas storage vessels. The leak test results strongly suggested that the rubber liner was insufficient to prevent air molecules from escaping the vessel, was not durable for repeated use and thus, not suitable for long-term gas storage. Therefore, it was concluded that the novel CFRP pressure vessel design concept was not yet suitable for hydrogen gas storage, but with improvements, could still prove possible for use in HFCPVs. Further work into these improvements could include improving the end cap design and testing other rubber liners.

Acknowledgements

There are numerous individuals and entities that all had a role to play in the completion of this dissertation, but I would like to award special thanks to the following:

God for the opportunity to pursue my postgraduate studies and for His guidance during these past two years.

My supervisor, Associate Prof Chris von Klemperer for the guidance, wisdom, patience, knowledge and assistance he shared towards my research as well as other important aspects of my life.

The UCT RCIPS Pre-seed Fund for providing the funding for my research and Prof Arnaud Malan of the Industrial CFD group for providing funds towards my tuition and other expenses.

My mom, sister and my girlfriend for their love and crucial support material or otherwise during these past two years. Outside my research pursuits, they have always been people I would count on in my time of need.

Prof Rob Knutsen, Soraya von Willingh, Penny Louw and fellow postgraduate students at CME who made my stay there memorable and worthwhile.

In other supporting roles I would also like to thank the following individuals for the roles that they played towards my research:

- Gavin Doolings for driving me to and from Paarden Eiland safely during the time I was performing my tests.
- Willie Slaverse and George du Plessis for their help in configuring my equipment and applying strain gauges onto specimen CFRP pressure vessels.
- Pierre Smith for ensuring my components were made in workshop on time without any problems and for lending me tools from time to time.
- Prof Genevieve Langdon and Dr Steeve Chung for allowing me access to the BISRU blast chamber to conduct my long-term leak tests.
- Executive Safety Services for allowing me the chance to use their hydrostatic pump for burst testing.

Table of Contents

List of figures

List of tables

List of abbreviations

ASME	American Society of Mechanical Engineers
ASTM	American Society of Testing and Manufacturing
CFRP	Carbon Fibre Reinforced Plastic
CNC	Computer Numeric Control
FRP	Fibre Reinforced Plastic
HFC	Hydrogen Fuel Cell
HFCT	Hydrogen Fuel Cell Technology
HFCPV	Hydrogen Fuel Cell Powered Vehicle
ICE	Internal Combustion Engine
NDE	Non-Destructive Test
PVC	Poly Vinyl Chloride
UD	Unidirectional
UTS	Ultimate Tensile Strength

1. Introduction

1.1 Background information

A group of undergraduate mechanical engineering students led by Stuart Swan designed, built and tested a novel water powered rocket at the University of Cape Town in 2015. They worked as part of the Industrial CFD group under Prof Arnaud Malan. The water rocket called the Ascension III, on its maiden flight, ascended to an altitude of 835 m which broke the previous world record (for the highest altitude reached) of 623 m by a margin of 212 m (i.e. 30%) [1].

Figure 1.1: The Ascension III water rocket before launch [2]

The Ascension III as shown in Figure 1.1 measured approximately 2.68 m in length and yet weighed less than 1.5 kg in mass as it was wholly made from non-metallic materials. At the top end of the rocket was the payload as shown in Figure 1.2. The payload contained an on-board flight computer, camera and a parachute which would be deployed to recover the rocket after it reached the apogee.

Figure 1.2: Payload and nose cone of Ascension III prior to launch [1]

Figure 1.3 is a photograph of the payload with the nose cone removed.

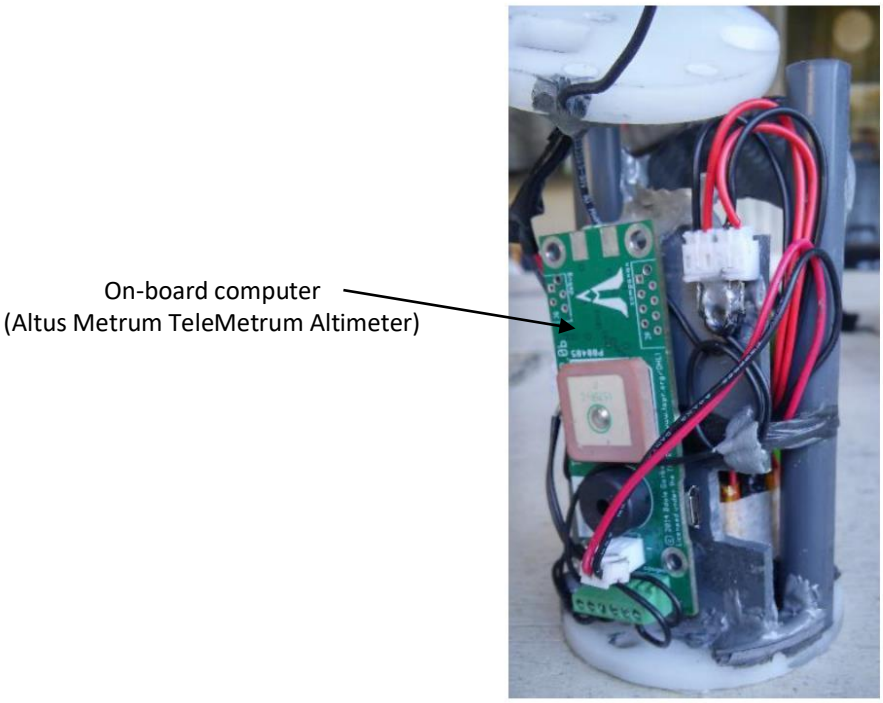

Figure 1.3: Partially assembled payload frame for test rocket [1]

The main component of the water rocket was the pressure vessel as shown in the drawing in Figure 1.4. It had a long thin-walled commercial filament wound CFRP cylindrical tube. These tubes are usually used in aerospace and ship-building industries for applications such piping networks [3,4]. Closing off and bonded to the two ends of the long CFRP tube, were two end caps (one with a nozzle and one without) both machined on a CNC lathe from Poly Vinyl Chloride (PVC) material. The pressure vessel would contain an air-water mixture (with 80% air and 20% water) held at 100 bar for 10 minutes before launching the rocket. The release of the pressurised mixture through the end cap with the nozzle provided the thrust required to propel the rocket upwards. Previous attempts to pressurise the CFRP pressure vessel hydrostatically during burst testing had resulted in leaking through the CFRP tube wall. This led Stuart to develop an innovative method of lining the inside wall of the CFRP tube with a thin rubber layer which proved successful in sealing the vessel and resulted in a patent application [5] being filed.

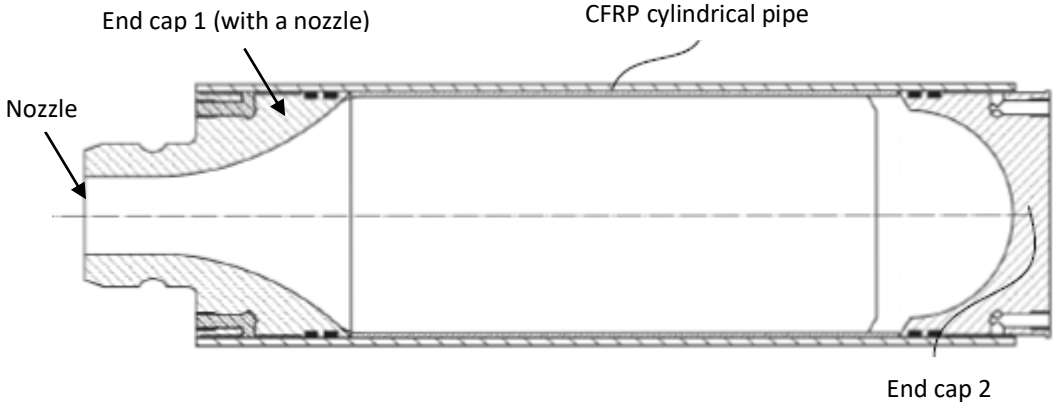

Figure 1.4: Schematic of the cross-sectional view of the CFRP pressure vessel derived from the water rocket [5]

The short documentary video of the world record attempt of the Ascension III water rocket can be found on this YouTube link: https://youtu.be/K8WP9QCa2co. The success of the water rocket project was identified to be primarily due to the novel, low-cost CFRP pressure vessel design that was developed. This gave rise to the idea to investigate possible alternative uses for the pressure vessel design. One area that could be explored was in Hydrogen Fuel Cell Powered Vehicles (HFCPVs) as a hydrogen gas storage vessel. As HFCPVs are considered a green technology, they have emerged as a potential replacement for the conventional Internal Combustion Engines (ICE) that burn fossil fuels [6]. The Hydrogen Fuel Cell (HFC) combines hydrogen with oxygen to give electrical energy before emitting water vapour as a by-product which is harmless to the environment and human beings alike [6–8]. The electrical energy produced by the HFC powers an electric motor that propels HFCPVs. However, for Hydrogen Fuel Cell Technology (HFCT) to be truly considered as a viable replacement for the conventional internal combustion engines, it must also be economically viable. Currently, HFCT is more expensive than ICE technology but important strides have been made towards significantly reducing the cost so that it can be more attractive to consumers [6,9]. Apart from the high cost associated with the HFCT, another significant challenge faced regarding its implementation is the storage of the hydrogen gas. The HFC does not have the capability of store the hydrogen gas within itself, thus, it must be stored in a storage vessel. Currently the most common method of storing hydrogen for HCFPVs is high pressure gas storage using high strength and lightweight Fibre Reinforced Plastic (FRP) composite pressure vessels. The novel, low-cost CFRP pressure vessel design was considered to be lightweight, low-cost, and yet strong enough to withstand the high storage pressures required. Therefore, in 2017, a project was partially funded by University of Cape Town's RCIPS Pre-Seed fund, for the further development of a commercial use of this novel pressure vessel. This report details the research aimed at determining the feasibility and suitability of the proposed pressure vessel concept for high pressure hydrogen gas storage for use in HFC applications.

To perform the investigation; initially the commercial filament wound CFRP tubes had to be designed and purchased. The CFRP tubes had to be safe enough to withstand the high pressures that are used in HFCPV applications. As the main component of the proposed pressure vessel, the CFRP tubes needed to be lightweight which would require optimization of the filament winding angle to maximize the burst or failure pressure. The mechanical properties of the CFRP tubes could be determined through standardized American Society for Testing and Materials (ASTM) tensile tests. These are important in performing stress and strain calculations that give information about the amount of CFRP material required and the consequent deformation behaviour of the CFRP tube. The water rocket end cap with a nozzle needed to be replaced by a new end cap design with connections that could be used to interface with industrial standard gas fittings. Stress analyses and material selection had to be performed on the end caps to ensure they would not yield or fracture due to the internal pressure load they would sustain. The adhesive bond on the end caps also had to be thoroughly tested to ensure there would not fail due to shear. The rubber liner's ability to prevent leakage through the CFRP tube wall also needed to be confirmed.

After assembling prototype CFRP pressure vessels, there are pressure tests that needed to be performed according to the American Society of Mechanical Engineers (ASME) Boiler and Pressure Vessel Code Section X for FRP pressure vessels [10]. This pressure vessel code is recognised by the South African Pressure Vessel Regulations of 2009 [11]. These codes are critical as they govern the certification of pressure vessels before use. As a minimum, the CFRP pressure vessels need to undergo hydrostatic burst tests, proof tests and leak tests. Initially, the hydrostatic burst tests would need to be performed to determine the pressure at which the CFRP pressure vessels would fail as well as the mode of failure. The maximum design pressure at which the CFRP pressure vessels could be safely operated at is derived from the failure pressure according to the FRP pressure vessel code [10]. The

proof tests are intended to assess the reliability and durability of the vessels while the leak tests are meant to detect any leaks. The leak tests are to be performed with a gas at the design pressure of the vessels and will provide a means to assess the ability of the rubber liner to prevent leakage. Air would need to be the first gas to be used in the leak tests before using a gas such as Helium which has smaller gas molecules. Helium gas would also serve as a suitable substitute for hydrogen gas which poses a significant safety risk for pressure vessel testing.

1.2 Plan of development

This report begins with the literature review in Chapter 2. The literature review describes the extensive background research on HFCT including the HFC, its applications and the methods of hydrogen storage in current use along with the ensuing challenges. Subsequently, the literature on the gas storage pressure vessels, their design, uses and testing methods are presented. The third sub-section under the literature review involves CFRP composite materials including how they are formed, used and analysed from a stress and strain perspective. The literature review chapter concludes with a description of the novel, low-cost CFRP pressure vessel concept that will be investigated. Chapter 3 involves the detailed aspects that were deployed in the design of the CFRP pressure vessel and Chapter 4 describes the tests that were performed on the vessels. The results of the tests in Chapter 4 are presented and discussed in Chapter 5. Chapter 6 articulates the conclusions that were drawn from the previous chapter(s) before giving recommendations for future use.

2. Literature review

To be able to design the proposed novel CFRP pressure vessel for hydrogen storage, all its aspects had to be adequately understood. This involved reviewing research on what has been done in the subject areas relating to the proposed vessel. The relevant subject areas pertaining to the proposed pressure vessel include the following:

- HFCT.
- Gas storage pressure vessels.
- CFRP composite materials.

This section delves into the content that is available on these subject areas in greater detail as well as links them to the proposed CFRP pressure vessel. Furthermore, this section will aim to highlight areas in previous studies that do not include the aspects of the proposed pressure vessel.

2.1 Hydrogen fuel cell technology

This section will initially describe what Hydrogen Fuel Cell Technology (HFCT) entails beginning with defining a hydrogen fuel cell, how it functions, and what fuels it. Subsequently, hydrogen as a fuel is discussed highlighting its pros and cons in comparison with conventional fossil-based fuels. The storage methods currently employed to store hydrogen are then briefly described with emphasis placed on the methods which pertain to hydrogen fuel cell powered vehicles.

2.1.1 Hydrogen fuel cell

A Hydrogen Fuel Cell (HFC) is basically a device that converts the mixture of hydrogen and oxygen gas into an electric current and water through electrolysis [12, 13]. The oxygen gas can be sourced from the atmosphere whilst the hydrogen has to be channelled from a storage vessel [12]. Typically, one HFC produces a small amount of current on its own, so to increase the electrical current (or energy) output, many are grouped together in series to produce a fuel cell stack [8]. The fuel stack will continue producing the electrical current so long as the HFCs in the stack are supplied with hydrogen and oxygen. The appeal of the HFC is derived from the fact that it produces no air pollution as it emits only water vapour as a by-product [6]. The HFC is becoming an increasing popular candidate to replace the conventional fossil fuel powered Internal Combustion Engine (ICE) that produces harmful carbon dioxide emissions [14–16]. There is a desperate need to reduce the carbon dioxide footprint which is the major cause of global warming by using clean technologies. An example is the HFCPV. However, there are still challenges associated with the HFC (e.g. cost of the system) that need to be overcome if it is to become economically viable in HFCPVs [6].

2.1.2 Hydrogen as a fuel

Hydrogen is considered a clean energy carrier and as mentioned, is a possible replacement for fossil based fuels [15, 16]. Hydrogen also has a higher energy content than most fossil fuels for the same mass of fuel [17] as can be seen in Figure 2.5. For example, hydrogen (120 MJ/kg) has almost three times the energy content of diesel (43 MJ/kg). On a volume basis, however, the situation is completely reversed in that hydrogen has an energy density of approximately 8 MJ/L whereas diesel has an energy density of 36 MJ/L. As a gas at atmospheric conditions, hydrogen contains even less volumetric energy content than that which is contained in gasoline of the same volume [15]. Hence, while the high gravimetric energy density of hydrogen makes it a more attractive fuel, it still has the distinct disadvantage of having a significantly lower volumetric energy density.

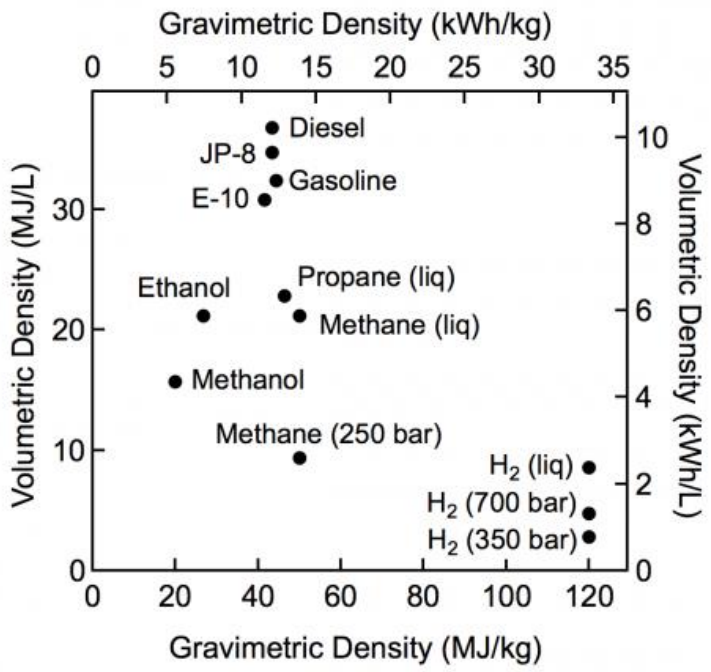

Figure 2.5: Comparison of gravimetric energy densities and volumetric energy densities for several fuels.[17]

2.1.3 Applications of HFCT

Broadly classified, HFCs are being used in stationary, portable and transportation applications [9, 17]. The choice of application is determined by various factors including the efficiency required, start-up time of the fuel cell and its dynamic behaviour [9]. Stationary applications as the name suggests, refer to instances where the HFCs used are fixed to one location as they are not designed to be moved. These applications require high efficiency (80% or higher) and quick tart-up times. An example is in Combined Heat and Power (CHP) systems usually used in residential areas in parts of Asia and Uninterruptible Power Systems (UPS) used to provide reliable backup power to grid systems in case of any disruptions [18]. Portable applications are where the HFCs are used in a more flexible manner and built into or charge up systems/devices designed to be moved around with relative ease [19]. Portable applications require relatively short start-up times for example in Auxiliary Power Units (APU) of lower power, small personal electronics and military applications that require off-the-grid operability [9, 19]. Relative to stationary or transportation applications of the HFC, portable applications have considerably lower power requirements (generally from 25W – 5kW) as their use is driven by the need to lower emissions and operating noise whilst efficiency is not a primary concern per se [9]. Finally, transportation applications are ones where the HFC is integrated into vehicular propulsion systems that provide power to vehicles [20]. Hydrogen Fuel Cell Powered Vehicles (HFCPVs) are an example of transport applications and they include light-duty cars, forklifts, buses, trucks, manned light aircraft, etc [20]. These HFCPVs include zero distributed emissions and better well-to-wheel efficiency than ICE powered vehicles [9]. HFCPV applications will be the primary focus of this report.

2.1.4 Hydrogen storage methods

Hydrogen storage is considered a key enabling technology for the HFC [17]. Figure 2.6 shows a simplistic top-down breakdown of the different methods in which hydrogen can be stored in its different phases of matter. The major categories shown are physical and material-based storage methods.

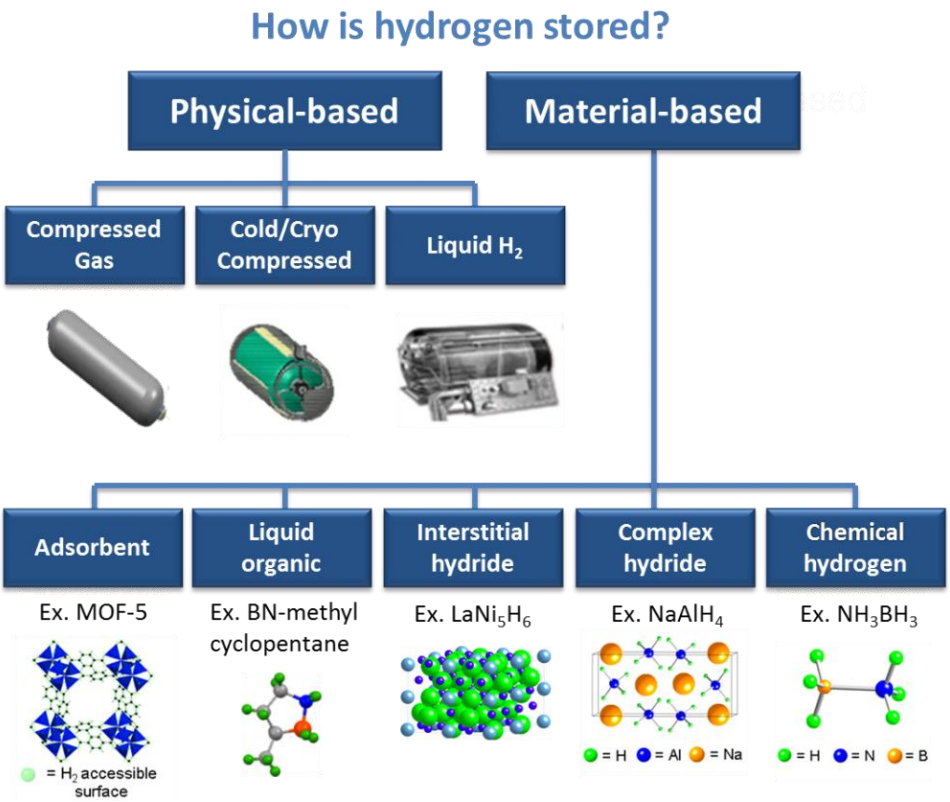

Figure 2.6: Illustration of the different methods of storing hydrogen [17]

2.1.4.1 Physical-based storage methods

The physical-based storage methods only deal with pure hydrogen in liquid or gaseous form [17]. There is a general consensus amongst various authors that physical storage methods are the most commonly used and advanced hydrogen storage methods available today for various applications [16, 21-22].

Compressed gas storage

Of the three available physical storage methods, compressed gas storage is the most widely used particularly in HFCPVs because of its simplicity in design and ease of implementation [16, 21, 23]. For stationary applications of HFCs, the gas is usually stored at low pressure but in high volumes since hydrogen gas has a relatively lower volumetric energy density [17]. However, for transport applications like in HFCPVs, large volume hydrogen tanks are not practical as space is at a premium [16, 23]. Because of the relatively low volumetric energy density of hydrogen gas, in HFCPVs, the hydrogen is typically stored at very high pressures that lie in the range of 350-700 bar [15]. The high pressures involved allow for the increase in gravimetric energy density of the hydrogen gas as more molecules can be fitted into the pressure vessel. Therefore, the higher the mass of hydrogen gas that can be stored, the more fuel that can be stored, resulting in a longer driving range for the HFCPV. For on-board storage of compressed hydrogen gas in HFCPVs, the medium of storage ought to be lightweight, inexpensive, safe, and take up as little space as possible [15, 21, 23]. The pressure vessels used to store hydrogen gas are mostly made from high strength Carbon Fibre Reinforced Plastic (CFRP) composites because of the need to reduce the weight contribution of the pressure vessel whilst not compromising on the strength of the vessel [16, 21]. Whilst these high strength CFRP composite vessels are lightweight, they still are expensive to manufacture [24]. The other concern regarding this storage method is safety, for instance in accidents where hydrogen gas might be exposed to fire which

could lead to a catastrophic explosion. On-going research is however, being conducted towards lowering the costs associated with storing the hydrogen gas within the CFRP composite pressure vessel [21, 25].

2.1.4.1.2 Liquid hydrogen storage

Liquid hydrogen exists at cryogenic temperatures (around -252°C) at an ambient pressure of 1 bar [17]. To maintain these cryogenic temperatures, specialist insulation equipment/material is required [23]. Liquid hydrogen has a higher volumetric energy density than hydrogen gas which lowers the pressure that is needed to store the liquid hydrogen [17]. However, the amount of energy expended in cooling the hydrogen to liquid form is at least 30 % of the energy within the hydrogen fuel itself. Furthermore, this energy requirement is about three times the amount required for compressed hydrogen storage [26]. In addition, liquid hydrogen evaporates easily which makes it unsuitable for long term storage and it might pose a safety hazard if the escaped hydrogen is ignited [27]. According to Zuttel [28], this restricts the possible use of these systems to applications where the cost of hydrogen is not a major issue and the fuel is expended in a short time, e.g. aerospace applications. Dublin et al suggest that while storing hydrogen as a liquid would increase the driving range of an HFCPV, it is unlikely that this method will be suitable for the HFCPVs in the future [23].

2.1.4.1.3 Cryo-compressed storage method

The third method illustrated in figure 2.4 under physical-based storage methods is called cold/cryo-compressed storage method. This method is a hybrid storage method that combines concepts from the two previously discussed physical storage methods. It involves cryogenic temperatures similar to those experienced in the liquid hydrogen storage method, but this method is flexible enough to have the hydrogen either in gaseous or liquid form [21]. Cryo-compressed hydrogen storage is generally preferred over the liquid hydrogen method because it is able to overcome the issue of evaporation of the hydrogen and also because there is less energy expended in cooling the hydrogen compared to traditional liquid hydrogen storage [23]. Because cooling the hydrogen gas increases the volumetric energy density of hydrogen, cryo-compressed hydrogen gas has more energy content (about 3 times more) than that of non-cooled compressed hydrogen gas [23]. However, the additional insulation required for this method adds significantly to the size, weight and the cost of the storage vessel [29]. This storage method shares the same application areas as the liquid hydrogen storage methods. However, from a cost perspective at this juncture in time, it is considered to be unsuitable for use in HFCPV applications [21].

2.1.4.2 Material-based storage methods

Hydrogen can also be stored on the surface of some solids through a process referred to as adsorption or within solids through another process called absorption in compounds referred to as hydrides [17].

2.1.4.2.1 Adsorption

This is a process that involves the adhesion of molecules of gas, liquid, or dissolved solids to a surface [30]. In this context, it describes a scenario by which hydrogen gas (H_2) molecules are adsorbed onto the surface of a material [17]. The reverse process to adsorption is referred to as desorption [31]. The materials used for this process include metal organic frameworks, carbon and other nanostructures which are commonly referred to as sorbents [16, 23]. Porosity and high surface areas for the aforementioned materials are required for this method to be effective in storing hydrogen [23]. In addition, the rate of adsorption also depends on the applied pressure and temperature [32]. "Despite the reversible nature of the hydrogen adsorption or desorption process for high surface area sorbents and carbon-based materials, they suffer from lower hydrogen capacity," according to Hwang et al [16].

It is a storage method with decent potential but further research is still required in order to improve on the shortcomings according to [16, 26, 33].

2.1.4.2.2 Chemical hydrides

A hydride is any class of chemical compound in which hydrogen atoms or molecules are combined with another element [34]. Metal hydrides often have higher gravimetric and volumetric energy densities as compared to the physical based storage methods [16, 23, 32]. A few metal hydrides have the potential for reversible on-board hydrogen storage and the ability to release hydrogen at relatively low pressures and temperatures (i.e. 1-10 bar and 25-100^{O}C) ideal for the HFC to function optimally [16, 29]. There also have been extensive studies done on complex hydrides (formed by Group I,II and III light metals [28]) that have shown high potential to improve on the gravimetric energy density of hydrogen. However, they still provide a relatively low hydrogen capacity and slow hydrogen uptake unsuitable for HFCPV systems [16]. Storing hydrogen fuel in chemical hydrides is considered a relatively safe and efficient storage method [28]. Conversely, for the current HFCPV market, the volumetric and gravimetric energy densities of the hydrogen produced is low and as such, there is still some room for improvement through further research into that area [21, 23, 26].

2.1.4.3 Comparison of the hydrogen storage methods

The Fuel Cell Technologies Office (FCTO) as part of the United States Department of Energy (US DOE), is one of the most recognised and leading organizations in the world that are responsible for developing regulations regarding on-board automotive hydrogen storage systems. There is a particular focus on systems that allow for a driving range of more than 300 miles (approximately 480 km) while meeting cost, safety, and performance requirements [17]. In Table 2.1 are the proposed targets for hydrogen storage methods for 2020 set by the FCTO [17]. The capacities of a storage system refer to the usable quantity of hydrogen deliverable to the fuel cell system divided by the total mass (or volume) of the complete storage system, including all stored hydrogen, media, and system components [17]. The capacities can be expressed in various quantities as shown in table 2.1 above. The underlying assumption when calculating the gravimetric capacities is that the system has a usable H_2 storage capacity of 5.6 kg which is a benchmark for lightweight vehicles [35]. There are other targets specified by the FCTO for 2020 which were excluded from the table for example durability and fuel quality were not included as they are not part of the scope of this report.

Table 2.1: FCTO proposed targets for hydrogen storage methods for 2020 [17]

	Storage parameter	**Unit(s)**	**2020 Target**
1	System Gravimetric Capacity (Net useful energy from hydrogen/maximum system mass)	kWh/kg (kg of H_2/kg of system)	1.5 (0.045)
2	System Volumetric Capacity (Net useful energy from hydrogen/maximum system volume)	kWh/L (kg of H_2/L of system)	1.0 (0.03)
3	Storage System Cost (Cost of the fuel)	$/kWh net ($/kg of H_2)	10 (333)

If all the targets in table 2.1 are met by any of the available storage methods, it would allow HFCPVs to at least compete with conventional ICE powered vehicles from an economic perspective as well as in terms of driving range. However, the ability to store hydrogen with a sufficiently high energy density remains a significant challenge for HFCPVs. Currently, none of the available hydrogen storage methods

have simultaneously met all of the set requirements proposed by the US DOE [17]. Compressed gas is the most widely used mature hydrogen storage method in HFCPVs currently according to multiple sources including [16, 21, 23, 25, 32]. In the short-term, it is the cheapest and easiest storage method to implement as seen by its use in the Honda Clarity FCX [36], Hyundai Tucson [37] and the Toyota Mirai [38]. However, it still has some disadvantages associated with it including the cost of the CFRP pressure vessel which needs to be significantly reduced without compromising on performance and safety as at least 75 % of the cost is attributed to the carbon fibre material [39]. While liquid hydrogen offers a higher volumetric energy density than compressed gas, it has problematic issues like boil off which result in the loss of the useable hydrogen and poses a safety risk [23, 27]. The relatively high amount of energy required for liquefaction also remains a challenge against the use of liquid hydrogen in HFCPVs [23]. The cryo-compressed storage method seems to address the boil-off issue for liquid hydrogen storage method whilst boasting a higher volumetric energy density at lower pressures than in the compressed hydrogen gas storage method. However, the relatively higher liquefaction energy as well as the cost and weight of the vessel remain a stumbling block for this method regardless of its potential in the current market [16, 29]. The two material-based storage methods still fall behind the physical-based storage methods in terms of ease of implementation and complexity in the short-term although there seems to be an agreement amongst several sources including [16-17, 25-26], that chemical hydrides and sorbents are the ideal long-term storage methods. However, Durbin et al [23] seem to disagree by suggesting that chemical hydrides are not a suitable storage media for on-board storage of hydrogen fuel in either the short-term or long-term. For this report, compressed gas storage is the sole focus of this research.

2.2 Gas storage pressure vessels

A pressure vessel is simply defined as a storage container that stores a fluid at a pressure higher than the atmospheric pressure [40]. The pressurised fluid can either be compressible or incompressible. A compressible fluid has a density and thus, volume, dependent on the pressure whilst an incompressible fluid's volume does not change with pressure [41]. In most cases, gases are considered as compressible fluids whilst liquids (such as water) are widely accepted as incompressible fluids in practice [41-42]. Because the fluid in a pressure vessel has a higher pressure than the ambient pressure, it usually makes them dangerous if the vessel was to burst or leak [43]. Hence, the higher the pressure within a pressure vessel, the higher the risk of injury or harm to whoever is within close range should the pressure vessel fail. Because of the risks posed by pressure vessels, safety precautions must be put in place to ensure that the level of the risks are lowered to the minimum [44]. One of the precautions involved with designing pressure vessels are pressure vessel codes which include large safety factors on strength. Safety factors in this regard are usually a ratio of the maximum allowable pressure within the vessel to the burst/failure pressure of the vessel [10]. Therefore, the higher the safety factor the lesser the risk. Other precautions can also lessen the risks involved with pressure vessels are the use of safety valves. Hence, what is critical in designing a pressure vessel is stress analysis, material selection, the fabrication process, and consideration of the underlying operating conditions [44-45]. Failure to adhere to any one of those aspects can lead to serious repercussions if a vessel were to fail and cause damage or injury [46].

2.2.1 Types of pressure vessels

This section will describe briefly the three common types of pressure vessels categorised according to their specific application. The three types of vessels are storage vessels, heat exchangers and process vessels [46-47]. Storage pressure vessels are used to store fluids at high pressure and they are the

most common of all vessels be it for industrial processes, commercial or residential use [46]. They can be of any shape including a cylindrical or spherical geometry though cylindrically shaped vessels are the most common because they are cheaper and less complex to fabricate [46, 48-49]. Storage vessels are used to store liquids or gases awaiting use in another process [47]. The second most common type of vessel is the heat exchanger type. A heat exchanger is a device used to transfer heat between two or more fluids [50]. The heat exchanger is used in different applications including refrigeration, vehicle cooling systems, air conditioning and within the food and service industry [46]. The third type of pressure vessel is the process vessel and it provides a medium in which processes can be performed such as blending, separation, cooling, purification and changing a material's state [51]. Process vessels often work in conjunction with the other two types of pressure vessels and they usually require specialized design and manufacturing to suit their specific function [46]. Examples of process vessels include columns and reactors [47]. Because this research is focussed on designing a vessel to store hydrogen gas, only storage pressure vessels will be further described.

2.2.2 Pressure vessel heads

A cylindrical pressure vessel has end caps that are also referred to as heads that close off the two ends of the vessel [52]. There are different types of pressure vessel heads with the commonly used in service being hemispherical, ellipsoidal, and torispherical heads [49, 53]. The hemispherical head shown in Figure 2.7 is an ideal shape for a head from a stress perspective because the pressure in the vessel is divided equally across the surface of the head [48], [53]. It is also the most efficient in terms of volume for storage since it is effectively half of a sphere although that makes it relatively more expensive to fabricate [54].

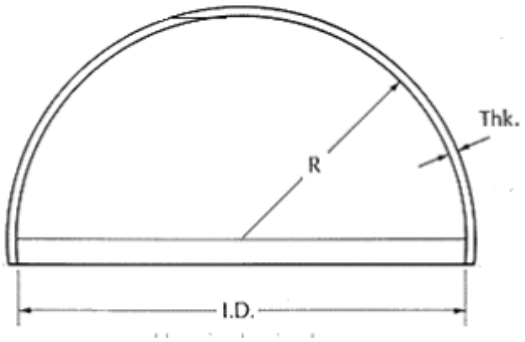

Figure 2.7: Typical hemispherical vessel head [48]

The ellipsoidal head has the shape of a semi-ellipse with the most common ratio used being 2:1 as shown in Figure 2.8 [54]. It also has a knuckle with a radius (KR) and is the transition between the cylindrical portion of the pressure vessel and the dish (DH). It has the advantage that the shape of this head is more economical, because the height of the head is just a quarter of the diameter of the cylindrical potion of the vessel [48]. However, the ellipsoidal head is not as efficient at handling stresses as the hemispherical head, hence, they tend to require thicker walls [54].

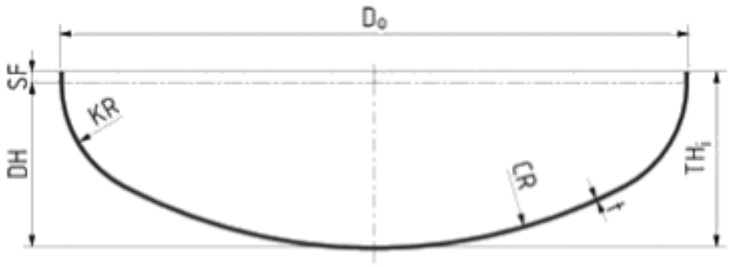

Figure 2.8: Typical ellipsoidal vessel head [48]

A torispherical head has a dish with a fixed radius (CR) as shown in Figure 2.9, the size of which depends on the type of torispherical head [48]. Like the ellipsoidal head, the torispherical head also has a knuckle.

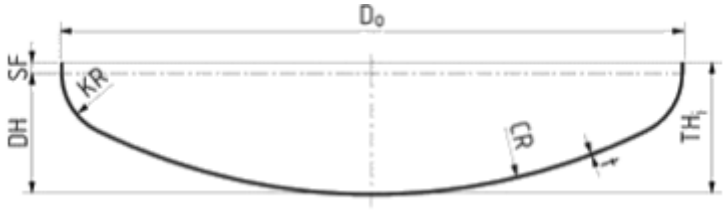

Figure 2.9: Typical torispherical vessel head [48]

As stated, the ellipsoidal and torispherical heads are cheaper to fabricate than the hemispherical head [53]. The torispherical head also takes up the least amount of space as it results in the shortest vessel length [54]. However, it still lags in terms of efficiency when dealing with stresses as compared to a hemispherical head which makes the head thicker and possibly heavier [53-54].

2.2.3 Pressure vessel codes

Before a pressure vessel can be used be it for commercial or industrial purposes, it should be certified according to standards or codes that are specific to a particular region or country in which the pressure vessel is to be used. There are commonly used pressure vessel standards globally which include the following:

- ASME (American Society of Mechanical Engineers) Boiler and Pressure Vessel Code (BPVC) used in the United States of America [55].
- The Pressure Equipment Directive (PED 2014/68/EU) [56], the Transportable Pressure Equipment Directive (TPED 2010/35/EU) [57], and the Simple Pressure Vessels Directive (SPVD 2009/105/EC) all applicable in Europe [58].
- CODAP: French Code for Construction of Unfired Pressure Vessel [59].
- B51-09 Canadian Boiler, pressure vessel, and pressure piping code [60].

For South Africa, the Pressure Vessel Regulations of 2009 [11] (fall under the Occupational Health and Safety Act (1993) for South Africa) govern the design, manufacture, operation, repair, modification, maintenance, inspection and testing of pressure equipment with a design pressure equal to or greater than 50 kPa (0.5 bar) [11]. Hence, the proposed CFRP pressure vessel falls under this category as it will be a pressure vessel with a design pressure greater than 50 kPa. The South African National Standard (SANS) 347 of 2012 [61] falls under the Pressure Equipment Regulations of 2009 and it further deals with the categorization and conformity assessment, as well as the selection of health and safety standards of pressure equipment for use by users, certification bodies and approved inspection authorities. However, the pressure standards available in South Africa [61] and [11] predominantly

have regulations and rules that apply to metallic pressure vessels. The ASME Pressure Vessel Code Section X [10] is recognised under the above mentioned regulations within South Africa and it deals specifically with Fibre Reinforced Plastic (FRP) pressure vessels which therefore applies to the CFRP pressure vessel pertaining to this research.

2.2.4 Hydrogen gas storage pressure vessels

As described previously, compressed gas storage of hydrogen fuel is the most widely used method for storing hydrogen for HFC applications. The reasons being its simplicity, lower cost and ease of implementation. It does however have one major disadvantage which is its relatively lower volumetric energy density capacity even after compressing the gas between 350-700 bar. However, it is arguably the most mature hydrogen storage method on the market currently [16, 21, 23, 25, 32]. There are currently four types of defined pressure vessels (Type I, II, III and IV) being used to store compressed hydrogen gas for various applications. The choice of the storage pressure vessel to use is based on the type of HFC application which requires a compromise between technical performances and cost [26]. Figure 2.10 pictorially summarizes the structural differences between the 4 types of hydrogen gas storage tanks.

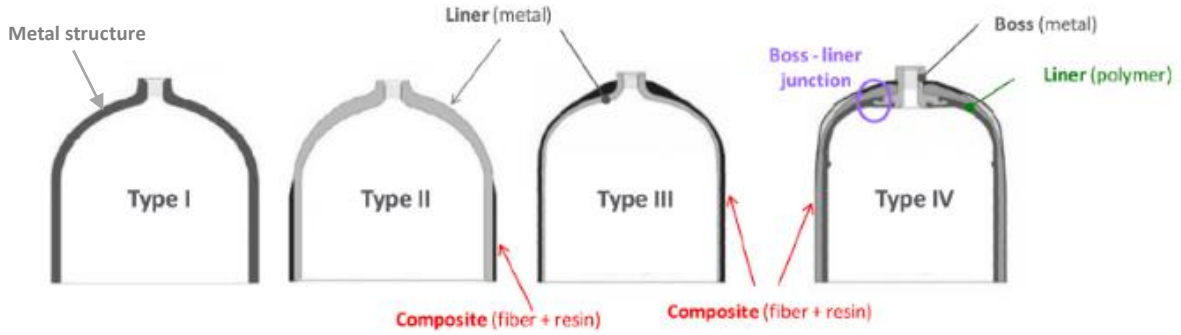

Figure 2.10:Schematic illustrating the structural differences in the Type I, II, III and IV hydrogen gas storage tanks [26]

Type I pressure vessel

This is a pressure vessel wholly constructed from a metallic material usually either steel or aluminium [24, 62]. Figure 2.11 shows an example of a typical Type I pressure vessel. Type I vessels are characterised by being bulky and heavy because of the relatively high mass densities of metals. They can store hydrogen gas at pressures up to approximately 200 bar which is the lowest operating pressure of the four types of vessels [26]. They are easy to manufacture and are the least expensive of all types of hydrogen gas storage pressure vessels. They are usually used in stationary applications because space or volume is not a substantial issue in these applications [17]. According to Jorgensen et al [21, 24], they are not suited for applications like HFCPVs because they take up a significant amount of space and would contribute significantly to the weight of the system.

Figure 2.11: Type I metallic hydrogen gas storage tanks [63]

Type II pressure vessel

This is a hybrid pressure vessel with a metallic pressure vessel (or thick metallic lining) with FRP material hoop-wrapped onto the outer surface of the vessel excluding the ends [24]. It is less bulky than a Type I vessel, and it can sustain higher pressures (up to 300 bar) owing to the added strength attributed to the FRP windings. Type II pressure vessels are about 50% more expensive to manufacture than Type I pressure vessels while being about 30-40% lighter [62]. They are also used in stationary applications when there is a need for higher storage pressures to those offered by Type I vessels [26].

Type III pressure vessel

This pressure vessel is made of a thin, rigid pre-formed aluminium liner with filament-wound FRP windings [24]. The FRP composite carries most of the load while the aluminium liner acts as a gas diffusion barrier. Type III vessels are similar to Type II vessels though they differ in that Type III vessels are wholly wound with layers of FRP material (including the ends) whereas Type II are only partially wound. Furthermore, in Type III pressure vessels, the fibres carry practically all the load as opposed to Type II pressure vessels where the load is shared between the fibres and the metallic section [62]. Because the FRP has a relatively high strength-to-weight ratio, Type III vessels have very high strength and yet weigh less than Type I or II vessels. They are capable of pressures in the range 350-700 bar in operation [28]. They are ideally suited for transportation applications like HFCPVs. However, they are considerably more expensive than Type I and II vessels with the majority of the cost attributed to the reinforced polymer materials.

Type IV pressure vessel

This is similar to a Type III pressure vessel with the difference being that where there is an aluminium pre-formed liner for a Type III, there is a pre-formed polymeric based liner for Type IV pressure vessels. A typical Type IV pressure vessel is shown in Figure 2.12 [62]. The polymer liners of type IV pressure vessels can be obtained by roto-moulding, blow moulding or by welding injected domes to extruded tubes of polymer [26]. Type IV vessels have very high strength and are lighter compared to all the types of hydrogen storage pressure vessels. They are also similarly capable of pressures in the range 350-700 bar as Type III vessels making them suited for use as on-board storage vessels for HFCPVs

[24]. However, the cost of manufacturing Type IV vessels is still an issue making them not yet viable [16, 21, 24]. The normalised cost (cost per kilogram of H_2 gas stored) for Type IV pressure vessels (350 bar and 700 bar) ranges between US$500 and US$700 as of 2015 i.e. between R6800 and R9520 [64]. Refer to Appendix E for a detailed cost breakdown of the two types of Type IV pressure vessels

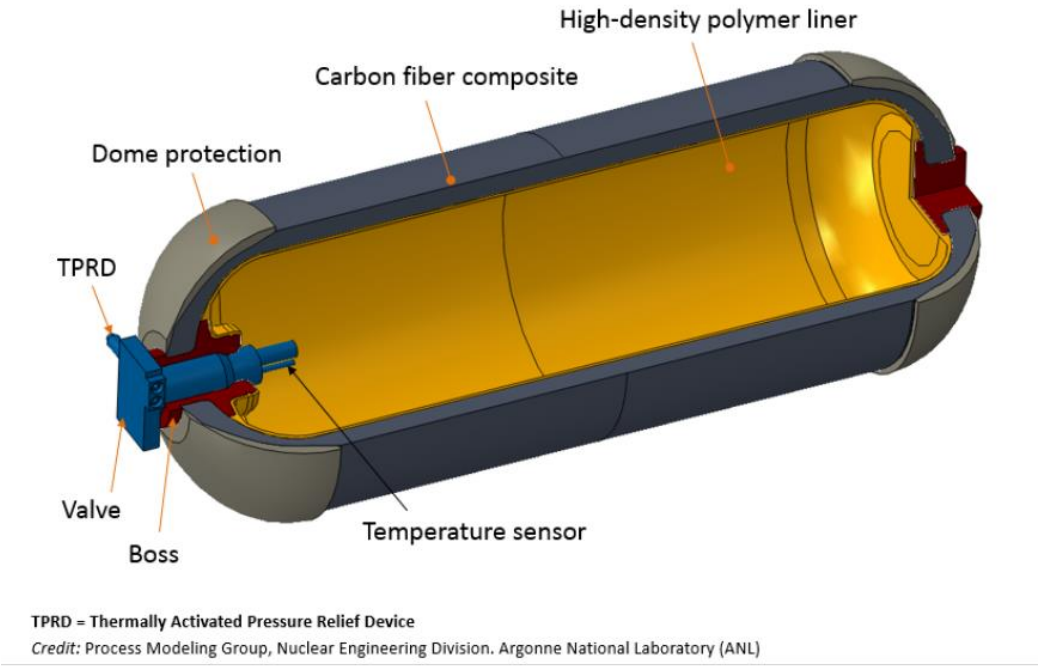

Figure 2.12: Type IV CFRP filament-wound tank [65]

Summary on the types of hydrogen gas storage pressure vessels

Below in Table 2.2 is a list of the different types of pressure vessels that are used to store hydrogen gas with the working pressures of each type of vessel.

Table 2.2: Comparison of the working pressures for the types of hydrogen storage vessels [66]

Type	Description	Working Pressure
I	Purely metallic tank	up to 200 bar
II	Metallic tank with carbon fibre windings	up to 300 bar
III	CFRP Filament Wound Tube with Aluminium Liner	350 - 700 bar
IV	CFRP Filament Wound Tube with Polymeric liner	350 -700 bar

Type I and II pressure vessels take up more space as they are bulkier and heavier than Type III and IV pressure vessels [21, 26]. Type III and IV are made from high strength FRP composites that have a better strength-to-weight ratio than metals. From a cost perspective, Type III and IV are more expensive than Type I and II pressure vessels (because of the costs of the material and manufacturing processes) but since space within a HFCPV is at a premium, Type III and IV are preferred. The only difference between Type III and IV pressure vessels is the liner material as they have similar pressure ranges and constructed from the same reinforcement fibrous materials.

2.2.5 Testing of pressure vessels

The safety of pressure vessels is of critical importance, hence, pressure vessels must undergo rigorous testing to ensure they attain the desired safety level depending on the application in which they are utilised. There are two categories under which most pressure tests fall under namely destructive and non-destructive tests. A destructive test is a method where the test specimen is destroyed irreparably mainly to determine mechanical properties such as strength [67]. For destructive tests, water is normally utilised through hydrostatic tests due to the fact that it is safer because the incompressible nature of water results in it releasing significantly less energy released when the vessel fails [68]. Nevertheless, pneumatic tests (i.e. using air as the gas) can still be used in pressure systems that are designed in such a way as that they cannot be filled with water [68]. Non-Destructive Tests (NDT) are employed to assess the vessels to check for in-service fitness, leak tightness and the reliability [68–70].

According to the ASME pressure vessel code for FRP pressure vessels, some of the following common tests ought to be performed on prototype FRP pressure vessels are as listed in Table 2.3 [10]:

Table 2.3: Pressure tests for prototype FRP pressure vessels

Name of test	**Description**
Burst test	A destructive test where the pressure vessel is filled with water and pressurized until it fails [67]. The purpose of this test is to determine the strength of the vessel as well as the maximum design pressure it can operate at. For CFRP pressure vessels, the maximum design pressure ought to be 2.25 times smaller than the failure pressure [10].
Proof test	A NDT that is used to test the reliability and durability of a pressure vessel in a controlled setting [71]. These pressure tests check if the vessel can withstand a pressure slightly higher than the design pressure without leaking or enduring permanent deformation.
Leak test	A NDT that aims to detect and localize any leaks from a pressure vessel [72]. This test utilises techniques such as bubble testing using dry air or measures trace gases using a mass spectrometer to detect any leaks from the pressure vessel.
Fatigue test	A test whereby the pressure vessel undergoes cyclical pressure loads (i.e. pressurizing and depressurizing) to determine the number of cycles the vessel can withstand before failure. The test aims to understand how the pressure vessel will perform under similar conditions in actual use [73].

The burst, proof and leak tests will be considered as part of the scope of this research.

2.2.6 Stress determination for a cylindrical pressure vessel

When a typical cylindrical pressure vessel with closed ends has a fluid stored within it at a pressure higher than that of the atmosphere, stresses will be induced in the vessel because of that pressure. Hence, determining the strength of a pressure vessel is important in the design of pressure vessels as it guides the designer in selecting suitable materials and appropriate dimensions for the vessel to be constructed.

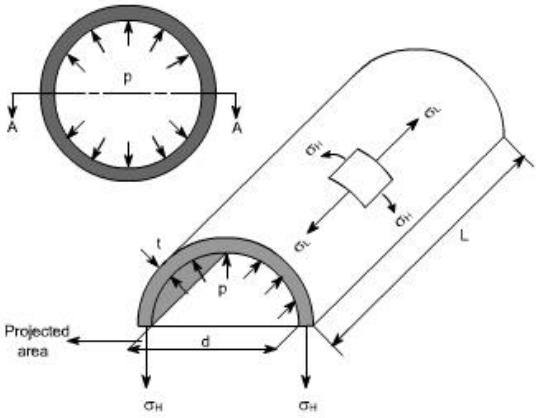

Figure 2.13: Illustration of the stresses induced within a typical cylindrical pressure vessel [74]

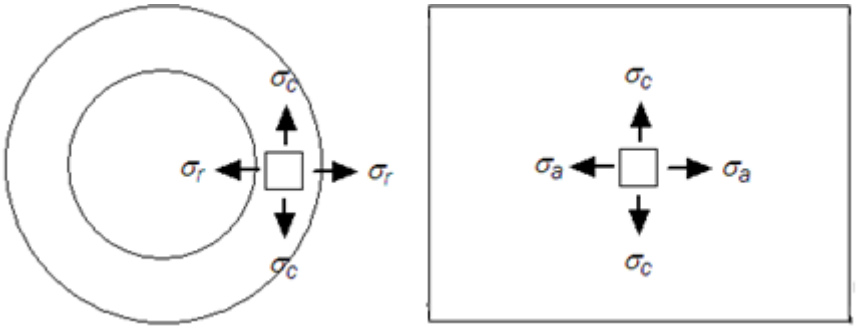

Figure 2.14: Illustration of all the stresses induced by an internal pressure in a vessel [75]

The types of stresses induced in a pressure vessel are usually classified into 3 types which are described below

- Hoop stress – it acts in the circumferential direction of the vessel. It is denoted by σ_H in Figure 2.13 and as σ_c in Figure 2.14.
- Longitudinal stress - acts in the direction along the axis of the cylinder. It is denoted by σ_L in Figure 2.13 and σ_a in Figure 2.14.
- Radial Stress - acts orthogonally to the axis of symmetry in the radial direction and is denoted as σ_r in Figure 2.14.

There are two theories generally used to analyse and determine stresses induced in a typical cylindrical pressure vessel. These include the Thin Cylinder and Thick Cylinder theories [76]. The Thin Cylinder theory is applicable if the internal diameter to wall thickness ratio is smaller than or equal to 20. Alternatively, in the case that the same ratio is less than 20 then the Thick Cylinder theory would apply. Another distinction between the two theories is that the radial stress is considered negligible by the Thin Cylinder theory whilst it is applicable with respect to Thick Cylinder theory. The two theories are described in detail in the following sub-sections:

Thin cylinder theory

The hoop stress (acting in the circumferential direction) is calculated using the following equation [77]

$$\sigma_H = \frac{PD_i}{2t} \quad \textbf{[2.1]}$$

where *P* is the internal pressure in the vessel, D_i is the internal diameter of the cylindrical section and *t* is the thickness of the vessel.

The longitudinal stress value is equivalent to half of the magnitude of the hoop stress and is calculated using the following equation [77].

$$\sigma_L = \frac{PD_i}{4t} = \frac{1}{2}\sigma_H \quad \textbf{[2.2]}$$

The radial stress is considered negligible with respect to the thin cylinder theory.

Thick cylinder theory

The hoop and radial stresses are calculated using the Lamé's equations [76] as shown below.

$$\sigma_H = A + \frac{B}{r^2} \quad \textbf{[2.3]}$$

$$\sigma_R = A - \frac{B}{r^2} \quad \textbf{[2.4]}$$

where **r** is any value of radius between the internal radius ($\mathbf{R_1}$) to the external radius ($\mathbf{R_2}$) of the cylinder, and **A** and **B** are Lamé's constants. To evaluate the constants A and B, two known conditions are needed. For this particular case, the conditions are summarised as follows:

$$(a)\ \ r = -R_1,\ \sigma_R = -P$$

$$(b)\ \ r = -R_2,\ \sigma_R = 0$$

It should be noted that the first condition infers that the radial stress is the negative of the internal pressure because the radial stress is causing the compression of the wall of the cylindrical vessel hence the radial stress is negative. Substituting for the two known conditions into equations 2.3 and 2.4 will result in the following equations for A and B:

$$A = \frac{PR_1^{\,2}}{R_2^{\,2} - R_1^{\,2}} \quad \textbf{[2.5a]}$$

$$B = \frac{PR_1^{\,2}R_2^{\,2}}{R_2^{\,2} - R_1^{\,2}} \quad \textbf{[2.5b]}$$

Thus,

$$\sigma_H = P\left[\frac{\left(R_2 / r\right)^2 + 1}{k^2 - 1}\right] \quad \textbf{[2.5]}$$

where $k = R_2 / R_1$

The longitudinal stress, given the aforementioned two known conditions, is calculated using the following formula [76] :

$$\sigma_L = \frac{PR_1^2}{R_2^2 - R_1^2} = A \quad \textbf{[2.6]}$$

2.3. Carbon Fibre Reinforced Plastic Composites

A composite is a material which consists of two or more distinct constituent materials combined at a macroscopic level where the materials are not soluble in each other [3]. Composites are popular material choices because one can tailor the properties of the resulting composite [78]. Carbon Fibre Reinforced Plastic (CFRP) is a type of fibre reinforced composite that offers a higher strength-to-weight ratio than most metals although is relatively more expensive [79]. It is formed by combining carbon fibres (reinforcing material) and a polymeric resin (matrix). The carbon fibres provide the required strength of the composites as they carry most of the applied loads whilst the resin holds the fibres together and transfers the loads to the fibres.

2.3.1 Applications of CFRP

CFRP composites are desired because of their relatively high tensile strength and elastic modulus as previously mentioned [3, 4]. This allows them to be used extensively in applications where there is need to use as little material as possible without compromising on strength. Such popular applications are in high performance industries like in aerospace and automotive [80]. There are also other desirable mechanical properties of CFRP composites including the high fatigue strength, good corrosion resistance and a small coefficient of thermal expansion [81]. High fatigue strength is an attractive trait for a CFRP pressure vessel as it would endure many cycles of pressurization and depressurization. The good corrosion resistance of CFRP composites makes sure that they will not react with the contents of the vessel as well as external elements from the atmosphere.

2.3.2 Types of carbon fibre fabric

After carbon fibre has been manufactured, it can be offered in different forms of fabric depending on the intended use [82]. A fabric is defined by long fibres (of carbon, aramid or glass) bundled to create tows which are then woven to produce a flat sheet of one or more layers of fibres of various forms [83]. The types of fabric differ according to their fibre orientations and the manufacturing method. Common types of fibre orientations are unidirectional and woven.

Unidirectional fabric

Unidirectional (UD) fabric is composed of bundles (or tows) of carbon filaments all oriented in the same direction as shown in Figure 2.15 [80]. It is useful in applications where most of the applied load on an object is in a particular direction allowing for it to be placed precisely where it is required, and in the optimum quantity (no more or less than required) [84]. This also has the effect of minimizing the weight of the constructed object. Furthermore, UD fibres are straight and not crimped which results in the highest possible fibre properties from the fabric in composite component construction [84].

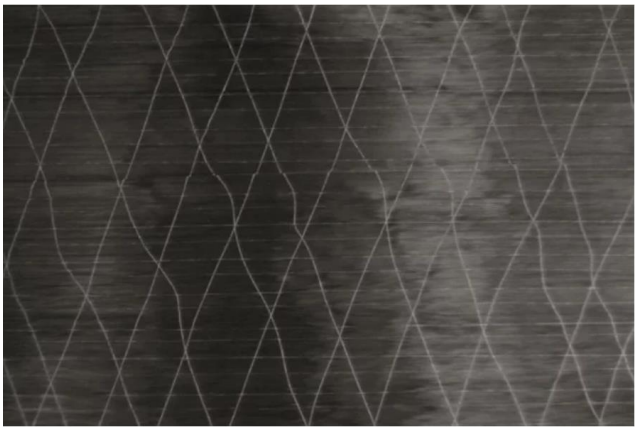

Figure 2.15: Unidirectional fabric [80]

However, it is not as flexible as woven cloth because of its single dimensional rigidity which makes it unlikely to use in applications where loads can come from all directions and it is sometimes more difficult to place into position [78, 82].

Woven fabrics

They are produced by the linking of warp fibres and weft fibres in a regular pattern or weave style and their integrity is maintained by the mechanical interlocking of the fibres [85]. There are several weave styles available for example plain weave and twill weave. The plain weave is the most fundamental weave where tows are woven together at right angles propagating laterally and vertically across the cloth as shown in Figure 2.16. As such, loads can be applied in multiple axes and the composite will retain its stiffness [80]. Its distinct pattern is not the strongest of all the weave patterns, but it is the one of the easiest to handle [86].

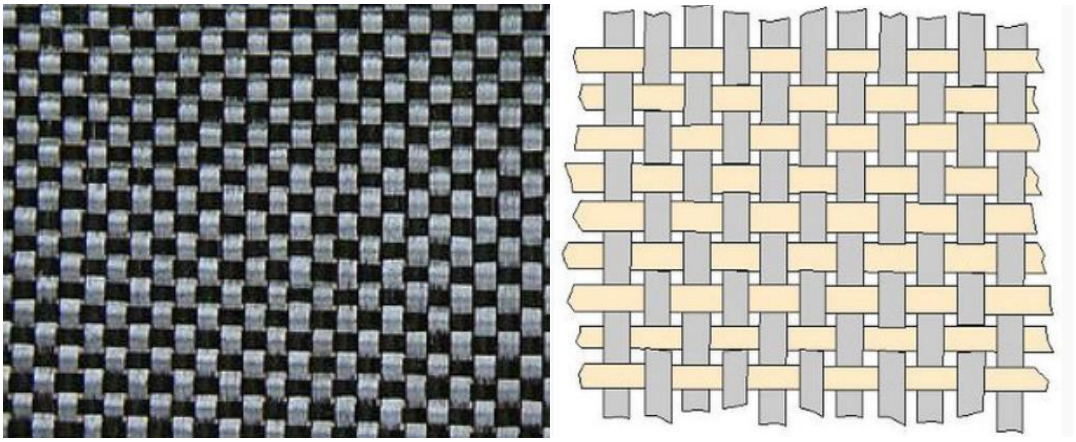

Figure 2.16: Actual (left) and simplified (right) version of plain weave pattern [86]

The twill weave fabric has one or more warp fibres alternately weaving over and under two or more weft fibres in a regular repeated manner [85]. An example of a 2x2 twill weave illustrated in Figure 2.17. The twill weave is more complex and modern than the plain weave pattern [80]. However, it is more flexible and has good durability for when complex shapes are required [82].

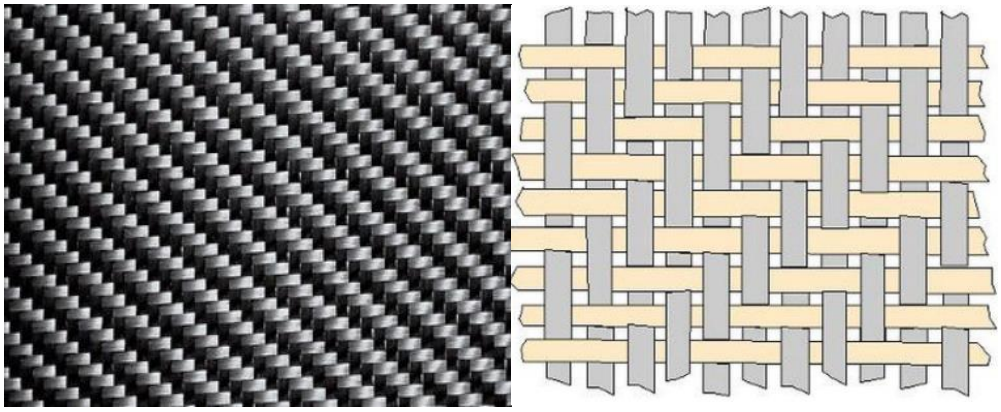

Figure 2.17: Actual (left) and simplified (right) version of Twill weave pattern [86]

Because of the scope of this report, where filament wound tubes will be used, unidirectional fibre is what will be focussed on in this report.

2.3.3 Manufacturing methods for CFRP composites

There are several ways in which composites (CFRP included) can be manufactured. The choice of manufacturing method depends on several factors including the intended application, type of matrix and fibres, temperature to form and cure the matrix, the geometry of the end product and cost effectiveness of the process [87]. The two major types of manufacturing methods are open moulding and closed moulding [4, 88]. Below is a brief description of each method and the respective advantages.

- Open mould processes – they involve placing the resin and the fibres in an open mould where they cure and harden when exposed to the atmosphere. Typical open mould processes include hand lay-up, spray-up, casting, and filament winding.
- Closed mould processes – they involve processing composite materials and curing them within vacuum bags on matched die moulds that are closed to the atmosphere for example hot press moulding. These processes are suited for when high production volumes are required.

In this work, the focus will be primarily on the filament winding process that will be used to manufacture the cylindrical section of the proposed CFRP pressure vessel.

Filament winding

This is a process of constructing open or closed composite objects such as cylindrical tubes or pressure vessels [89]. It is achieved when continuous reinforcements (for example UD tape or tow), either previously impregnated with a matrix material or impregnated during the winding, are placed over a rotating mandrel [90]. Dry winding is the type of filament winding operation that winds prepregs (i.e. ready-made tape composed of fibres pre-impregnated with resin [3, 91]) onto the mandrel directly without using resin [92]. Wet winding alternatively, is where fibre strands or tows are impregnated with resin in a bath immediately before they make contact with the mandrel as shown in Figure 2.18 [4, 93]. Wet winding is advantageous in that it is inexpensive and allows one to accurately control the properties of the composite [3]. On the other hand, dry winding is cleaner, but more expensive and thus quite uncommon [3]. Hence, the choice of which filament winding process is driven by application specific factors which may include cost and control of the final properties of the composite object.

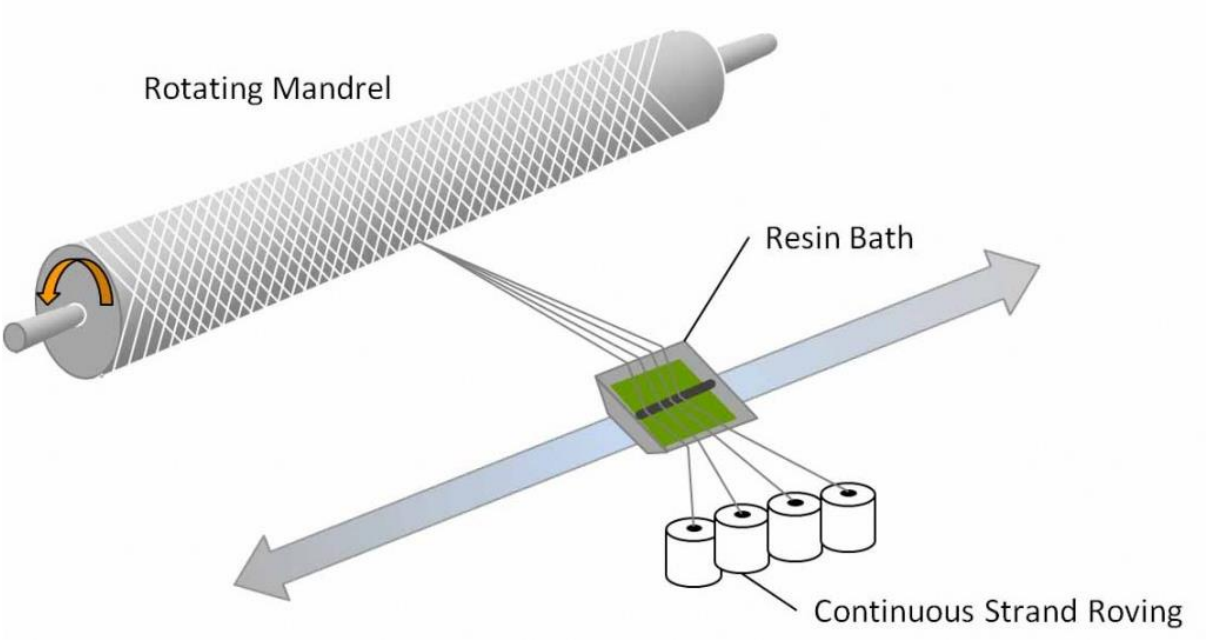

Figure 2.18: Illustration of the wet filament winding process [94]

2.3.4 Strength analysis of composites

As a composite material consists of two or more constituents, the analysis of the mechanical behaviour and design of such materials is different from that for conventional homogeneous isotropic materials such as metals [3]. Isotropic in the context of materials means that the material has the same properties in all directions whilst homogeneous materials are ones that have the same properties at all points on that material [4]. Composites commonly fall in neither category. For example if a CFRP composite is pulled along the fibre direction, it will have a different tensile strength as compared to pulling in a direction transverse to the direction of the fibres, hence it is anisotropic. Composites are heterogeneous which can be observed when the properties are analysed for different points. For example, the properties differ between a point which has fibre and one that has the matrix material.

2.3.4.1 Micromechanical analysis of composites

Micromechanics analyses the interaction between the two constituent materials and their properties on a microscopic level with the aim of trying to predict the final properties of the composite [3, 78]. To determine the properties of a composite, ordinarily experiments have to be conducted on the material to determine its properties. Experiments usually are time consuming and expensive so in order to resolve those issues, micromechanical models have been developed to try to predict the properties of the composite basing on the properties of the known constituent materials [4, 78].

Fibre volume and mass fraction

The volume fraction of fibres within a composite is the ratio of the volume of fibres compared to the total volume of the composite. The fraction of fibres within the composite can also be expressed in terms of mass though the volume fraction of fibres is more commonly used [4]. The volume fraction of fibres (V_f) can be expressed as follows:

$$V_f = \frac{v_f}{v_f + v_m} \quad \textbf{[2.8a]}$$

where v_f is the volume of the fibres and v_m is the volume of the matrix.

It should be noted that equation 2.8a is only applicable when the volume occupied by voids (v_{void}) in the composite material is insignificant [3], [87]. To include the effects of voids, equation 2.8a can be rewritten as follows:

$$V_f = \frac{v_f}{v_f + v_m + v_{void}} \quad \textbf{[2.8b]}$$

The mass fraction of fibres can be expressed as follows:

$$M_f = \frac{m_f}{m_f + m_m} \quad \textbf{[2.9]}$$

Where m_f is the mass of the fibres and m_m is the mass of the matrix.

The concept of the volume fraction of fibres is critical to the evaluation of the stiffness and strength properties of the composite [3].

Density

Density of the composite can be derived from the volume fractions as shown below:

$$m_c = m_f + m_m \quad \textbf{[2.10]}$$

where m_c is the mass of the composite

Rewriting the equation in terms of volume and density and simplifying further:

$$\rho_c v_c = \rho_f v_f + \rho_m v_m$$

$$\rho_c = \rho_f \frac{v_f}{v_c} + \rho_m \frac{v_m}{v_c}$$

$$\rho_c = \rho_f V_f + \rho_m V_m \quad \textbf{[2.11]}$$

The above result means that the density of the composite can be determined from the densities and volume fractions of the fibres and the matrix.

Void content

During the manufacture of laminated composites, there is a possibility of the formation of voids due to air being trapped in the material [87].Voids have the effect of exaggerating the density of a composite and can be detrimental to its mechanical properties for example transverse tensile strength, fatigue resistance, and moisture resistance [3]. If the volume occupied by voids is less than 5% then their effects are considered insignificant [87]. The space occupied by voids (v_{void}) in a composite laminate can be estimated by comparing the theoretical density with its actual density of the composite using the following equation [87]:

$$v_{void} = \left(\frac{\rho_{ct} - \rho_{ce}}{\rho_{ct}} \right) 100 \quad \textbf{[2.12]}$$

where ρ_{ct} is the theoretical density of the composite and ρ_{ce} is the experimental density of the composite.

Stiffness properties

The mechanical properties to be covered in this section are listed as follows:

- Elastic longitudinal modulus, E_1.
- Elastic transverse modulus, E_2.
- Major Poisson's Ratio, v_{12}.
- In-plane shear modulus, G_{12}.

The strength approach used to determine the above mentioned constants is based on the following assumptions [3, 78, 91]:

- The bond between fibres and the matrix is perfect.
- The elastic moduli, diameters, and spaces between fibres are uniform.
- The fibres are continuous and parallel.
- The fibres and matrix are linearly elastic and follow Hooke's law.
- The fibres possess uniform strength.
- The composite is free of voids.

However, these listed assumptions are not necessarily true in practice.

Elastic longitudinal modulus (E_1)

This is the elastic modulus of the composite along the direction of the fibres. If a force, P, pulls on the lamina element shown in Figure 2.19 below, it will undergo a strain (ε_1) as well as a stress (σ_1) on its cross section.

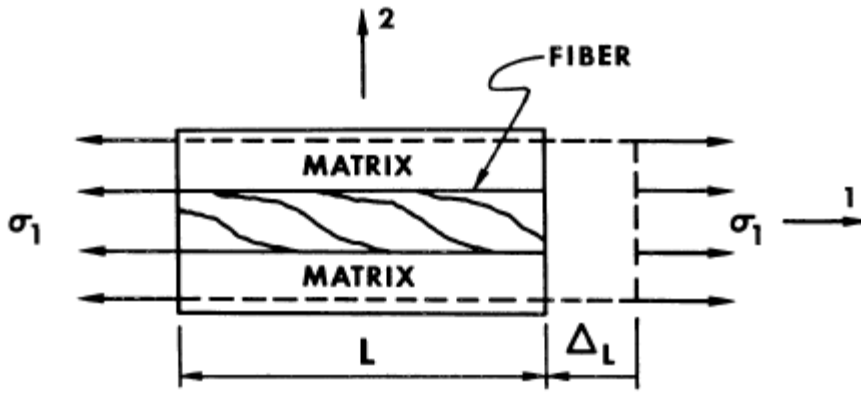

Figure 2.19: Portion of a unidirectional lamina that is being pulled in the 1-direction (along the fibre direction) [78]

The strain can be calculated as follows:

$$\varepsilon_1 = \frac{\Delta L}{L} \quad \textbf{[2.12]}$$

where ΔL is the extension and L is the original length.

The strain, ε_1, is the same between the fibres and the matrix as they stretch by the same amount across the portion of the lamina. The stresses in the fibres and the matrix are expressed as follows

$$\sigma_f = E_f \varepsilon_1 \quad \textbf{[2.13]}$$

$$\sigma_m = E_m \varepsilon_1 \quad \textbf{[2.14]}$$

The average stress across the lamina (σ_1) acts on the cross-sectional area (A_1) of the portion of the lamina. The stress across the fibres and the matrix acts on the respective areas A_f and A_m. The resultant force, P, is shared by the fibres and can be expressed as follows

$$P = \sigma_1 A_1 = \sigma_f A_f + \sigma_m A_m \quad \textbf{[2.15]}$$

Substituting for the stresses and removing of the common factor ε_1:

$$E_1 A_1 = E_f A_f + E_m A_m$$

$$E_1 = E_f \frac{A_f}{A_1} + E_m \frac{A_m}{A_1}$$

Where the ratios of the areas can be expressed as volume fractions [78]:

$$E_1 = E_f V_f + E_m V_m \quad \textbf{[2.16]}$$

Hence, the longitudinal elastic modulus is a function of the volume fractions and the elastic moduli of the fibres and the matrix. The equation to determine the elastic longitudinal modulus is commonly known as the rule of mixtures [3, 78]. It can be inferred that the volume fraction of the fibres contributes largely to the longitudinal modulus as the modulus of the fibres is larger than that of the matrix to a greater extent. It can thus, be reasonably concluded that the longitudinal modulus is dominated by the fibres.

Elastic transverse modulus (E_2)

This is the elastic modulus measured transverse to the direction of the fibres. In this case, instead of pulling a sample lamina in the fibre direction, the lamina will be pulled in the transverse (orthogonal) direction as shown in Figure 2.20. Due to the pulling of the lamina in the 2-direction, the fibres and the matrix are assumed to have a common stress, σ_2. The strains therefore are different for the fibres and the matrix. The two strains can be expressed by rearranging equations 2.13 and 2.14 as shown below:

$$\varepsilon_f = \frac{E_f}{\sigma_2} \quad \textbf{[2.17]}$$

$$\varepsilon_m = \frac{E_m}{\sigma_2} \quad \textbf{[2.18]}$$

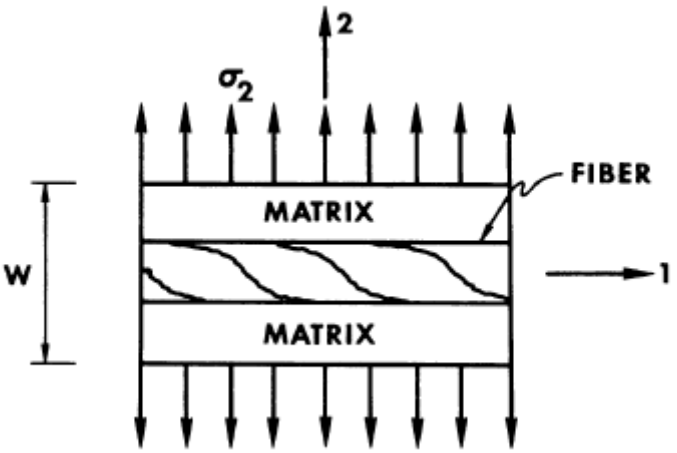

Figure 2.20: Representative portion of a unidirectional lamina being pulled in the 2-direction (transverse to the fibre direction) [78]

The total extension and hence strain of the lamina shown above, is the sum of the strains in the fibres and that of the matrix. The original lengths of the fibres and the matrix can be approximated in terms of the volume fractions as $V_f W$ and $V_m W$ respectively (where W is the length of the element in Figure 2.20 in the loading direction).

Hence,

$$\Delta W = \varepsilon_2 W = \varepsilon_f V_f W + \varepsilon_m V_m W$$

$$\varepsilon_2 = \varepsilon_f V_f + \varepsilon_m V_m \qquad \textbf{[2.19]}$$

Substituting for the for the strain equations above:

$$\varepsilon_2 = \frac{\sigma_2}{E_f} V_f + \frac{\sigma_2}{E_m} V_m \qquad \textbf{[2.20]}$$

But $\varepsilon_2 = \frac{\sigma_2}{E_2}$ hence:

$$\frac{\sigma_2}{E_2} = \frac{\sigma_2}{E_f} V_f + \frac{\sigma_2}{E_m} V_m$$

$$\frac{1}{E_2} = \frac{1}{E_f} V_f + \frac{1}{E_m} V_m$$

$$E_2 = \frac{E_m E_f}{V_f E_m + V_m E_f} \qquad \textbf{[2.21]}$$

From the equation for E_2 above, it can be deduced that the fibres do not contribute significantly to the transverse modulus unless if the fibre volume fraction is impractically high i.e. (about 70 percent or more) [78]. Therefore, the transverse modulus is considered to be matrix dominated.

Major Poisson's ratio (v_{12})

The Major Poisson's ratio can be defined as the negative ratio of the strain in the transverse direction to that of the longitudinal direction when a composite is loaded the longitudinal direction only.

$$v_{12} = -\frac{\varepsilon_2}{\varepsilon_1} \qquad \textbf{[2.21]}$$

where ε_1 is the longitudinal strain and ε_2 is the transverse strain.

If it is assumed that the composite is to be loaded in the direction parallel to the fibres (see Figure 2.21) and that the strains within the fibres is similar to those in the matrix in the 1-direction.

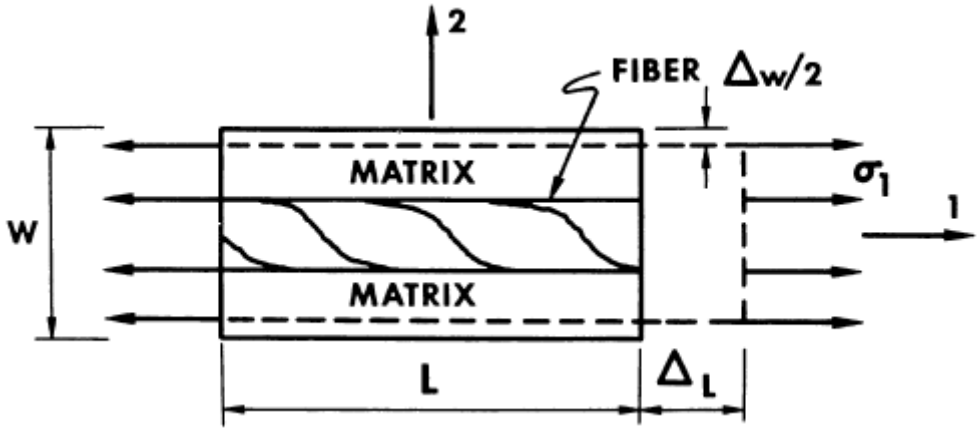

Figure 2.21: Representative volume element loaded in the direction parallel to the fibres i.e. 1-direction [78]

The transverse extension (Δw) of the volume element shown above can be expressed as follows

$$\Delta w = -\varepsilon_2 \cdot W = v_{12} \cdot \varepsilon_1 \cdot W \qquad \textbf{[2.22]}$$

where *W* is the length of the element in Figure 2.21 in the direction transverse to the loading direction.

The transverse extension can also be expressed as the sum of the extensions of the fibres and of the matrix:

$$\Delta w = \Delta w_f + \Delta w_m \qquad \textbf{[2.23]}$$

Treating the transverse strains in the fibres and the matrix separately, they can be expressed in terms of the respective Poisson's ratios and volume fractions as follows [78]:

$$\Delta w_m = W \cdot V_m \cdot v_m \cdot \varepsilon_1 \qquad \textbf{[2.24]}$$

$$\Delta w_f = W \cdot V_f \cdot v_f \cdot \varepsilon_1 \qquad \textbf{[2.25]}$$

Combining the previous equations, the expression for the Major Poisson's ratio simplifies to:

$$v_{12} = v_f \cdot V_f + v_m \cdot V_m \qquad \textbf{[2.26]}$$

The equation of the Major Poisson's ratio (2.26) is also a variation of the rules of mixtures method [91].

In-plane Shear Modulus (G_{12})

The main assumption used in the determination of this constant is that the fibres and the matrix have the same shear stresses.

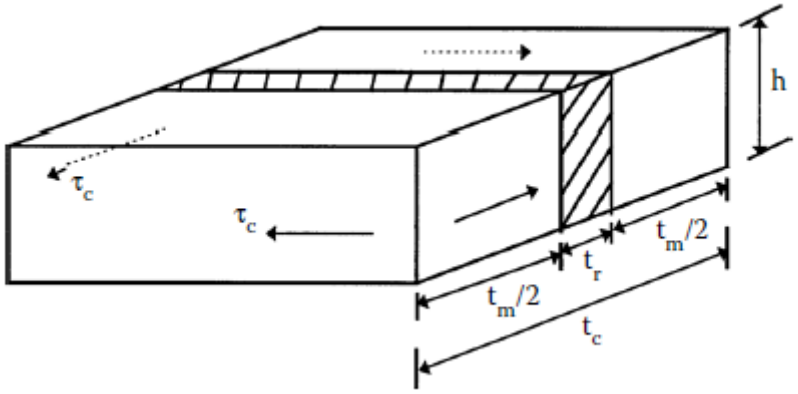

Figure 2.22: Representative volume element with an in-plane shear stress applied onto it [3]

If such an in-plane stress is applied to the volume element shown in Figure 2.22 above, the resulting shear deformation, δ_C, can be expressed as follows:

$$\delta_c = \delta_f + \delta_m \qquad \textbf{[2.27]}$$

Expressing the shear deformations in terms of shear strains:

$$\delta_c = \gamma_c t_c \qquad \textbf{[2.28]}$$

$$\delta_f = \gamma_f t_f \qquad \textbf{[2.29]}$$

$$\delta_m = \gamma_m t_m \qquad \textbf{[2.30]}$$

where γ_c, γ_f, and γ_m are shear strains of the composite, fibres and matrix respectively

t_c, t_f and t_m are the thicknesses of the composite, fibres and matrix respectively

The shear strains can also be defined in terms of the in-plane shear modulus and shear stresses:

$$\gamma_c = \frac{\tau_c}{G_{12}} \qquad \textbf{[2.31]}$$

$$\gamma_f = \frac{\tau_f}{G_f} \qquad \textbf{[2.32]}$$

$$\gamma_m = \frac{\tau_m}{G_m} \qquad \textbf{[2.33]}$$

where τ_c, τ_f and τ_m are the composite, fibre and matrix shear stresses respectively

G_f and G_m are the shear moduli for the fibres and the matrix respectively

Combining the equations above and replacing ratios of thicknesses as volume fractions, yields the following expression of the in-plane shear modulus of the composite[3]:

$$G_{12} = \frac{G_f G_m}{G_m V_f + G_f V_m} \qquad \textbf{[2.34]}$$

Micromechanics also allows designers of composite laminate structures to see the effect of the property values of the constituent materials without having to construct the physical composite structure. However, micromechanical models have within themselves, considerable inherent limitations [78]. An example is the assumption made that there is a perfect bond between the matrix and the fibres which is not necessarily true in practice. Hence, there is a need to validate the discrepancy between the theoretical predictions with the actual experimental data.

2.3.4.2 Macromechanical analysis of composites

Macromechanical analysis involves studying the material behaviour basing on the main assumption that the composite is homogeneous and that the effects of the constituent materials are detected only as averaged apparent properties of the composite material [78].

Unidirectional Lamina

A unidirectional lamina (also referred to as a ply) is a flat singular layer of fibres arranged parallel to each other within a matrix. Figure 2.23 is an illustration of a unidirectional lamina.

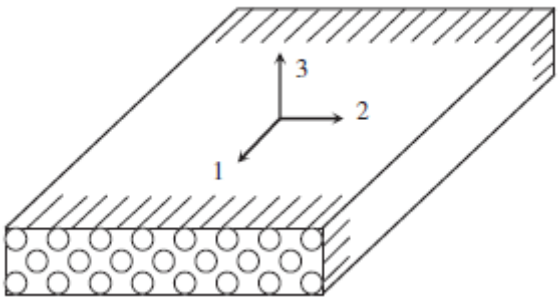

Figure 2.23: A unidirectional lamina [95]

When laminae are bonded and stacked on top of one another, a laminate is formed as shown in Figure 2.24. Each lamina within a laminate may have fibres oriented in different directions as well as different thicknesses to other laminae within the laminate.

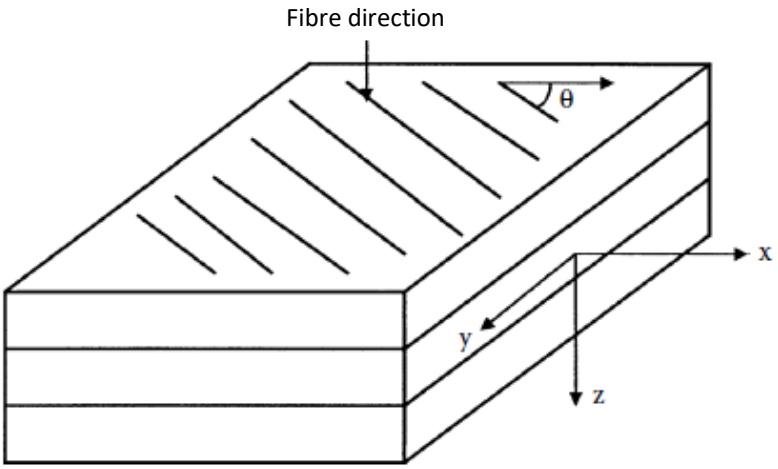

Figure 2.24: Typical laminate structure[3]

Therefore, the building block of the laminate is a lamina, hence, understanding the mechanical analysis and behaviour of a single lamina would need to precede the understanding of a laminate [3].

Laminate codes

Each laminate structure has a laminate code that describes the angle of orientation of each laminar relative to the next lamina. An example of such a code is [10/45/90] which describes a laminate structure with the first layer having an angle of 10°, the next at 45° and the last oriented at 90° in that order from top to bottom along the z-axis.

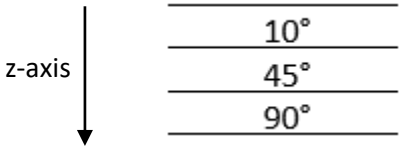

There are several common ways into which laminates can be formed. Below are two types of special laminates accompanied by a description:

- Balanced Laminate - A laminate is balanced if layers at angles other than 0° and 90°occur only as plus and minus pairs of + θ and – θ [3]. An example is [+50/-50/+50/-50].
- Symmetric Laminate - A laminate is called symmetric if the material, angle, and thickness of plies are the same above and below the mid-plane [3]. An example is [20/40/40/20] usually denoted as $[20/40]_s$.

Stress-strain relationships for a lamina

The stress-strain relationships for composite materials are more complicated to express than those for isotropic material. Making the assumption that composite materials are linear and elastic is widely considered acceptable whilst assuming that composite materials are isotropic is considered unacceptable [3]. Therefore, it follows that Hooke's Law applies to composites [91].

A unidirectional lamina falls under the orthotropic material category which are materials that have three mutually perpendicular planes of material symmetry [78]. They are considered a subset of anisotropic materials because their properties change when measured from different loading directions [3].

Hence, the stress-strain relationship for an orthotropic material is more complicated than the one for isotropic materials. An orthotropic material in a three-dimensional (3D) stress state, can be described by the following system of equations:

$$\begin{bmatrix} \sigma_1 \\ \sigma_2 \\ \sigma_3 \\ \tau_{23} \\ \tau_{31} \\ \tau_{12} \end{bmatrix} = \begin{bmatrix} C_{11} & C_{12} & C_{13} & 0 & 0 & 0 \\ C_{21} & C_{22} & C_{23} & 0 & 0 & 0 \\ C_{31} & C_{32} & C_{33} & 0 & 0 & 0 \\ 0 & 0 & 0 & C_{44} & 0 & 0 \\ 0 & 0 & 0 & 0 & C_{55} & 0 \\ 0 & 0 & 0 & 0 & 0 & C_{66} \end{bmatrix} \bullet \begin{bmatrix} \varepsilon_1 \\ \varepsilon_2 \\ \varepsilon_3 \\ \gamma_{23} \\ \gamma_{31} \\ \gamma_{12} \end{bmatrix} \quad \textbf{[2.35]}$$

Where the 6 x 6 matrix is called the stiffness matrix [C]. To the left of matrix [C] is the stress vector while strain vector is to the right side.

In the stress vector on the left-hand side of the equation, σ represents a normal stress is a certain direction and τ represents a shear stress in a certain plane. Similarly, in the strain vector on the right-hand side, ε represents a normal strain in a certain direction and γ represents a shear strain in a certain plane.

However, if a lamina is sufficiently thin and does not carry any out of plane loads, one can assume plane stress conditions [3],[95] i.e. $\sigma_3 = \tau_{23} = \tau_{31} = 0$. This will reduce the 3D system of equations to a two-dimensional (2D) problem with the following system of equations which are easier to analyse and solve.

$$\begin{bmatrix} \sigma_1 \\ \sigma_2 \\ \tau_{12} \end{bmatrix} = \begin{bmatrix} Q_{11} & Q_{12} & 0 \\ Q_{12} & Q_{22} & 0 \\ 0 & 0 & Q_{66} \end{bmatrix} \bullet \begin{bmatrix} \varepsilon_1 \\ \varepsilon_2 \\ \gamma_{12} \end{bmatrix} \quad \textbf{[2.36]}$$

Where the 3 x 3 matrix is now referred to as the Reduced Stiffness Matrix, Q, which is different to the Stiffness matrix, [C]. Alternatively, the equation 2.36 can be rewritten as follows

$$\begin{bmatrix} \varepsilon_1 \\ \varepsilon_2 \\ \gamma_{12} \end{bmatrix} = \begin{bmatrix} S_{11} & S_{12} & 0 \\ S_{12} & S_{22} & 0 \\ 0 & 0 & S_{66} \end{bmatrix} \bullet \begin{bmatrix} \sigma_1 \\ \sigma_2 \\ \tau_{12} \end{bmatrix} \quad \textbf{[2.37]}$$

Where the 3 x 3 matrix is referred to as the Compliance Matrix which is the inverse of the Reduced Stiffness Matrix [Q].

The four elements (S_{11}, S_{12}, S_{22} and S_{66}) of the compliance matrix, S, can be evaluated from the following four independent engineering elastic constants shown below:

- E_1 – Elastic Modulus along the fibres in the lamina
- E_2 – Elastic Modulus transverse to the fibre direction in the lamina
- v_{12}- Major Poisson's Ratio
- G_{12} – In-plane shear modulus for the plane 1-2

These four independent engineering constants can be found empirically through mechanical testing for example using ASTM (American Society for Testing and Materials) tests [96]. Then the following

equations relate the elements of the compliance matrix and the independent constants as shown below [3, 78]:

$$S_{11} = \frac{1}{E_1}, \qquad \textbf{[2.38]}$$

$$S_{12} = -\frac{\nu_{12}}{E_1}, \qquad \textbf{[2.39]}$$

$$S_{22} = \frac{1}{E_2} \qquad \textbf{[2.40]}$$

$$S_{66} = \frac{1}{G_{12}} \qquad \textbf{[2.41]}$$

The engineering constants can be related to the elements from the reduced stiffness matrix [Q] as follows:

$$\nu_{21} = \nu_{12} \times \frac{E_2}{E_1} \qquad \textbf{[2.42]}$$

where ν_{21} is the Minor Poisson's ratio.

$$Q_{11} = \frac{E_1}{1 - \nu_{12}\nu_{21}}, \qquad \textbf{[2.43]}$$

$$Q_{12} = \frac{\nu_{12}E_2}{1 - \nu_{12}\nu_{21}}, \qquad \textbf{[2.44]}$$

$$Q_{22} = \frac{E_2}{1 - \nu_{12}\nu_{21}} \qquad \textbf{[2.45]}$$

$$Q_{66} = G_{12} \qquad \textbf{[2.46]}$$

Stress-strain relationships for an angled lamina

An angled lamina is one in which the fibres are aligned at an angle, θ, to either one of the principal axes (i.e. x and y axes) as shown in Figure 2.25. Angled lamina are common in practice because sometimes loads applied on laminae do not act along any one of the principal directions.

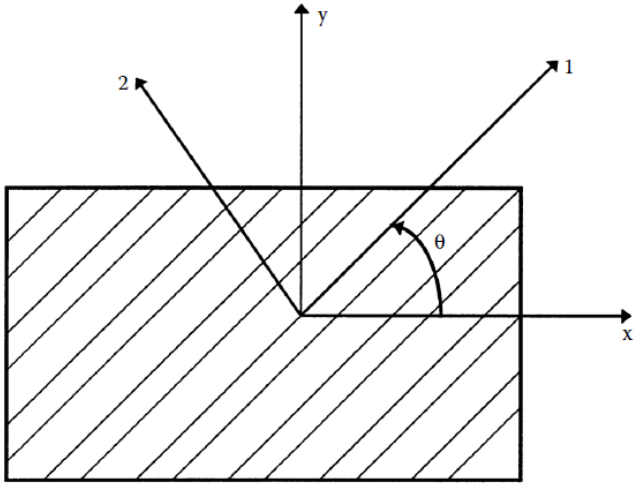

Figure 2.25: Angled lamina with fibres oriented at an angle, ϑ, to the x-axis [3]

Referring to Figure 2.25, fibres are oriented in the 1-direction which is orthogonal to the 2-direction. The 1 and 2 axes are referred to as the local (or material) axes and the x and y axes are called global axes. Commonly, stresses and strains would initially be dealt with in the global axis system before being transformed into the local axis system. The stresses and strains from the global axes are related to those of the local axes system through a transformation matrix [T] that incorporates the angle θ into them as shown below [3, 90]:

$$\begin{bmatrix} \sigma_1 \\ \sigma_2 \\ \tau_{12} \end{bmatrix} = [T] \bullet \begin{bmatrix} \sigma_x \\ \sigma_y \\ \tau_{xy} \end{bmatrix} \quad \textbf{[2.47]}$$

$$\text{and} \begin{bmatrix} \varepsilon_1 \\ \varepsilon_2 \\ \frac{\gamma_{12}}{2} \end{bmatrix} = [T] \bullet \begin{bmatrix} \varepsilon_x \\ \varepsilon_y \\ \frac{\gamma_{xy}}{2} \end{bmatrix} \quad \textbf{[2.48]}$$

$$\text{Where } T = \begin{bmatrix} \cos^2\theta & \sin^2\theta & 2\sin\theta\cos\theta \\ \sin^2\theta & \cos^2\theta & -2\sin\theta\cos\theta \\ -\sin\theta\cos\theta & -\sin\theta\cos\theta & \cos^2\theta - \sin^2\theta \end{bmatrix} \quad \textbf{[2.49]}$$

Combining equations 2.9 and 2.20 yields the following equation:

$$[Q] \bullet \begin{bmatrix} \varepsilon_1 \\ \varepsilon_2 \\ \gamma_{12} \end{bmatrix} = [T] \bullet \begin{bmatrix} \sigma_x \\ \sigma_y \\ \tau_{xy} \end{bmatrix} \quad \textbf{[2.50]}$$

The left-hand side of equation 2.48 can be rewritten as shown in equation 2.51 before combining with equation 2.50 and can be expressed as follows:

$$\begin{bmatrix} \varepsilon_1 \\ \varepsilon_2 \\ \gamma_{12} \end{bmatrix} = [P] \bullet \begin{bmatrix} \varepsilon_1 \\ \varepsilon_2 \\ \frac{\gamma_{12}}{2} \end{bmatrix} \qquad \textbf{[2.51]} \quad where\,[P] = \begin{bmatrix} 1 & 0 & 0 \\ 0 & 1 & 0 \\ 0 & 0 & 2 \end{bmatrix}$$

$$[Q] \bullet [P] \bullet \begin{bmatrix} \varepsilon_1 \\ \varepsilon_2 \\ \frac{\gamma_{12}}{2} \end{bmatrix} = [T] \bullet \begin{bmatrix} \sigma_x \\ \sigma_y \\ \tau_{xy} \end{bmatrix}$$

$$[Q] \bullet [P] \bullet [T] \bullet \begin{bmatrix} \varepsilon_x \\ \varepsilon_y \\ \frac{\gamma_{xy}}{2} \end{bmatrix} = [T] \bullet \begin{bmatrix} \sigma_x \\ \sigma_y \\ \tau_{xy} \end{bmatrix} \qquad \textbf{[2.52]}$$

Equation 2.51 can be rearranged as shown below before being substituted into equation 2.52 to give equation 2.53. After simplifying equation 2.53, one will arrive at equation 2.54:

$$\begin{bmatrix} \varepsilon_x \\ \varepsilon_y \\ \frac{\gamma_{xy}}{2} \end{bmatrix} = [P]^{-1} \bullet \begin{bmatrix} \varepsilon_x \\ \varepsilon_y \\ \gamma_{xy} \end{bmatrix} \qquad \textbf{[2.51]}$$

$$\begin{bmatrix} \sigma_x \\ \sigma_y \\ \tau_{xy} \end{bmatrix} = [T]^{-1}[Q] \bullet [P] \bullet [T] \bullet [P]^{-1} \bullet \begin{bmatrix} \varepsilon_x \\ \varepsilon_y \\ \gamma_{xy} \end{bmatrix} \qquad \textbf{[2.53]}$$

$$\begin{bmatrix} \sigma_x \\ \sigma_y \\ \tau_{xy} \end{bmatrix} = \begin{bmatrix} \bar{Q}_{11} & \bar{Q}_{12} & \bar{Q}_{16} \\ \bar{Q}_{12} & \bar{Q}_{22} & \bar{Q}_{26} \\ \bar{Q}_{16} & \bar{Q}_{26} & \bar{Q}_{66} \end{bmatrix} \bullet \begin{bmatrix} \varepsilon_x \\ \varepsilon_y \\ \gamma_{xy} \end{bmatrix}$$

$$\begin{bmatrix} \sigma_x \\ \sigma_y \\ \tau_{xy} \end{bmatrix} = [\bar{Q}] \begin{bmatrix} \varepsilon_x \\ \varepsilon_y \\ \gamma_{xy} \end{bmatrix} \qquad \textbf{[2.54]}$$

Where $[\bar{Q}]$ is referred to as the transformed reduced stiffness matrix. The elements of the $[\bar{Q}]$ can be calculated as follows [3]:

$$\bar{Q}_{11} = Q_{11}\cos^4\theta + Q_{22}\sin^4\theta + 2(Q_{12} + 2Q_{66})\sin^2\theta\cos^2\theta \quad \textbf{[2.55]}$$

$$\bar{Q}_{12} = (Q_{11} + Q_{22} - 4Q_{66})\sin^2\theta\cos^2\theta + Q_{12}(\sin^4\theta + \cos^4\theta) \quad \textbf{[2.56]}$$

$$\bar{Q}_{22} = Q_{11}\sin^4\theta + Q_{22}\cos^4\theta + 2(Q_{12} + 2Q_{66})\sin^2\theta\cos^2\theta \quad \textbf{[2.57]}$$

$$\bar{Q}_{16} = (Q_{11} - Q_{12} - 2Q_{66})\sin\theta\cos^3\theta - (Q_{22} - Q_{12} - 2Q_{66})\cos\theta\sin^3\theta \quad \textbf{[2.58]}$$

$$\bar{Q}_{26} = (Q_{11} - Q_{12} - 2Q_{66})\sin^3\theta\cos\theta - (Q_{22} - Q_{12} - 2Q_{66})\sin\theta\cos^3\theta \quad \textbf{[2.59]}$$

$$\bar{Q}_{66} = (Q_{11} + Q_{22} - 2Q_{12} - 2Q_{66})\sin^2\theta\cos^2\theta + Q_{66}(\sin^4\theta + \cos^4\theta) \quad \textbf{[2.60]}$$

After determining each element of matrix [Q], one can use equation 2.54 to determine the global stresses acting on a lamina if the global strains are known. Alternatively, one can also determine the global strains if the global stresses are known.

Failure theories for laminae

For isotropic materials like metals, there exists failure theories which serve the purpose of attempting to predict the failure stress and/or strains of an object made of those materials that has been subjected to a load. Failure theories allow for more efficient designs depending on their relative accuracies in predicting when the composites will fail. Hence, depending on the application, no lesser or greater amount of material need to be utilised for that application as determined by the failure theory used. Composites also have failure theories that differ to those of isotropic materials. For composites, the strength of laminate structures is related to the strength of each individual lamina and the connectors between the laminae [3]. "This allows for a simple and economical method for finding the strength of a laminate using the various failure theories," as suggested by Dametew [97].

Maximum Stress failure theory

Similar to isotropic materials (e.g. steel), there is a Maximum Stress failure theory for a unidirectional lamina for composites as well. However, where isotropic materials have two main strength parameters (normal and shear stresses), laminae have five strength parameters in total, two (tension or compression stresses) for each principal material axis direction i.e. in the direction that is parallel to the fibres and the one transverse to the fibres [91]. The fifth parameter is the shear stress acts parallel to the 1-2 plane. Because laminae are not isotropic, they have different strengths in different directions of loading. The longitudinal direction refers the direction parallel to the fibres and the transverse direction refers to the direction at right angles to the fibre direction. The strength parameters are listed below:

$\sigma_{1-uts-C}$ - Ultimate Longitudinal Stress in Compression

$\sigma_{1-uts-T}$ - Ultimate Longitudinal Stress in Tension

$\sigma_{2-uts-C}$ - Ultimate Transverse Stress in Compression

$\sigma_{2-uts-T}$ - Ultimate Transverse Stress in Tension

τ_{12-max} - Ultimate Shear Stress

The conditions for the Maximum Stress failure theory are that the applied stresses (σ_1, σ_2 or τ_{12}) should not exceed any of the above ultimate stresses for each type of loading.

$$-\sigma_{1-uts-C} \leq \sigma_1 \leq \sigma_{1-uts-T} \quad \textbf{[2.61]}$$

$$-\sigma_{2-uts-C} \leq \sigma_2 \leq \sigma_{2-uts-T} \quad \textbf{[2.62]}$$

$$-\tau_{12-max} \leq \tau_{12} \leq \tau_{12-max} \quad \textbf{[2.63]}$$

Maximum Strain failure theory

The Maximum Strain failure theory is based on the maximum normal strain theory by St. Venant and the maximum shearing stress theory by Tresca for isotropic materials [3]. It also shares similarities with the Maximum Stress failure theory described above with the only difference that it uses ultimate strains as bounds for failure in place of ultimate stresses. Initially, the local strains on the lamina must be derived from the global strains induced by the load on the lamina. These applied local strains are then compared with the ultimate strains at failure with the conditions for failure shown as follows:

$$-\varepsilon_{1-uts-C} \leq \varepsilon_1 \leq \varepsilon_{1-uts-T} \quad \textbf{[2.64]}$$

$$-\varepsilon_{2-uts-C} \leq \varepsilon_2 \leq \varepsilon_{2-uts-T} \quad \textbf{[2.65]}$$

$$-\gamma_{12-max} \leq \gamma_{12} \leq \gamma_{12-max} \quad \textbf{[2.66]}$$

Where:

$\varepsilon_{1-uts-C}$ -Ultimate Longitudinal Strain in Compression

$\varepsilon_{1-uts-T}$ -Ultimate Longitudinal Strain in Tension

$\varepsilon_{2-uts-C}$ -Ultimate Transverse Strain in Compression

$\varepsilon_{2-uts-T}$ - Ultimate Transverse Strain in Tension

γ_{12-max} - Ultimate Shear Strain

Tsai-Hill failure theory

Tsai-Hill Failure Theory is based on the distortion energy failure theory of Von-Mises' distortional energy yield criterion for isotropic materials [91]. Distortion energy is part of the total strain energy of the body and it comes about due to the change in shape of a body under stress [77]. When this distortion energy exceeds the failure distortion energy of the material then failure would have occurred. The Tsai-Hill failure theory is an adaption of the distortion energy failure theory as applied to anisotropic materials and in particular, to unidirectional laminae [3]. Assuming plane stress conditions, the lamina would have been considered to have failed if it does not satisfy the following condition:

$$\left[\frac{\sigma_1}{\sigma_{1-uts-T}}\right]^2 - \left[\frac{\sigma_1\sigma_2}{\sigma_{1-uts-T}^2}\right] + \left[\frac{\sigma_2}{\sigma_{2-uts-T}}\right]^2 + \left[\frac{\tau_{12}}{\tau_{12-max}}\right]^2 < 1 \quad \textbf{[2.67]}$$

As can be seen in the condition above, there is a coupling between the different applied stresses unlike in the previous two failure theories. Because the transverse compressive strength ($\sigma_{2\text{-}UTS\text{-}C}$) is usually significantly larger than the transverse tensile stress ($\sigma_{2\text{-}UTS\text{-}T}$) [4], [81], the Tsai–Hill failure theory tends

to underestimate the failure stress of the lamina [3]. To incorporate the compressive strengths (for each loading orientation) that are not utilised in the condition above, it can be modified to do just that as follows:

$$\left[\frac{\sigma_1}{A_1}\right]^2 - \left[\frac{\sigma_1\sigma_2}{A_2^{\,2}}\right] + \left[\frac{\sigma_2}{A_3}\right]^2 + \left[\frac{\tau_{12}}{B}\right]^2 < 1 \qquad \textbf{[2.68]}$$

Where:

$$A_1 = \sigma_{1-uts-T} \; if \; \sigma_1 > 0$$
$$= \sigma_{1-uts-C} \; if \; \sigma_1 < 0 \qquad \textbf{[2.69]}$$

$$A_2 = \sigma_{1-uts-T} \; if \; \sigma_2 > 0$$
$$= \sigma_{1-uts-C} \; if \; \sigma_2 < 0 \qquad \textbf{[2.70]}$$

$$A_3 = \sigma_{2-uts-T} \; if \; \sigma_2 > 0$$
$$= \sigma_{2-uts-C} \; if \; \sigma_2 < 0 \qquad \textbf{[2.71]}$$

$$B = \tau_{12-max} \qquad \textbf{[2.72]}$$

To provide a reasonable prediction of the failure mode of a lamina, calculating the ratio of the applied stress and the corresponding ultimate failure stress for each mode and comparing the ratios is considered to be a good assumption [3]. The ratio giving the maximum value would likely be the mode of failure responsible [91].

Tsai-Wu failure theory

The Tsai-Wu failure theory is one used for anisotropic materials (like the Tsai-Hill failure theory) that have different strengths in compression and tension for example a unidirectional laminae [91]. This failure theory is based on the total strain energy failure theory of Beltrami that was developed for isotropic materials [3]. Assuming plane stress conditions, the lamina can be considered to have failed if the following condition is not met:

$$H_1\sigma_1 + H_2\sigma_2 + H_6\tau_{12} + H_{11}\sigma_1^{\,2} + H_{22}\sigma_2^{\,2} + H_{66}\tau_{12}^{\,2} + 2H_{12}\sigma_1\sigma_2 < 1 \qquad \textbf{[2.73]}$$

The constants used in the above condition are evaluated as follows:

$$H_1 = \frac{1}{\sigma_{1-ult-T}} - \frac{1}{\sigma_{1-ult-C}} \qquad \textbf{[2.74]}$$

$$H_{11} = \frac{1}{\sigma_{1-ult-T} \times \sigma_{1-ult-C}} \qquad \textbf{[2.75]}$$

$$H_2 = \frac{1}{\sigma_{2-ult-T}} - \frac{1}{\sigma_{2-ult-C}} \qquad \textbf{[2.76]}$$

$$H_{22} = \frac{1}{\sigma_{2-ult-T} \times \sigma_{2-ult-C}} \qquad \textbf{[2.77]}$$

$$H_6 = 0 \qquad \textbf{[2.78]}$$

$$H_{66} = \frac{1}{\tau_{12-ult}^{\ 2}} \qquad \textbf{[2.79]}$$

The final constant, H_{12}, can be determined empirically by determining the biaxial stress at which the unidirectional lamina fails:

$$H_{12} = -\frac{1}{2 \times \sigma_{1-ult-T}^{\ 2}} \quad \text{as per the Tsai-Hill Failure Theory [3]} \qquad \textbf{[2.80]}$$

Summary on failure theories for laminae

The four failure theories fall under two categories namely interactive and limit/non-interactive theories [3, 91, 98]. The Maximum Stress and Strain failure theories fall under non-interactive failure theories because of there being no interactions between stress or strain components when checking for failure for each of three loading orientations [91]. The Tsai-Hill and Tsai-Wu failure theories are interactive theories that include all the stress components in one expression (failure criterion) [3, 98]. Because of the interactive nature, the Tsai-Hill and Tsai-Wu failure theories are considered to be more accurate in predicting failure stresses of laminae [91]. The Tsai-Hill and Tsai-Wu failure theories have also been found to agree with experimental data with a higher degree of accuracy than the Maximum Stress and strain failure theories [3, 78].

Classical Lamination Theory

The Classical Lamination Theory (CLT) is an analytical tool that attempts to predict the behaviour of the laminate when a load is applied based from prior knowledge of the material properties of the individual laminae and the laminate geometry [99]. This theory is used to relate forces and moments on the laminate structure to the resulting applied stresses and strains in each lamina. The CLT is governed by the following assumptions given by Kaw [3]:

- Each lamina is orthotropic.
- Each lamina is homogeneous.
- A line straight and perpendicular to the middle surface remains straight and perpendicular to the middle surface during deformation ($\gamma_{xz} = \gamma_{yz} = 0$).
- The laminate is thin and is loaded only in its plane (plane stress conditions) hence $\sigma_z = \tau_{xz} = \tau_{yz} = 0$.
- Displacements are continuous and small throughout the laminate (|u|, |v|, |w| << |h|) where **h** is the laminate thickness and **u, v,** and **w** are unit vectors in the x, y and z direction respectively.
- Each lamina is elastic.
- No slip occurs between the lamina interfaces i.e. no delamination.

The strain-displacement equations are derived from the assumptions of the CLT above and are written as follows:

$$\begin{bmatrix} \varepsilon_x \\ \varepsilon_y \\ \gamma_{xy} \end{bmatrix} = \begin{bmatrix} \varepsilon_x^{\ o} \\ \varepsilon_y^{\ o} \\ \gamma_{xy}^{\ o} \end{bmatrix} + z \begin{bmatrix} \kappa_x \\ \kappa_y \\ \kappa_{xy} \end{bmatrix} \qquad \textbf{[2.81]}$$

Where $\begin{bmatrix} \varepsilon_x^{\,o} \\ \varepsilon_y^{\,o} \\ \gamma_{xy}^{\,o} \end{bmatrix}$ *is a vector that represents midplane strains and*

$\begin{bmatrix} \kappa_x \\ \kappa_y \\ \kappa_{xy} \end{bmatrix}$ *is a vector that represents midplane curvatures of each lamina*

And Z which represents the position of a lamina along the z-axis relative to the mid-plane

This system of equations is used to determine the strains in the x-y plane and the x and y directions in a laminate [91]. The strain-displacement equations describe a linear relationship between the strains in a laminate and the curvatures of the laminate while it also goes to show the independence of strains to coordinate axes, x and y.

Strain and stresses in laminates

The strain and stress matrix equations (equations 2.8 through to 2.27) for a unidirectional lamina were described and listed in the previous section(s). Since laminates are groupings of laminae stacked together in a specific order, it follows that laminae strain and stress equations can be applied to laminates as well according to the derivations and assumptions of the CLT. Combining the stress and strain equation for a lamina (2.27) and the strain displacement equation (2.48) for a laminate structure, the result is as follows:

$$\begin{bmatrix} \sigma_x \\ \sigma_y \\ \tau_{xy} \end{bmatrix} = \begin{bmatrix} \bar{Q}_{11} & \bar{Q}_{12} & \bar{Q}_{16} \\ \bar{Q}_{12} & \bar{Q}_{22} & \bar{Q}_{26} \\ \bar{Q}_{16} & \bar{Q}_{26} & \bar{Q}_{66} \end{bmatrix} \bullet \begin{bmatrix} \varepsilon_x^{\,o} \\ \varepsilon_y^{\,o} \\ \gamma_{xy}^{\,o} \end{bmatrix} + z \bullet \begin{bmatrix} \bar{Q}_{11} & \bar{Q}_{12} & \bar{Q}_{16} \\ \bar{Q}_{12} & \bar{Q}_{22} & \bar{Q}_{26} \\ \bar{Q}_{16} & \bar{Q}_{26} & \bar{Q}_{66} \end{bmatrix} \bullet \begin{bmatrix} \kappa_x \\ \kappa_y \\ \kappa_{xy} \end{bmatrix} \quad \textbf{[2.82]}$$

The equation 2.49 applies to each lamina within the laminate structure. The equation describes the scenario in which the stress varies across the thickness of each lamina (along the z-axis). If the transformed reduced stiffness matrix is the same for all laminae in the laminate structure, then the only variable becomes the position of each lamina from the mid-plane given by the z-coordinate.

Determination of force and moment resultants for each lamina

This section describes how to determine the mid-plane strain and curvature values from the strain-displacement equation 2.48 after loading the laminate structure as described by Kaw [3]. The resultant forces and moments sustained by each lamina can be calculated through integrating the stress over the thickness of each lamina [3]. Having prior knowledge of the applied force, then the mid-plane strains and curvatures can be found. The relationship between the applied load and the mid-plane strains and curvatures will be explained in this sub-section.

Equation 2.83 calculates the thickness of a laminate by summing up the thicknesses of each lamina along the z-axis.

$$h = \sum_{k=1}^{n} t_k \quad \textbf{[2.83]}$$

Where ***h*** is the laminate thickness and ***t*** is the thickness of each lamina. The mid-plane of the lamina will obviously be located halfway through the laminate structure i.e. at *h/2.* The mid-plane will be used as the reference point when locating the position of each lamina for example the top surface of the first lamina from the top will be [*+h/2*] whilst the bottom surface of the last lamina will be [*–h/2*].

The resultant force per unit length (N) through the laminate thickness in the x-y plane can found by integrating the global stress over the thickness of each lamina. Similarly, the resultant moments per unit length (M) through the laminate thickness can be found by integrating the global stresses on each lamina through the lamina thickness along the z-axis.

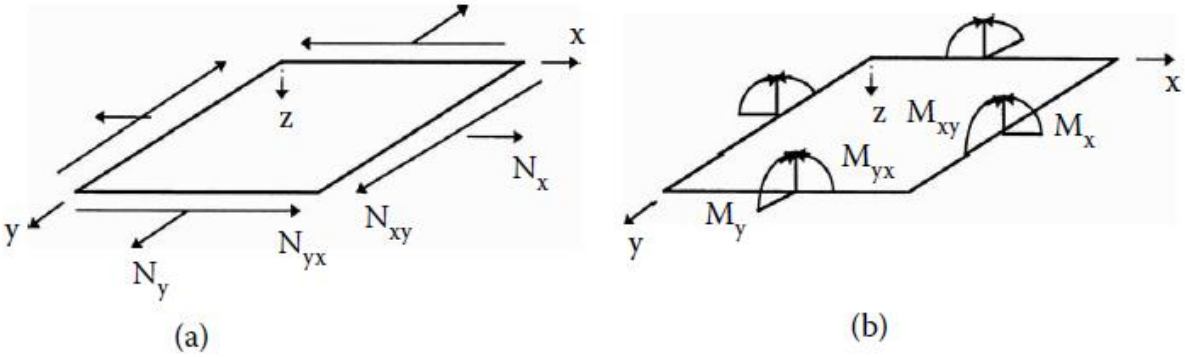

Figure 2.26: Resultant forces and moments on a lamina[3]

The stresses acting on a lamina within the laminate (Figure 2.26) can be replaced by resultant forces and moments as shown the following equations:

$$N_x = \int_{-h/2}^{h/2} \sigma_x dz \qquad \textbf{[2.84]} \qquad M_x = \int_{-h/2}^{h/2} \sigma_x z dz \qquad \textbf{[2.87]}$$

$$N_y = \int_{-h/2}^{h/2} \sigma_y dz \qquad \textbf{[2.85]} \qquad M_y = \int_{-h/2}^{h/2} \sigma_y z dz \qquad \textbf{[2.88]}$$

$$N_{xy} = \int_{-h/2}^{h/2} \tau_{xy} dz \qquad \textbf{[2.86]} \qquad M_{xy} = \int_{-h/2}^{h/2} \tau_{xy} z dz \qquad \textbf{[2.89]}$$

In matrix form, the equations can be written as follows:

$$\begin{bmatrix} N_x \\ N_y \\ N_{xy} \end{bmatrix} = \int_{-h/2}^{h/2} \begin{bmatrix} \sigma_x \\ \sigma_y \\ \tau_{xy} \end{bmatrix} dz \qquad \textbf{[2.90]} \qquad \begin{bmatrix} M_x \\ M_y \\ M_{xy} \end{bmatrix} = \int_{-h/2}^{h/2} \begin{bmatrix} \sigma_x \\ \sigma_y \\ \tau_{xy} \end{bmatrix} z dz \qquad \textbf{[2.91]}$$

Equations 2.90 and 2.91 for a single lamina simplifies to the following:

$$\begin{bmatrix} N_x \\ N_y \\ N_{xy} \end{bmatrix} = \sum_{k=1}^{n} \int_{-h_{k-1}}^{h_k} \begin{bmatrix} \sigma_x \\ \sigma_y \\ \tau_{xy} \end{bmatrix}_k dz \qquad \textbf{[2.92]} \qquad \begin{bmatrix} M_x \\ M_y \\ M_{xy} \end{bmatrix} = \sum_{k=1}^{n} \int_{-h_{k-1}}^{h_k} \begin{bmatrix} \sigma_x \\ \sigma_y \\ \tau_{xy} \end{bmatrix}_k z dz \qquad \textbf{[2.93]}$$

Substituting for the global stresses from equation 2.54 results in the following:

$$\begin{bmatrix} N_x \\ N_y \\ N_{xy} \end{bmatrix} = \sum_{k=1}^{n} \int_{-h_{k-1}}^{h_k} \begin{bmatrix} \bar{Q}_{11} & \bar{Q}_{12} & \bar{Q}_{16} \\ \bar{Q}_{12} & \bar{Q}_{22} & \bar{Q}_{26} \\ \bar{Q}_{16} & \bar{Q}_{26} & \bar{Q}_{66} \end{bmatrix}_k \bullet \begin{bmatrix} \varepsilon_x^{\,o} \\ \varepsilon_y^{\,o} \\ \gamma_{xy}^{\,o} \end{bmatrix} dz + \sum_{k=1}^{n} \int_{-h_{k-1}}^{h_k} \begin{bmatrix} \bar{Q}_{11} & \bar{Q}_{12} & \bar{Q}_{16} \\ \bar{Q}_{12} & \bar{Q}_{22} & \bar{Q}_{26} \\ \bar{Q}_{16} & \bar{Q}_{26} & \bar{Q}_{66} \end{bmatrix}_k \bullet \begin{bmatrix} \kappa_x \\ \kappa_y \\ \kappa_{xy} \end{bmatrix} dz \qquad \textbf{[2.94]}$$

$$\begin{bmatrix} M_x \\ M_y \\ M_{xy} \end{bmatrix} = \sum_{k=1}^{n} \int_{-h_{k-1}}^{h_k} \begin{bmatrix} \bar{Q}_{11} & \bar{Q}_{12} & \bar{Q}_{16} \\ \bar{Q}_{12} & \bar{Q}_{22} & \bar{Q}_{26} \\ \bar{Q}_{16} & \bar{Q}_{26} & \bar{Q}_{66} \end{bmatrix}_k \bullet \begin{bmatrix} \varepsilon_x^{\,o} \\ \varepsilon_y^{\,o} \\ \gamma_{xy}^{\,o} \end{bmatrix} z dz + \sum_{k=1}^{n} \int_{-h_{k-1}}^{h_k} \begin{bmatrix} \bar{Q}_{11} & \bar{Q}_{12} & \bar{Q}_{16} \\ \bar{Q}_{12} & \bar{Q}_{22} & \bar{Q}_{26} \\ \bar{Q}_{16} & \bar{Q}_{26} & \bar{Q}_{66} \end{bmatrix}_k \bullet \begin{bmatrix} \kappa_x \\ \kappa_y \\ \kappa_{xy} \end{bmatrix} z^2 dz \qquad \textbf{[2.95]}$$

By evaluating the integrals and summation signs, the above equations simplify to:

$$\begin{bmatrix} N_x \\ N_y \\ N_{xy} \end{bmatrix} = \begin{bmatrix} A_{11} & A_{12} & A_{16} \\ A_{12} & A_{22} & A_{26} \\ A_{16} & A_{26} & A_{66} \end{bmatrix} \bullet \begin{bmatrix} \varepsilon_x^{\,o} \\ \varepsilon_y^{\,o} \\ \gamma_{xy}^{\,o} \end{bmatrix} + \begin{bmatrix} B_{11} & B_{12} & B_{16} \\ B_{12} & B_{22} & B_{26} \\ B_{16} & B_{26} & B_{66} \end{bmatrix} \bullet \begin{bmatrix} \kappa_x \\ \kappa_y \\ \kappa_{xy} \end{bmatrix} \qquad \textbf{[2.96]}$$

$$\begin{bmatrix} M_x \\ M_y \\ M_{xy} \end{bmatrix} = \begin{bmatrix} B_{11} & B_{12} & B_{16} \\ B_{12} & B_{22} & B_{26} \\ B_{16} & B_{26} & B_{66} \end{bmatrix} \bullet \begin{bmatrix} \varepsilon_x^{\,o} \\ \varepsilon_y^{\,o} \\ \gamma_{xy}^{\,o} \end{bmatrix} + \begin{bmatrix} D_{11} & D_{12} & D_{16} \\ D_{12} & D_{22} & D_{26} \\ D_{16} & D_{26} & D_{66} \end{bmatrix} \bullet \begin{bmatrix} \kappa_x \\ \kappa_y \\ \kappa_{xy} \end{bmatrix} \qquad \textbf{[2.97]}$$

Where elements of the [A], [B] and [D] matrix are calculated as follows:

$$A_{ij} = \sum_{k=1}^{n} [\bar{Q}_{ij}]_k (h_k - h_{k-1}) \quad i = 1,2,6 \ \ and \ \ i = 1,2,6 \qquad \textbf{[2.98]}$$

$$B_{ij} = \frac{1}{2} \times \sum_{k=1}^{n} [\bar{Q}_{ij}]_k ({h_k}^2 - {h_{k-1}}^2) \quad i = 1,2,6 \ \ and \ \ i = 1,2,6 \qquad \textbf{[2.99]}$$

$$D_{ij} = \frac{1}{3} \times \sum_{k=1}^{n} [\bar{Q}_{ij}]_k ({h_k}^3 - {h_{k-1}}^3) \quad i = 1,2,6 \ \ and \ \ i = 1,2,6 \qquad \textbf{[2.100]}$$

The [A], [B] and [D] matrices are referred to as the extensional, coupling and bending stiffness matrices respectively. The extensional stiffness matrix [A] relates the resultant in-plane forces to the in-plane strains, and the bending stiffness matrix [D] relates the resultant bending moments to the plate curvatures [3]. The coupling stiffness matrix [B] couples the force and moment terms to the mid-plane strains and mid-plane curvatures[3].

Summary on the CLT

As summarized concisely by Kaw [3], the following are the steps for analysing a laminated composite subjected to the applied forces and moments using the CLT:

1. Determine the value of the reduced stiffness matrix [Q] for each lamina using its four elastic moduli, E_1, E_2, v_{12}, and G_{12}.
2. Find the value of the transformed reduced stiffness matrix for each lamina using the [Q] matrix calculated and the fibre orientation angle of each lamina. The elements of the transformed reduced stiffness matrix can be found using Equations 2.55 to 2.60.
3. Knowing the thickness, $\boldsymbol{t_K}$, of each lamina, find the coordinate of the top and bottom surface, $\boldsymbol{h_i}$ (i = 1…,n), of each lamina, using Equation 2.83.
4. Use the transformed reduced stiffness matrices and the locations of each lamina from step 3 to find the three stiffness matrices [A], [B], and [D] using Equations 2.98-2.100.
5. Substitute the stiffness matrix values found in step 4 and the applied forces and moments in Equations 2.96 and 2.97
6. Solve the six simultaneous equations (2.96 and 2.97) to find the mid-plane strains and curvatures.
7. Using the location of each lamina, find the global strains in each lamina using Equation 2.81.
8. For finding the global stresses in each lamina, use the stress–strain Equation 2.82.
9. For finding the local strains, use the transformation Equation 2.48.
10. For finding the local stresses, use the transformation Equation 2.47.

After determining the local stress and strain values for each lamina, they can be substituted into the expressions or conditions for each failure theory to check for failure.

2.4 Novel, low-cost CFRP pressure vessel

2.4.1 Background

Stuart Swan, along with other students, designed, built and tested a water powered rocket at the University of Cape Town in 2015. The students worked under the Industrial CFD research group that is led by Prof Arnaud Malan. The water rocket went on to break the previous world record for the vertical altitude reached by a water rocket (623m) by a significant margin of about 30% [1]. During the development of the water rocket, a novel, low-cost, design of a pressure vessel was created. The pressure vessel was made up of a standard commercial filament wound CFRP composite cylindrical pipe PVC end caps bonded on either end of the tube by SpaBond 340 LV adhesive. The pressure vessel was low cost, lightweight and possessed a high strength-to-weight ratio. The inner surface of the vessel was lined with a rubber which was meant to prevent leakage. An international patent application was filed for the lining method using a liquid rubber [5].

2.4.2 Description of patent

The CFRP pressure vessel had three main features (see Figure 1.4) namely the following:

- CFRP cylindrical tube
- End caps
- Rubber lining

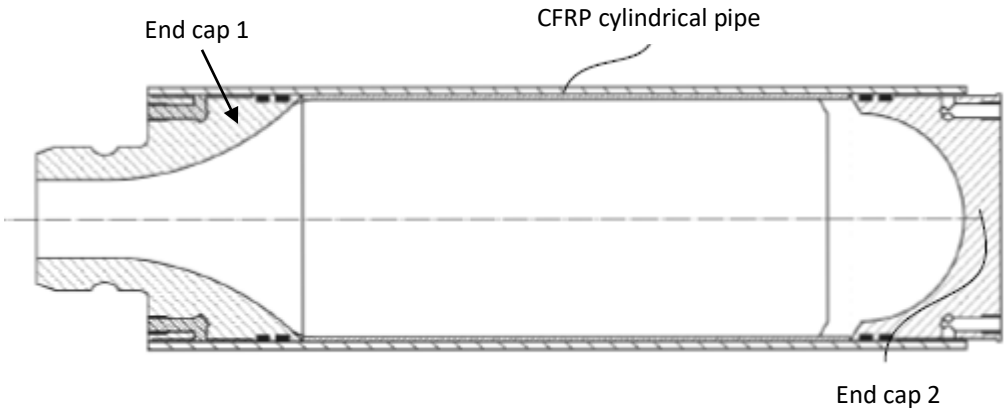

Figure 2.27: Cross-sectional view of the CFRP pressure vessel derived from the patent application [5]

The functions of those features are concisely described in Table 2.*4*.

Table 2.4: Features of the CFRP pressure vessel

Feature	**Description and function**
CFRP cylindrical tube	• Made from CFRP through standard commercial filament winding • Main section of the vessel that bears the hoop, axial and potentially radial stresses induced due to the internal pressure.
End caps	• Custom built (i.e. machined) and bonded onto both ends of the cylindrical section using SpaBond 340 LV adhesive. • Close off and seal the open ends of the CFRP tube section to prevent leakage of the fluid contained within the vessel. • Resist the pressure load without yielding/fracturing.
Rubber lining	• Coated onto the inner surface of the CFRP cylindrical tube. • Serves the purpose of "closing up" any micro-cracks in the CFRP tube to prevent the contents of the vessel from leaking through the CFRP tube's wall.

This type of pressure vessel is mostly composed of filament wound CFRP making it similar to a Type IV hydrogen gas vessel they both have polymeric based liners. However, it differs from the Type IV vessel in three main aspects.

- Type IV vessels are made through filament winding CFRP onto pre-formed polymeric liner [66]. The rubber lining used in the novel CFRP pressure vessel alternatively is applied post-manufacture of the CFRP tubes [1].
- The liner for the Type IV vessel is structurally rigid while the rubber liner for the novel vessel is not rigid.
- For the Type IV vessels, winding CFRP onto their curved ends could only performed through specialist multi-axis filament winding machines while the novel, low-cost vessel only requires a simple two-axes filament winding machine [100-101]. This tends to make the manufacturing process for the novel CFRP pressure vessel less expensive.

The liners for Type IV vessels are pre-formed which is time-consuming and requires specialist manufacturing processes to ensure the structural integrity of the liner before the carbon fibres are wrapped around them [62]. As a result, the pre-formed rigid polymeric liners tend to have a

substantial mass as they need to have sufficient structural integrity, thus, adding significantly to the weight of the pressure vessel [1]. The use of a thin rubber lining in this novel pressure vessel makes it less expensive and lighter than those for Type IV vessels. Hence, from those points of views, it can be inferred that the pressure vessel design based on the record-breaking water rocket might potentially be a lighter and lower cost alternative as a pressure vessel to Type IV pressure vessels. Therefore, after designing and manufacturing the novel pressure vessel, several pressure tests need to be performed to ensure the vessel has sufficient strength and assessing the ability of the liner to prevent the escape of the pressurized fluid from the vessel in the long term.

3. Design and manufacture of the CFRP pressure vessel

This chapter deals with the design of the components of the CFRP pressure vessel namely the CFRP cylindrical tube section, end caps and rubber liner. The aspects pertaining to the design of the CFRP pressure vessel include but are not limited to stress analysis, sizing and material selection.

3.1 CFRP tube design

The CFRP Tube is the part of the pressure vessel which will sustain most of the loading i.e. hoop, longitudinal and possibly radial stresses (depending on the thickness of the vessel). The CFRP tube will have to be appropriately designed to handle the stresses induced by the internal pressure. However, since the CFRP material is not isotropic like the conventional metals, conventional stress and strain models, and/or failure theories for isotropic materials will not suffice. The Classical Lamination Theory (CLT) considers the orthotropic nature of the laminate structure and was chosen to be used to predict the mechanical behaviour of the laminate structure under the applied stresses.

3.1.1 Manufacturing

The CFRP tube is to be manufactured through filament winding. The filament winding is to be performed by a local company called GRP Tubing in Cape Town, South Africa. The carbon fibre is to pass through a bath of an epoxy resin under tension before being wound onto a cylindrical shaped mandrel until the desired thickness for the laminate structure is reached. Both the carbon fibre and the epoxy resin are locally sourced at AMT Composites and Aerontec respectively. The CFRP tubes are to be post-cured according to the prescribed method for the epoxy resin AR600 + AH2336 hardener [102]. The post-curing schedule was as follows: 2 hours at 80°C + 3 hours at 150°C + 4 hours at 180°C. According to the data sheet for the epoxy resin AR600 [102], the increase in temperature between the 3 different temperature plateaus (for example the increase in temperature between 80°C and 150°C) was to be between 1.5°C and 2.0°C. The cooling down between the plateaus until the room temperature was reached had to be at the same rate. The choice in using the epoxy resin AR600 and its associated hardener was mainly because of its low cost, availability and desirable properties which include the following:

- Low viscosity
- Good mechanical properties
- Good thermal properties
- Suitability for use in filament winding

3.1.2 Laminate stacking arrangement

Before choosing the stacking arrangement however, a decision needed to be made as to whether the laminate structure was balanced or symmetric or both. A balanced laminate structure causes the coupling stiffness matrix [B] to be a zero matrix. The uncoupling between extension and bending in symmetric laminates makes the analysis of such laminates simpler while it also prevents a laminate from twisting due to the effects of thermal loads which may be a result of temperature fluctuations [3]. Alternatively, symmetric laminates have higher bending stiffness than that of any asymmetric laminate composed of the same layers [95]. This also makes them advantageous from that perspective. Therefore, it was chosen that the laminate structure for the CFRP tube had to be balanced and symmetric about the mid-plane of the laminate. The angle-ply laminate structure was then chosen as the stacking arrangement because inherently, they have a balanced structure and have relatively higher stiffness and strength properties [3].

.

3.1.3 Stress analysis for the CFRP tube

According to Hearn [77], if an internal pressure is induced in a cylindrical shaped vessel with closed ends, it will experience hoop, longitudinal and possibly radial stresses. There are two theories that were used to evaluate the applied stresses namely the Thin and Thick cylinder theories. However, the choice of which theory to use depended on the ratio of the pressure vessel's internal diameter to wall thickness.

Sizing the CFRP tube

The volumetric capacity of Type III and IV CFRP pressure vessels used in a HFCPV is at least 180 litres for a vessel of 1 m length [28]. That would translate to an internal diameter of about 240 mm. The costs involved in procuring CFRP tubes of that diameter would have been relatively expensive as it would have required a substantial amount of carbon fibre tow material to be used. However, the same stresses experienced by a CFRP tube with a 240 mm internal diameter would be the same as the stresses induced in a 50 mm internal diameter tube so long as the ratio of the internal diameter to wall thickness of the tubes remained the same in both cases [76]. Because 50 mm diameter was the smallest internal diameter size GRP Tubing could produce through filament winding, it was the internal diameter that was ultimately chosen for the CFRP tube test specimens.

To determine the required wall thickness sufficient for the CFRP tube to withstand induced stresses, the tube was first assumed to be a thin cylinder with a wall thickness that is 5% of the internal diameter i.e. 2mm thick. Subsequently, the Thin Cylinder theorem was to be used to determine the hoop and longitudinal stresses acting on the entire laminate structure. These two stresses would be the global stresses acting on the laminate structure.

The initial set of mechanical strength and stiffness properties for the CFRP tubes were determined using the results of the ASTM tensile tests described in chapter 5. This initial set of material properties were substituted into the equations based on the CLT (see section 2.3.4.2 for more details) to determine the local stresses and strains of each lamina within the laminate structure of the CFRP tube. The applied local stresses and strains along with the strength properties of the CFRP tube could then be used in conjunction with the failure theories to determine if the CFRP tube would burst at a given pressure. The Maximum Stress failure theory was chosen as the failure theory that would be used in initially sizing the wall thickness of the first CFRP tube. It was chosen because it is simple to use, predicts the failure mode and is widely used in industrial applications [103]. In addition, the UTS of the CFRP in the direction transverse to the fibre direction was found to be significantly lower than the other two strength property values (see Table 3.*6*). According to M. J. Hinton et al and N. Tiwari [103, 104], the failure of individual unidirectional laminae in transverse-tension loading conditions is better characterized by a Maximum Stress failure criterion within each affected lamina. Hence, it was reasonable to assume that the CFRP tube would fail in the direction of loading transverse to the fibre direction. This further justified the use of the Maximum Stress failure theory. The detailed steps and calculations that were taken to size the tube through stress analysis is detailed below.

CLT calculations

The main design constraints that were used in the sizing of the CFRP tube were as follows:

- Failure Pressure [P] - 350 bar
- Internal Diameter [D_i] - 50 mm
- Wall thickness [t] - 2 mm

Because the wall thickness was chosen to be 2 mm initially, eight laminae of unidirectional CFRP material were required since each layer (or lamina) was approximately 0.25 mm thick. It should be noted that the failure pressure in this instance refers to the pressure at which the CFRP would be permanently damaged.

Applied stresses on the CFRP tube

The stresses calculated based on the Thin Cylinder theorem using equations 2.1 and 2.2 as follows:

Hoop stress: $\sigma_H = \frac{PD_i}{2t} = 437.5MPa$

Longitudinal stress: $\sigma_L = \frac{PD_i}{4t} = 218.8MPa$

The CLT was developed to deal with two dimensional plane stresses acting on a thin laminate [3, 98]. The plane stresses that were acting on the laminate structure at every point on the surfaces (internal or external) of the cylindrical tube were the hoop and longitudinal stresses.

In the context of loading a laminated composite structure, the stresses exerted on the laminate are termed global stresses (in the x-y coordinate system). The global stresses had to be resolved on an infinitesimal element on the surface as shown in Figure 3.28.

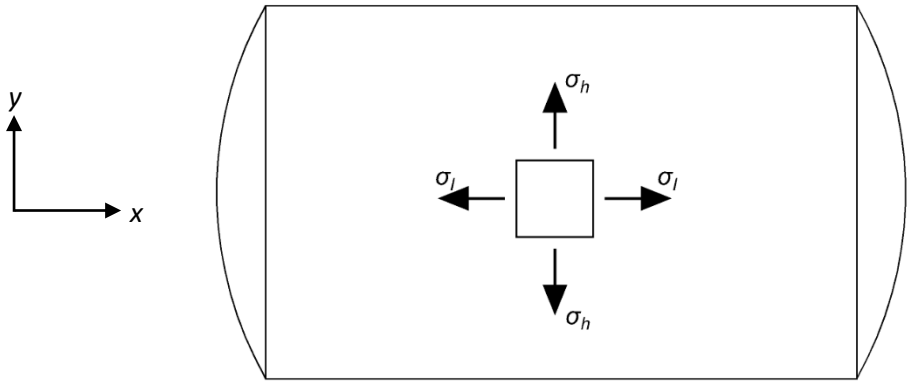

Figure 3.28: Illustration of the stresses acting on an infinitesimal point on the surface of cylinder [105]

The longitudinal stress acts along the axis of the cylinder in the x-direction and the hoop stress acts perpendicular to the axis of the cylinder in the vertical y-direction. Because of the induced load due to the internal pressure, there were no shear stresses involved according to Hearn [77].

$$\begin{bmatrix} \sigma_x \\ \sigma_y \\ \tau_{xy} \end{bmatrix} = \begin{bmatrix} \sigma_L \\ \sigma_H \\ 0 \end{bmatrix} = \begin{bmatrix} 218.8 \\ 437.5 \\ 0 \end{bmatrix} MPa$$

According to Shultz et al [106], the optimum winding angle for maximum burst strength of a CFRP cylindrical pressure vessel when using the Maximum Stress failure theory is 50°. Therefore, the symmetric angle-lamina laminate structure was set with fibres oriented at +50° and -50°. The transformation matrix [T] for each lamina is dependent on the fibre orientation angle. Laminae with fibres oriented at +50° had a specific transformation matrix [T_1] and those with fibres oriented at –50° had their own specific transformation matrix [T_2]. The respective transformation matrices were determined using equation 2.49 are as follows:

$$T_1 = \begin{bmatrix} 0.413 & 0.587 & 0.985 \\ 0.587 & 0.413 & -0.985 \\ -0.492 & 0.492 & -0.174 \end{bmatrix} \text{ and } T_2 = \begin{bmatrix} 0.413 & 0.587 & -0.985 \\ 0.587 & 0.413 & 0.985 \\ 0.492 & -0.492 & -0.174 \end{bmatrix}$$

Reduced and transformed reduced matrices

The values of the elements in the reduced stiffness matrix [Q] were not dependent on the fibre orientation angle for the laminae. This is because the elements of matrix [Q] are only dependent on the material properties of the CFRP tube composite. Therefore, the [Q] matrix was the same for all laminae. The initial material stiffness property values (see section 5.1 for more details) as well as the Major and Minor Poisson's ratios for the CFRP material with a fibre volume fraction of 50% are shown in Table 3.5. The fibre volume fraction of 50% was assumed for tensile test specimens (see section 5.1) and was intended to be used in making the CFRP tubes as well.

Table 3.5: Initial material property values for the CFRP composite material

Property	**Symbol**	**Value**
Longitudinal Elastic Modulus	E_1	109 GPa
Transverse Elastic Modulus	E_2	6 GPa
Major Poisson's Ratio	υ_{12}	0.3
Minor Poisson's Ratio	υ_{21}	0.02

$$Q = \begin{bmatrix} Q_{11} & Q_{12} & Q_{16} \\ Q_{12} & Q_{22} & Q_{26} \\ Q_{16} & Q_{26} & Q_{66} \end{bmatrix} = \begin{bmatrix} 109.5 & 1.809 & 0 \\ 1.809 & 6.03 & 0 \\ 0 & 0 & 5 \end{bmatrix} GPa$$

Because the value of elements of the transformed reduced stiffness matrix $[\bar{Q}]$ depends on the fibre orientation angle, laminae with fibre orientation angle of + 50^0 had a different $[\bar{Q}]$ matrix to those with fibre orientation angles of -50^0. For laminae with fibre orientation angles of +50^o and -50^o, the transformed reduced stiffness matrices were $[\bar{Q}_1]$ and $[\bar{Q}_2]$ respectively.

$$\bar{Q}_1 = \begin{bmatrix} 26.5 & 24.1 & 21.6 \\ 24.1 & 44.5 & 29.4 \\ 21.6 & 29.4 & 27.3 \end{bmatrix} GPa \quad and \quad \bar{Q}_2 = \begin{bmatrix} 26.5 & 24.1 & -21.6 \\ 24.1 & 44.5 & -29.4 \\ -21.6 & -29.4 & 27.3 \end{bmatrix} GPa$$

Extensional, coupling and bending stiffness matrices

Looking at the cross section of the CFRP tube's laminate structure, the top and bottom surfaces of each lamina were allocated a position with respect to the z-coordinate. The mid-plane had a z-position of 0 mm whilst the topmost and bottom surfaces of the laminate were half of the thickness of the laminate on either side of the laminate (i.e. ± 1 mm). The positions of the top and bottom surfaces of the laminae ($\mathbf{h_K}$) in the laminate were determined using equation 2.83 (see section 2.3.4.2 for more details).

Using the positions of the top and bottom surfaces of each lamina as well as the transformed reduced stiffness matrix, the extensional [A], coupling [B] and bending [D] stiffness matrices were evaluated using equations 2.98-2.100. The coupling stiffness matrix [B] resulted in a null matrix as expected which meant the forces and the moment terms were de-coupled.

$$A = \begin{bmatrix} 0.053 & 0.048 & 0 \\ 0.048 & 0.089 & 0 \\ 0 & 0 & 0.055 \end{bmatrix} GPa \cdot m$$

$$B = \begin{bmatrix} 0 & 0 & 0 \\ 0 & 0 & 0 \\ 0 & 0 & 0 \end{bmatrix} Pa \cdot m^2$$

$$D = \begin{bmatrix} 0.018 & 0.016 & 0.005 \\ 0.016 & 0.030 & 0.007 \\ 0.005 & 0.007 & 0.018 \end{bmatrix} kPa \cdot m^3$$

Stresses and strains in the laminate

The global stresses acting on the laminate structure were integrated over each lamina to give the resultant forces per unit length (N) acting on each lamina within the x-y plane through the laminate thickness. Similarly, integrating the global stresses over the thickness of each lamina gave the moments acting per unit length (M) acting on each lamina. All the moment terms (M_x, M_{xy} and M_y) and the shear force term (N_{xy}) yielded a zero value apparently because there were no applied moments or shear stresses according to the Thin Cylinder theorem.

The resultant forces and moments per unit length acting on each lamina was then substituted into the equations 2.96 and 2.97 along with the [A], [B] and [D] matrices to form simultaneous equations. The simultaneous equations were solved to determine mid-plane strains and curvatures. To determine the global strains for each lamina within the laminate, the mid-plane strains and curvatures were substituted into the strain displacement equation 2.81 as follows:

$$\begin{bmatrix} \varepsilon_x \\ \varepsilon_y \\ \gamma_{xy} \end{bmatrix} = \begin{bmatrix} \varepsilon^o{}_x \\ \varepsilon^o{}_y \\ \gamma^o{}_{xy} \end{bmatrix} + z \begin{bmatrix} \kappa_x{}^o \\ \kappa_y{}^o \\ \kappa_{xy}{}^o \end{bmatrix} = \begin{bmatrix} -0.002919 \\ 0.009212 \\ 0 \end{bmatrix}$$

The result was that all laminae within the laminate had the same strain vector because the mid-plane curvature vector was a null vector. Hence, the strain across the thickness of the laminate, did not depend on the position of the lamina along the z-axis. As a result, the laminae supposedly were "strained" similarly for all orientations thereby preventing a situation where adjacent laminae have different strains which would probably result in failure due to interlaminar shear.

Having determined the strains for each lamina in the x-y coordinate system, the global stresses for each lamina were determined using equation 2.54. Laminae with fibres oriented at +50° effectively had the same magnitude of the global stresses to those with the fibre orientation angle of -50° as shown:

For laminae with fibre orientation angle of +50°: For laminae with fibre orientation angle of -50°:

$$\begin{bmatrix}\sigma_x\\ \sigma_y\\ \tau_{xy}\end{bmatrix} = \bar{Q}_1 \begin{bmatrix}\varepsilon_x\\ \varepsilon_y\\ \gamma_{xy}\end{bmatrix} = \begin{bmatrix}144.7\\ 339.4\\ 208.1\end{bmatrix} MPa \qquad \begin{bmatrix}\sigma_{x-2}\\ \sigma_{y-2}\\ \tau_{xy-2}\end{bmatrix} = \bar{Q}_2 \begin{bmatrix}\varepsilon_x\\ \varepsilon_y\\ \gamma_{xy}\end{bmatrix} = \begin{bmatrix}144.7\\ 339.4\\ -208.1\end{bmatrix} MPa$$

Using the transformation matrices [T_1] and [T_2], the local stresses and strains for the laminae were determined as shown below.

For laminae with fibre orientation angle of +50°:

$$\begin{bmatrix}\sigma_1\\ \sigma_2\\ \tau_{12}\end{bmatrix} = T_1 \begin{bmatrix}\sigma_x\\ \sigma_y\\ \tau_{xy}\end{bmatrix} = \begin{bmatrix}463.8\\ 20.22\\ 59.731\end{bmatrix} MPa \qquad \begin{bmatrix}\varepsilon_1\\ \varepsilon_2\\ \gamma_{12}\end{bmatrix} = T_1 \begin{bmatrix}\varepsilon_x\\ \varepsilon_y\\ \gamma_{xy}\end{bmatrix} = \begin{bmatrix}0.00420\\ 0.00209\\ 0.00597\end{bmatrix}$$

For laminae with fibre orientation angle of -50°:

$$\begin{bmatrix}\sigma_{1-2}\\ \sigma_{2-2}\\ \tau_{12-2}\end{bmatrix} = T_2 \begin{bmatrix}\sigma_{x-2}\\ \sigma_{y-2}\\ \tau_{xy-2}\end{bmatrix} = \begin{bmatrix}463.8\\ 20.22\\ -59.731\end{bmatrix} MPa \qquad \begin{bmatrix}\varepsilon_{1-2}\\ \varepsilon_{2-2}\\ \gamma_{12-2}\end{bmatrix} = T_2 \begin{bmatrix}\varepsilon_x\\ \varepsilon_y\\ \gamma_{xy}\end{bmatrix} = \begin{bmatrix}0.00420\\ 0.00209\\ -0.00597\end{bmatrix}$$

The CFRP material strength properties (see section 5.1 for more details) given in Table 3.*6* for the three loading orientations. They were compared with the local applied stresses within each lamina as required by the Maximum Stress failure theory.

Table 3.6: Ultimate strength values for the CFRP tube for each orientation of loading

Property	**Symbol**	**Value [MPa]**
Ultimate Tensile Strength in the 0 ^{O} direction	$\sigma_{1-\max}$	1357
Ultimate Tensile Strength in the 90 ^{O} direction	$\sigma_{2-\max}$	14.8
Ultimate In-plane shear strength	$\tau_{12-\max}$	60

The result was that each lamina in the 2 mm CFRP tube laminate structure would fail in the direction transverse to the fibres since the respective applied local stress (20.22 MPa) was higher than the corresponding ultimate transverse strength (14.8 MPa). Therefore, the CFRP tube needed more layers/laminae to prevent failure. Therefore, more layers were added sequentially and iterations of the CFRP tube's stress analysis were performed until it was determined that the minimum thickness had to be 4 mm to avoid failure. The local applied stresses for each lamina in the 4 mm CFRP tube laminate structure was determined to be as follows:

$$\begin{bmatrix}\sigma_1\\ \sigma_2\\ \tau_{12}\end{bmatrix} = \begin{bmatrix}325.764\\ 13.056\\ 41.618\end{bmatrix} MPa$$

The detailed calculations for the 4 mm CFRP tubes can be found in Appendix A.

3.1.4 Optimization of filament winding angle

Because most of the load carrying capacity of a polymer matrix type composite is within its unidirectional long and continuous fibres, they are usually designed with most of the fibres oriented in the direction of loading [3, 78, 91]. This allows the designer of the composite to save in terms of its weight which is one of the advantages of a composite over a conventional isotropic material in the context of cylindrical pressure vessels. Since the hoop stress is approximately twice the value of the longitudinal stress, the former is the limiting case when designing a pressure vessel constructed from an isotropic material. The pressure vessel becomes over-designed in the longitudinal direction as a result. In a filament wound CFRP pressure vessel, the filament winding angle of the CFRP tube becomes a significant design consideration which needs to be optimized to ensure the maximum load carrying capacity of the vessel. In turn, this would ensure that relatively less material (or layers of carbon fibre) is needed to make the vessel which lowers the weight and the cost incurred in constructing the pressure vessel.

As stated previously, it was predicted that the CFRP tube would probably fail in the direction transverse to the fibres [104, 107]. Hence, it was decided to use the Maximum Stress failure theory to predict the optimum filament winding angle for a failure pressure of 350 bar. Given the material properties shown in Table 3.*6*, the local stresses and strains were determined using the CLT model calculations for each lamina within the 4 mm thick CFRP tube laminate for a range of filament winding angles from 45^{o} till 60^{o}.

The safety factors for the same range of filament winding angles were calculated as the ratios of the maximum local stresses to the applied local stresses for each loading orientation. A sample calculation of the safety factor for the winding angle of 50^{o} is given below:

The applied local stresses for each lamina:
$$\begin{bmatrix} \sigma_1 \\ \sigma_2 \\ \tau_{12} \end{bmatrix} = \begin{bmatrix} 325.764 \\ 13.056 \\ 41.618 \end{bmatrix} MPa$$

The safety factors for each direction of loading:
$$\begin{bmatrix} n_1 \\ n_2 \\ n_{12} \end{bmatrix} = \begin{bmatrix} \frac{\sigma_{1-\max}}{\sigma_1} \\ \frac{\sigma_{2-\max}}{\sigma_2} \\ \frac{\tau_{12-\max}}{\tau_{12}} \end{bmatrix} = \begin{bmatrix} 4.17 \\ 1.13 \\ 1.44 \end{bmatrix}$$

The safety factors were plotted against the winding angles of the fibres in the laminae within the laminate as shown in Figure 3.29. According to the graph, the curve for the direction of loading along the fibres (1-direction) has a minimum peak between 50^{o} and 53^{o} then increases in either direction. The curve for direction 2 (transverse to the fibres), peaks just above 51^{O} as well and decreases in either direction from that angle. The loading in the 1-2 plane peaks at 60^{O} and decreases from that peak at a faster rate than the other two curves. In this case, the loading orientation with the minimal safety factor values was that of the direction of loading transverse to the fibres. It was therefore the limiting case and it was reasonably assumed that the laminate structure would fail in the direction transverse to the fibres which has a strength dominated by the matrix [3-4, 95].

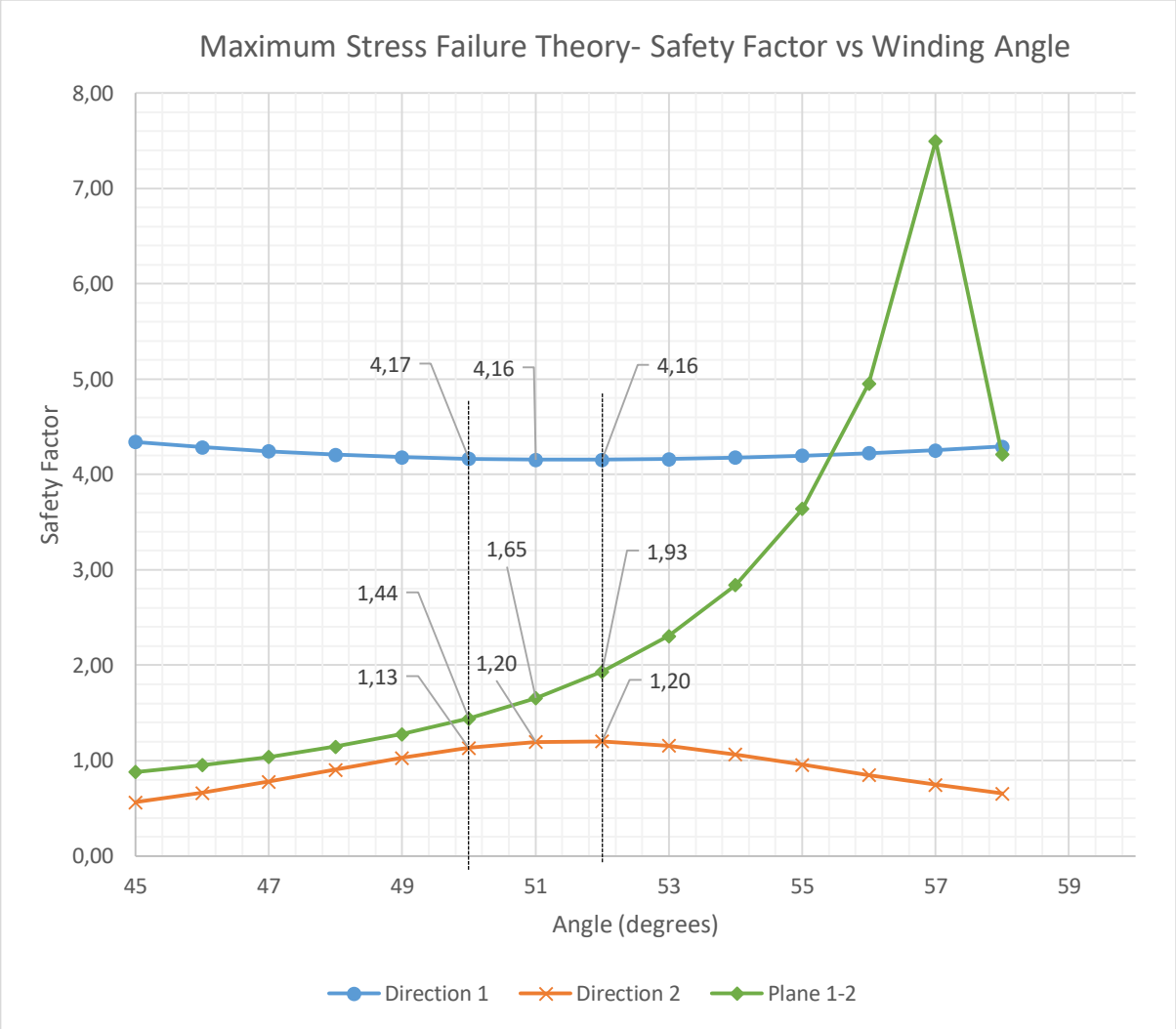

Figure 3.29: Graph of the safety factor vs the filament winding angle for each orientation

Therefore, the peak of the curve for direction 2 was determined to be the point that would give the optimal design safety factor. The other safety factors for direction 1 and plane 1-2 were inferred from the line that passes through the optimal point which was at approximately 52^0. However, the manufacturer (GRP Tubing) could only guarantee a filament winding angle of 50^o which was also the reported optimal winding angle by Shultz et al [106]. It was eventually used in the manufacturing of the CFRP tubes.

3.2 End cap design

The end caps are to be secured to each end of the filament wound CFRP cylindrical tube using SpaBond 340 LV adhesive in a similar fashion to that employed in the water rocket design. The end cap design used underwent several iterations to improve it to better suit the pressure vessel requirements. The functions of the end caps are three-fold, to resist the load due to the pressure of the fluid, to seal the pressure vessel thereby preventing leakage and to allow gas storage fittings to be incorporated onto the vessel. The end caps will incorporate O-rings in their design which will assist in containing the contents of the vessel from leaking to the outside. Stress analysis and suitable material selection were essential in the design of the end cap if it is to fulfil its intended purposes.

3.2.1 Geometrical features of the end cap

To achieve the three functions of the end cap, there were certain geometrical features that had to be designed including grooves for O-rings and provision for a bond area. Below are schematics of the simplified end cap concept. This was adopted from the water rocket design [1].

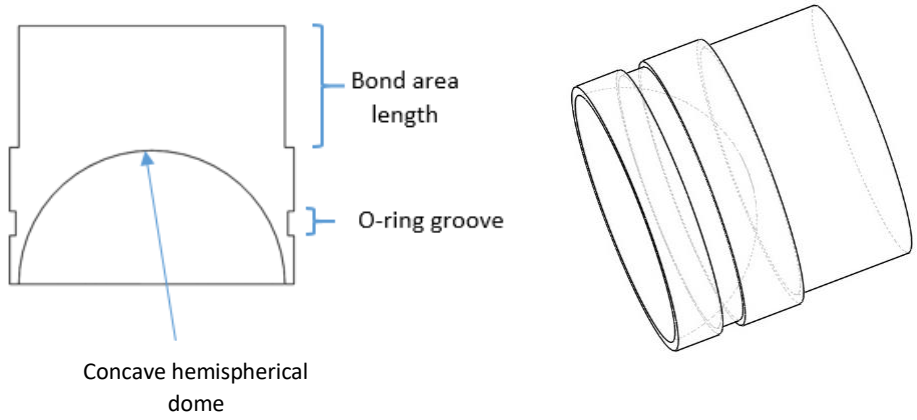

Figure 3.30: Cross-sectional schematic (left) and isometric view (right) of the simple end cap design employed in the water rocket project [1]

The hemispherical dome shown in Figure 3.30 above allows the pressure in the vessel to be divided equally across the surface which reduces the possibility of stress concentrations [48]. According to [54], the hemispherical shape on the end cap is also the most efficient shape for pressurized storage. The pressure acting on the hemispherical dome will not only result in the end cap being pushed longitudinally outwards but also in the hoop direction against the internal surface of the CFRP tube. This will ensure that the adhesive layer should not experience tension but always be in compression. This is helpful as the adhesive is generally weak under tension [108]. There is an O-ring which should effectively seal the vessel preventing any contact between the contents of the vessel with the outside environment. The bond area on the external surface of the end cap will be the designated area where the SpaBond 340 LV adhesive will be applied. The adhesive layer will effectively bond the end cap onto the inner surface of the CFRP tube at the end. The bond in this configuration would experience predominantly shear as a result of the internal pressure being exterted on the end cap. A visual representation of how the end cap will be assembled onto one of the ends of the CFRP tube is shown in Figure 3.31.

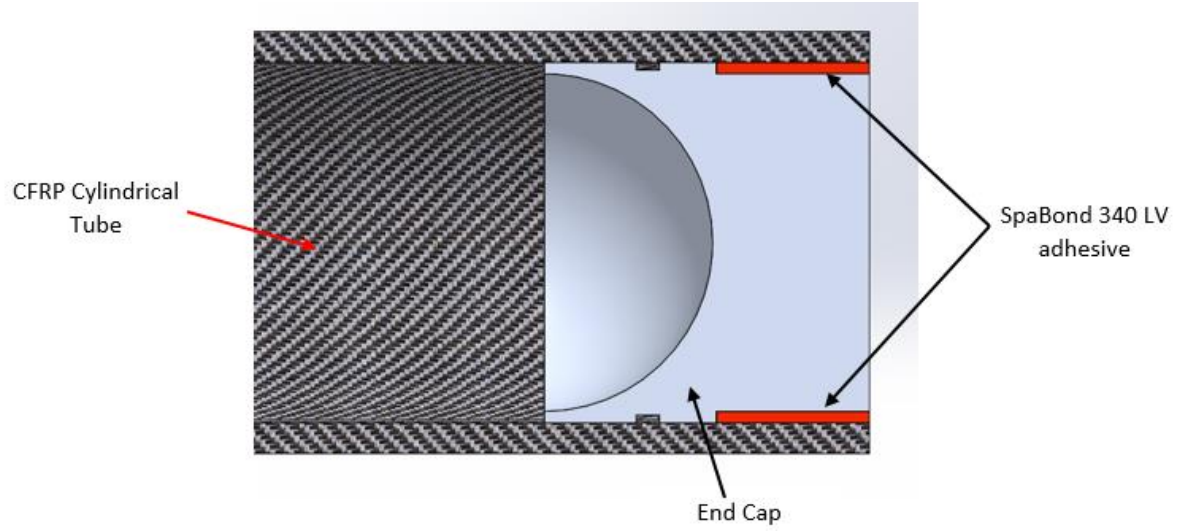

Figure 3.31: Cross-sectional view of one of the ends of the CFRP tube with an end cap secured by SpaBond 340 LV adhesive

Two end caps are needed to seal off the open ends of the CFRP tube. However, one of the two end caps will have to accomodate appropriate end fittings that will facilitate the insertion or removal of the fluid(s) contained within the pressure vessel. To achieve this, one of the end caps will require a threaded hole for a male threaded connection of an appropriate end fitting. The threaded hole was chosen to be of British Standard Pipe (BSP) standard which is quite common in industry for pressure vessel connections. Figure 3.32 illustrates both of the end caps bonded onto the both ends of the CFRP tube.

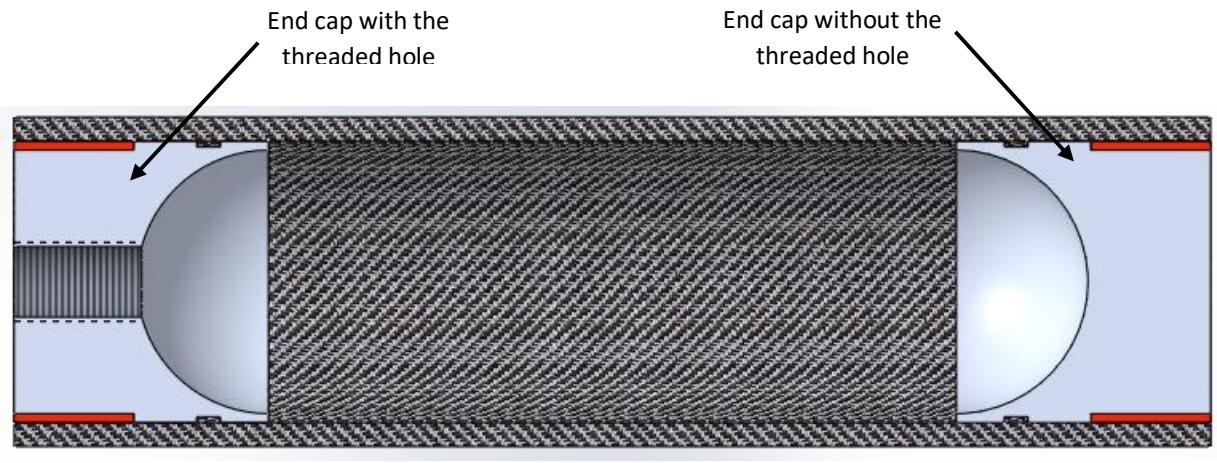

Figure 3.32: CFRP tube with the two end caps secured on both ends

3.2.2 Material selection

The material selection for the end cap was guided by the following design considerations:

- The material should have a sufficiently high yield strength to resist failure due to the loading induced by the internal pressure of the fluid in the vessel.
- The material should have a lower elastic modulus than the CFRP tube in the hoop-direction.
- The material should be compatible with SpaBond 340 LV which is a suitable epoxy-based adhesive used to bond the end cap to the CFRP tube.
- The material should be easy to fabricate/machine.
- The material should be as cheap as possible.

- The material should have a low mass density.

The material selection was mainly performed by using the CES EduPack 2017 software [109] as it contained most of the conventionally available materials in use currently. The parameters used were based on the above-mentioned design factors as shown below:

(a) The material had to have a minimum yield strength of 200 MPa and a maximum elastic modulus of 100GPa. These 2 parameters were entered the respective input fields which filtered out most of the materials leaving only 11 materials (mostly metallic) from which to choose from.

(b) The second step involved choosing a material with a tensile strength of at least 300 MPa from the remaining 11 materials which narrowed down the list of materials to 6 with 5 of them being metallic based materials and the other being CFRP composite.

(c) Ultimately, the last selection criteria were based on the mass density and the cost of procurement for the materials. Below is Table 3.7 that was drawn up containing the materials left from the previous step (except for CFRP) along with their respective densities and unit cost which were available within the software.

Table 3.7: Typical costs of the different materials as quoted from the CES Edupack software [109]

Material	**Density [kg/m^3]**	**Cost per unit mass [US$/kg]**
Age-hardening wrought Aluminium Alloys	2500-2900	1.9-2.0
Brass	7900-8500	4.29-5.03
Bronze	8500-9000	5.97-6.98
Commercially pure titanium	4500-4520	12.7-14.3
Zinc die-casting alloys	4950-7000	2.21-2.42

Because of the need to build a lightweight CFRP pressure vessel, the material for the end caps had to have a low mass density to contribute as little weight as possible to the total weight of the CFRP pressure vessel. In addition, the material to be chosen also had to have a relatively low cost which would not add considerably to the pressure vessel's total cost. Of all the materials available, aluminium was the best choice based on mass density and cost as it ranked lowest in both cases. Zinc also had low cost and densities relative to other materials but compared to aluminium it had almost twice the density. Titanium had also a reasonably low density though it costs almost six times more than aluminium which disqualified it from further consideration. Brass and bronze both had densities that were about three times more that of aluminium whilst costing significantly more which made the not ideal for this application. Hence, aluminium was the clear choice of material to use to make the end caps. Aluminium 6082-T6 was the type of aluminium that had the required mechanical properties and was readily available to use. A summary of its mechanical properties is listed in Table 3.8.

Table 3.8: Aluminium 6082-T6 mechanical properties [110]

Property	**Unit**	**Value**
Proof stress	MPa	245
Tensile strength	MPa	300
Tensile Modulus	GPa	70
Density	kg/m^3	2700

3.2.3 Stress analysis for the end cap

The end cap will experience two different types of loading namely the distributed direct force due to internal pressure from the fluid pushing on the end cap and the shearing on the epoxy adhesive layer. Figure 3.33 exhibits the end cap with the uniformly distributed pressure load (in blue) and the shear force applied by the adhesive layer (in orange).

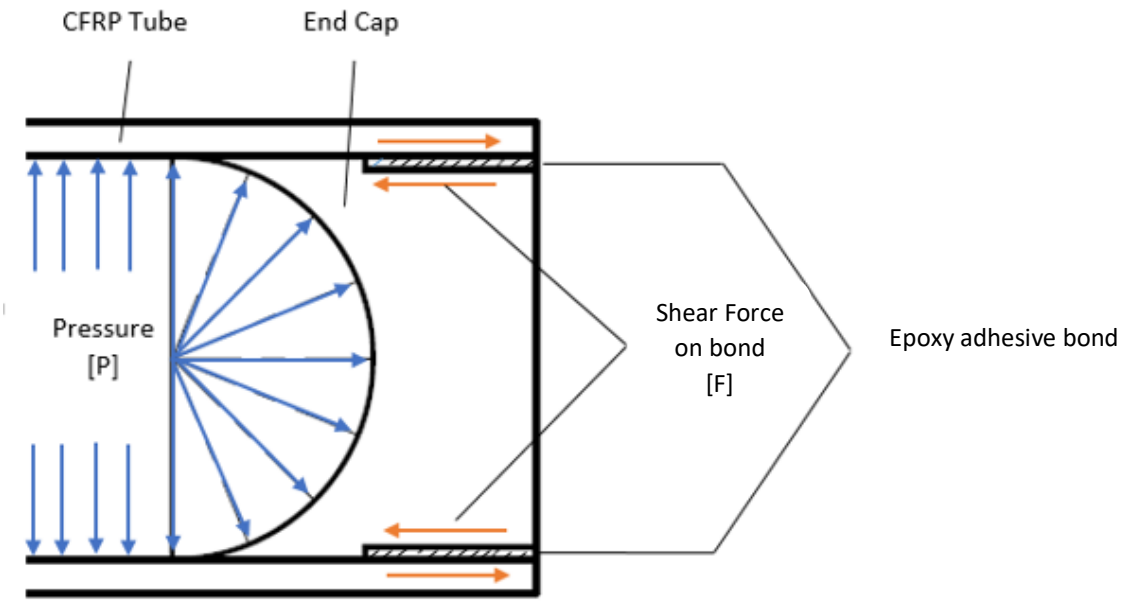

Figure 3.33: Illustration of the types of loading on the end cap

Shear stress due to the epoxy adhesive bond

Because the pressure will be acting on the side of the end cap with the hemispherical dome, the interface with the epoxy adhesive will experience shear stress. This is a result of the end cap being "pushed" outwards by the pressure of the fluid while the adhesive layer resists the pressure by holding the end cap. The equation 3.1 was used for calculating the shear stress as shown below:

$$\tau_s = \frac{F}{A_s} \quad \textbf{[3.1]}$$

where τ_s is the shear stress in [MPa],

F is the shearing force in [N] and

A_s is the bond area undergoing shear [mm^2]

The shearing force, F, due to the pressure acting on the hemispherical dome of the end cap is determined by equation 3.2 below:

$$F = P \cdot A_p \quad \textbf{[3.2]}$$

where P is the internal pressure of the vessel in [MPa] and

A_p is the projected area of the hemispherical end in [mm^2]

Sizing the end cap

The end cap has several dimensions as shown in Figure 3.34. The outer diameter was derived from the internal diameter of the CFRP tube. Hence, the outer diameter of the end cap had to be 50 mm. The bond area has two main dimensions namely the bond line thickness and the length. The bond line thickness is the distance between the inner surface of the CFRP tube and the bond area. The recommended bond line thickness when using epoxy adhesives to bond aluminium was in the range of 0.5-1.5 mm [111]. Thus, a bond line thickness 1.5 mm was chosen. Knowing both the end cap outer diameter and the bond line thickness, meant that the bond area diameter could be computed.

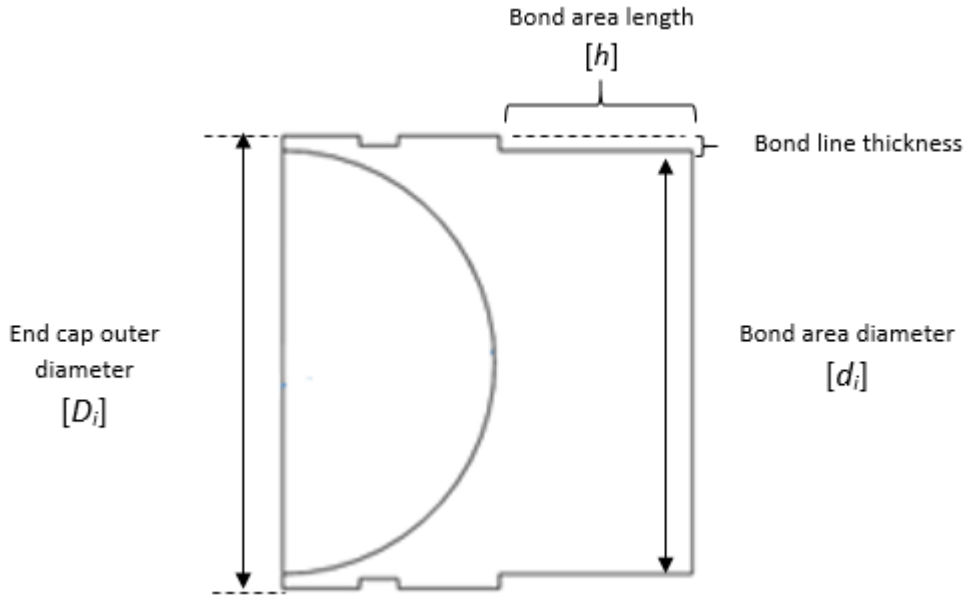

Figure 3.34: Schematic of a simple end cap with the respective dimensions

Calculations of the bond area length

Using the properties and dimensions in Table 3.9 below, some basic calculations were performed to obtain the maximum applied shear stress on the epoxy adhesive bond.

Table 3.9: Dimensions of the end cap and other properties

Property	**Symbol**	**Value**	**Units**
Internal diameter of vessel or end cap outer diameter	D_i	50	mm
The diameter of the bond area	d_i	47	mm
Internal pressure within the vessel	P	350 [35]	bar [MPa]
Theoretical shear strength of the Spabond 340 LV	τ_s	34	MPa
Safety factor	n	2.5	

The pressure acting on the end cap manifests as a shearing force that will attempt to push the end cap outwards. That maximum applied force was found to be the following:

$$F_s = P \cdot A_p = 68.722kN$$

There were two bond interfaces namely (a) the interface between the adhesive layer and tube and (b) the interface between the adhesive layer and the end cap. The adhesive bond was likely to fail on one of those two interfaces which was later established by the end cap adhesive shear tests covered in the next chapter. The applied shear stresses of both the interfaces were determined as shown below:

(a) Interface between the adhesive layer and the CFRP tube

Shear Area $A_{S1} = \pi D_i h = \pi \times 50 \times h = 50\pi h \ \ mm^2$

Minimum bond area length, $h = \dfrac{F_s \, n}{50 \, \pi \, \tau_s} = 32.2 \ mm$

(b) Interface between the adhesive layer and end cap

Shear Area $A_{S2} = \pi d_i h = \pi \times 47 \times h = 47\pi h \ \ mm^2$

Minimum bond area length, $h = \dfrac{F_s \, n}{47 \, \pi \, \tau_s} = 34.2 \ mm$

Case (b) gave a higher value for the bond area length proving to be the worst case. Therefore, the minimum bond area length was rounded up to be 35 mm.

Applied stress and deflection due to the pressure

Besides causing shear, the pressure, P, will also cause the end cap to deform as previously explained. Assuming the adhesive layer's bond does not fail in shear, a direct uniformly distributed force will be applied directly onto the end cap in the form of a pressure acting on the curved surface area of the hemispherical dome. As such, the end cap will also need to resist yielding under the influence of this load. Because of the shape of the end cap, determining the applied stress acting on each point on the end cap is complex. The values of applied stresses and hence induced strains on the end cap are not uniform for every point. However, this problem can be simplified if one is to assume that the end cap takes on the shape of a circular disc/plate with clamped flat ends as shown in Figure 3.35. An analytical solution could be simpler to solve for the circular disc of constant thickness than the end cap in Figure 3.33.

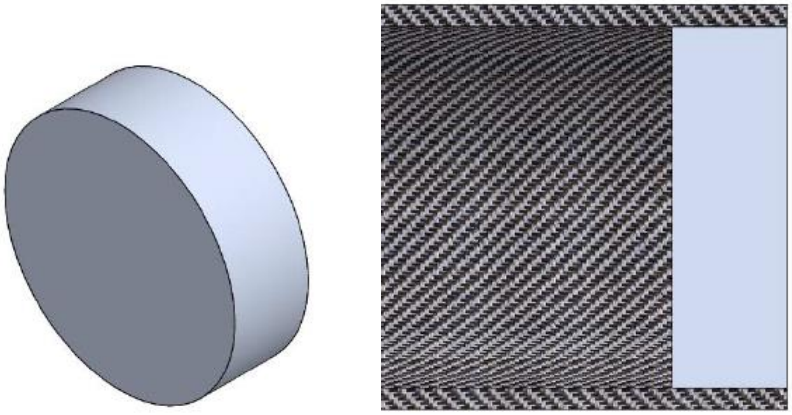

Figure 3.35: Isometric view (left) of a simple circular disc as well as the same disc when secured onto one of the ends of the CFRP tube (right)

Some of the assumptions that were made are as follows:

1. The pressure acting on the flat face of the disc is constant at all points on that face
2. The circular edge was fully constrained/clamped by the epoxy adhesive bond
3. The CFRP tube was considered to have negligible deformation in the hoop direction since the tube had a higher elastic modulus than the circular aluminium disc.

According to E.J. Hearn [76], the circular disc similar to the one shown above can be analysed analytically and the applied stress as well the deflection could be determined. The maximum deflection occurred at the centre of the disc whilst the maximum stress occurred on the clamped/constrained circular edge. The equations for the maximum deflection and applied stress were as follows:

$$\text{Maximum deflection: } \delta = \frac{3qR^4}{16Et^3}(1-\nu^2) \quad \textbf{[3.3]}$$

$$\text{Maximum applied stress: } \sigma_R = \frac{3qR^2}{4t^2} \quad \textbf{[3.4]}$$

Where ***q*** is the pressure, ***R*** is the radius of the disc, ***v*** is the Poisson's ratio for the material of disc, ***E*** is the elastic modulus for the disc and ***t*** is the disc thickness.

With most of the variables required to solve the above equations known, the disc thickness was the only unknown in this case. To determine the minimum thickness required for the disc to avoid permanent deformation, the maximum applied stress had to be equated to the yield strength of the material of the circular disc (i.e. Aluminium 6082-T6)

Table 3.10: Design variables for sizing and analysing the stresses on the end cap

Property	**Symbol**	**Value**
Radius of the disc	R	25 mm
Poisson's ratio for Aluminium [112]	ν	0.35
Elastic Modulus of Aluminium 6082-T6 [110]	E	70 GPa
Yield Strength of Aluminium 6082-T6 [110]	σ_y	255 MPa
Maximum pressure within the vessel	q	35 MPa

Given the data in Table 3.10, the minimum thickness required for the circular plate was as follows:

$$t = \sqrt{\frac{3qR^2}{4\sigma_R}} = \sqrt{\frac{3(35)(25^2)}{4(255\times10^6)}} = 8.02\ mm$$

For a plate thickness of 8.02 mm, the maximum deflection at the centre of the circular plate was determined to be as follows:

$$\delta = \frac{3(35\times10^6)(25\times10^{-3})^4}{16(70\times10^9)(8.02\times10^{-3})^3}(1-0.35^2) = 0.0623\ mm$$

However, the actual thickness of the end cap was determined to be at least 35 mm (i.e. the bond length) which made it reasonable to conclude that the end cap would not fail due to the applied stress nor would it have a significant deflection.

The actual aluminium end cap was modelled in SolidWorks 2017-18 with a total length of 50 mm with a hemispherical dome with a 19 mm radius. The Finite Element Analysis (FEA) tool within the software was used to model all the types of loading on the end cap (see Figure 3.36 below) and investigate the resulting effects. The major assumption that was made for the FEA tool was that the surface on the end cap in contact with internal wall of the CFRP tube was fixed meaning that it was constrained from deforming in the hoop direction. The assumption was based on the fact that CFRP tube was stiffer than aluminium in the hoop direction.

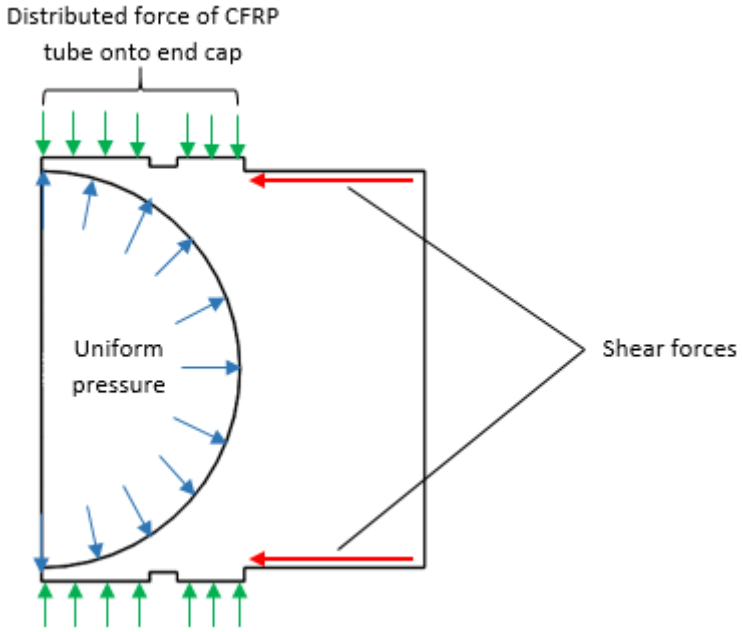

Figure 3.36: Illustration of the applied forces on the end cap as modelled in the FEA software

After running the FEA model, the maximum deflection was determined to occur at the centre of the hemispherical dome (which was characterized by the red in colour in the Figure 3.37) with a value of 0.01311 mm.

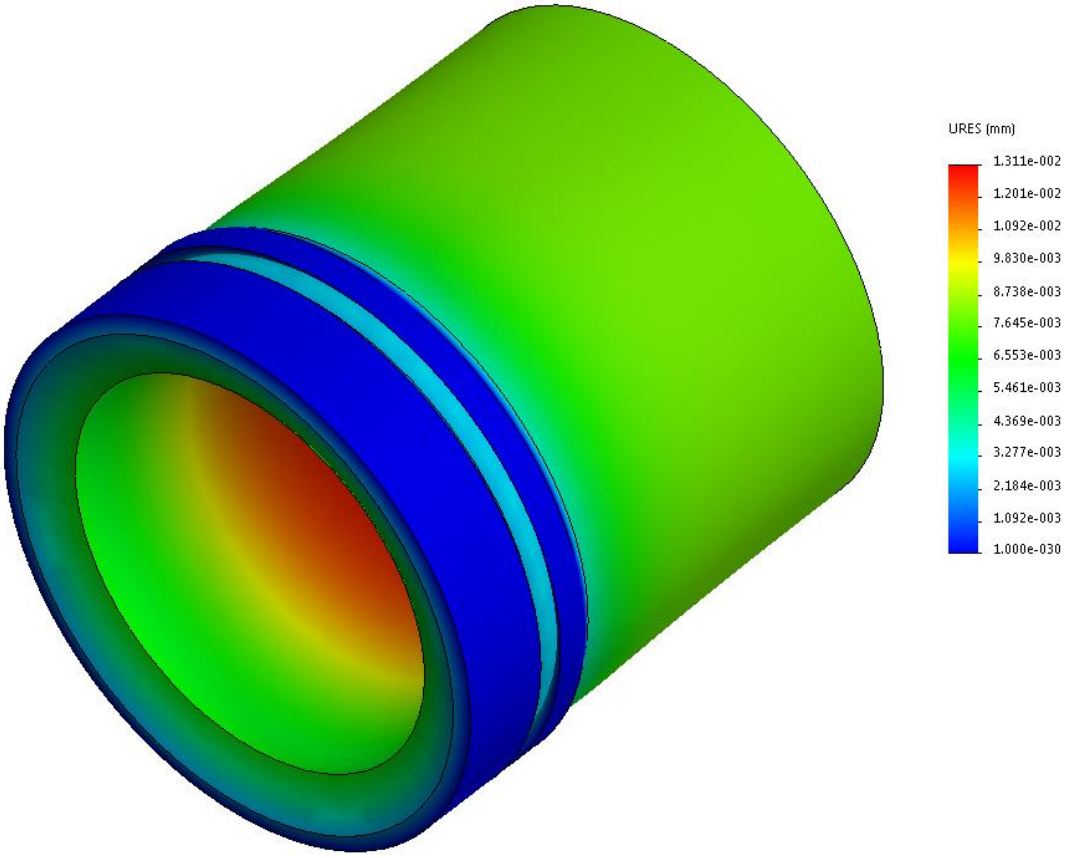

Figure 3.37: Illustration of the FEA deflection/deformation result for the first end cap design

It was also worth noting that there was a significant amount of deformation on the bond area according to colour spectrum scale on the right side of the above figure. This meant that the bond area would press the epoxy adhesive bond against the internal wall of the CFRP tube which was favourable for its shear properties [108]. If the bond was to experience tension, cleavage would have likely occurred at a lower pressure than 350 bar. In addition, there was also an appreciable amount of outward deformation in the groove in which the O-ring would sit which meant that the O-ring would be pushed against the inner wall of the CFRP tube ensuring that the O-ring should adequately seal the vessel.

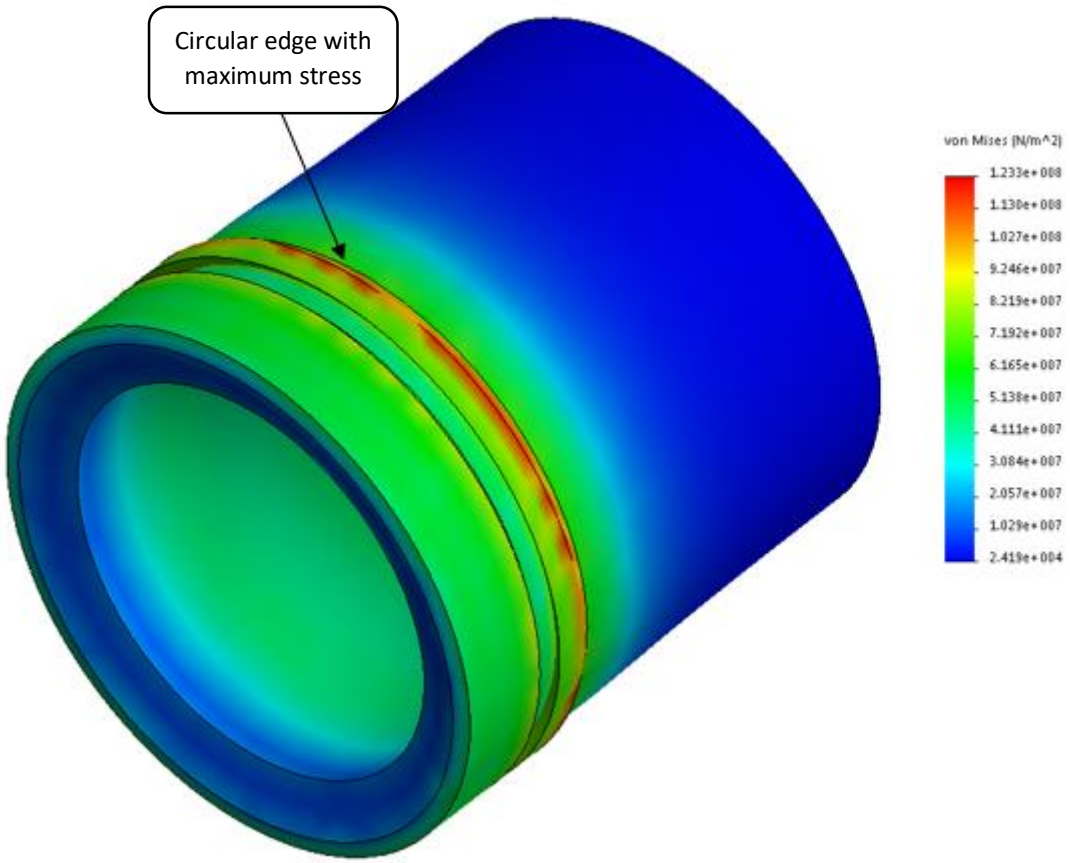

Figure 3.38: Illustration of the FEA stress result for the first end cap design

In Figure 3.38 above, the FEA results for the applied stress showed that the maximum stress occurred on a circular edge of the end cap that would be in contact with CFRP tube and was immediately adjacent to the bond area. The value of the stress at that edge was about 123 MPa which was approximately half of the yield strength of Aluminium 6082-T6. Therefore, the FEA result confirmed that the end cap should not yield under these loading conditions.

3.2.4 Design iterations

The end cap underwent two design iterations after the first design in a bid to ensure they fulfil their predetermined functions. This section will describe each of the three end cap designs that were developed. The detailed drawings for each of the designs can be found in Appendix B.

First end cap design

The initial design geometry employed for the end cap was based solely on the design used in the water rocket project [1]. Figure 3.39 shows a cross section of the schematic of the first end cap design with hemispherical dome, end cap groove and the designated bond area labelled.

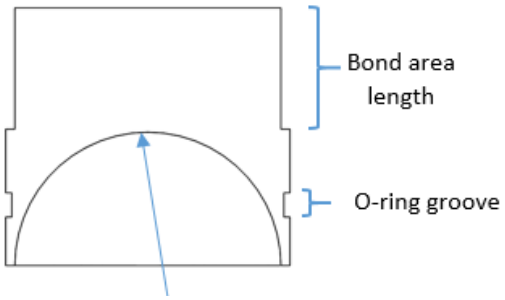

Figure 3.39: Schematic of the cross section of first end cap design

The end caps based on the first design were machined (see section 7.2.5 for more details on end cap manufacturing) and bonded with SpaBond 340 LV adhesive onto the CFRP tubes to form a prototype specimen CFRP pressure vessel. The resin for the SpaBond 340 LV adhesive had been mixed with a slow hardener to form a grey adhesive mixture as shown in the photographs in Figure 3.40. The prototype vessel was subjected to a hydrostatic burst test (more details to be covered in the later chapters). The bond area on one of the two end caps of the pressure vessels failed through shear at a pressure of just over 130 bar which was significantly lower than what was expected. The shear failure occurred on the surface of the aluminium end cap that was in contact with the bond as anticipated. After failure, the end caps were pressed into the vessel so that the bond area could be inspected visually. Figure 3.40 below displayed the voids that formed on the end cap to adhesive layer interface in great detail.

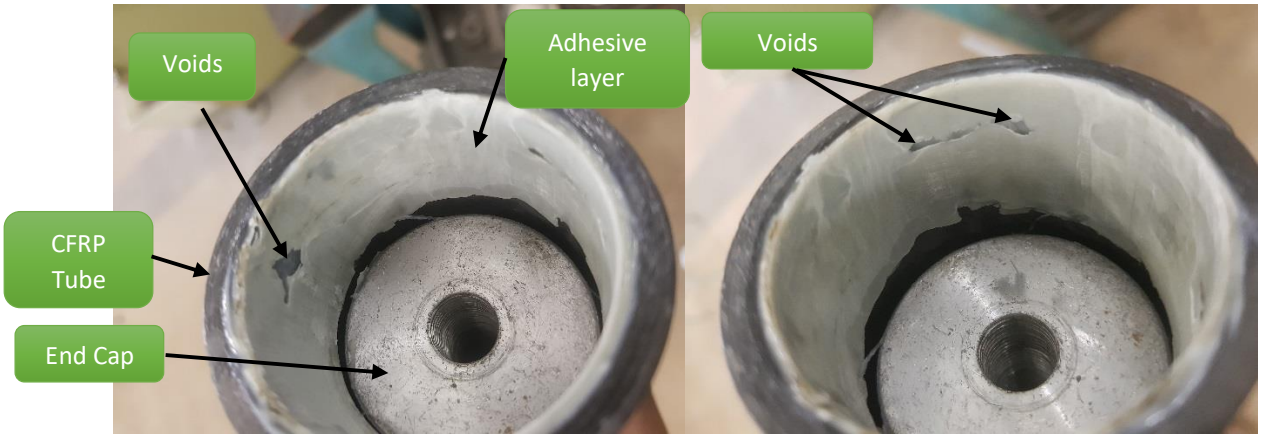

Figure 3.40: Photographs illustrating failure through shear on the surface of the first design of the end caps

The voids effectively reduced the surface area of the bond that was in contact with the end cap which possibly resulted in the lower shear strength value of the bond (about 5 MPa as compared to the theoretical value of 34 MPa). The formation of voids was observed to have been attributed to the application method of the adhesive. This method involved applying the adhesive on the bond area on the external surface of the end cap by smearing it on before pushing it into one of the ends of the CFRP tube as illustrated in Figure 3.41:

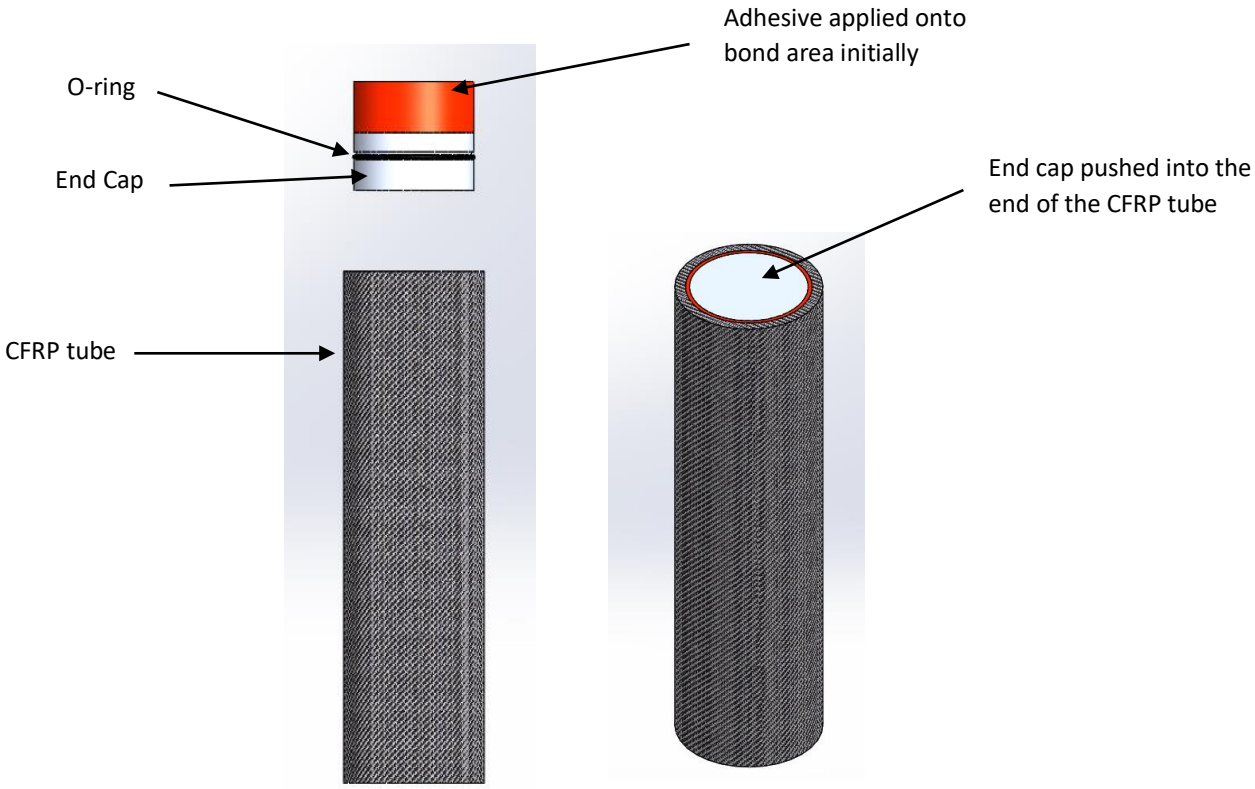

Figure 3.41 Illustration of the initial application method of the epoxy adhesive onto the first end cap design

The initial adhesive application method involved the following steps:

- The internal surface of the CFRP tube and the external surface of the end cap had to be abraded with emery cloth with grit of 80.
- The two surfaces then had to be cleaned using acetone.
- After mixing the Spabond 340 LV resin with the slow hardener, the adhesive mixture would be smeared onto the bond area on the end cap as shown in the left image above
- The end cap will finally be pushed into the CFRP tube and left in that position until the adhesive sets.

Because of the pushing of the end caps into one of the ends of the CFRP tube, some of the adhesive would likely be displaced by trapped air pockets. The trapped air pockets remained in the bond area even after the adhesive would have set and formed voids. Consequently, this compromised the strength of the bond when it was cured. Hence, the design of the end cap had to be altered to improve the shear strength by eliminating the formation of voids.

Second end cap design

To eliminate the formation of voids in the bond area, altering the method of applying the adhesive was required. The new method involved placing the end cap into an end of the CFRP tube then introducing the adhesive into the bond area afterwards. The end caps had to have holes drilled into them to provide a path for the adhesive to flow into the bond area as displayed in Figure 3.42.

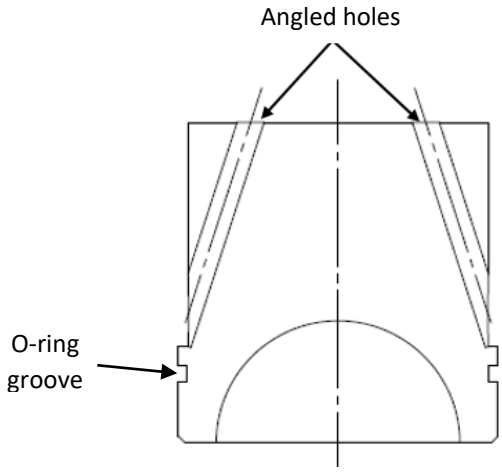

Figure 3.42: Schematic of the cross section of the second end cap design

The adhesive mixture would flow through the angled holes to the bottom of the bond area before flowing up to the top of the bond area thereby "displacing" any air (see Figure 3.43 below). The SpaBond 340 LV in this case was used with the fast hardener as this was observed to produce a less viscous adhesive mixture than when the slow hardener was used previously. The less viscous adhesive mixture was ideal it allowed the bond area to be filled easily.

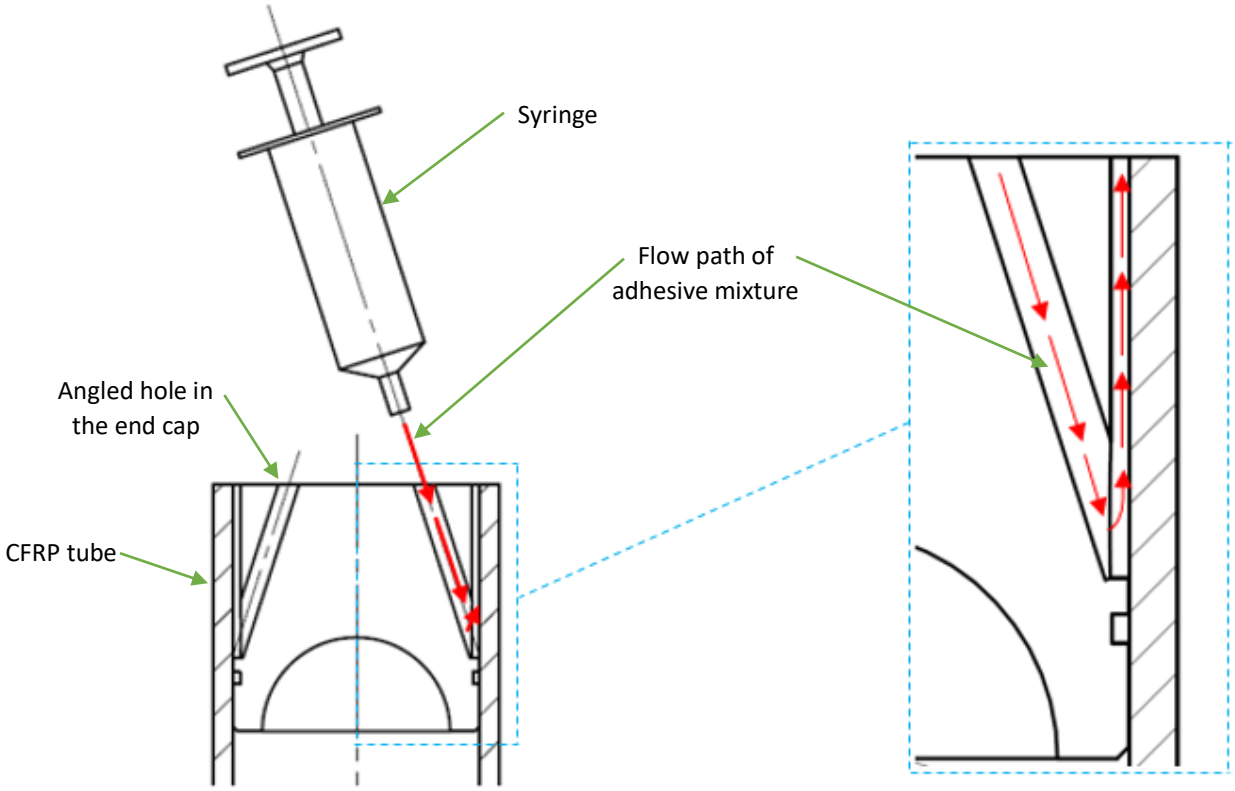

Figure 3.43: Illustration of how the new adhesive application method works with a detailed view of the flow path of the adhesive from the syringe, through the angled holes into the designated bond area

In Figure 3.44 is a photograph showing a uniform adhesive layer on the inner surface of the CFRP tube after the end cap was pressed out. It shows that the second adhesive application method was more successful as there were no discernible voids that formed on the bond. This resulted in a higher shear

area (and strength) than from the previous method. This was supported by the second set of end cap adhesive shear tests that were performed (more details in the next chapter).

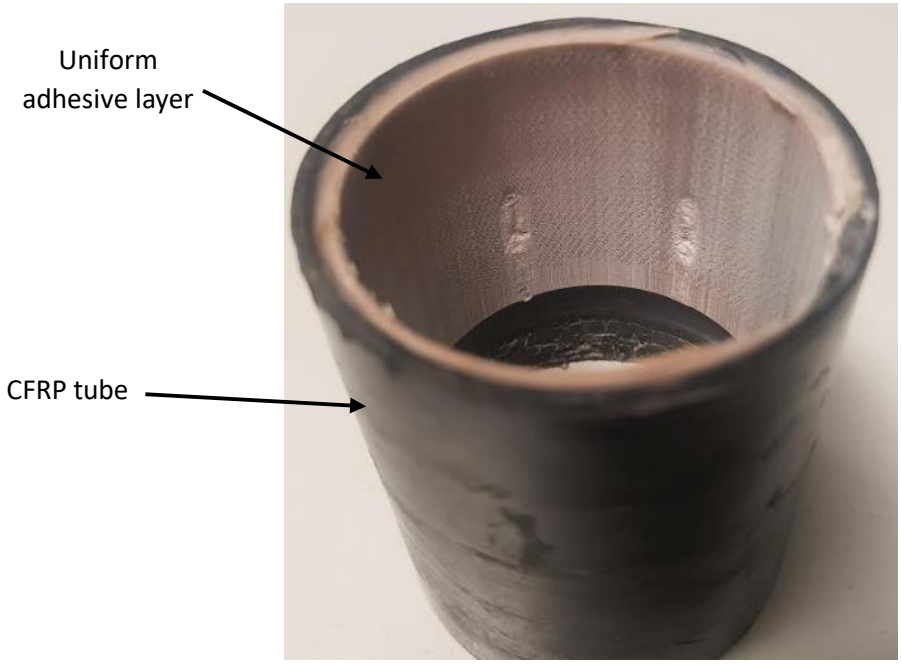

Figure 3.44: Photograph showing the adhesive layer after end cap had been removed

There were two prototype pressure vessels that were constructed using the second design that underwent hydrostatic burst tests. The burst tests resulted in the two vessels failing at pressures of 162 bar and 220 bar which was an improvement from the previous test. However, the average shear strength of the bond from the second set of shear tests (covered in the next chapter) was still far lower than the value in the datasheet for SpaBond 340 LV. This may have been because the surface of the end cap in contact with the bond was not rough enough to grip effectively onto the bond. In addition, the big difference between the two failure pressures was likely due to the inconsistency in the surface roughness between the end caps in those two vessels. Therefore, there was a need for rougher bond area surface with a consistent surface roughness. Therefore, the leakage and surface roughness issues needed to be addressed in the next end cap design.

Third end cap design

The third and final design improves on the results of the two previous designs firstly by further improving leak tightness. To address the leaking issue, two O-rings were to be accommodated instead of one, with two O-rings being more difficult to by-pass. The two grooves are shown in the schematic in Figure 3.45. Secondly, to improve on the surface roughness, it was decided to have the bond surface on the end cap knurled on a lathe. Knurling increases the surface roughness which is essential in increasing the mechanical bond of the surface in contact with the adhesive layer. In addition, the knurling would be consistent for all the end caps in terms of surface roughness which would also mean that the shear strengths would be similar for all the pressure vessels. To increase the pressure at which shear failure would occur, it was decided to increase the length of the bond surface on the end cap by 20 % (through increasing the bond area length from 35 mm to 42 mm). The 20% increase in the bond area length would only be applied to the end caps used in pressure vessels not in the end cap adhesive shear tests. The second cap design can be found in Appendix B1.3.

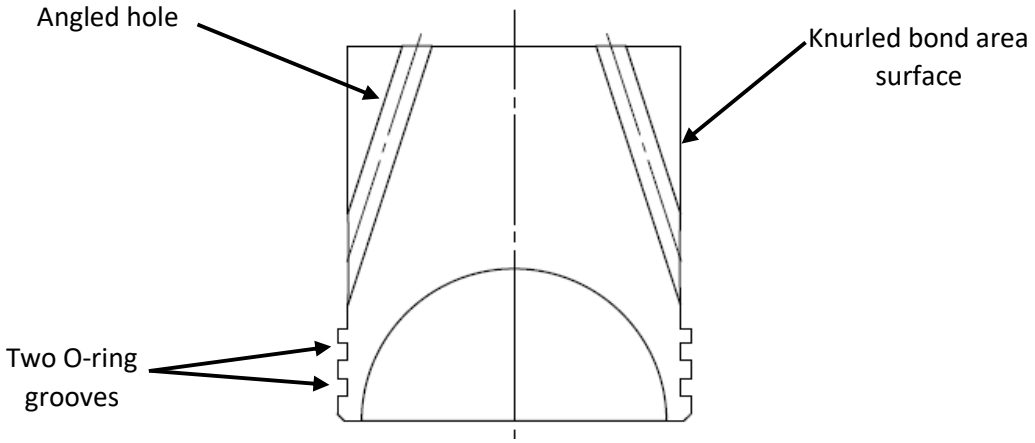

Figure 3.45: Schematic showing cross-sectional view of the third end cap design with 2 O-ring grooves and a knurled bond area surface

3.2.5 End cap manufacturing

The material to manufacture the end cap was selected to be Aluminium 6082-T6. Because the end cap is to fit into the internal surface of the CFRP tube, it also has to be cylindrical in shape symmetrical about a mutual central axis shared by both the tube and the end cap. The aluminium was initially sourced in the form of a cylindrical bar of a higher diameter (60 mm) than the nominal external diameter of the end cap. The bar of aluminium was secured on a lathe where it was turned which reduced the diameter to the nominal diameter of 50 mm. The other lathe operations performed to produce the desired end cap features (i.e. grooves, holes, hemispherical dome and knurled surface) included parting off, drilling, knurling and internal boring.

3.3 Rubber liner

Composites are generally porous in nature [3-4, 113]. The CFRP pressure vessel being designed and manufactured might also form micro-cracks because of various phenomenon like varying thermal cyclical loads that may arise due to filling the vessel with a gas [114]. These micro-cracks need to be sealed lest the fluid contained within the vessel seeps out through them. To counter this problem, Stuart Swan developed a method of lining the pressure vessel portion of the water rocket he built with rubber [1]. For the CFRP pressure vessel, the rubber liner will also serve the main purpose of sealing the internal surface of the CFRP tube to prevent leakage of the pressurized fluid within the vessel through the CFRP tube section. Because the rubber lining is applied post-manufacture of the CFRP tube, it saves on assembly and manufacturing costs making it cheaper as compared to those incurred in manufacturing Type III and IV pressure vessels. Rubber as a material is also cheaper to purchase than the pre-formed rigid aluminium and polymeric liners within the Type III and IV vessels. Rubber has a relatively lower mass density meaning that the use of a rubber liner would lower the weight of the pressure vessel considerably which should help increase its gravimetric density.

3.3.1 Liner application method

The rubber that was used in the water rocket [1] is called VytaFlex 60 urethane rubber and it was to be used in the CFRP pressure vessel as well. The rubber comes in the form of two separate liquid components which are mixed by a 1:1 ratio and applied onto the inner surface of the pressure vessel before it is left to set and then cure for 16 hours at room temperature as per the technical data sheet provided by the manufacturer [115].

Procedure

Below is an in-depth description of the procedure that is followed when applying the rubber liner. This procedure assumes CFRP tube has already has one end cap bonded to the CFRP tube with the other end left open.

- The open end of the tube had tape attached onto the section that would have the other cap bonded onto the tube as shown in Figure 3.46. The tape was meant to prevent the rubber from settling and curing onto that area as the rubber could have prevented the SpaBond 340 LV from bonding well with the inner surface of the CFRP tube.

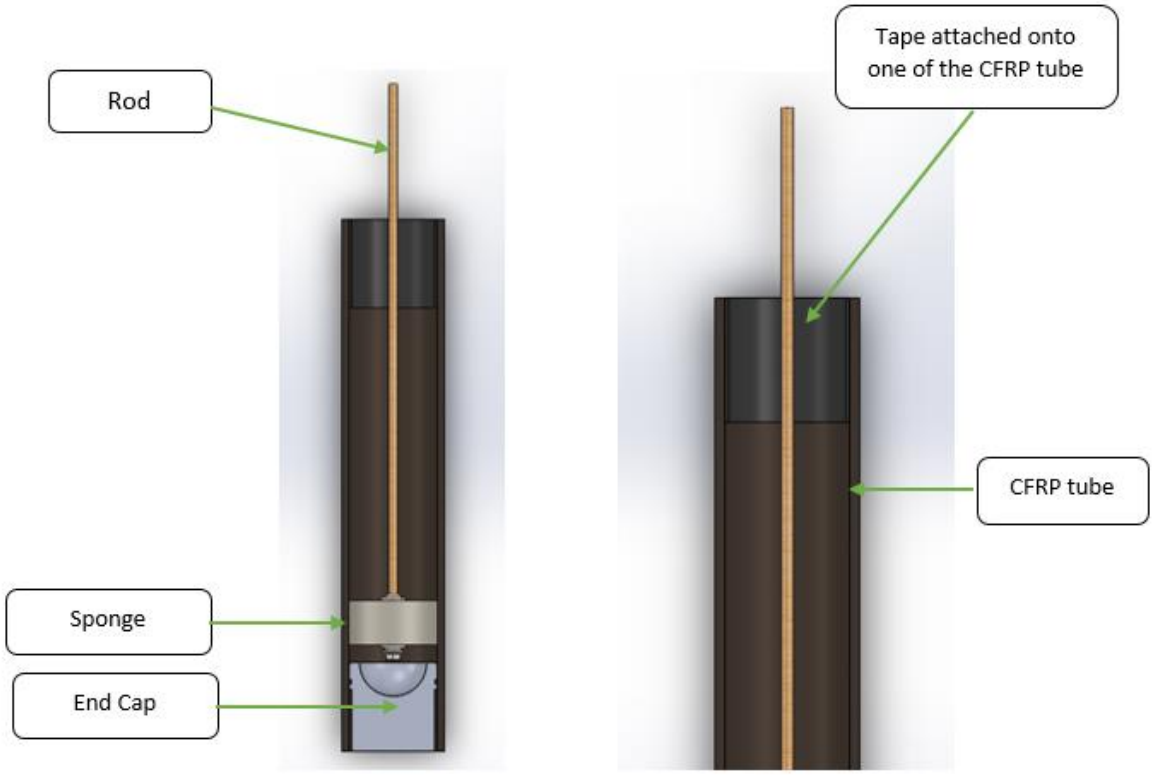

Figure 3.46: Illustration of the rubber application method

- The inner surface of the CFRP tube was first cleaned by a cloth to remove any dirt before being wiped by a cloth with Acetone to remove any chemicals, residual dirt and/or oils that might prevent the rubber from bonding well with the inner surface of the CFRP tube.
- A rod with a sponge attached and secured (by washers, O-rings and a nut) as shown in Figure 3.47 was inserted into the CFRP tube.

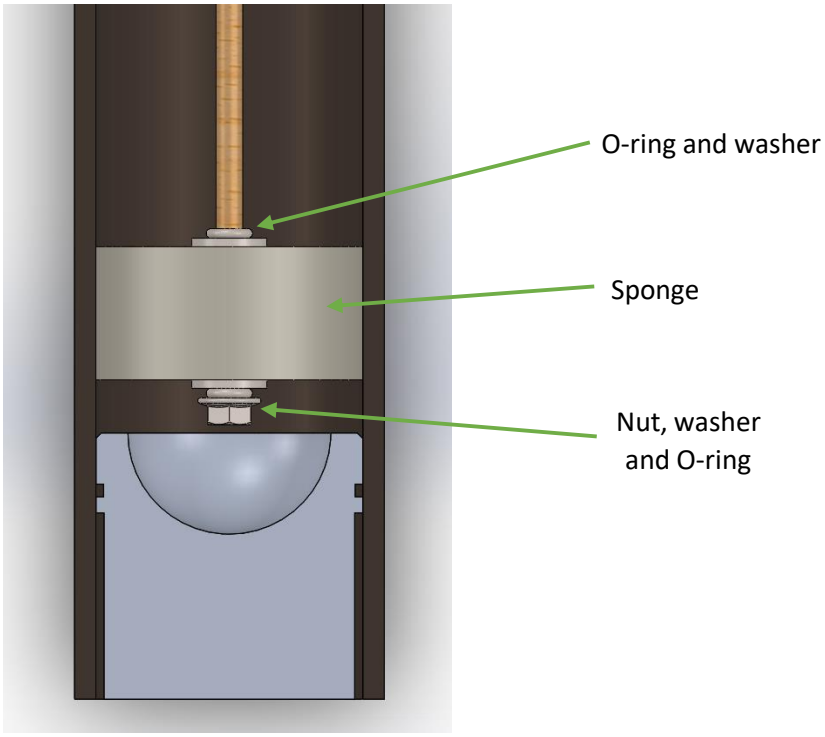

Figure 3.47: Illustration of the components used in applying the rubber

- The thoroughly mixed liquid rubber was then poured into the tube and was allowed to "seek its level" and be fully absorbed by the sponge for about 1 minute.
- The rod was then pulled out and pushed back in repeatedly. In the process, the sponge applying the liquid rubber onto the inner surface of the tube with each stroke. This step was repeated until the sponge could no longer ooze out and apply any of the liquid rubber onto the internal surface of the tube. At this point, the rod with the sponge was then removed from the tube.
- For about 30 minutes, the tube is left in the same vertical position before it is flipped vertically to have the open end in contact with the surface. This process was then repeated at least 4 times to ensure that there was an even thickness of the rubber at almost every point along the inner surface of the tube.
- The lined CFRP tube would then be left to cure for a period of 16-24 hours [115] before the procedure is repeated until the desired rubber layer thickness of approximately 1 mm was reached.
- The tape protecting the end cap bond region would then be removed.

3.3.2 Thickness of the rubber liner

The procedure of applying the rubber liner in the previous section only allowed for one layer of rubber that had a certain thickness. For the surface of the rubber lining to be smooth (when judging by eye), it was necessary to not exceed a particular amount of mixed liquid rubber before its application. Exceeding that amount would have resulted in an uneven rubber lining as the excess rubber would start flowing due to gravity which resulted in sizeable lumps forming on the inner wall of the CFRP tube. The lumps of rubber would not flow all the way down the inner wall of the tube because of the high viscosity of the liquid rubber. To determine the maximum thickness of the layer of rubber lining per time, different amounts of liquid rubber were prepared as well as different tube specimens to apply the rubber lining on. In total, seven rubber liner layers were applied to the different seven

specimens and the maximum thickness that would result in a smooth layer was determined to be about 0.2 mm. As was mentioned in the procedure for application of rubber previously, another layer of rubber lining could be applied on top of another layer to have a thicker layer. It was implemented by Stuart Swan for the water rocket [1] where he used three layers of rubber liner of approximately 0.07 mm thickness to get to a total thickness of 0.21 mm. It was decided to have a rubber lining with a total thickness of at least 3.5 times that of the water rocket which resulted in an intended thickness between 0.8-1.0 mm (i.e. 4-5 layers of approximately 0.2 mm thickness each).

3.4 Assembling the pressure vessel

This section will elaborate the steps that were followed in assembling the CFRP pressure vessel from its components. The CFRP pressure vessel was composed of three components namely the CFRP tube, end caps and the rubber lining as shown in Figure 3.48 below.

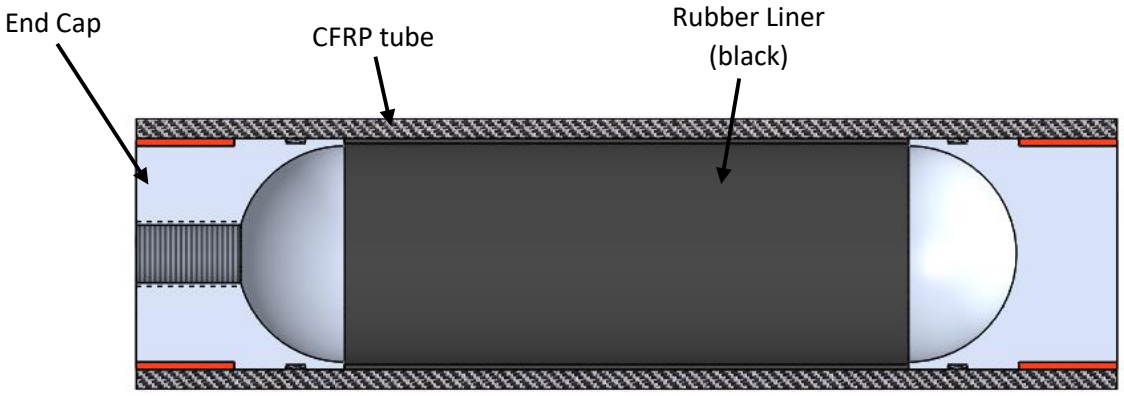

Figure 3.48: Cross section of a fully assembled CFRP pressure vessel

Initially, the CFRP tube was to be cut such that the total length would result in a length to diameter ratio of 4 which is common among vessels used in practice [116]. Therefore, the effective length would be 200 mm since the internal diameter of the tube was 50 mm. The total length of the pressure vessel includes the end caps as well (each at least 50 mm in length) which resulted in an overall length of at least 300 mm. In terms of surface preparation before bonding, both ends of the CFRP tube were to be sanded thoroughly using emery cloth of a grit of 80 with the focus being on the bond area on the inner surface of the tube. Both bond areas on one of the ends of the CFRP tube and on the end caps would be cleaned with a cloth with acetone to remove any dirt or oils that may prevent the epoxy adhesive from bonding well with either surfaces. The O-ring(s) were then placed in the respective groove(s) on the end cap before it was bonded onto the end of the tube. The adhesive layer between the end cap and the CFRP tube was then left to cure overnight before the rubber lining would then be applied using the application method described previously in section 3.3.1. The other end cap was then bonded onto the other end of the CFRP tube and also left to cure overnight. Subsequently, the CFRP pressure vessel would be placed in an oven and post cured using the schedule prescribed by the technical data sheet for SpaBond 340 LV [108]. This post-curing of the SpaBond 340 LV also benefitted the rubber lining as it provided further post-curing of the rubber [115].

3.5 Summary of the design and manufacture of the CFRP pressure vessel

The CFRP tube's design entailed initially choosing the inherently balanced angle ply laminate structure as the stacking arrangement which also had to be symmetric about the mid-plane. Next, the CLT was used to model the strain behaviour of the CFRP tube subject to the internal pressure. The Maximum Stress, Maximum Strain, Tsai-Hill and Tsai-Wu failure theories were then used to predict the burst pressure of the CFRP tube. In addition, the Maximum Stress failure theory determined that the optimum filament winding angle is 50^{o}. The manufacturing of the designed CFRP tube was performed using an automated filament wet winding process. The carbon fibre chosen was the HTS45 from Toho Tenax and the epoxy resin chosen was AR600 with the AH2336 hardener from Aerontec.

The initial design of the end caps was based on the water rocket design and SpaBond 340 LV was chosen as the epoxy adhesive to bond the end caps to the CFRP tube. The stresses acting on the end caps were the direct stress due to the internal pressure and the shear stress from the bond. Stress analyses were performed to determine the deflection and the maximum stress on the end cap using a simple analytical approach as well as FEA. The material chosen was Aluminium 6082-T6 and the manufacture of the end cap was to be performed on a lathe. However, the adhesive application method associated with the first end cap design resulted in the formation of voids in the adhesive layer thereby weakening the bond's shear strength. Firstly, the second end cap design had angled holes introduced allowing for direct injection of the adhesive into the bond area. This prevents void formation thereby increasing the shear strength of the bond. Secondly, two O-ring grooves were also introduced to prevent leakage of water during the hydrostatic burst testing. Knurling was performed on the designated bond area on the end cap for the third end cap design to give a consistent surface roughness.

The liner chosen to be applied on the inner walls of the CFRP tube was VytaFlex 60 series urethane liquid rubber. A sponge was used to absorb the liquid rubber before it would be used to apply the liner onto the tube's inner walls. This was left to cure for 16 hours before another layer of liner could be applied.

4. Testing methodology

To be able to fully design the CFRP pressure vessel, there was a need to know the design variables related to the strength of the CFRP composite and of the end cap's adhesive bond. Determining these values was necessary as it allowed for the correct sizing of the vessel's components as well as for the further optimization of the vessel to ensure that minimum material was used. This would lead to a lowering of the vessel's weight and costs involved in manufacturing the vessel. Once the vessels were manufactured, they had to undergo certain pressure tests to assess functionality. This included burst tests, hydraulic proof tests and leak tests which assessed failure pressure, tested reliability and checked for pressure retention without leaking.

4.1 Determination of mechanical properties of the CFRP laminate structure

As the values of the mechanical properties of the final filament wound CFRP composite were unknown, experiments had to be performed to determine these properties. These mechanical properties included elastic moduli, ultimate strengths and strains in the transverse and longitudinal orientations of the CFRP composite.

4.1.1 Description

The carbon fibre that was used for the filament wound pressure vessel was supplied by AMT Composites [117]. The manufacturer of the carbon fibre is Toho Tenax based in Europe. The product data sheet illustrated only the typical repeated values for the tensile properties (tensile strength and modulus) of the fibre [118]. The epoxy resin that was used with the carbon fibre was called AR 600 in conjunction with the AH 2336 hardener which were procured from Aerontec in Cape Town [119]. The product data sheets can be found in Appendix A.

Since the carbon fibres were to be mixed with epoxy resin (the matrix) to form the composite in particular volume fractions, the resulting properties of the composite would lie in between the properties of the fibre and the resin [3-4, 78]. Of particular interest was the expected longitudinal and transverse mechanical properties of the composite which would be used in the stress calculations section to determine the amount of material required, find safety factors, burst pressures etc. The American Society for Testing and Manufacturing (ASTM) D3039/D3039M standard was identified as suitable for finding the properties of the CFRP composite material. The ASTM D3039/D3039M describes a tensile test that determines the tensile strength of the laminated composite along the fibre direction (at 0^o) as well as those transverse to the direction of the fibres (at 90^o) [96]. Figure 4.49 illustrates the specimens for each of the two loading directions. It can also be used to determine the tensile moduli in the two orientations and the Major Poisson's ratio (v_1). The tensile tests required thin, flat rectangular specimens with unidirectional fibres and a constant thickness. They would need to be mounted onto the grips of a tensile testing machine before being pulled in tension until failure. The force and the corresponding strain of the specimens would be recorded until the specimen fails. The data recorded by the force and strain transducers could then be used to derive the stress-strain curve from which the ultimate tensile stresses (and strains), tensile moduli and Poisson's ratio could be determined which could then be implemented in the design of the CFRP pressure vessel.

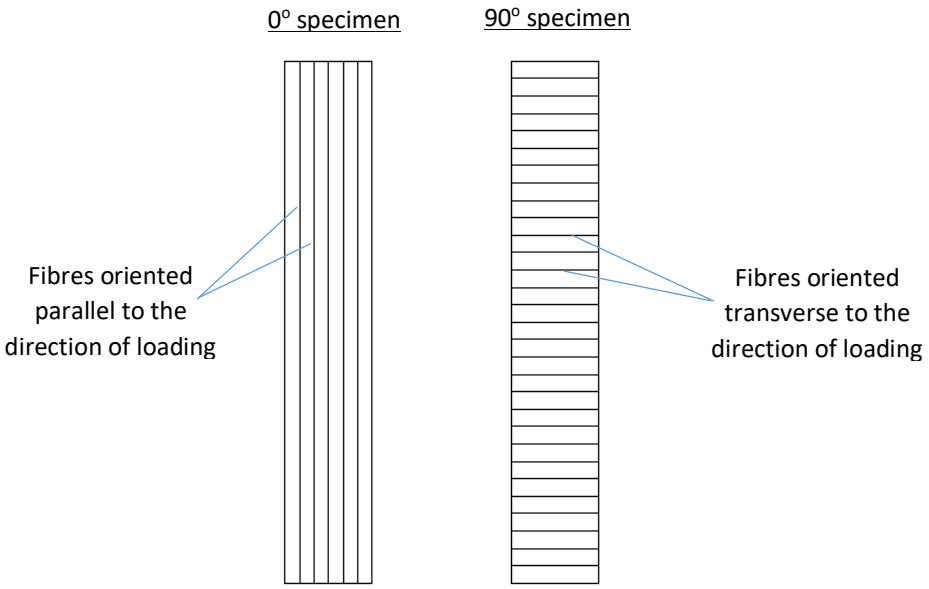

Figure 4.49: Schematic showing the fibre directions in the 0° and 90° CFRP specimens

4.1.2 Geometry of the specimens

The recommended geometry for the ASTM D3039/D3039M tensile test specimens as well as the actual geometry that was used are listed in Table 4.11 below [120]:

Table 4.11: Recommended vs actual tensile test specimen dimensions according to ASTM D3039/D3039M

Fibre orientation	**0 ° unidirectional**		**90 ° unidirectional**	
Geometry	**Recommended**	**Actual**	**Recommended**	**Actual**
Width (mm)	15	15	25	25
Overall length (mm)	250	180	175	180
Thickness (mm)	1	1.25	2	1.25
Tab length (mm)	56	50	25	50
Tab thickness (mm)	1.5	1.2	1.5	1.2
Tab bevel angle (°)	7 or 90	90	90	90

The test standard [120] gave room for adjustments to the geometry specifications given in the table above. Some adjustments were made as shown by the actual dimensions in the table above. The adjustments were necessary because test specimens were to be cut from a single flat panel with a constant thickness (1.25 mm). The 0 ° unidirectional specimens were cut along the fibre direction and the 90 ° unidirectional samples would be cut transverse to the direction of the fibres. If both set of specimens for the two orientations were cut from the same flat panel, it would help ensure consistency in the results. The other advantage was that only one panel with a constant thickness needed to be made. The tabs were cut off from an aluminium flat sheet that was approximately 1.2 mm thick. The tab dimensions were according to those given in Table 4.11. The tabs were glued onto the specimens with an epoxy adhesive (Spabond 340 LV) before being left to set. After the epoxy adhesive had set, the specimens were post cured in an oven according to the prescribed curing schedule for the adhesive [108]. The longitudinal and transverse test specimens that were cut and had tabs stuck on them as illustrated in Figure 4.50:

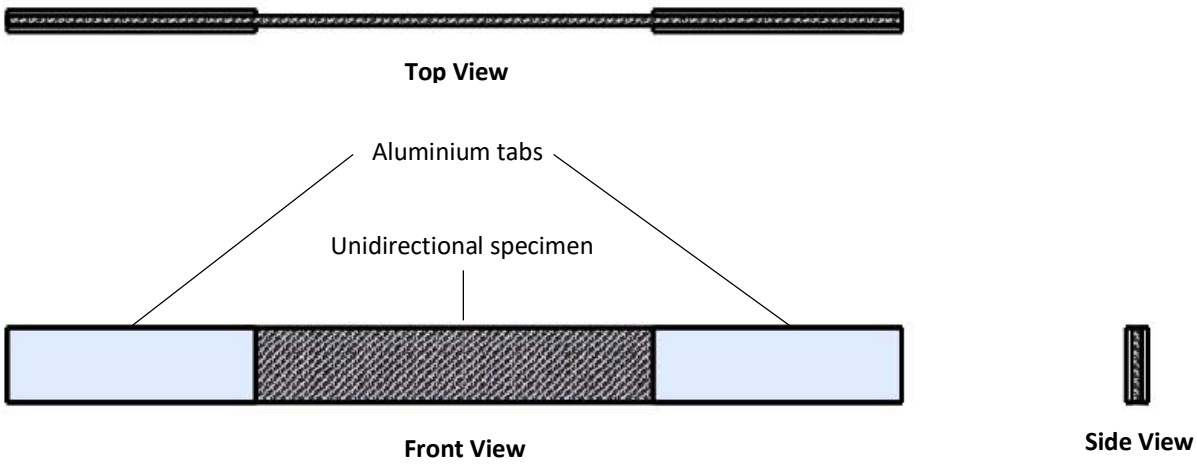

Figure 4.50: Front, top and side views of a typical unidirectional test specimen with tabs stuck on

4.1.3 Manufacturing the specimens

The flat panel was made using the same epoxy resin and carbon fibre proposed for constructing the CFRP pressure. One difference however was that whilst the filament winding process that was going to be performed by GRP Tubing was automated, the flat panel that was made in the lab by manually wrapping the carbon fibre tows over the prepared pattern mould. Thus, a simplified manual filament winding process was performed on a rectangular prism shaped block of wood that had two thin flat panels of aluminium glued onto it as shown in Figure 4.51 below:

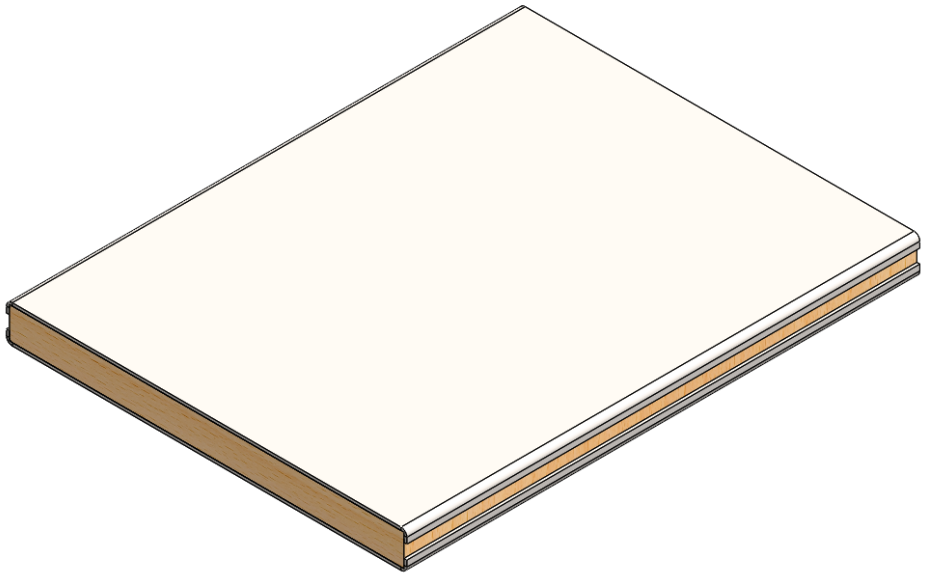

Figure 4.51: Representation of the block of wood with two flat sided panels of aluminium glued onto it

After wrapping the flat sided block to the thickness of approximately 2 mm with carbon fibre tow post impregnated with epoxy resin, the entire setup was put into a vacuum bag before the resin was allowed to cure overnight. Next, it was placed into an oven and then cured according to the curing procedure stipulated by the epoxy resin's data sheet in Appendix D (i.e. 2 hours at 80°C + 3 hours at 150°C + 4 hours at 180°C) [102]. After successfully curing, two flat panels were cut off the two flat sides of the pattern block. However, the final thickness of the flat panels was approximately 1.25 mm

possibly due to the compaction due to the "vacuum bagging" process. A drawing template of how specimens were to be cut based on the dimensions specified in Table 4.11 was developed in SolidWorks 2017 Computer Aided Design (CAD) software before being fed into the Computer Aided Manufacturing (CAM) program for a CNC router cutter which cut the 0° and 90° unidirectional specimens.

4.1.4 Mechanical testing procedure

The Zwick 1484 testing machine was used for testing both the 0^{O} and 90^{O} unidirectional test specimens. The main parameters that were adjusted were the cross-head speed (2 mm/min) and the extensometer was utilised (over a gauge length of 60 mm) to measure the strain in real time to ensure that the strain data could be later analysed. A summary of the procedure is provided below:

1. The variables were set to the appropriate values (i.e. cross-head speed of 2mm/min and the extensometer set at a length of 60mm).
2. A specimen was inserted onto the grips and aligned properly also making sure that the specimen was gripped sufficiently.
3. A preload was set at 20 N and was applied to the specimen before the extensometer gripped the sample.
4. The test commenced, and the specimen was pulled until failure of the specimen.

The steps 2-4 were repeated for both the 0^{O} and 90^{O} unidirectional specimens for at least 5 specimens of each fibre angle. The results are presented in section 5.1 in the next chapter.

4.2 End cap adhesive shear tests

As part of the design process for the end caps, the epoxy adhesive bond strength had to be tested to size the bond area appropriately. The adhesive that was used for the shear tests was SpaBond 340 LV. An adhesive shear test was devised to determine the shear strength of the bond between the CFRP tube and the end cap. This section will cover the design and the results of the shear test.

4.2.1 Description

Dummy end caps were made for this test which instead of having a hemispherical dome machined, had a flat end and were shorter (see Figure 4.52). The dummy end caps were cheaper to manufacture as they required less material and time to manufacture than the vessel's end caps. The bond line thickness of 1.5 mm (i.e. perpendicular distance between the edge of the bond area on the end cap to the internal surface of the CFRP tube) was the same as that of the vessel's end caps. The direction in which the loads acted differed between the pressure tests and the end cap adhesive shear test. However, this should not have caused a difference between the shear strength values from those tests as the shear strength value does not depend on the direction of the applied load. The dummy end caps did not have O-rings like the end caps used in the pressure vessels. The dummy end caps were machined to a diameter such that they had a transition fit with the internal diameter of the CFRP tube. This meant that a slight push was required to put them in place before bonding occurred. This was done to mimic the friction effect of the O-rings on the end caps used for pressure vessels. These considerations were made so that the results of the end cap adhesive shear test would be similar and could be applied to actual end cap design.

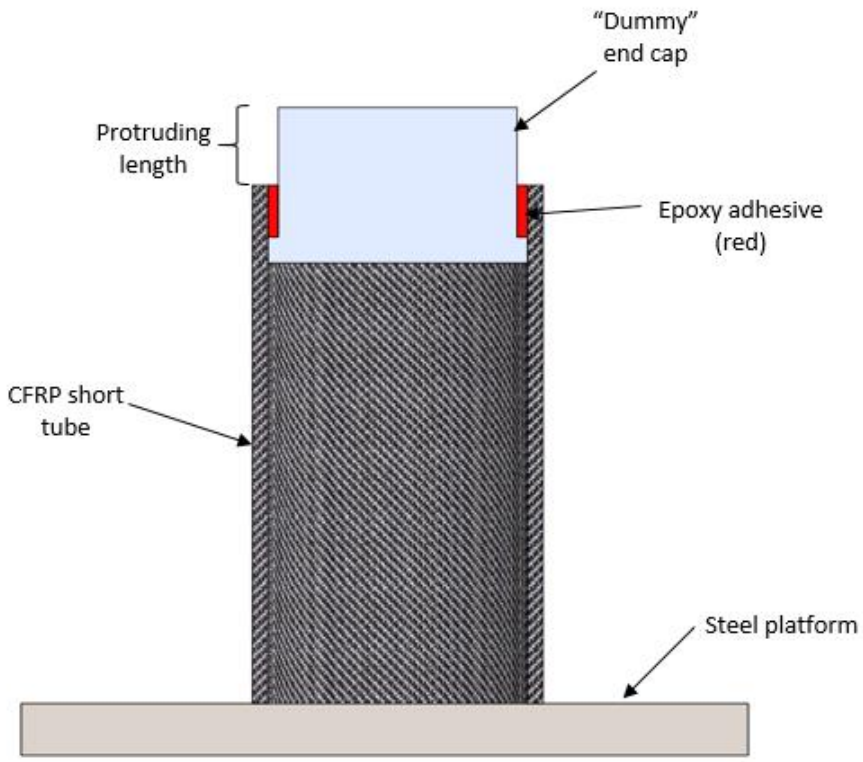

Figure 4.52: Shear test setup

As shown in Figure 4.52, on one end of a short length of the CFRP tube, a dummy end cap was partially bonded to the tube. The partial bond meant that only a portion of the bond area would be utilised whilst the rest would protrude out of the CFRP tube as shown above. The protruding flat end would then have had a downwards force applied by the Zwick 1484 universal machine as can be seen in Figure 4.53.

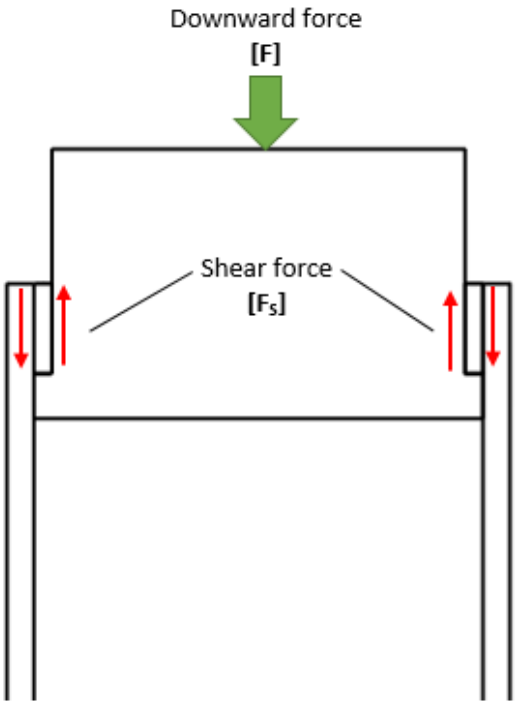

Figure 4.53: Illustration of the interaction in the forces acting on the end cap and CFRP tube through the bond

The downward force (F) on the dummy end cap would be primarily resisted by the bond. The maximum shear force (and stress) would thus correspond to the maximum applied downward force that resulted in shear failure.

4.2.2 Specimen preparation

Each specimen was made up of a dummy end cap partially bonded to a short CFRP tube. There were two hardeners that were used to mix with the SpaBond 340 LV resin namely the slow and fast hardeners. The slow hardener was used to make the specimens for the first shear test while the fast hardener was used for the remaining two sets shear tests. One notable difference between the two hardeners was that the quoted maximum shear strength of the SpaBond 340 LV [108] with the slow hardener was slightly higher than when the fast hardener was used (34.5 MPa as compared to 33.3 MPa). Before applying the adhesive, the surfaces to be bonded on the dummy end caps and the CFRP tube's internal surface had to be prepared accordingly. The two surfaces had to be abraded by a medium grit sand paper (or emery cloth) and any dust/dirt had to be wiped clean with acetone. This ensured that the bond on both surfaces had sufficient grip whilst also ensuring the strength would not be compromised as a result of contaminants like dust and oils. Below is a description of the design decisions, processes and methods employed for each of the three shear tests.

4.2.2.1 First shear test specimens

The specimens for the initial shear test were similar to what is shown in Figure 4.52. The SpaBond 340 LV was used to bond mild steel dummy end caps using the first bond application method (as described in section 3.2.4 for more details). Mild steel was used instead of aluminium for the dummy end caps because it was readily available and inexpensive. The slow hardener was used in the bonding of the dummy end caps for the specimens for the first test because it had a reasonably long pot life (45 mins at 20^{o}C) which allowed the adhesive to be applied and thoroughly spread on the bond area. However, the clamp time associated with the slow hardener (17 hours 40 minutes was longer than when a fast hardener (3 hours 50 mins). After allowing the adhesive to set, the specimens were put into an oven where they were to be cured according to the schedule below [108]:

- From the room temperature (20 ^{O}C) to 70^{O}C in an hour and 20 mins.
- The oven temperature was then maintained at 70^{O}C for 5 hours.
- From 70^{O}C to room temperature in an hour and 20 mins.

Hence, the total post-curing time amounted to 7 hours 40 mins. After curing, the specimens were ready for the shear test.

4.2.2.2 Second and third shear test specimens

The second and third set of shear test specimens were also made to mimic the behaviour of the second and third design of end caps respectively. Both sets had angled holes that allowed for the direct injection of the adhesive into the bond area. The fast hardener was used because the resulting SpaBond 340 LV adhesive was less viscous than when slow hardener was used. This allowed the adhesive to fill the bond area easier. The post-curing schedule was the same as that of the slow hardener. The third set of dummy end caps were distinct from the second set in that the surface of the bond area for the third set was knurled. Knurling was applied on the bond area of the dummy end caps to ensure a consistently rough surface that would increase the mechanical bond.

4.2.2.3 Summary on the shear test specimens

Below is Table 4.12 that compares the similarities and differences in the specimens that were utilised for the shear tests.

Table 4.12: Similarities and differences in the 3 sets of shear test specimens			
Specimen features	**First specimen**	**Second specimen**	**Third specimen**
Bond area on the dummy end cap	• Abraded with 80 grit sand paper • No angled holes	• Abraded with 80 grit sand paper • Angled holes	• Knurled surface • Angled holes
Hardener used	• Slow	• Fast	• Fast
Post curing duration	• 7 hours 40 mins	• 7 hours 40 mins	• 7 hours 40 mins
Shear strength of the Spabond 340 adhesive	• 34.5 MPa	• 33.3 MPa	• 33.3 MPa

4.2.3 Adhesive shear test procedure

The Zwick 1484 testing machine with the flathead attached, provided the load that would be resisted by the bond of the adhesive layer until failure. The process was as follows:

1. The protruding length of the dummy end cap on each specimen was measured using a pair of Vernier Callipers at 5 different locations around the circumference and the values were recorded.
2. The specimen was then placed directly underneath the Zwick 1484 machine flathead.
3. The flathead would then be vertically adjusted such that it would almost be in contact with the top flat surface of the dummy end cap on the specimen.
4. The Zwick was zeroed before the test was started and the test was only completed when the bond of the adhesive layer failed.
5. The (force vs standard travel of the machine head) data from the machine was saved for that specific specimen before the test was repeated for the rest of the specimens.
6. The recorded data was then processed, analysed and plotted into graphs of shear stress against standard travel as illustrated in the next chapter.

4.3 Pressure tests

The first pressure test that was performed on the CFRP pressure vessel specimens was a hydrostatic burst test. Another secondary objective of the burst tests was to collect strain data from the CFRP section of the pressure vessel as it deformed under the influence of an induced pressure. The strain data would then be analysed and compared to validate the theoretical strain data derived from the design calculations. The second pressure test that was to be employed was the proof pressure test which is a part of the non-destructive test (NDT) procedures. The proof test involves testing the pressure vessel for leaks at a slightly higher pressure than the design pressure to ascertain that there are no leaks or premature failure of the pressure vessel [10]. The final test was the long-term leak test which involved using a dry gas such as air to detect the presence any localised leaks anywhere on the vessel. Passing the leak test would have meant the CFRP tube rubber liner, and the end caps are sufficient to prevent gas (i.e. a compressible fluid) from escaping the vessel.

4.3.1 Burst pressure test

For the burst tests, water was pumped into the pressure vessel until it failed. This could be through either cracking of the CFRP or shear failure of the end caps. Leaking and the resulting drop in pressure from the gauge were the visual indications of failure of the pressure vessel. The purpose of the burst test was two-fold, the first reason was to determine the failure pressure then secondly, to be able to predict the deformation behaviour (i.e. induced strain) of the CFRP portion of the pressure vessels.

4.3.1.1 Requirements

The requirements for class III FRP pressure vessels are described in section 8-700.5.3 of the ASME Boiler and Pressure Vessel Code Section X [10]. They are listed below as follows:

- Three vessels shall be tested hydraulically, to destruction, by pressurizing at a rate of no more than 5 bar/second.
- The test shall be carried out under ambient conditions.
- Prior to the commencement of the test, no air should be trapped in the system.

4.3.1.2 Analysis of experimental results

The important parameters that needed to be recorded were the failure (or burst) pressure and the pressure time curve according to [10]. The failure pressure ought to be at least 2.25 times the value of the intended design pressure.

4.3.1.3 Design of the burst test setup

The following equipment/apparatus were required to design the equipment setup for the burst test:

- The CFRP pressure vessel.
- Steel piping.
- Calibrated pressure gauge.
- End fitting that interfaces with the piping network and the vessel.
- Ball valves.
- Various connectors.

Because the proposed design pressure of the pressure vessel was 350 bar, it meant that the equipment mentioned above had to be able to sustain a pressure of at least 787.5 bar (2.25 times the design pressure). Since the burst test was a hydrostatic test, the equipment had to be setup in such a way as to have vents at high point [10]. Vents were meant to provide a passage through which air could escape while the pressure vessel was being filled with water. With those considerations in mind, the equipment setup shown in Figure 4.54 was designed for the burst test.

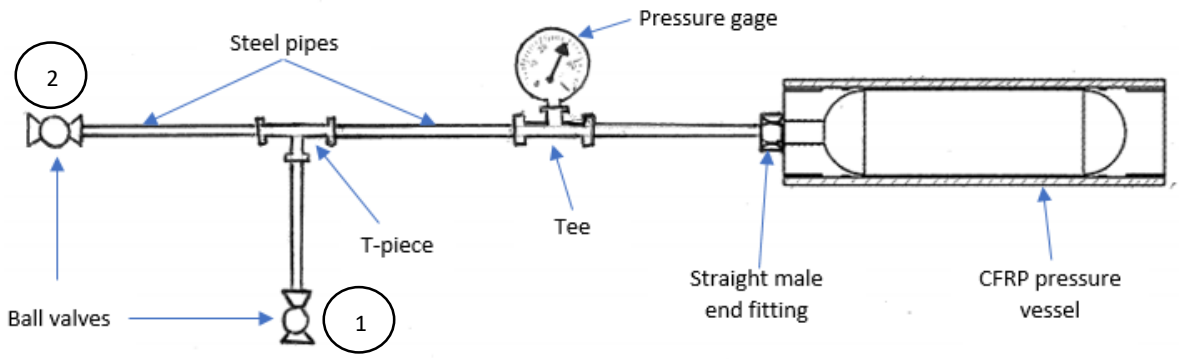

Figure 4.54: Schematic of the horizontal setup for the pipe network equipment that was to be used for burst tests.

The ball valve labelled number 1 would be connected to the hydrostatic pump and when open, would provide a pathway for water to be pumped into the pressure vessel. Filling the pressure vessel would be done when the test apparatus is in a vertical configuration as shown in Figure 4.55.

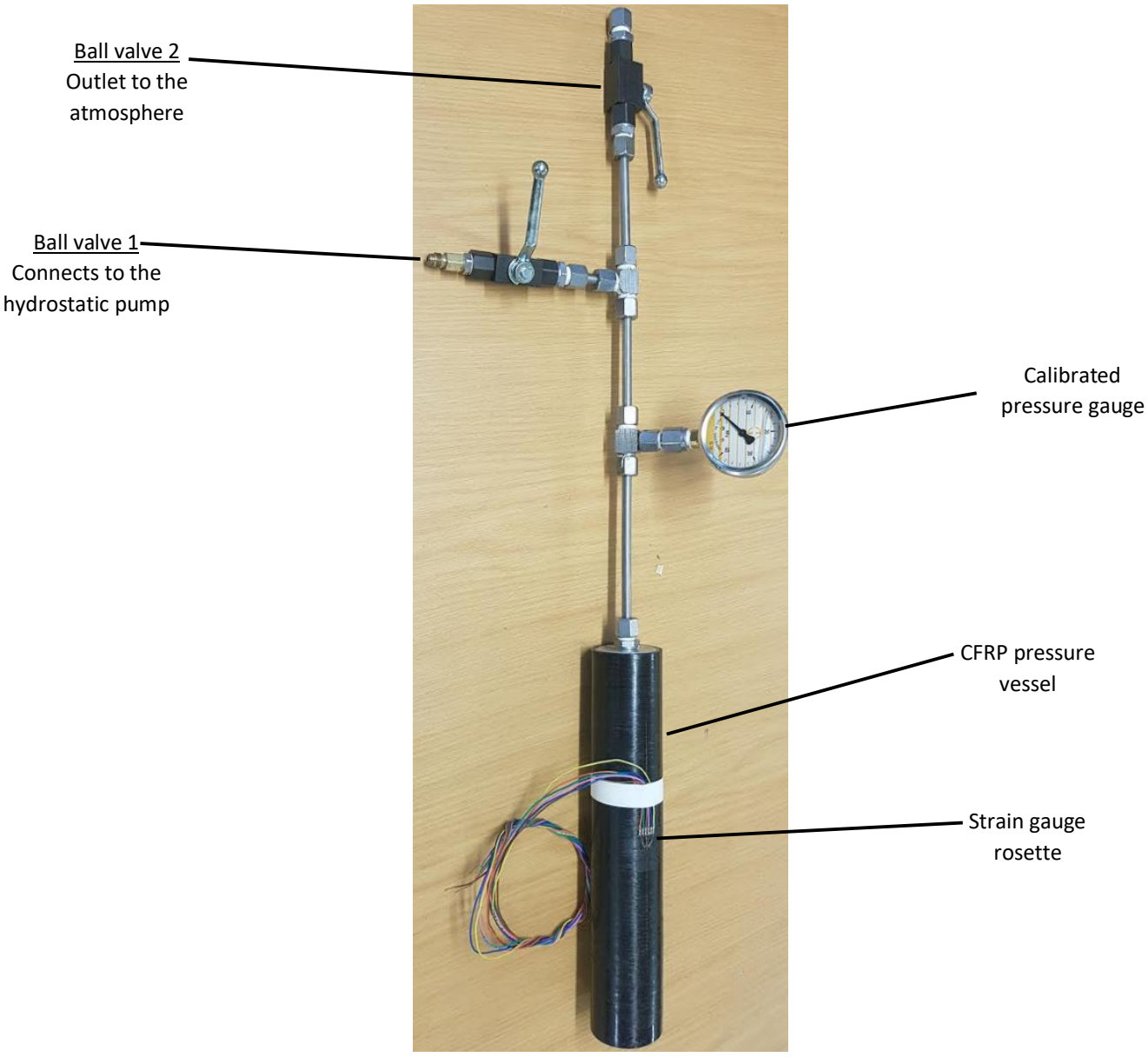

Figure 4.55: Vertical setup for the actual burst test equipment

After filling up the pressure vessel, more water would need to be pumped to ensure all the pipes are filled with water. With all the pipes filled completely with water, the excess water would have to flow out of ball valve 2. When the water flowing out of ball valve 2 was clear of any air bubbles, it signified that there are no more air bubbles within the system and that valve was to be closed before the test could commence.

4.3.1.4 Strain gauge selection

A strain gauge is simply a device used to measure the strain on objects subject to an applied load [121]. An example of a strain gauge is illustrated in Figure 4.56. The strain gauge measures the strain as a change in its length (when stretched) which manifests as a change in electrical resistance [122].

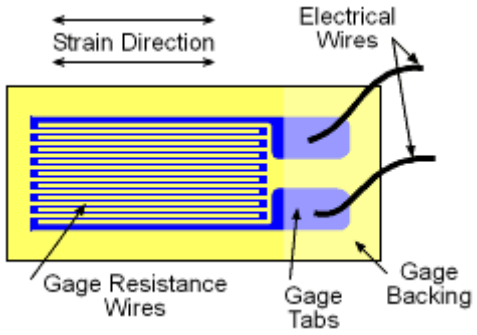

Figure 4.56: A typical strain gauge [123]

Hence, the more the gauge is stretched, the more its electrical resistance increases. When connected to an electrical circuit, the change in electrical resistance will reflect as a change in the voltage across it which can then be transformed into a corresponding strain value.

Strain gauges can only measure strain in one direction hence why a single strain gauge is referred to as a uniaxial strain gauge. In this scenario however, there is a need to measure strain in more than one direction (the bi-axial stress state resulting from hoop and longitudinal stress on the cylindrical vessel), a two-element strain gauge rosette was required to measure the hoop and longitudinal strain for the CFRP pressure vessel. The two-element strain gauge rosette involved two adjacent conventional strain gauges orientated at 0^{O} (longitudinal) and 90^{O} (hoop) respectively as shown in Figure 4.57 below. The strain gauge rosette was to be attached onto the outer surface of the pressure vessel.

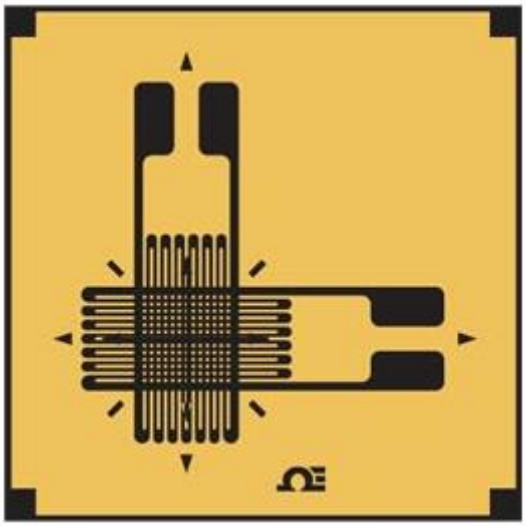

Figure 4.57: A 0^{o} and 90^{o} strain gauge rosette [124]

Selection Parameters

To install a strain gauge onto an object for strain measurement, careful consideration needs to be taken in order to select the appropriate gauge for that application. This is to ensure that correct and reliable strain measurements may be obtained, the gauge installation cost may be reduced and to facilitate ease of installation [125]. There were several parameters that were considered for selecting a strain gauge, some of which are the gauge length, gauge pattern and self-temperature compensation number. Generally, the process of selecting strain gauges involves compromises as one parameter choice may satisfy one of the requirements and yet work against other requirements [125].

The gauge length of a strain gauge is the active or strain sensitive length of the grid as can be seen in Figure 4.58 [14, 15]. The other features like the solder tabs are considered insensitive to strain because of their relatively large cross-sectional area and low electrical resistance [125].

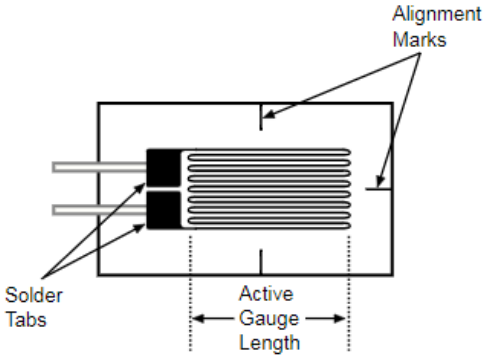

Figure 4.58: Illustration of the components of a typical strain gauge [124]

For this application, the gauges were going to be attached onto the curved outer surface of the CFRP pressure vessel. Because the surface was not flat but curved, the longer the gauge length was going to be the more likely the strain reading was going to be distorted particularly in the hoop direction. This meant that the gauge length of the strain gauge(s) had to be as short as possible. However, strain gauges with a short gauge length (< 3mm) in general, tend to offer less accuracy than longer ones in terms of the maximum allowable elongation, the stability under static strain, and endurance when subjected to alternating cyclic strain [125-126]. It was felt that the need to measure the undistorted strain outweighed the potential errors from the shorter gauge length. Hence, a short active gauge length of 2 mm was chosen for this application.

The gauge pattern refers to the shape of the grid, the number (uniaxial/multi-axial) and orientation of the grids in a multiple-grid gauge [125]. For a uniaxial stress state scenario, a single grid gauge would have sufficed. However, with an internal pressure applied onto the CFRP pressure vessel in this application, there will be at least a bi-axial stress state due to the hoop and longitudinal stress. Hence, at the very least a two-gauge rosette would have been required to measure the strain induced by those principal stresses. Hence, a 0^{o} and 90^{o} strain gauge rosette was chosen to measure the induced longitudinal and hoop strain respectively.

Materials generally expand with increase in temperature. The resulting strain that is generated is called apparent strain. Apparent strain depends on the material property called the expansion coefficient measured in ppm/K where ppm is parts per million and K is Kelvin. For each material, there is a unique expansion coefficient [107] for instance steel has an expansion coefficient of about 11ppm/K and aluminium has about 23 ppm/K [127]. The temperature response of strain gauges is matched to that of a specific material such that they compensate for the apparent strain caused by temperature changes within that material. Hence, a strain gauge should be chosen which matches the temperature response of the matching material in order to eliminate the effects of apparent strain.

During hydrostatic testing in a room with a constant temperature, there would be no significant change in temperature of the water being pressurized, the CFRP vessel or the immediate surroundings unless external heat is supplied to the testing apparatus. Carbon fibre has a relatively low temperature compensation number of -0.1 ppm/K [118] as compared to metals like steel and aluminium (11 ppm/k and 23 ppm/K respectively [127]). However, strain gauges matched for carbon fibre were far more expensive than ones for metals like steel or aluminium. For these particular hydrostatic burst tests, there was no discernible cause for any significant temperature change which could have caused any

significant error. Hence, steel matched strain gauges were chosen to measure the strain on the CFRP pressure vessel for the following reasons:

- Steel matched strain gauges are significantly less expensive than CFRP matched gauges.
- Steel matched strain gauges could be sourced locally.
- Steel had the lowest coefficient of expansion (or temperature compensation number) among the locally available strain gauges.

The specifications of the particular steel strain gauge rosette sourced from Peter Jones Electrical are shown in the Table 4.13:

Table 4.13: Steel strain gauge rosette specifications

Property	**Description**
Manufacturer	KYOWA
Type	KFG-2-120-D17-11
Gauge factor (24°C, 50% RH)	2.08 ± 1.0%
Gauge length	2 mm
Gauge resistance (24°C, 50% RH)	120.4 ± 0.4Ω
Adoptable thermal expansion	11.7 ppm/ °C

4.3.1.5 Measurement of strain

When an object onto which a strain gauge is attached expands/contracts due to stress, the strain gauge will also be deformed in kind by the same amount [123]. The deformation of the strain gauge is manifested as a change in its electrical resistance. The change in electrical resistance is usually very small to detect and to detect this small change a Wheatstone bridge is used [122]. The Wheatstone bridge is shown schematically in Figure 4.59 and it is used to connect the strain gauges in such a way so as to detect the small changes in resistance through measurement of potential differences across the strain gauges.

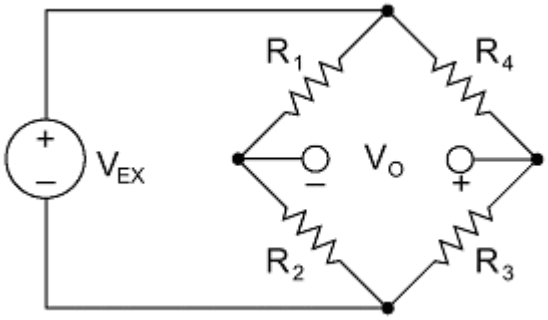

Figure 4.59: Strain gauges are configured in Wheatstone bridge circuits to detect small changes in resistance.[122]

The measured output comes in the form of a voltage difference, V_O, which is caused by a change in resistance. The voltage difference can be amplified and then converted into a strain reading. There are 3 common strain gauge configurations within the Wheatstone bridge namely the quarter, half or full bridge configuration.

Strain gauge configurations

The quarter bridge has one active strain gauge connected in the Wheatstone bridge, the half bridge has two active strain gauges connected and the full bridge has 4 active strain gauges connected. The

sensitivity to the small change in strain differs with each configuration with the least sensitive being the quarter bridge and the most sensitive being the full bridge configuration [122]. The quarter bridge configuration was chosen of the 3 different configurations because it was the least complex and cheapest configuration since it only needed one active strain gauge. The half and full bridge configurations would require two and four active strain gauges respectively.

Strain measuring device

The equipment that was chosen to measure the induced strain on the CFRP pressure vessel was the P-3500 strain indicator (see Figure 4.60). It was convenient to use in this application as it is robust, easy to use and portable.

Figure 4.60: Top view of a P-3500 strain indicator

Additionally, the P-3500 had other useful features including the following [128]:

- Choice of 4-1/2 Digital Liquid Crystal Display (LCD) or Light Emitting Diode (LED) readout.
- Direct reading of strain.
- Battery or line-voltage operation.
- Gauge factor setting (to 4 significant digits) displayed on readout.
- Quarter-, Half- and Full-Bridge circuits.
- Compatible with 120 and 350 Ohm strain gauges.
- Portable, lightweight, rugged for field use.

Evaluation of hoop and longitudinal strain values

After installing the strain gauge rosette on the outer surface of the pressure vessel, it was to be connected to the P-3500 strain indicator which facilitated the measurement of direct strain values. Since a two strain gauge rosette was chosen, there were to be two separate direct strain reading for each orientation (i.e. 0^o and 90^o) to be read via the digital display on the P-3500. If one strain gauge (i.e. SG 2) is in line with the axis of the cylindrical pressure vessel, it would measure the direct value of the longitudinal strain as shown in Figure 4.61. If a second strain gauge (i.e. SG 1) is then placed at right angles to the first, it would measure the direct value of the hoop strain.

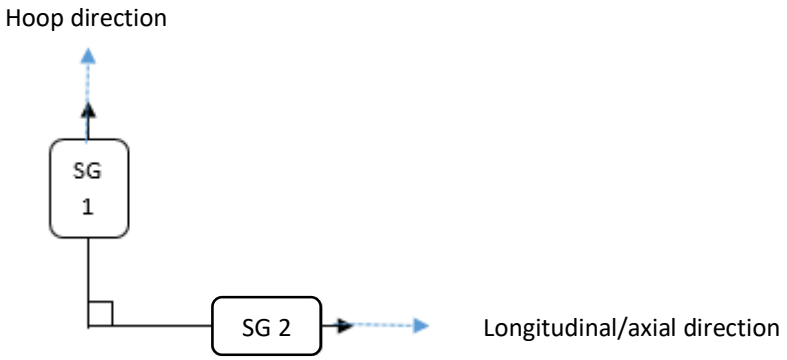

Figure 4.61: Schematic of the strain gauge rosette with the gauges oriented at 0^O (longitudinal) and 90^O (hoop).

4.3.1.6 Burst test procedure

After purging the air bubbles from the pressure vessel and the burst testing apparatus, the hydrostatic test would be ready to commence. Each of the two strain gauges in the 0^o and 90^o strain gauge rosette would be connected in a quarter bridge configuration on the P3500 strain indicator. The gauge factor would be adjusted to the quoted value for that strain gauge before both the AMP ZERO and balance settings are zeroed. The zeroing ensured that all readings would be made relative to a reference reading (i.e. zero) thereby eliminating systematic errors.

The hydrostatic pump would then raise the pressure of the water in the system (including the pressure vessel) to a value between 20-30 bar and the first set of two strain readings would be recorded. Increments of between 20-30 bar were then implemented in accordance with the test requirements for each time step and the resulting strain readings would also be recorded. However, there was an exception to this as the equipment that was used had no steady pressure increase rate of 5 bar/second but the 20-30 bar increase occurred over a period of about 5 seconds (i.e. a rate of pressure increase of between 4-6 bar/second). Between increments/readings, the value for the pressure was allowed to settle for a period of at least a minute before the set of readings were recorded. This process was repeated incrementally until the pressure vessel failed. The recorded failure pressures and observed modes of failure are detailed in section 5.3.

4.3.2 Hydraulic proof pressure test

The hydraulic proof pressure test is a type of Non-Destructive Test (NDT) that was to be used to prove the durability of a given test sample in a controlled setting [71].The other purpose of this test was mainly to verify that the vessel(s) would withstand pressure above its intended use without experiencing any leaks or succumbing to failure.

4.3.2.1 Requirements

The requirements for this test according to the ASME Boiler and Pressure Vessel Code Section X were as follows [10]:

- The hydraulic pressure in the vessel has to be increased gradually and regularly to 1.25 times the design pressure.
- The vessel shall be held at the proof pressure (i.e. 1.25 times the design pressure) for 30 minutes followed by a reduction to the design pressure and held for 10 minutes to ascertain that there are no leaks and no failure.
- In the occurrence of leakage in the piping and fittings, the vessels may be re-tested after repair of such leakages.

There were two types of CFRP pressure vessels that were burst tested (see next chapter for more details) prior to the commencement of the proof test. They were distinguished by the wall thickness of the CFRP tube. One was 2 mm thick and the other was 4 mm. The design pressures at which these two types of CFRP pressure vessels were determined by the burst pressure test. The failure pressure had to be divided by 2.25 to determine the design pressure in accordance with the burst test requirements. The proof pressure values of the two vessels had to be 1.25 times the respective design pressure values. The design and proof pressure values for the two types of vessels are summarised in Table 4.14.

Table 4.14: The design and proof pressures for the two different vessels

Type of vessel	**Design pressure [bar]**	**Proof pressure [bar]**
2 mm wall thickness	147	184
4 mm wall thickness	182	228

After the test concluded, vessels would be rejected in the case of failure to retain pressure, leakage or visible permanent deformation after depressurization [10].

4.3.2.2 Procedure

The same equipment and setup for the burst tests were used for the proof tests. The two types of vessels listed in the table above were tested to ascertain if they would fail according to the requirements. The pressure was increased by 20-30 bar per step and in between the increments, there was a brief period of 15-20 seconds that passed before the pressure was increased again. This allowed the pressure vessel to adjust and the strain readings to settle before they were recorded. After the test pressures were reached for each type of vessel, the valve was closed and disconnected from the hydrostatic pump. The vessel would be held at the test pressures for at least 30 minutes before the pressure was reduced to the design pressure for a minimum of 10 mins. The results of the tests can be found in the next chapter.

4.3.3 Leak pressure test

The primary purpose of a leak detection test is detecting and localizing leaks from the pressure vessel and the general method employed is pneumatic because it is relatively inexpensive [72].

4.3.3.1 Requirements

The requirements for leak testing were listed below as according to the ASME Pressure Vessel Code Section X [10]:

- Leak testing should be conducted on a completed vessel.
- Acceptable methods for leakage testing include, but are not limited to, bubble testing with dry air.
- The leak testing should be performed at the design pressure.

4.3.3.2 Procedure

The equipment setup that was designed for the leak test is shown in the schematic in Figure 4.62. The air that would fill the CFRP pressure vessel was to be channelled from a steel cylinder which held 11.5 kg of compressed air at 200 bar. Because the CFRP vessels had a smaller volume, they would require only a relatively smaller mass of air, less than 150 g, to reach the required design pressures of 147 bar and 182 bar (see ideal gas calculations in the Appendix C). During connecting the equipment for the leak test caution was taken to ensure the leaks from the equipment were negligible. This was achieved

by testing the setup. This involved replacing the pressure vessel with a valve which would be kept closed whilst valves 1 and 2 were kept open. The relief valve was also kept closed to ensure no air would escape.

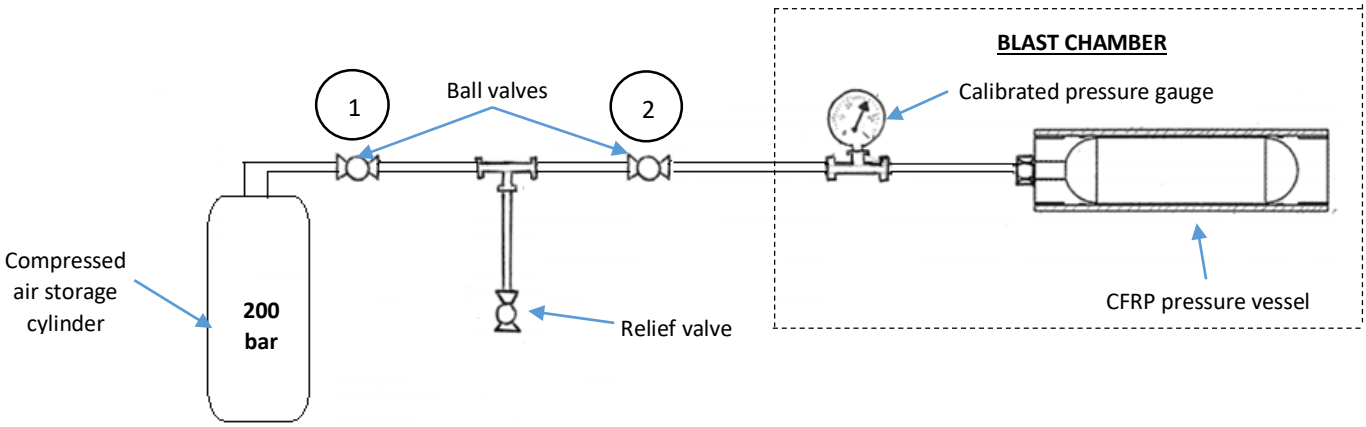

Figure 4.62: Equipment setup for the long-term gas leak pressure test

It should be noted that because of the safety implications involved in leak testing with air (i.e. a compressible fluid), the test was conducted in a blast chamber. The steel cylinder was kept outside the blast chamber as the tap had to be operated manually. Only the calibrated pressure gauge and the CFRP pressure vessel were in the blast chamber as illustrated in Figure 4.62. The blast chamber had a window through which the reading on the pressure gauge could be monitored to ensure the desired pressure was reached.

The tap on the steel cylinder would be opened and the air would flow into and fill the piping until the reading on the pressure gauge would settle at just under 200 bar. Then the valves 1 and 2 would be closed before opening the relief valve to facilitate the trapped air in between the valves to dissipate. This allowed for the steel supply cylinder to be disconnected from the equipment. The pressure reading on the gauge would be monitored over time and any drop in the reading would signify the presence of a leak from the equipment. A soapy water solution would be applied on every joint of the pipe network equipment setup prior to the start of the leak test. This was necessary for detecting and localizing any leaks through checking for “bubbling”. The leaking joints would be carefully retightened ensuring that they were sufficiently tight and leak-proof. After ensuring that there were no leaks in the equipment, the CFRP pressure vessels were connected as shown in figure 8.14. The tap was then opened as mentioned before and the vessel filled up with air until the reading on the pressure gauge reflected the design pressure i.e. 147 bar and 182 bar for the 2 mm and 4 mm vessels respectively. Valves 1 and 2 were closed and the relief valve was opened to purge the air in the pipes and the steel cylinder disconnected leaving only the vessel pressurized with the pressure gauge to monitor the reading. The pressure reading was then monitored and recorded over a period of up to 72 hours to assess if there were any leaks from the vessel. The results of the long-term leak tests that were performed are detailed in section 5.5.

4.4 Summary of the testing methodology

The ASTM D3039/D3039M tensile tests involved making specimens with the aim of determining the in-plane tensile properties (i.e. elastic moduli and strengths) of the CFRP material used in the manufacture of the tube section of the pressure vessel. These in-plane tensile strengths and stiffnesses were necessary for accurately estimating the pressure at which the CFRP tube laminate structure would fail.

The end cap adhesive shear tests were designed to determine the shear strength of the bond on the SpaBond 340 LV adhesive layer and the two interfaces. The specimens of this test were manufactured by bonding “dummy” end caps onto short CFRP tubes. The dummy end caps had flat protruding ends which a Zwick 1484 machine’s crosshead would apply a constant strain rate until the bond of the adhesive layer fails.

After constructing prototype CFRP pressure vessels, they had to undergo different pressure tests. The first test was the hydrostatic burst pressure test which was aimed at determining the pressures at which the vessels would fail. The second objective of the burst test was to learn how the CFRP would deform under pressure by measuring the induced hoop and longitudinal strains of the CFRP tubes. To do this, strain gauges were attached to the tube sections of the vessels prior to the burst test. Furthermore, the hydraulic proof tests were performed on new CFRP pressure vessels to verify if they would withstand pressures above their intended (i.e. maximum working pressures) use without experiencing any leaks or failure. Lastly, a long-term leak test was devised to test durability and to detect any leaks from the pressure vessel. A pneumatic leak test was chosen because it is relatively inexpensive.

5. Results and discussion

This section describes and discusses the results from the various tests that were performed on the CFRP pressure vessels and their components.

5.1 Tensile tests of the CFRP specimens

The objective of the ASTM D3039/D3039M tensile test was to determine the following properties:

- The UTS in the 0^{O} and 90^{O} directions ($\sigma_{1\text{-UTS}}$ and $\sigma_{2\text{-UTS}}$ respectively)
- The elastic modulus in the 0^{O} and 90^{O} directions (E_1 and E_2 respectively)
- The failure strain in the 0^{O} and 90^{O} directions (ε_1 and ε_2 respectively)

5.1.1 Results

Determination of the theoretical CFRP property values

These tests had to determine these property values so that they could be used in the design calculations of the pressure vessel. A micromechanics approach using datasheet values was initially used to predict most of the mechanical properties of composites (see section 2.4.4). However, this approach was purely theoretical and relied on manufacturers' data as well as some simplifying assumptions for example assuming the composite is perfectly bonded which is not necessarily true. Table 5.15 shows the manufacturers' data on the carbon fibre and epoxy.

Table 5.15: Supplied mechanical property values for the carbon fibre [118] and the epoxy resin [102]

Material	**Property**					
	Elastic Modulus		**UTS**		**Failure Strain**	
	E_1 [GPa]	E_2 [GPa]	σ_L [MPa]	σ_T [MPa]	ε_1 [%]	ε_2 [%]
Carbon Fibre (HTS45) [118]	240	-	4500	-	1.8	-
Epoxy Resin AR600 and AH2336 Hardener [102]	2.5	2.5	73	73	5.5	5.5

Table 5.16 shows the calculated theoretical property values for the CFRP material determined using the micromechanics approach described in section 2.3.4.1.

Table 5.16: Theoretical property values of the CFRP material

Property	**Symbol**	**Theoretical Value**
Ultimate Tensile Strength in the 0^{O} direction	σ_1	2287 MPa
Ultimate Tensile Strength in the 90^{O} direction	σ_2	14.8 MPa
Elastic Modulus in the 0^{O} direction	E_1	121.7 GPa
Elastic Modulus in the 90^{O} direction	E_2	6 GPa
Maximum Tensile Strain in the 0^{O} direction	ε_1	1.05%
Maximum Tensile Strain in the 90^{O} direction	ε_2	0.5%

There was no information regarding the UTS of the fibres in the transverse direction from the manufacturers (Toho Tenax) [118]. This meant that the respective micromechanics equation could not be used to determine the theoretical UTS value for the CFRP specimens in the transverse direction (σ_2). It is common to treat the strength of the resin as the transverse UTS of FRP composites [3, 91]. This tends to be overly simplistic and ignores the fact that the introduction of fibres into the resin causes a decrease in the strength in the direction transverse to the fibres and as the fibre volume fraction increases, the transverse tensile strength of the FRP composite decreases [4]. Therefore, a simple yet very conservative approach suggested by Hull [4] was used instead and is shown below:

$$\sigma_2 = \sigma_{m-t}\left(1-2\left(\frac{v_f}{\pi}\right)^{0.5}\right) \qquad \textbf{[5.1]}$$

where:

σ_2 is the transverse UTS of the composite

σ_{m-t} is the transverse UTS of the matrix material

v_f is the volume fraction of the fibres (i.e. 50%)

Similarly, because there was no information on the elastic modulus and failure strain in the direction transverse to the fibres from the manufacturer's technical data sheet [118], the micromechanics equation for E_2 and ε_2 could not be used. The value for E_2 was inferred from Performance Composites Ltd [81] as it listed the property values acquired from extensive testing of a wide range of CFRP composites composed of similar carbon fibre and epoxy resin. Additionally, according to other sources [3-4, 95], the value for E_2 for CFRP material generally did not vary amongst different carbon fibres with similar stiffness properties in the transverse direction that ranged in the range 6-10 GPa.

Tensile test results of the 0° CFRP specimens

The tensile test results for the five 0° CFRP specimens are listed in Table 5.17 below. It should be noted that the observed failure strain was derived from the Zwick machine test data using the displacement traversed by the machine head. The calculated failure strain rate was determined by dividing the UTS by the determined elastic modulus. The same applies for the 90° CFRP specimen test results.

Table 5.17: Tensile test results for the 0° specimens

Specimens	**Elastic Modulus [GPa]**	**UTS [MPa]**	**Observed Failure Strain [%]**	**Calculated Failure Strain [%]**
Specimen 1	115.3	1379	1.40%	1.09%
Specimen 2	113.4	1490	1.81%	1.20%
Specimen 3	96.2	1327	1.45%	1.26%
Specimen 4	110.3	1321	1.22%	1.09%
Specimen 5	110.4	1269	1.28%	1.05%
Average	**109**	**1357**	**1.43%**	**1.14%**
Standard deviation	**6.71**	**75**	**0.206%**	**0.0708%**
Expected value	**121.7**	**2287**	**1.05%**	

The elastic modulus was at least 110 GPa for four of the specimens with one outlier with a value of 96.2 GPa. The mean value of the Elastic modulus was 109 GPa and the standard deviation of the mean was 6.71 GPa which indicated a reasonably small amount of variation in the results. The mean elastic modulus value was smaller than the theoretical value by approximately 11 GPa (i.e 11% difference). The UTS values ranged from 1269 MPa to 1490 MPa with a mean value of 1357 MPa. The standard deviation value was only 5.5% of the mean value thereby showing a small variation in the values. The mean value determined was approximately 59 % of the theoretical value demonstrating a significant discrepancy. The observed failure strain values were consistently higher than the calculated values for all five specimens. As expected, the mean value for the observed failure strain (1.43%) was larger than that of the calculated failure strain (1.14%). The standard deviation of the observed failure strain was found to be approximately 14.5 % indicating a relatively high variation in the data as compared to that of the calculated failure strain which was only about 6% of its mean.

Plotting a stress vs strain graph for all specimens, it was observed that the relationships were all linear for all five specimens according to Figure 5.63. For the longitudinal direction, the linear behaviour was observed until the fracture point which is similar to what is expected typically in CFRP composite specimens [4, 91].

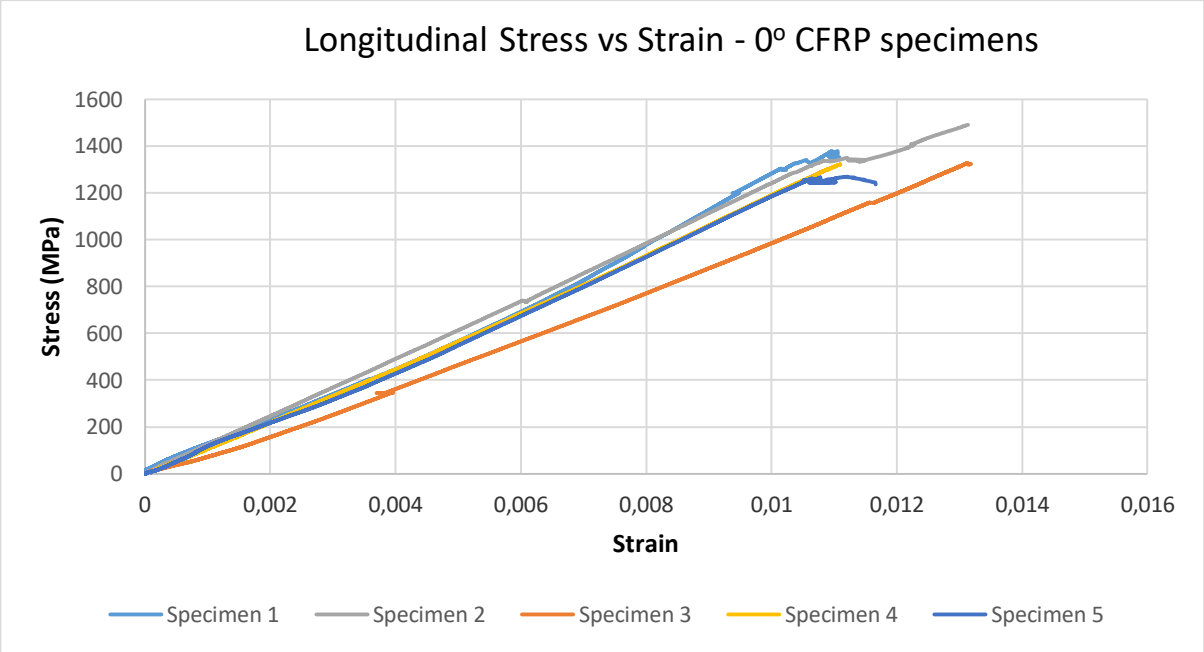

Figure 5.63: Graph of the longitudinal stress against the strain of the CFRP specimens along the 0º direction (longitudinal direction)

The consistency in the slopes of most of the specimens suggested that their elastic moduli were also similar except for specimen 3 which was noticeably lower. This was supported by the results in Table 5.17 as Specimen 3 had an elastic modulus value of 96.2 GPa while the other four specimens had values of at least 110 GPa.

After inspecting the five failed 0º CFRP specimens, it was observed that the predominant failure mode (for four of the five specimens) was cracking and splitting of the specimen along the fibre direction. This was an acceptable failure mode given by the ASTM D3039/D3039M standard though it was not a true tensile failure as there was no lateral failure of the carbon fibres [120]. Figure 5.64 illustrates this type of failure mode.

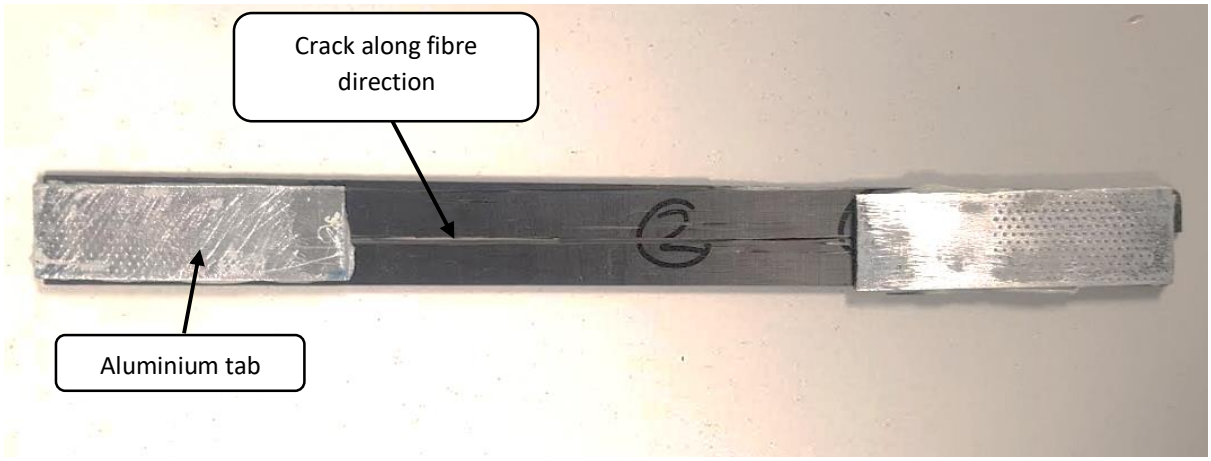

Figure 5.64: Photograph of a failed 0° tensile test specimen with a crack along the fibre direction

Specimen 4 exhibited an additional failure mode to the one in Figure 5.64. The specimen also had partial failure transverse to the fibre direction indicating fibre breakage as shown in Figure 5.65. This type of failure mode was also considered acceptable according to the ASTM D3039/D3039M standard [120]. However, this difference in failure mode did not seem to affect the experimental results i.e. elastic modulus and UTS.

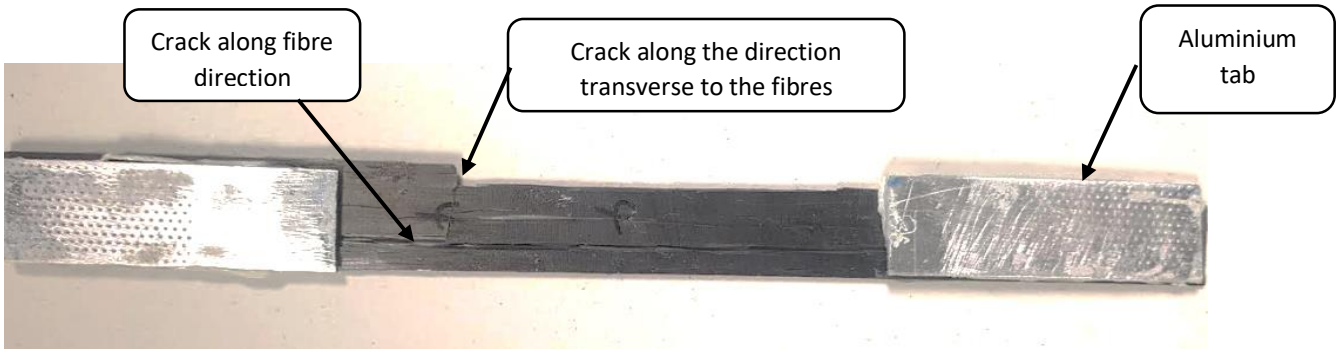

Figure 5.65: Photograph of a failed 0° tensile test specimen with two failure modes

90° CFRP specimens

The results of the tensile test for the three 90° CFRP specimens are shown in Table 5.18.

Table 5.18: Tensile test results for the 90° specimens

Specimens	**Elastic Modulus [MPa]**	**UTS [MPa]**	**Observed Failure Strain [%]**	**Calculated Failure Strain [%]**
Specimen 1	632	3.38	0.584%	0.535%
Specimen 2	423	2.53	0.600%	0.598%
Specimen 3	738	4.16	0.548%	0.568%
Average	**598**	**3.36**	**0.578%**	**0.567%**
Standard deviation	**131**	**0.666**	**0.0216%**	**0.0257%**
Expected value	**10000**	**14.8**	**0.5%**	

For the elastic modulus, the mean value of 598 MPa was very low (approximately 10 times lower than the expected value of 6 GPa). The standard deviation was 22 % of the mean value for the elastic modulus which showed a high variation. The mean UTS value of 3.36 MPa was also considerably smaller than the expected value i.e. by about 4 times. As in the case of the elastic modulus, the standard deviation was determined to be approximately 20 % of the mean. This also signified a high variation in the experimental data. Both the observed and calculated failure strains (0.578% and 0.567% respectively) were higher than the expected value of 0.5 %. The standard deviations of the observed and calculated failure strains were similar with values of approximately 4% and 5% respectively. Figure 5.66 shows the stress vs strain relationship for the three specimens loaded in the direction transverse to the fibres.

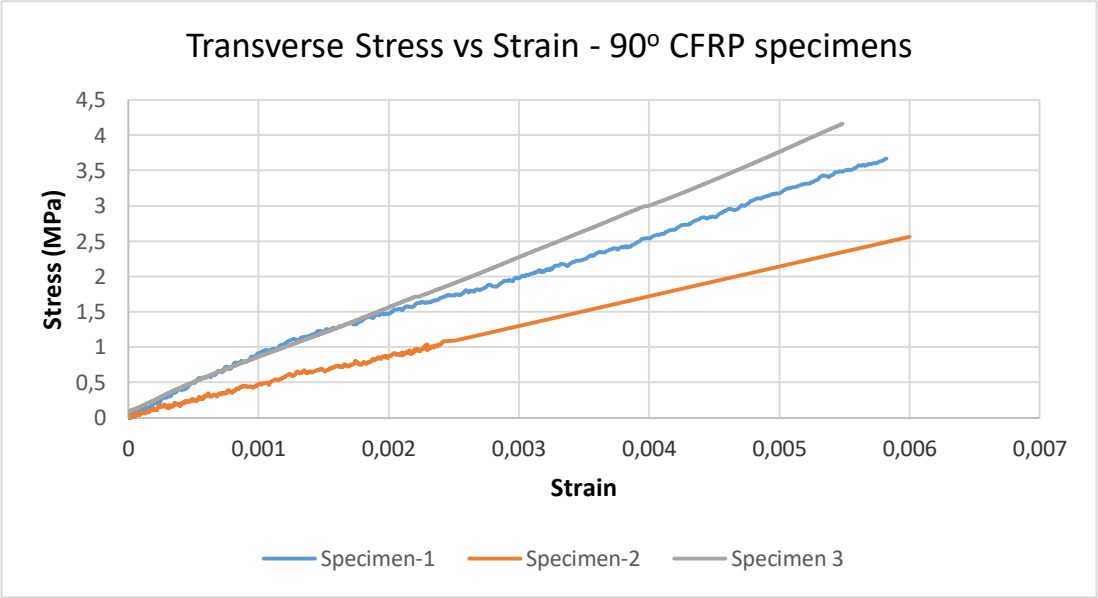

Figure 5.66: Graph of the transverse stress against the strain of the CFRP specimens along the 90° direction (transverse direction)

The gradients were also reasonably linear although they were noticeably different as shown in Figure 5.66. The 90° CFRP specimens were also visually inspected before and after the tensile tests. Before the tests, it was observed that all the specimens were warped (about an axis orthogonal to the fibre direction) shortly after post-curing in an oven (see section 4.1 for more details). In addition, there were cracks that were observed on the surface of the specimens in the direction perpendicular to the direction that the specimens were to be loaded. After the test, it was observed that the failures of all the three specimens initiated at one of these cracks as illustrated in Figure 5.67.

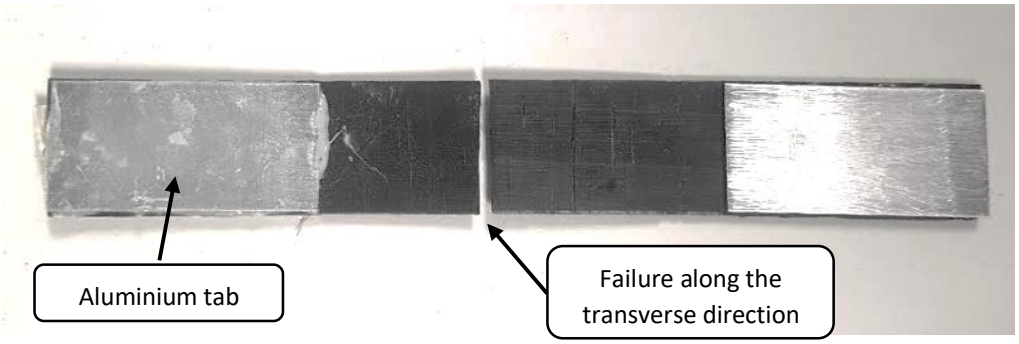

Figure 5.67: Photograph of a failed 90° tensile test specimen

5.1.2 Discussion of the tensile test results

As can be observed from the results, most of the values of the mechanical properties from the tensile tests were consistently lower than the theoretical values for both the 0^{O} and 90^{O} directions. However, the property values for the UTS and Elastic Modulus in the 90^{O} direction were found to be very low in comparison to the expected values as well as those from several credible sources [3-4, 81, 95]. The reasons for the various mismatches in the property values of the 0^{O} and 90^{O} CFRP specimens determined by the tensile tests could have been the result of the following factors:

- Presence of voids which could have been likely introduced during the manufacture of the specimens. Voids are known to result in a lower transverse tensile strength value if the void content is sufficiently high [3].
- The 90^{O} specimens were warped after being post-cured and discernible cracks were observed on the surface. During the manual filament winding process, the winding angle was judged by eye which may have introduced inaccuracies in the winding angle. This could have caused warping when the specimens were post-cured, thereby forming cracks on the surface because of the residual stresses caused by heat. The cracks were therefore stress concentrations where failure could initiate.
- Non-uniform material properties. During the filament winding process, after each layer of carbon fibre was wound on the rectangular block (Figure 4.3), the layer was post-impregnated with epoxy resin by hand. Because of the human factor, the epoxy resin content on the flat panels was likely not constant for each point (i.e. inconsistent material properties). As such, areas of low or high epoxy resin content could have been formed resulting in localised areas of weakness on the specimens.
- For most of the 0^{o} specimens, failure occurred in the fibre direction and not in the direction transverse to the loading direction. This meant that most of the fibres in the specimens did not fail due to tension which should have occurred at a higher tensile load than was witnessed.
- The assumptions made on the theoretical property values were incorrect. For example that there was a perfect bond between the fibres and the resin.

The set of mechanical properties determined from these tensile tests appeared lower than anticipated, but they provided the initial set of design values that were used to model the behaviour of the CFRP tube. The CFRP tube would eventually be tested and their actual behaviour would be used to confirm the behaviour modelled using the initial set of properties.

5.2 End cap adhesive shear

There were three sets of end cap adhesive shear tests that were performed with five test specimens per test. The three tests coincided with each of the three designs of the end caps covered in section 4.2. The objective of this test was to determine the actual shear strength of the SpaBond 340 LV adhesive when used to bond each of the three end cap designs to the inner wall of the CFRP tube.

5.2.1 First Test

For the first end cap adhesive shear test, the slow hardener was used in conjunction with the SpaBond 340 LV resin resulting in a theoretical shear strength of SpaBond 340 LV of 34.5 MPa according to the manufacturer [108].

Results

Table 5.19 provides a summary of that data that was recorded for the first test. The maximum applied shear stress was calculated by dividing the maximum applied shear force by the calculated shear area

as shown in the last column. The calculated shear area represented the area of the end cap that was bonded onto the adhesive layer.

Table 5.19: First end cap adhesive shear test results

Specimens	Max Shear Force [kN]	Protruding Length [mm]	Bond Length [mm]	Shear Area [mm^2]	Shear Strength [MPa]
Specimen 1	32.72	10.40	14.60	2151	15.2
Specimen 2	23.34	11.40	13.60	2004	11.6
Specimen 3	24.05	8.27	16.73	2465	9.8
Specimen 4	26.05	11.63	13.37	1969	13.2
Specimen 5	28.72	10.47	14.53	2141	13.4
				Average	**12.7**
				Std dev	**1.8**
				Expected	**34.5**

The average of the applied stresses was determined to be 12.7 MPa whilst the theoretical shear strength of SpaBond 340 LV is 34.5 MPa [108]. This meant that the mean shear strength value was only 37% of the theoretical value. The standard deviation (std dev) was approximately 15% of the mean which showed a notable amount of scatter of the shear strength values about the mean. The graph in Figure 5.68 illustrates the plotted experimental results of the first shear test.

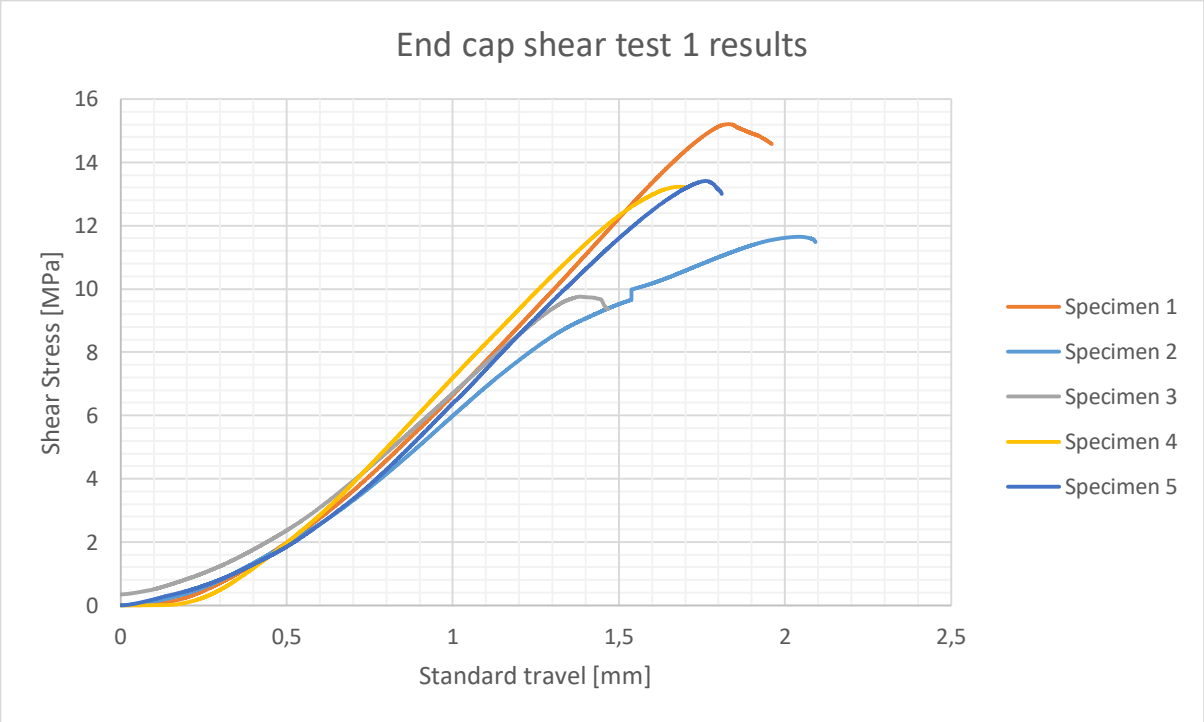

Figure 5.68: Graph showing the results for the first shear test

Figure 5.68 shows that all the curves for the shear test specimens all had a similar trend although the peak values were somewhat scattered about the mean. All five curves were smooth which suggested a consistency in the response of the adhesive layer to the shear force. The curve for specimen 3, had a considerably lower peak shear strength value of 9.8 MPa in comparison to the other four specimens

that had shear strength values of at least 11 MPa. Only the curve for specimen 5 differed slightly in terms of the slope compared to the rest of the specimens beyond the standard travel value of 1 mm.

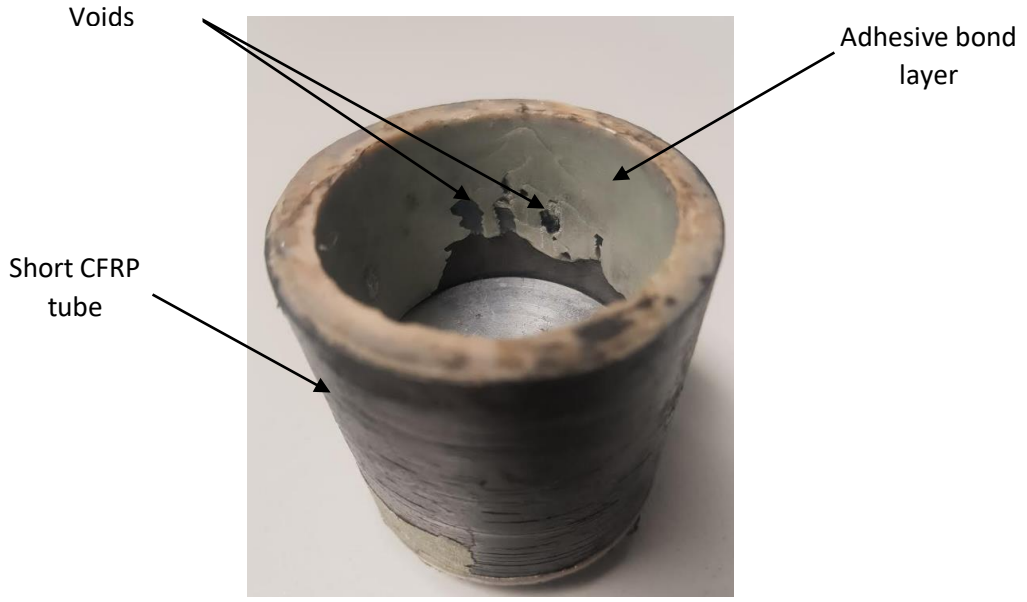

Figure 5.69: Photograph of an example of a specimen that failed due to shear during the first set of tests

Figure 5.69 illustrates a specimen that failed in shear during the first adhesive shear test. After pressing the dummy end cap out, the adhesive layer could be visually inspected. Of note, were the voids in the adhesive layer which were likely due to the first adhesive application method in the designated area. It was also worth noting that all five specimens experience shear failure on the end cap to adhesive layer interface rather on the adhesive layer to CFRP interface. This was a strong indication that the end cap to adhesive layer interface was the limiting case for this type of loading.

Discussion

The mean shear strength for the first test was only 37% of the theoretical value of 34.5 MPa for the SpaBond 340 LV adhesive. After visually inspecting the adhesive layer in Figure 5.69, voids were observed. Voids effectively lessened the shear area used to determine the shear strength thereby resulting in a shear strength value that is lower. However, the voids in Figure 5.69 appeared to cover less than 20% of the shear area of the adhesive meaning that the actual shear strength would be at most approximately 20 % more than the mean value i.e. approximately 15.3 MPa. This was still less than half of the theoretical shear strength value suggesting there was one or more other factors causing these differences.

5.2.2 Second test

The second end cap design was prompted by the need to eliminate the formation of voids (see section 3.2.4 for more details). A fast hardener was used for SpaBond 340 LV adhesive in this case and thus, the resulting theoretical shear strength was 33.3 MPa [108]. In addition, the dummy end caps used for the second test were bonded onto the short CFRP tubes using a different adhesive application method to the one used previously. This method involves the use of a syringe to inject resin directly into the bond region between the end cap and the internal wall of the CFRP tube.

Results

The second end cap adhesive shear test results are recorded Table 5.20. The mean shear strength of the adhesive for the second test showed a small increase from the first test (i.e. from 12.7 MPa to 14.7

MPa) though it still amounted to only 44 % of the theoretical shear strength of SpaBond 340 LV. The increase in the mean shear strength value may have been due to the second adhesive application method. The standard deviation was 2.9 MPa which indicated a slightly higher variation than the one from the first tests.

Table 5.20: Second adhesive shear test results

Specimens	**Max Shear Force [kN]**	**Protruding Length [mm]**	**Bond Length [mm]**	**Shear Area [mm^2]**	**Shear Strength [MPa]**
Specimen 1	25.468	11.77	13.2	1950	13.1
Specimen 2	19.360	12.60	12.4	1826	10.6
Specimen 3	47.655	8.39	16.6	2447	19.5
Specimen 4	29.496	12.18	12.8	1890	15.6
Specimen 5	17.1	17.13	7.87	1160	14.7
				Average	**14.7**
				Std dev	**2.9**
				Expected	**33.3**

The graph in Figure 5.70 illustrated the results of the second shear test.

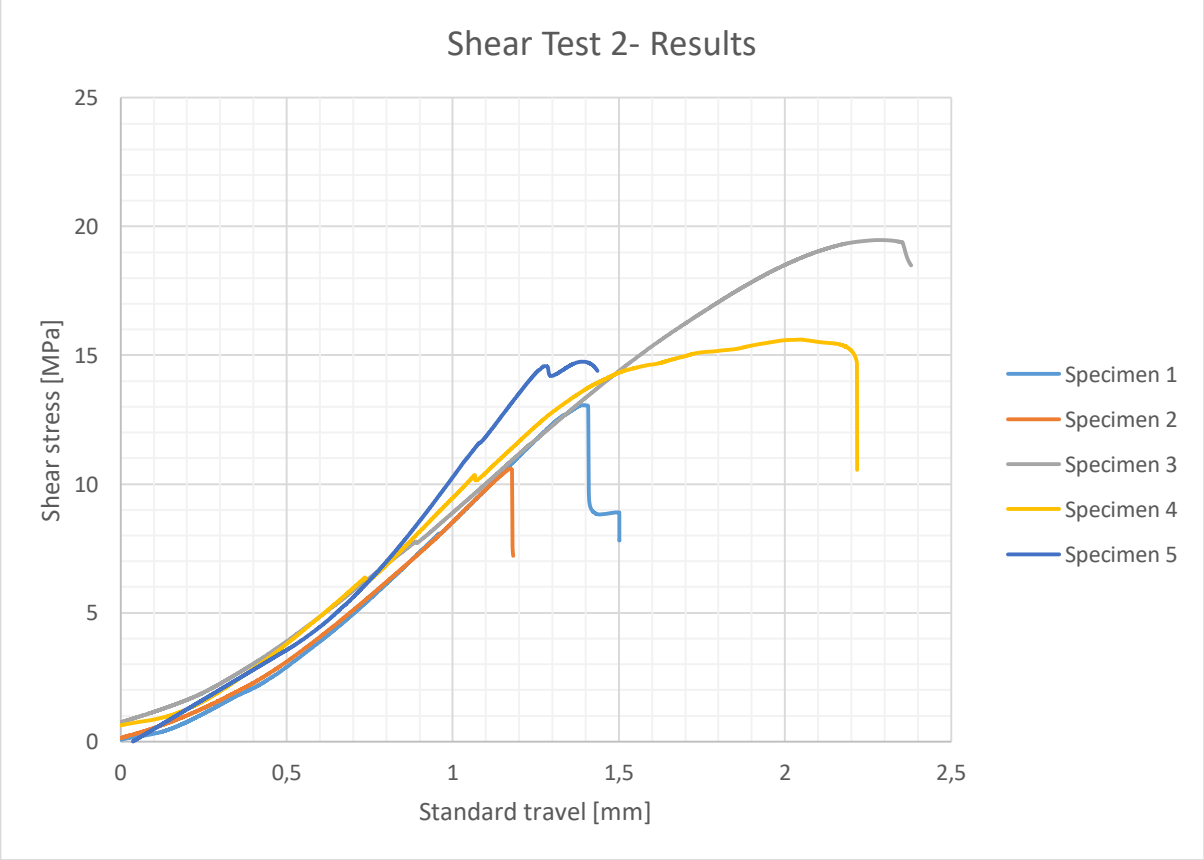

Figure 5.70: Graph showing the results for the second shear test

The graph shows that the trends for all five curves were similar initially which showed that the specimens had a similar response when a shear force was applied. However, the graph also showed that the shear strength peak values of the specimens varied by a greater amount than in the first test

which was consistent with the fact that the standard deviation was 20% of the mean shear strength value.

In Figure 5.71 is a photograph of one of the specimens that failed in shear during the second adhesive shear test. It was observed that the adhesive bond layer was uniform and had no voids like the previous sample specimen used in the first test (see Figure 5.71). This strongly suggested that absence of voids was the result of the change in the adhesive application method. The only mode of failure observed for the second set of specimens was a shear failure on the end cap to adhesive layer interface.

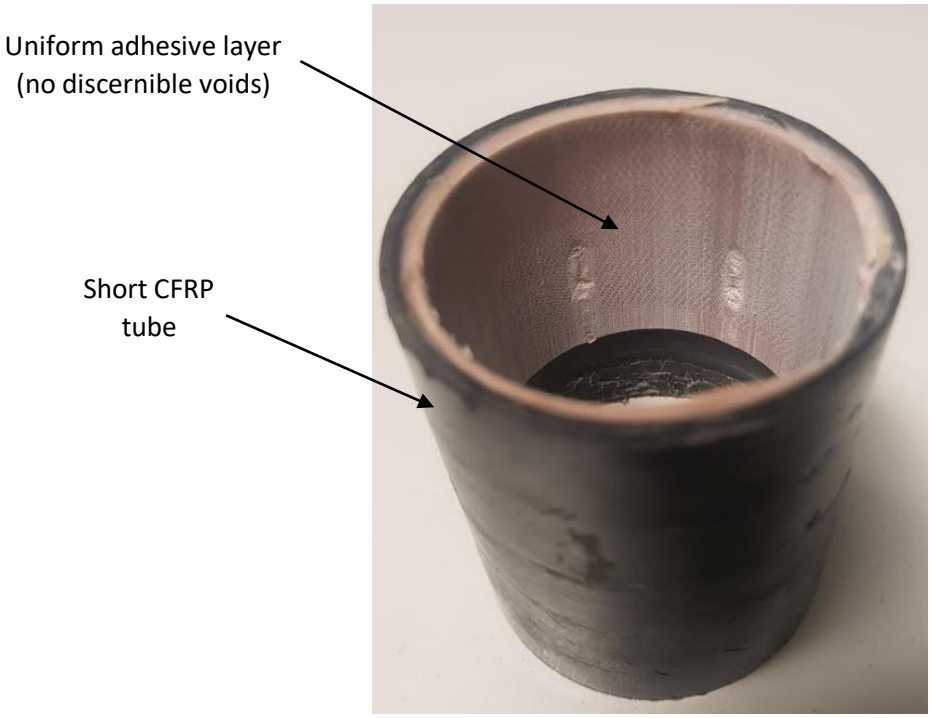

Figure 5.71: Photograph of a failed specimen from the second shear test

Discussion

There was a small improvement in the shear strength of the adhesive from the first test to the second test i.e. from 12.7 MPa to 14.7 MPa. The second adhesive application method was implemented for the dummy end caps used in the second set of shear tests as a way to counter the formation of voids. The adhesive layer of all failed second test specimens were visually inspected, and no discernible voids were observed as illustrated in Figure 5.71. This confirmed that the second adhesive application method was successful in eliminating void formation in the adhesive layer. It could be concluded that the increase in the shear strength of the adhesive was attributed to the absence of voids in the adhesive layer. However, the mean shear strength remained less than 50% of the theoretical shear strength value. The standard deviation also remained undesirably high at 20% of the mean which was worse than that of the first test at 15% of its respective mean value. It was deduced that the surface finish on the bond area of the dummy end cap was likely not consistent at all points which might have caused the variation observed in both the first and second shear test results. As part of the surface preparation, the bond area on the end cap was hand abraded with an 80-grit emery cloth before the adhesive was applied which was the most likely cause of the uneven surface finish. It was also assumed that increasing the surface roughness of the bond area on the end cap would increase the mechanical

grip of the adhesive layer which could possibly increase the mean shear strength value. Therefore, it was decided that knurling be introduced on the bond area on the end cap for the third end cap design which would be assessed in the third adhesive shear test.

5.2.3 Third test

The third dummy end cap design included a knurled designated bond area. This was the only feature that differentiated the third dummy end cap design with the second design. The fast hardener was again used for the third set of adhesive shear test specimens.

Results

Table 5.5 summarizes the results from the third test. The average shear strength for the third shear test of 13.3 MPa was lower than that of the second shear test by a margin of about 10%. Conversely, the standard deviation value was only 4 % of the mean shear strength value which was at its lowest as compared to the previous two tests. This was an indication that there were less inconsistencies in the preparation of the specimens.

Table 5.5: Third adhesive shear test results

Specimens	**Max Shear Force [kN]**	**Protruding Length [mm]**	**Bond Length [mm]**	**Shear Area [mm^2]**	**Shear Strength [MPa]**
Specimen 1	17.902	15.58	9.42	1391	12.87
Specimen 2	19.843	14.98	10.02	1480	13.41
Specimen 3	19.639	14.8	10.2	1506	13.04
Specimen 4	15.362	16.89	8.11	1197	12.83
Specimen 5	25.017	13.2	11.8	1742	14.36
				Average	**13.3**
				Std dev	**0.57**
				Expected	**33.3**

Figure 5.72 shows the graph with the results of the third and final adhesive shear test that was performed. The curves were observed to have a similar trend to the previous tests. It was also observed that the adhesive layer was uniform as was the case in the second test (see Figure 5.71). As with the first and second tests, the shear failure occurred on the end cap to adhesive layer interface.

Figure 5.72: Graph showing the results of the third shear test

Discussion

For the third adhesive shear test, the standard deviation dropped to 4% of the mean shear strength value from 20 % in the second test. The low standard deviation value was desirable as it gave more confidence in the calculated mean shear strength value of the adhesive layer. This was critical in the choosing of a safety factor to use with regards to accounting for shear failure of the end cap. The higher the standard deviation value, the higher the uncertainty which in turn meant increasing the safety factor considerably. Increasing the safety factor for shear failure was undesirably because it meant increasing the bond area length on the end cap which would in turn increase the size and mass of the end cap as well as that of the entire pressure vessel. Therefore, knurling the bond area on the end caps seemed to guarantee a low standard deviation in the mean shear strength value. Conversely, between the second and the third shear test, the mean shear strength value dropped from 14.7 MPa to 13.3 MPa. This suggested that knurling did not result in the improvement of the mechanical bond which would increase the shear strength value as initially expected. The shear strength value for the 13.3 MPa was thus used in the design calculations for the third end cap design.

The shear failure was observed to be consistently occurring only on the end cap to adhesive layer interface for all specimens in the three tests. In section 3.2.3 on sizing the end cap bond area, it was assumed (based on calculation) that the adhesive layer would experience shear failure on the end cap to adhesive layer interface i.e. limiting case. This was based on the fact that shear area of that interface was less than that of the interface between the adhesive layer and the internal wall of the CFRP tube. Therefore, the results from the shear tests proved that for this type of loading, the assumption that failure would occur on the end cap to adhesive layer was reasonable.

5.3 Hydrostatic burst pressure tests

According to the requirements stipulated by the ASME Pressure Vessel Code Section X for FRP pressure vessels, the failure pressure of a CFRP pressure vessel had to be at least 2.25 times the maximum working/design pressure [10]. Therefore, determining the failure pressure of a CFRP

pressure vessel was essential and was one of the primary objectives of the burst test. There were various modes by which the CFRP pressure vessel could fail. These included bursting (i.e. failure of the CFRP section of the vessel), shear failure of the end caps or leaking through the end caps. The second objective of the burst test was to measure and analyse strain readings (for the longitudinal and hoop directions). The specimen CFRP pressure vessels were fitted with strain gauges that could measure longitudinal and hoop strain as the vessels were pressurised. The strain measurements would allow the resulting deformation behaviour of the CFRP section of the vessel to be understood which would be useful for future designs of similar CFRP tubes. In addition, the strain response or deformation behaviour in the hoop and longitudinal directions would give information regarding the stiffness of the CFRP tube. This information would allow the validation/correction of the initially estimated stiffness properties (see sections 3.1.3 and 5.1.1) implemented in the CLT based calculations used for designing the CFRP tubes.

5.3.1 First set of CFRP pressure vessels

There were three CFRP pressure vessels that made up the first set of vessels and they all had a 4 mm wall thickness. The first end cap design was used in vessel 1 whilst the second end cap design was used for vessels 2 and 3. There were two sets of results, the first being of the recorded failure pressures and modes, the second being the results of the strain measurements.

5.3.1.1 Results on failure pressures of the first set of burst tests

The hydrostatic burst pressure tests were performed for each of the three 4 mm CFRP vessels until failure occurred. The failure pressures, maximum design pressures and causes of the failures are summarised in Table 5.21 below:

Table 5.21: Failure pressures, maximum design pressure and modes for the first set of CFRP pressure vessels

Vessel No	Failure Pressure [bar]	Max Design Pressure [bar]	Failure mode and description
1	136	60	Shear failure between the end cap to adhesive layer interface resulting in the end cap being partially pushed out (Figure 5.73)
2	162	72	Leaking past the adhesive layer at one of the ends of the pressure vessel
3	220	98	An initial partial shear failure of one end cap to adhesive layer interface and then on the interface between the adhesive layer and the internal wall of the CFRP tube (Figure 5.75)

Table 5.22 shows the predicted pressures that were determined using the four failure theories from section 5.1. It can be noted that none of the three vessels failed due to the bursting of the CFRP tube. Therefore, the failure pressures of the three vessels in Table 5.21 could not be directly compared to the predicted burst pressures in Table 5.22.

Table 5.22: Predicted burst pressures for 4 mm CFRP tube using the initial estimate strength properties

Failure theory	Predicted Burst Pressure [bar]
Maximum Stress	360
Maximum Strain	500
Tsai-Hill	327
Tsai-Wu	344

For vessel 1, the shear failure occurred on the end cap to adhesive layer interface is illustrated in Figure 5.73.

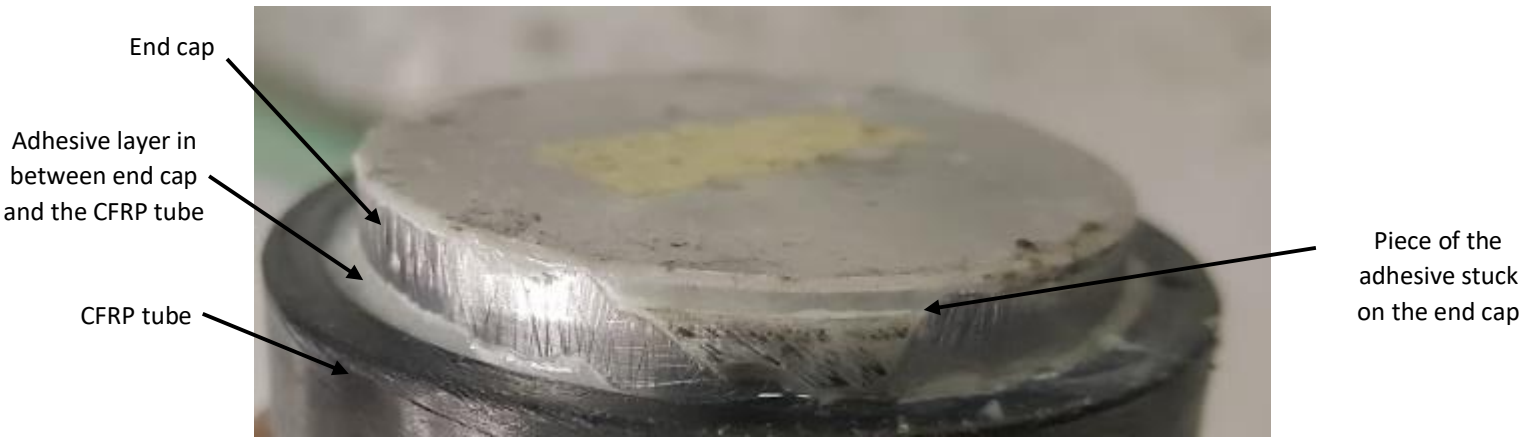

Figure 5.73: Photograph showing shear failure between the end cap (i.e. first design) to adhesive layer interface for vessel 1

This vessel had end caps based on the first design where the epoxy adhesive was applied using the first adhesive application method. The shear failure occurred at a low pressure of 136 bar on the interface between the end cap and the adhesive layer. Shear failure on the same interface was also confirmed through the first end cap adhesive shear tests. The formation of voids as shown in Figure 5.74 also further confirmed the problems identified in the first end cap shear tests.

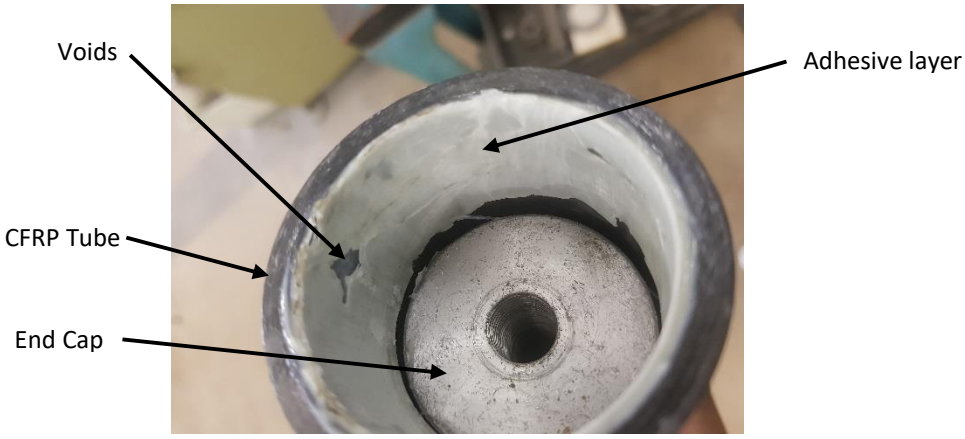

Figure 5.74: Photograph showing void formation on the adhesive layer after shear failure of vessel 1 during a burst test

The failure pressure of 136 bar represented a shear stress of about 5 MPa for the end cap to adhesive layer interface. However, this was not consistent with the mean value of the shear strength from the first shear test which was determined to be 12.7 MPa. This suggested that there may be a factor that caused the adhesive layer to underperform in the burst test.

The second design of the end cap was utilised in vessels 2 and 3 and both vessels failed at higher pressures than in the case of vessel 1. Vessel 2 failed due to leaking past the adhesive layer at one of the ends of the vessel at a pressure of approximately 162 bar. This essentially meant that the water managed to pass through the rubber liner first before bypassing the O-ring and seeping out past the adhesive layer. It was difficult to establish the exact sequence of events that led to this type of failure in the form of leakage. However, it was probable that there may have been some movement of the end cap initially that could have been enough to tear the rubber liner thereby allowing water to pass

through. Secondly, the end cap movement could also have displaced the O-ring sufficiently so that it would not be able to seal properly thereby allowing the pressurized water to pass through. Consequently, the bond between one of the two interfaces can be considered to have failed for the water to leak at the end cap.

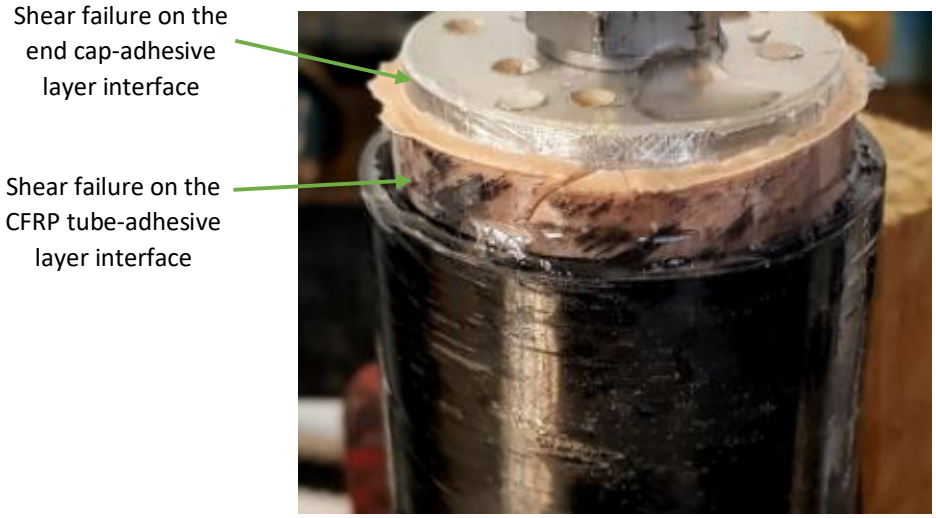

Figure 5.75: Photograph showing multiple modes of failure of the adhesive layer on both interfaces for vessel 3

For vessel 3, there was a combination of failures that occurred on both interfaces of the adhesive layer as shown in Figure 5.75. Initially, upwards movement of the end cap was observed as it was being pushed out. However, when the end cap had slightly moved relative to the adhesive layer and tube it temporarily stopped moving during the burst test. Shortly afterwards at a higher pressure just below 220 bar, there was upwards movement on the interface between the adhesive and CFRP tube before water started leaking out. There was also a suggestion of delamination as can be seen by the fragments of CFRP remaining on the adhesive layer to CFRP tube interface in Figure 5.75.

5.3.1.2 Results on strain measurements from the first set of burst tests

During the hydrostatic burst tests for the first set of three 4 mm thick CFRP tubes, the hoop and longitudinal strain measurements were recorded. The strain measurements are plotted on graphs as described in this sub-section.

The longitudinal strain for the 4 mm vessel in all three cases was observed to be negative as shown in Figure 5.76 meaning the vessel was “shrinking” in the longitudinal direction. The deformation behaviour of the three vessels in the longitudinal direction was linear showing that the stiffness (i.e. inverse of the gradient) was constant for all pressures up to 220 bar. Furthermore, they also had had similar gradient values (and therefore stiffness). The best fit line on the graph represented the average deformation response of all three vessels in the longitudinal direction. The best fit line was also used in the hoop direction as illustrated in Figure 5.77.

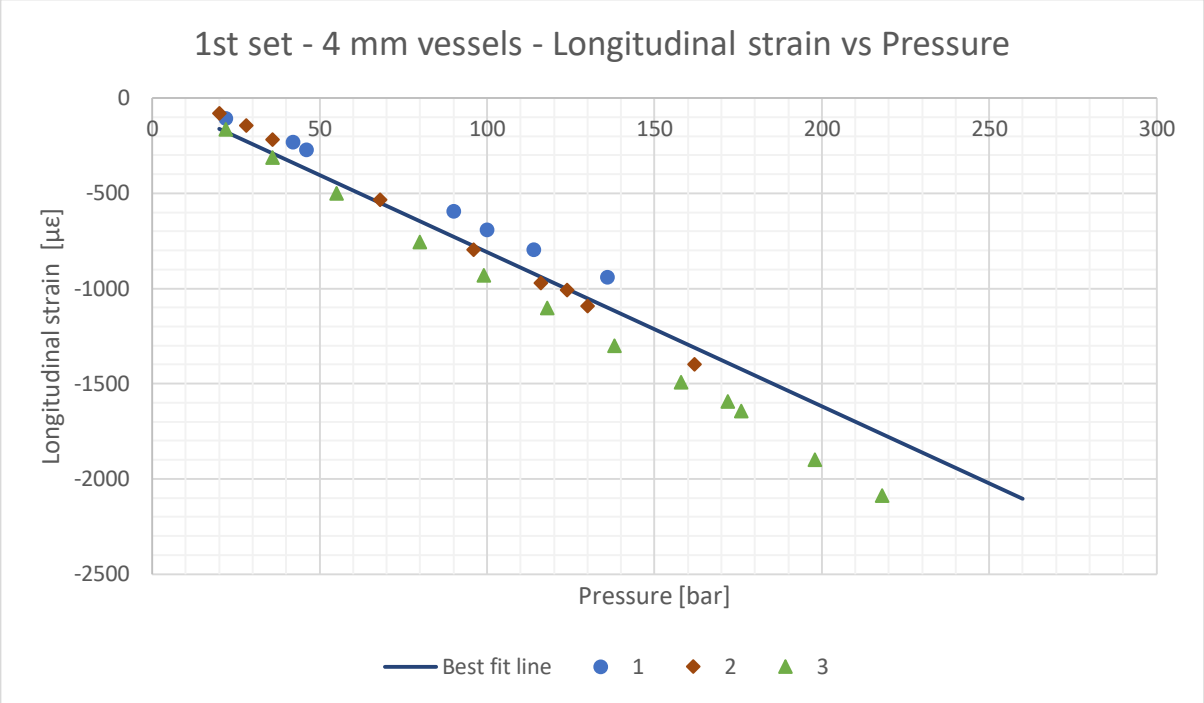

Figure 5.76: Graph of the longitudinal strain vs the pressure for the first set of CFRP pressure vessels

The hoop strain was positive as shown in Figure 5.77 signifying an increase in diameter for all pressures. The deformation behaviour of each of the three vessels was also linear in nature indicating constant stiffness up until their respective failure pressures. The graph in Figure 5.77 also showed that there was a very close agreement in the deformation behaviours of the three vessels as all the three sets of data points essentially lay on top of each other. The data points from the three vessels were practically on top of the best fit line indicating a strong correlation.

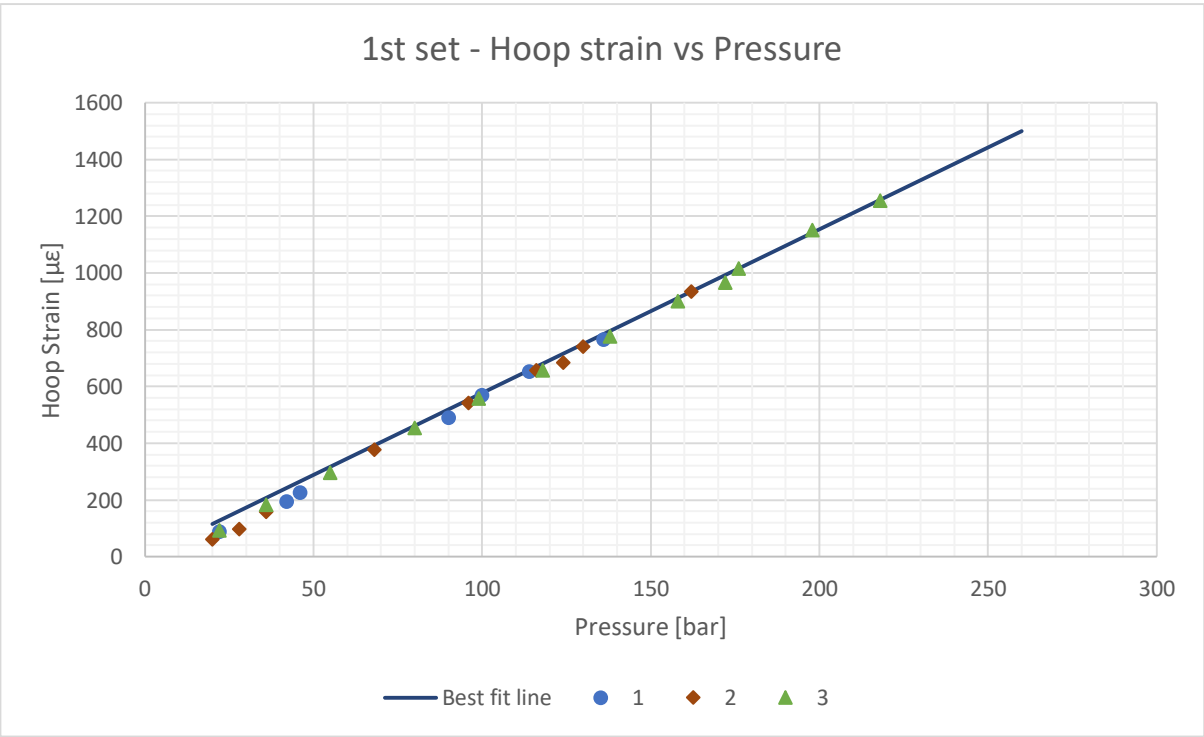

Figure 5.77: Graph of the hoop strain vs the pressure for the first set of CFRP pressure vessels

5.3.1.3 Discussion of the first burst test results

Failure pressures

Vessel 1 of the first set of CFRP 4 mm vessels failed due to shear at the interface between the end cap and adhesive layer. Vessel 1 had the first end cap design and failed at a pressure of 136 bar that was equivalent to an applied shear stress of 5 MPa which was significantly lower than anticipated. The adhesive layer shown in Figure 5.74 showed the presence of voids that undermined the shear strength of the adhesive layer as the actual shear area was lower than the one used in the calculations. However, judging simply by the area that was occupied by voids in Figure 5.74, it could not have accounted for the entire difference between the 5 MPa and 12.7 MPa values. There should have been another cause which was probably related to the method of preparation and bonding of the end caps. It could have been that the bond area on the end caps was not abraded enough to give the necessary surface roughness to grip effectively onto the adhesive layer thereby resulting in a lower shear strength value.

The remaining two vessels of the first set of vessels failed at higher pressures than the first vessel. They both used end caps based on the second design. Vessel 2 failed due to leaking at the adhesive layer's interface(s) at a pressure of 162 bar. This suggested that the rubber liner and O-ring, failed to prevent the water from leaking out at one of the ends of the vessel. The rubber liner should have failed first as it is the first sealant in contact with water in the vessel. Since leaking did not occur in the other two vessels, it is reasonable to suggest that vessel 2 likely had a unique defect which made it an outlier.

The last vessel in the first set failed due to multiple failure methods at 220 bar (see Figure 5.75). The partial shear failure on the end cap to adhesive layer interface occurred initially and facilitated the upward movement of the end cap. The eventual failure occurred on the adhesive layer to CFRP tube wall interface which appeared to be a combination of shear and delamination. Shear failure dominated while there was a little delamination as only a small portion of a layer from the CFRP tube wall was stuck on the adhesive layer. However, the occurrence of delamination possibly suggests that the adhesive layer was under tension. This could have been possible if the CFRP tube was expanding more in the hoop direction than the end cap. This tensile load would have then aided delamination of the thin layer of the CFRP tube interfacing with the adhesive layer. Therefore, the combination of shear and delamination at the adhesive layer to CFRP tube wall interface was what could have caused the failure of the vessel.

It was noted that none of the three CFRP vessels of the first set of vessels failed due to bursting of the CFRP tube section. The failure pressure/strength of the CFRP tube section of the vessel could not be determined. Thus, it was established that the 4 mm CFRP tube could only fail at a pressure higher than 220 bar.

Strain measurements from the first set of burst tests

The longitudinal strain was negative which indicated compression of the CFRP tube in the longitudinal direction. This supports the possibility of the adhesive layer being under tension. For both longitudinal and hoop directions the strain response of the CFRP tube was linear. The stiffness of the CFRP tube was represented by the inverse of the gradient and in both directions, the stiffness values were constant. It can be noted that the stiffness values in the hoop and longitudinal directions were in close agreement to each other as the scatter about the best fit line seemed minimal. This consistency in the results for all three 4 mm CFRP tubes was expected and encouraging given that they were cut from the same CFRP tube. The stiffness properties of the CFRP tube material were adjusted until the

calculated strain values (from the CLT based calculations) matched the average response or best fit line of the CFRP tube in both the longitudinal and hoop directions. This was necessary in order to validate the stiffness properties determined from the tensile tests in section 5.1.

Importance of the first burst test results

The initial strength properties (i.e. σ_1 and σ_2) used to predict the pressures at which the CFRP tube would burst (using the four chosen failure theories) in Table 5.22 could not be validated. This was because none of the three CFRP tube sections failed. Therefore, more CFRP vessels had to be manufactured and hydrostatically tested with the objective of determining the failure strength of the CFRP tube section of the pressure vessel. Rather than use only 4 mm thick CFRP tubes, it was decided to procure 2 mm thick CFRP tubes that were manufactured in the same manner as the 4 mm CFRP tubes. Because the 2 mm CFRP tubes were thinner and had half the number of laminae, it meant they were weaker and more likely to fail through bursting.

5.3.2 Second set of CFRP pressure vessels

The second set was composed of two types of CFRP pressure vessels distinguished by the wall thickness. One type had a wall thickness of 2 mm while the other 4 mm. For each type, five vessels were tested to failure and the results recorded.

5.3.2.1 Results on failure pressures of the second set of burst tests

2 mm pressure vessels

The failure modes and pressures of the five 2 mm CFRP vessels are detailed in Table 5.23.

Table 5.23: Failure pressures and modes for the 2mm CFRP pressure vessels

Vessel No	Burst Pressure [bar]	Max Design Pressure [bar]	Failure mode and description
1	340	151	The CFRP tube section cracked before leaking commenced resulting in loss of pressure. The crack formed in the region of the CFRP tube close to one of the end caps.
2	360	160	The CFRP tube section cracked before leaking commenced resulting in loss of pressure. The crack formed in the region of the CFRP tube close to one of the end caps.
3	380	169	The CFRP tube section cracked before leaking commenced resulting in loss of pressure. The crack formed in the region of the CFRP tube close to one of the end caps.
4	350	156	The CFRP tube initially bulged visibly in the hoop direction at the bottom end before failure due to delamination occurred between the adhesive layer to CFRP tube wall interface at the end cap.
5	330	147	The CFRP tube section cracked before leaking commenced. The crack formed in the region of the CFRP tube close to one of the end caps.
Average	**352**	**157**	
Std Dev	**17.2**	**7.6**	

All 2 mm pressure vessels experienced failure at pressures between 330 bar and 380 bar. The predominant mode of failure was bursting of the CFRP tube section with vessel 4 being the exception. The average burst pressure was determined to be 352 bar which translated to a design pressure of

157 bar with a standard deviation of about 8 bar. The scatter of the burst pressures about the mean was minimal as the standard deviation was approximately 5% of the mean. The predicted pressures at which the bursting of the CFRP tube would occur according to the failure theories using the strength properties from section 5.1 are listed in Table 5.24. All five 2 mm CFRP pressure vessels failed at higher pressures than expected indicating that the predicted burst pressures were conservative. Consequently, this implied that the initial strength properties used for burst pressure predictions were also conservative.

Table 5.24: Initial predictions of the burst pressures for the 2 mm CFRP vessels using the initial strength properties

Failure theory	**Predicted Burst Pressure [bar]**
Maximum Stress	178
Maximum Strain	295
Tsai-Hill	160
Tsai-Wu	169

It was observed that for all five 2 mm pressure vessels before the occurrence of failure, there was bulging of the CFRP tube at the locations close to both end caps as shown in Figure 5.78. Unfortunately, the bulging of the vessels could not be captured on camera during burst testing because of the way in which the test was set up.

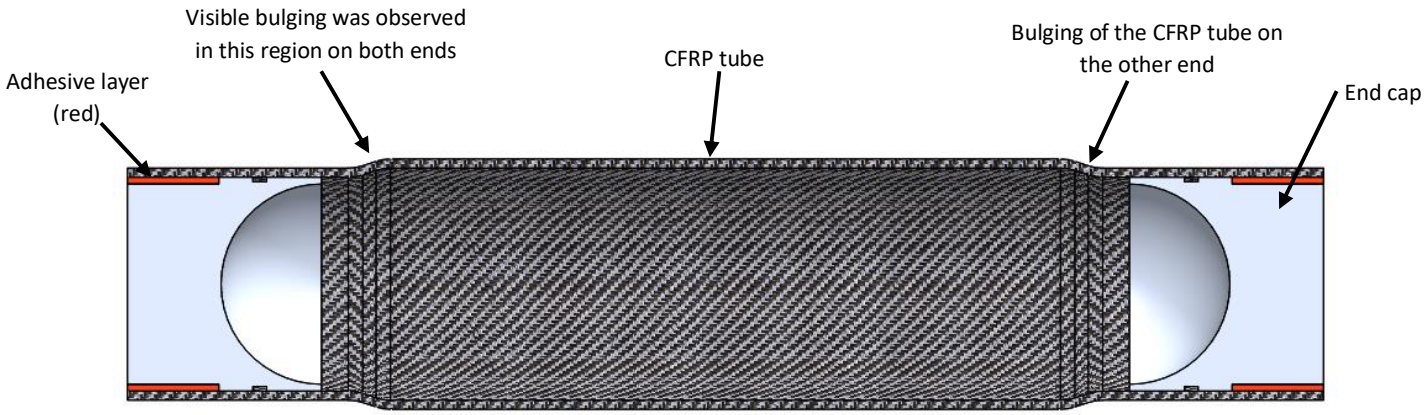

Figure 5.78: Visual representation of the deformation observed on of the 2 mm CFRP vessels before failure

The bulging phenomenon suggested that the CFRP tube was expanding more than the end cap in the hoop direction. The phenomenon depicted in Figure 5.78 preceded either the cracking of the CFRP tube or delamination of a layer of the CFRP at one of the ends of the vessel. For the failure due to delamination, a thin layer of CFRP was "peeled" off the internal wall of the CFRP tube and became stuck onto the adhesive layer which, with the end cap, was pushed out partially as illustrated in Figure 5.79.

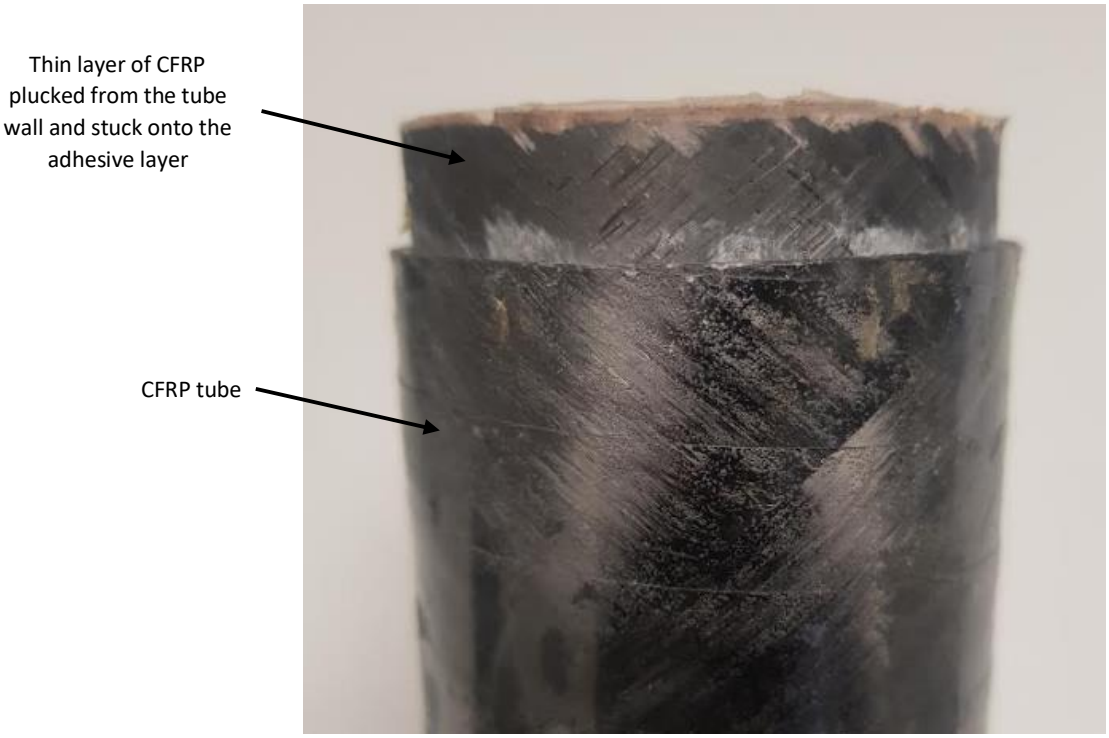

Figure 5.79: Photograph showing failure due to delamination between the adhesive to CFRP tube wall interface

4 mm pressure vessels

Five CFRP pressure vessels with a wall thickness of 4 mm were tested to failure through hydrostatic burst pressure tests. Four of the five 4 mm pressure vessels failed due to the shear failure on the end cap to adhesive layer interface as shown in Figure 5.80. This was consistent with the end cap shear test results where all specimens failed on the end cap to adhesive layer interface.

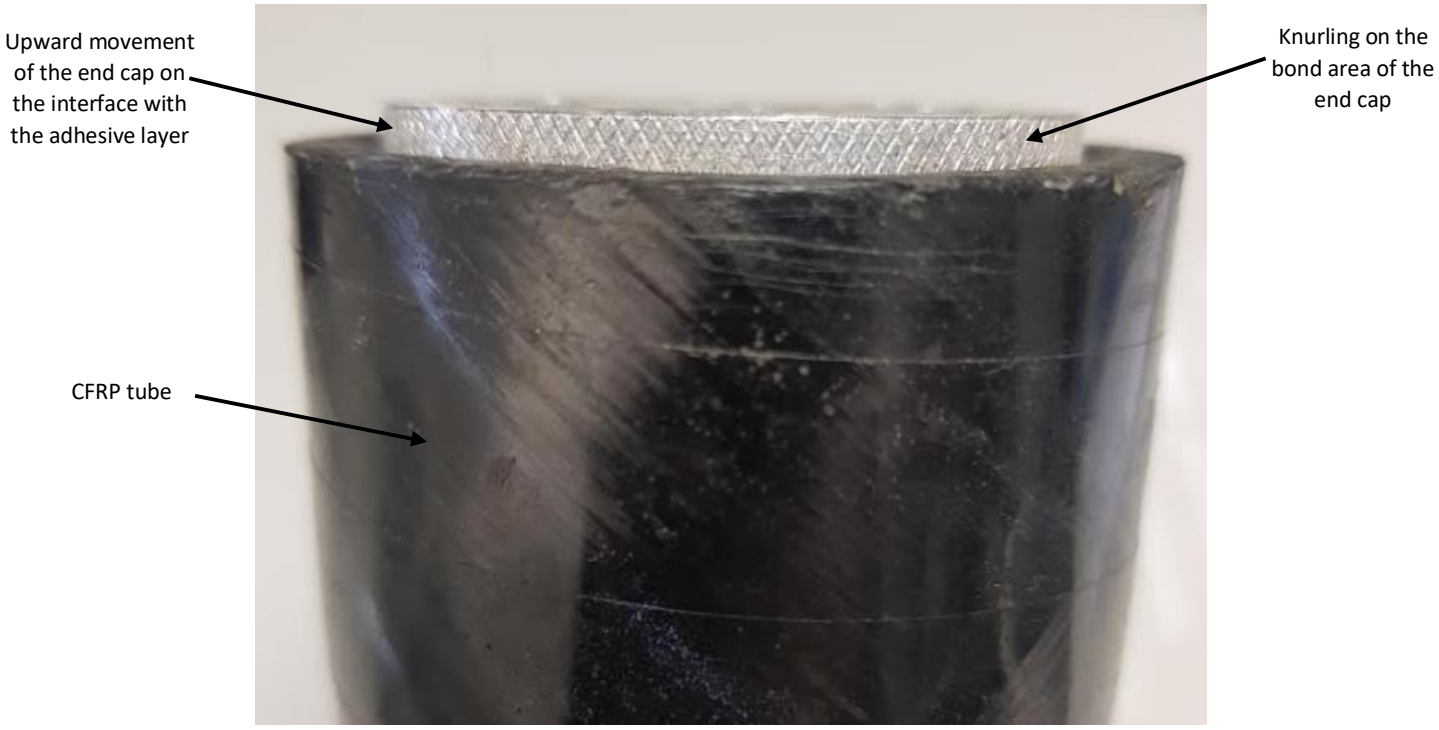

Figure 5.80: Photograph showing shear failure on the end cap to adhesive layer interface for a 4 mm vessel

However, vessel number 2 experienced multiple modes of failure as shown in Figure 5.81. This was similar to what was experienced by vessel 3 from the first set of CFRP pressure vessels (see Figure 5.75).

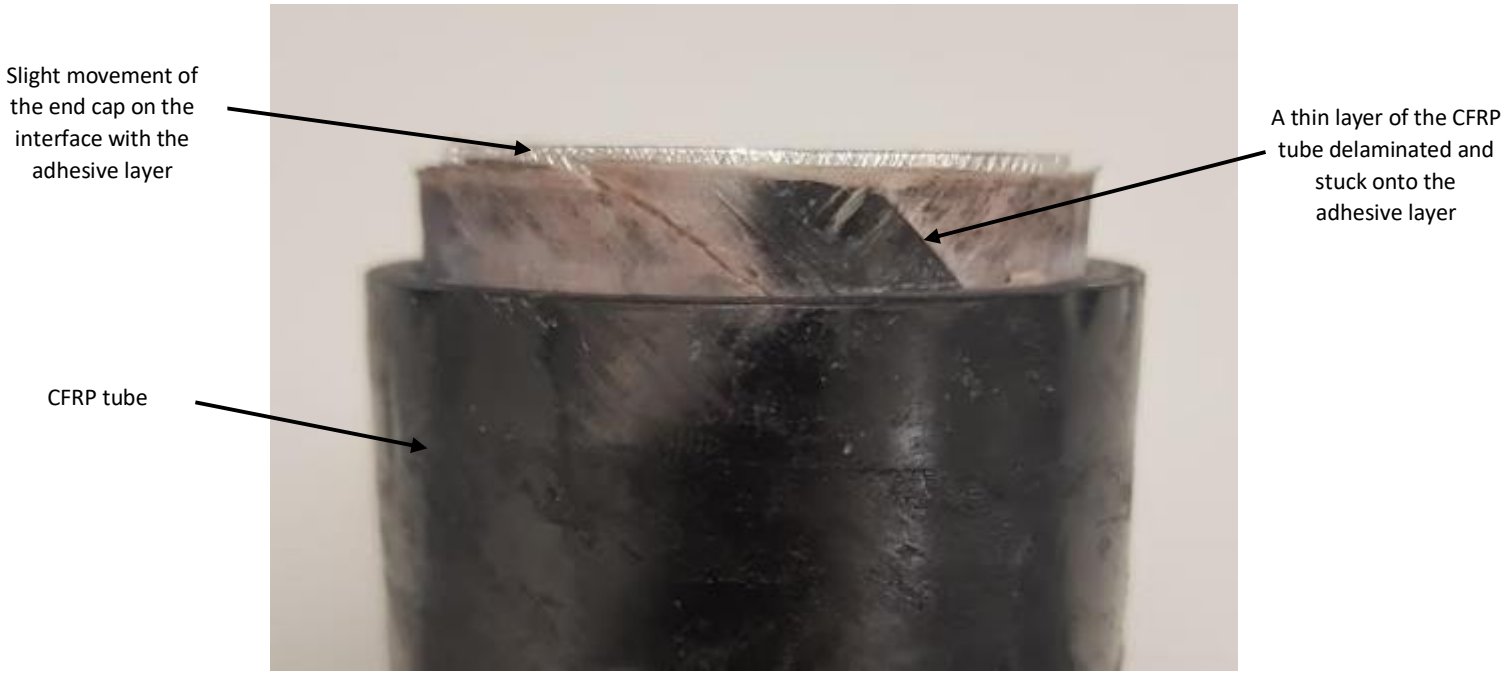

Figure 5.81: Photograph showing multiple modes of failure modes for a 4 mm CFRP pressure vessel

It was highly likely that the initial mode of failure was the partial shear failure on the end cap to adhesive interface which caused the end cap to move upwards slightly. Just like the case of vessel 3 from the first set, what followed was probably a combination of shear failure on the adhesive layer to CFRP tube wall interface and delamination. The delamination was seemingly not as significant as the shear failure on the adhesive to tube wall interface as only a small portion of the thin layer CFRP material remained stuck onto the adhesive layer as shown in Figure 5.81. The multiple modes of failure on both interfaces with the adhesive layer (shown in Figure 5.81) was different to what transpired during the end cap adhesive shear tests described in section 5.2. The reason for this difference was likely because the CFRP was expanding in the hoop direction in the burst pressure tests unlike in the end cap adhesive shear tests where the only type of loading on the adhesive layer was shear.

Table 5.25 provides a summary of the recorded hydrostatic burst test results. In addition, the equivalent shear strength values were calculated using the failure pressures as shear was considered to be the predominant mode of failure.

Table 5.25: Failure results of the five 4 mm CFRP pressure vessels

Vessel No	Failure Pressure [bar]	Max Design Pressure [bar]	End cap adhesive shear strength [MPa]
1	425	189	12.6
2	430	191	12.8
3	450	200	13.4
4	430	191	12.8
5	410	182	12.2
Average	**429**	**191**	**12.8**
Standard deviation	**12.8**	**5.7**	**0.39**

Comparing the determined mean shear strength of SpaBond 340 LV from Table 5.25 (12.8 MPa) with the one from the third end cap shear test (13.3 MPa) showed only a 4% difference in the values. The predominant failure mode for the 4 mm CFRP vessels was shear failure which was indication that the pressure at which the CFRP tube section would burst was not reached.

The observed failure pressures for the five 4 mm CFRP pressure vessels ranged in the narrow band of pressures between 410 bar and 450 bar with a mean value of 429 bar. The mean maximum design pressure was determined to be 191 bar with a small standard deviation that was only 3 % of the mean. The predicted burst pressures for the 4 mm CFRP pressure vessels (from Table 5.22) using the four failure theories are shown in Table 5.26.

Table 5.26: Predicted burst pressures for 4 mm CFRP tube using the initial strength properties from the tensile tests

Failure theory	**Predicted Burst Pressure [bar]**	**Average Failure Pressure [bar]**
Maximum Stress	360	429
Maximum Strain	500	
Tsai-Hill	327	
Tsai-Wu	344	

The predictions were made using the initial strength properties determined from the tensile tests in section 5.1. The actual mean failure pressure exceeded the predictions (with the exception of the Maximum Strain failure theory) by a significant margin. Again, this was an indication that the initial burst pressure predictions were conservative.

5.3.2.2 Results on strain measurements from the second set of burst tests

As was the case with the results of the failure pressures for the second set of pressure vessels, the results of the strain measurements are presented separately for the 2 mm and 4 mm pressure vessels. The graphs for the measured strains against the applied pressure are plotted and described accordingly.

2 mm pressure vessels

The graph in Figure 5.82 displays the longitudinal strain response of the five 2 mm CFRP pressure vessels. It was observed that all five curves were initially linear in the range from 0 bar to about 160 bar of internal pressure. The stiffness (i.e. inverse of the gradient) was constant for that range. It was also observed that all five pressure vessels displayed the same deformation behaviour as the shape of each of the curves was approximately the same. In that range, the strains on the best fit line were in close agreement with the measured longitudinal strains. Above 160 bar, the value of the gradient of the curves started to increase, and they became non-linear, which meant that the stiffness started to decrease. The decrease in stiffness probably signified the onset of some form of damage sustained by the CFRP tube that continued until the vessels eventually failed. Additionally, the variation between the curves started to increase noticeably the further the pressure rose beyond 160 bar.

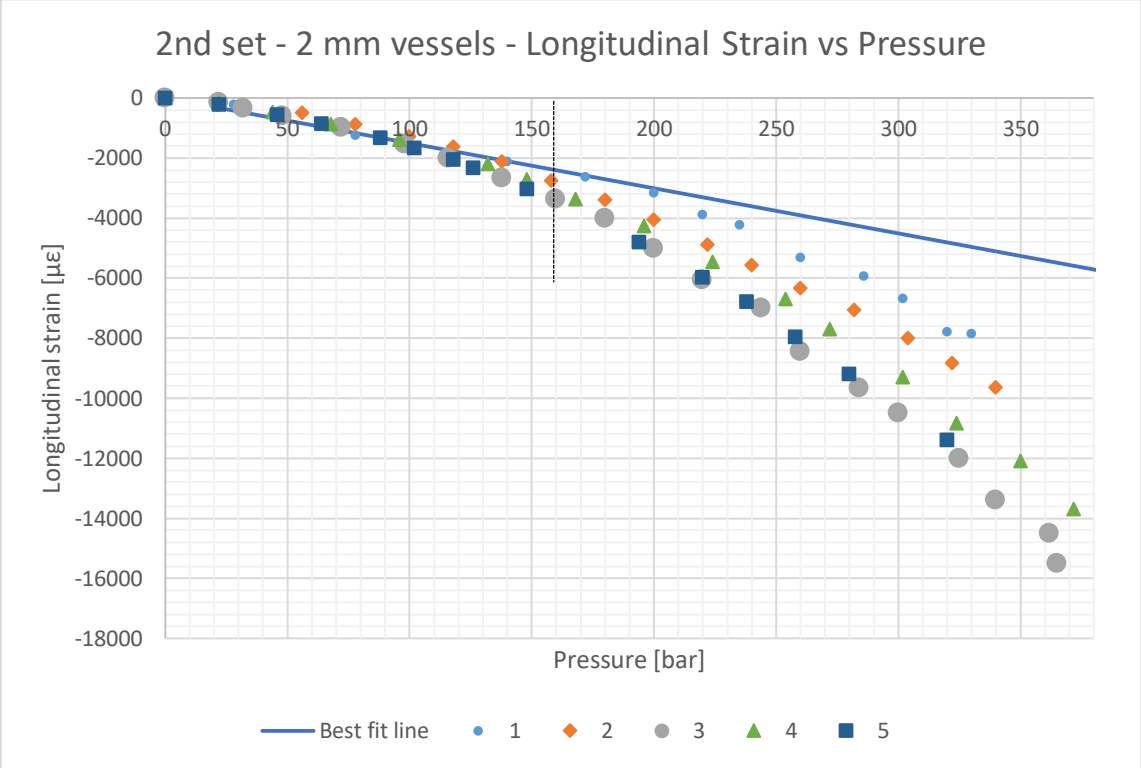

Figure 5.82: Graph of longitudinal strain vs pressure for five 2 mm vessels from the second set

The graph of the hoop strain against the pressure for the five 2 mm CFRP pressure vessels is shown in Figure 5.83. For all tests, up to approximately 200 bar, all pressure vessels exhibited a linear relationship between the applied pressure and the measured hoop strain.

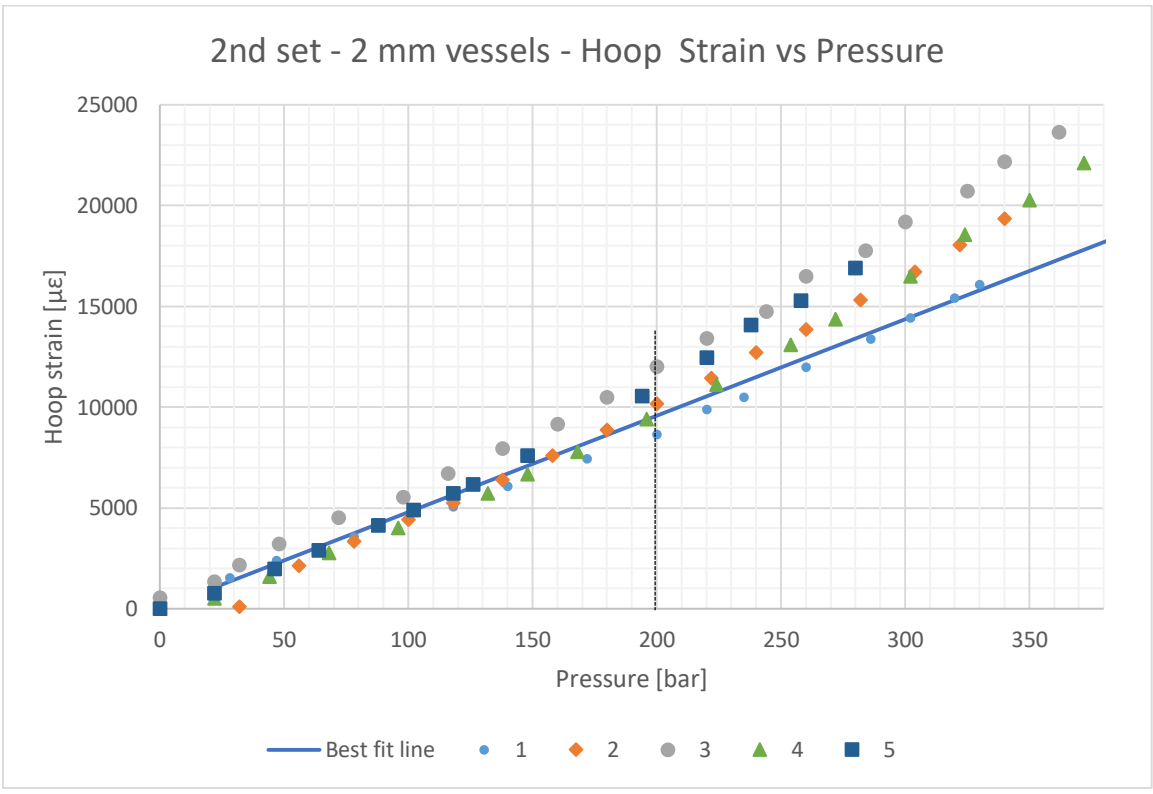

Figure 5.83: Graph of hoop strain vs pressure for five 2 mm vessels from the second set

Above 200 bar, the gradient started to increase. This non-linearity was not as pronounced as witnessed for the longitudinal strain behaviour according to the graph in Figure 5.83. Therefore, the start of the decrease in stiffness in the hoop direction manifested at a slightly later pressure than in the longitudinal direction.

4 mm pressure vessels

Figure 5.84 shows the longitudinal strain behaviour for the five burst tested 4 mm CFRP pressure vessels under the effect of the applied pressure. In the longitudinal direction, all pressure vessels exhibited the same deformation behaviour as the curves had the same trend. Up to approximately 250 bar, all the curves were observed to have a linear trend after which, the graphs started to curve downwards as the gradients started increasing (negatively) which corresponded to a decrease in stiffness. The best fit line was only in close agreement with the measured longitudinal strains for pressures below approximately 250 bar. This is the region where the five vessels showed a linear longitudinal strain behavioural response. Therefore, damage seemed to commence at a later stage for the 4 mm vessels than the 2 mm vessels. This was probably because they were thicker and therefore, stronger than the 2 mm vessels.

Alternatively, no significant decrease in longitudinal stiffness was observed in the first set of 4 mm CFRP pressure vessels as seen in Figure 5.76. This was likely because the highest pressure reached for the first set of 4 mm vessels was 220 bar. That failure pressure fell short of 250 bar which is when the damage was observed to commence for the second set of 4 mm CFRP pressure vessels.

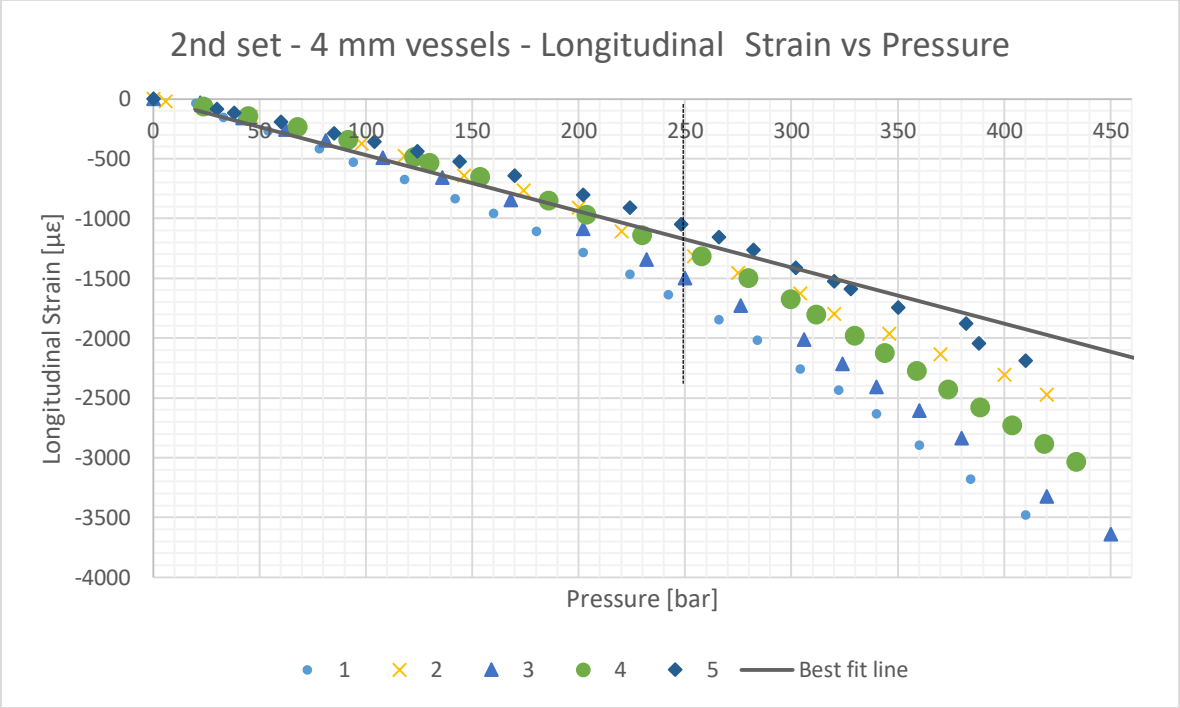

Figure 5.84: Graph of longitudinal strain vs pressure for five 4 mm vessels from the second set

In the hoop direction, the strain measurements for the five pressure vessels (see Figure 5.) exhibited the same deformation behaviour and had the same linear trend for pressures below 280 bar.

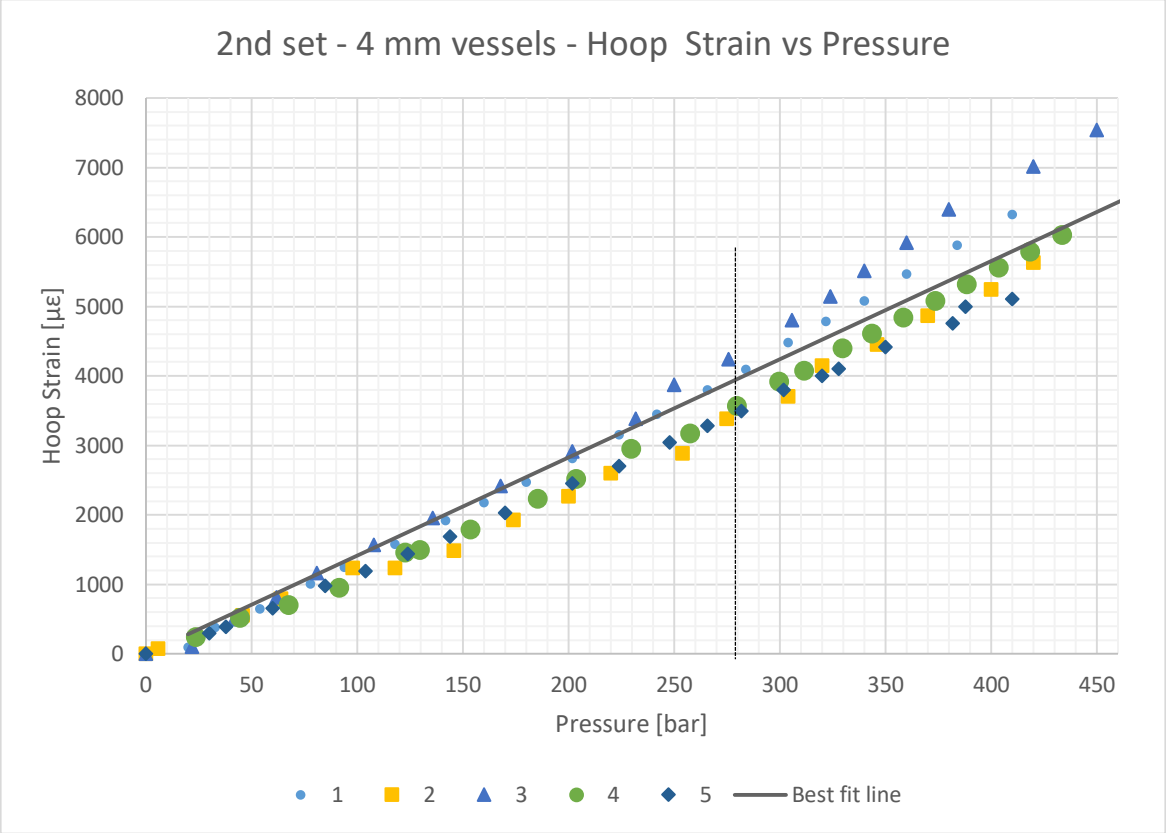

Figure 5.85: Graph of hoop strain vs pressure for all five 4 mm vessels from the second set

Beyond 280 bar, the gradients started to increase albeit gradually which suggested the onset of damage of the CFRP tube. Similar to the graph of the longitudinal strains for the 4 mm vessels (in Figure 5.84), the data points for the pressure vessel agreed more with the predicted strain data below this point. The stiffness was observed to start becoming non-linear at a higher pressure in the hoop direction than the longitudinal direction. Therefore, in both cases of the second set of 2 mm and 4 mm CFRP vessels, the stiffness started to decrease (or the onset of the damage occurred) at a higher pressure for the hoop direction than the longitudinal direction.

5.3.2.3 Discussion of the second burst test results

Failure pressures of the 2 mm pressure vessels

Achieving bursting or failure of the CFRP tube section for all 2 mm CFRP vessels meant that the adhesive layer on the end caps was able to withstand the shear force exerted on them because of the internal pressure. The predicted burst pressures (from Table 5.24) for the 2 mm CFRP pressure vessels were all found to be lower than the tested results. The Tsai-Hill and Tsai-Wu failure theories were chosen as the references to which the actual burst strength values of the vessels were compared. This was because of their expected higher levels of accuracy in predicting the burst strengths of CFRP cylindrical pressure vessels as compared to the Maximum Stress and Strain failure theories [3, 4, 105]. The burst pressures predicted by the Tsai-Hill and Tsai-Wu failure theories (i.e. 160 bar and 169 bar respectively) were very conservative in comparison with that minimum observed burst pressure value of 330 bar. This result established that the initial strength property estimates (σ_1 and σ_2) of the CFRP were too low as suspected in section 5.1.2.

While the CFRP tube section cracked for most of the tested 2 mm CFRP vessels, one of them (i.e. Vessel 4) failed due to delamination at the adhesive layer to CFRP tube wall interface after having initially experience bulging of the type shown in Figure 5.79. The bulging could only have been possible if the CFRP tube section was expanding in the hoop direction significantly more than the aluminium end cap. Because the portions of the CFRP tube at both ends were bonded to the adhesive layer on the end caps, they could not deform as much as the CFRP tube portion in between the end caps. This resulted in the adhesive layer being put under tension at its interface with the internal wall of the CFRP tube. The tensile load could then have caused the inter-laminar failure of the CFRP tubes laminate structure thereby resulting in the thin layer of CFRP being stuck on the adhesive layer (see Figure 5.79).

Failure pressures of 4 mm pressure vessels

The predominant failure mode for the second set of 4 mm CFRP pressure vessels was shear failure on the end cap to adhesive layer interface. As such, the pressure at which the CFRP tube would burst was not reached. This established that the 4 mm CFRP tubes would burst at a mean pressure of not less than 429 bar which meant that they were also stronger than initially predicted. The mean failure pressure of 429 bar was indicative of the pressure at which the adhesive bond layer failed since it was predominant failure mode. The shear stress on the SpaBond 340 LV adhesive at that pressure was calculated to be 12.8 MPa (Table 5.25). This was only 0.5 MPa smaller than the mean shear strength value from the third end cap shear tests. This minor difference may have been because there was an additional hoop stress acting on the CFRP tubes that were burst tested while there was only a pure shear load for the end cap adhesive shear tests.

Strain measurements from the second set of burst tests

For the second set of CFRP pressure vessels, it was observed that the strain response for the CFRP tubes was initially linear showing a constant stiffness up to a certain pressure. Then it was observed that the stiffness started to decrease with the responses becoming increasingly non-linear. For the 2 mm CFRP vessels, the decrease in stiffness started at a pressure of approximately 160 bar and it occurred at about 250 bar for the 4 mm CFRP vessels. The decrease in stiffness could have been caused by the onset of damage in the CFRP tubes' laminate structures which could have come in the form of localised fibre breakage, cracking due to matrix failure transverse to the fibre direction on a microscale, etc. From the point the damage commenced, as the pressure increased, the stiffness continued to decrease showing more damage occurring in the CFRP tubes until they failed. It should be noted that damage in both 2 mm and 4 mm CFRP tubes started at an earlier pressure in the longitudinal direction than in the hoop direction. This strongly suggested that both types of CFRP tubes were stronger in the hoop direction than in the longitudinal direction. Since the winding angle was 50^{o}, it followed that the fibres were more skewed towards the hoop direction than the longitudinal direction. This would have meant that the CFRP tube had a higher strength to stress ratio in the hoop direction than in the longitudinal direction.

It should be noted that the mean value of the determined maximum design pressure of the 2 mm vessels (157 bar) was within the linear region of the longitudinal strain vs pressure graph in Figure 5.82. It was therefore reasonable to conclude that the maximum design pressure for the 2 mm vessels was safe enough to reach without compromising the safety of the vessel. For the 4 mm vessel, the maximum design pressure from the burst test was 191 bar which also fell within the linear region of the longitudinal strain vs pressure plot in Figure 5.84. Therefore, it was also a safe pressure to reach for the 4 mm CFRP vessel to reach. However, the maximum design pressure of 191 bar was derived from predominant shear failures of the end caps and not the bursting of the CFRP tubes. The damage

in the 4 mm CFRP tubes only started occurring at approximately 250 bar suggesting that the 4 mm CFRP pressure vessels could operate safely to a higher pressure than the one determined from the burst tests. This decrease in stiffness behaviour was not observed at all in the first set of 4 mm vessels. They only exhibited a linear deformation behaviour probably because they all failed at pressures below 220 bar.

5.4 Hydraulic proof test

One of each of the 2 mm and 4 mm CFRP pressure vessels were constructed and underwent hydraulic proof tests as per the procedure detailed in section 4.3.2. The purpose of the test was to assess the reliability and the ability to retain pressure for the two types of vessels.

5.4.1 Results

The requirements for the proof test necessitate that the pressure of the vessel be held at the proof pressure for at least 30 minutes before dropping and holding it at the design pressure for a further 10 minutes. However, the tests were performed for a longer duration of just over 24 hours. The vessels were kept at their respective proof pressures for 30 mins before being dropped and left at the respective design pressures for the remaining 24 hours. The pressure was kept at the respective design pressures for 24 hours to assess the ability of the rubber liner to prevent leakage of water over a longer period than the 10 minutes that were suggested. Table 5.15 summarises the results of the proof test. It should be noted that the design pressures for both types of pressure vessels were the minimum values determined from the second set of hydrostatic burst tests i.e. 147 bar for the 2 mm vessel (Table 5.23) and 182 bar for the 4 mm vessel (Table 5.25).

Table 5.27: The respective design and proof pressures of the 2 mm and 4 mm CFRP pressure vessels

Type of pressure vessels	**Maximum Design Pressure [bar]**	**Proof pressure [bar]**
2 mm vessel	147	184
4 mm vessel	182	228

No damage or leaks were observed in either type of vessels at the proof and design pressures. This indicated that the vessels were able to retain pressure and were reliable based on that criteria. After cutting the 2 mm CFRP pressure vessel in half along its axis as shown in Figure 5.87, there were no visible signs of damage on the rubber liner.

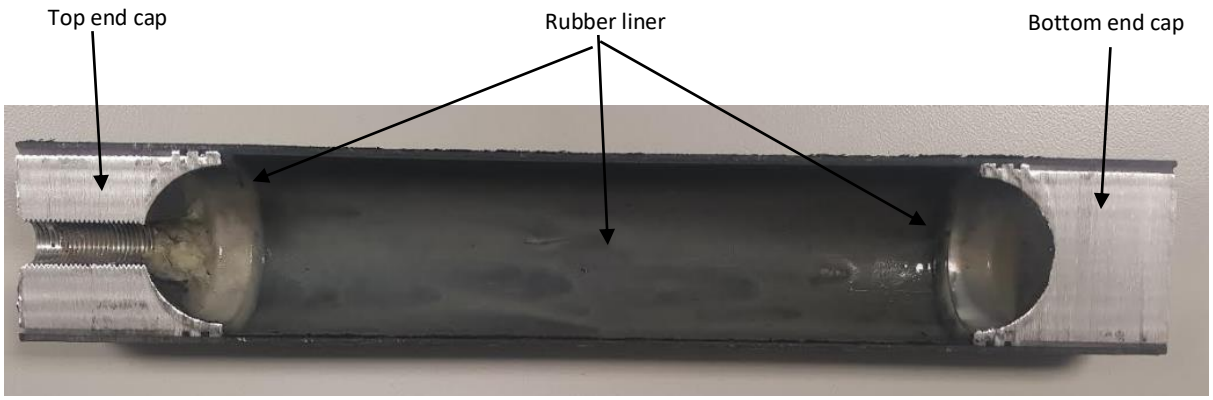

Figure 5.86: Photograph of the cross section of a 2 mm CFRP pressure vessel used during the hydraulic proof tests

5.4.2 Discussion

Both types of vessels managed to hold test and working pressures without failure, leakage or any visible permanent deformation. Hence, both vessels successfully passed the test which meant the rubber liner and the end caps were able to sufficiently seal the pressure vessels thereby preventing the leakage of water.

5.5 Long term gas leak testing

The objective of the long-term gas leak test was to assess the ability of the CFRP pressure vessel to prevent leakage of a gas at the design pressure i.e. testing for long periods with a compressible fluid.

5.6.1 Results

Before the first leak tests, the 2 mm and 4 mm CFRP pressure vessel specimens had to be hydrostatically proof tested to check if they could safely maintain the respective design pressures. These proof tests described previously were performed successfully without any leaking or failure occurring. Initially, a gas leak test with only the steel pipe network setup was also performed for a period of 120 hours (5 days). This was to ensure that they were no leaks from the joints or pipes that would interfere with the leak test for its duration when the CFRP pressure vessels were connected instead. The leak tests were then performed on four vessels at their respective design pressures according to the stipulated requirements (see section 4.3.3.1). The leak test results are summarised as shown in Table 5.28.

Table 5.28: Long term gas leak test result for the CFRP pressure vessels

Type of vessel	Vessel Number	Test Number	Duration of test [hours]	Leak test pressure [bar]		Average leak rate [bar/hour]
				Initial reading	Final Reading	
2 mm vessels	1	1	48.75	146	130	0.328
		2	0.72	144	130	19.4
	2	1	46	146	136	0.217
		2	0.17	146	130	94.1
4 mm vessels	1	1	65	172	100	0.947
		2	8.45	172	0	20.3
	2	1	17.1	160	104	3.27
		2	0.42	174	152	52.4

It was observed that for all four vessels, there was leaking which varied between 0.328 bar/hour to 3.27 bar/hour for the first test run. A soapy water solution had been applied on both ends of all vessels as well as on the CFRP tube section prior to the start of the test. In all cases, bubbling was observed and appeared to be more concentrated on the adhesive layer between one of the end caps and the internal CFRP tube wall as shown in Figure 5.87.

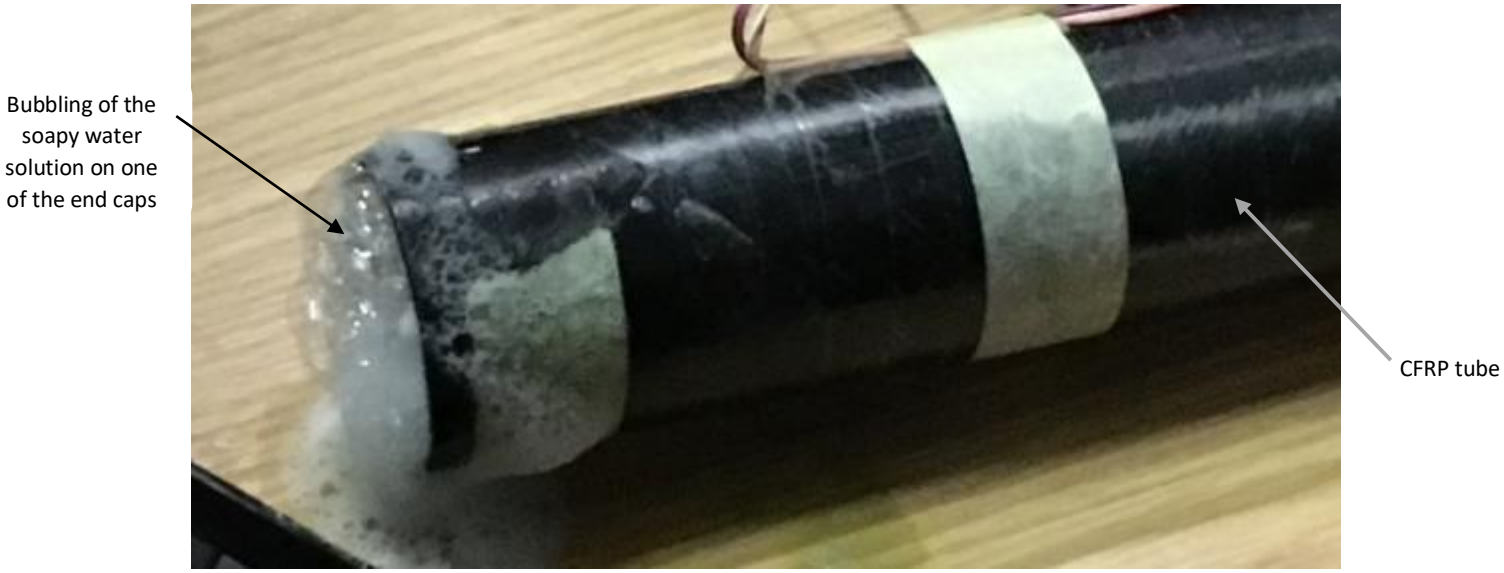

Figure 5.87: Photograph showing bubbling of the soapy water solution at one of the ends of a CFRP pressure vessel

However, significantly higher leak rates of at least 19 bar/hour were observed for the second test runs (i.e. tests with number 2 from Table 5.28). The bubbling for those second leak test runs were more aggressive indicating the leak rates were also higher. It should be noted that there was no obvious deformation or movement of end caps observed during and after the testing.

Three of the four vessels were cut in half in a direction parallel to the axis of the CFRP cylindrical pressure vessel for visual inspection. An example is the cut 2 mm CFRP pressure vessel shown in Figure 5.88. What is apparent is the bubbles (white spots) of trapped air underneath the rubber liner in this case. They appeared to be concentrated near the bottom end cap where the bubbling was observed.

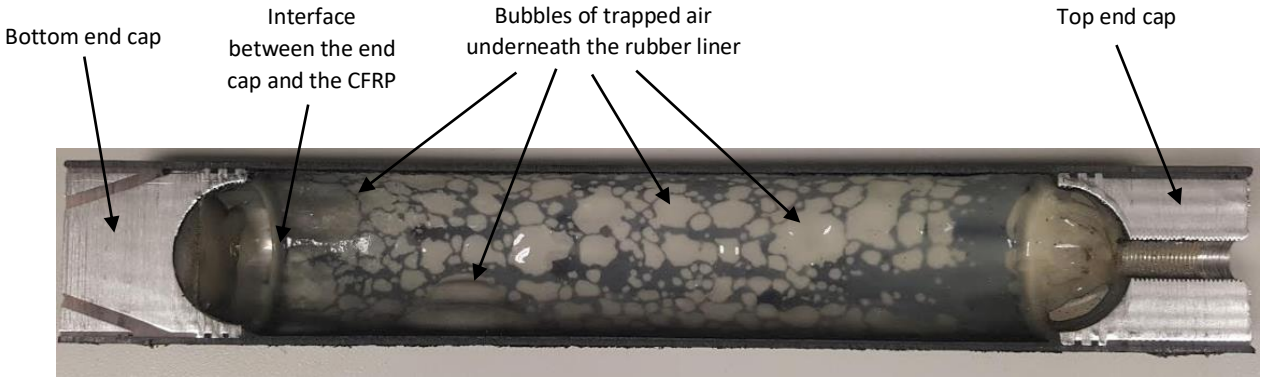

Figure 5.88: Photograph of the cross section of a 2 mm CFRP pressure vessel used during the long term leak tests

The rubber liner did not seem obviously damaged at that location, however, air must have leaked through it on its way to the outside of the vessel past the two O-rings and the adhesive layer. It was observed the portion of the rubber liner on the interface between the end cap and the CFRP tube appeared thinner as if it had been stretched causing it to weaken as shown in Figure 5.89.

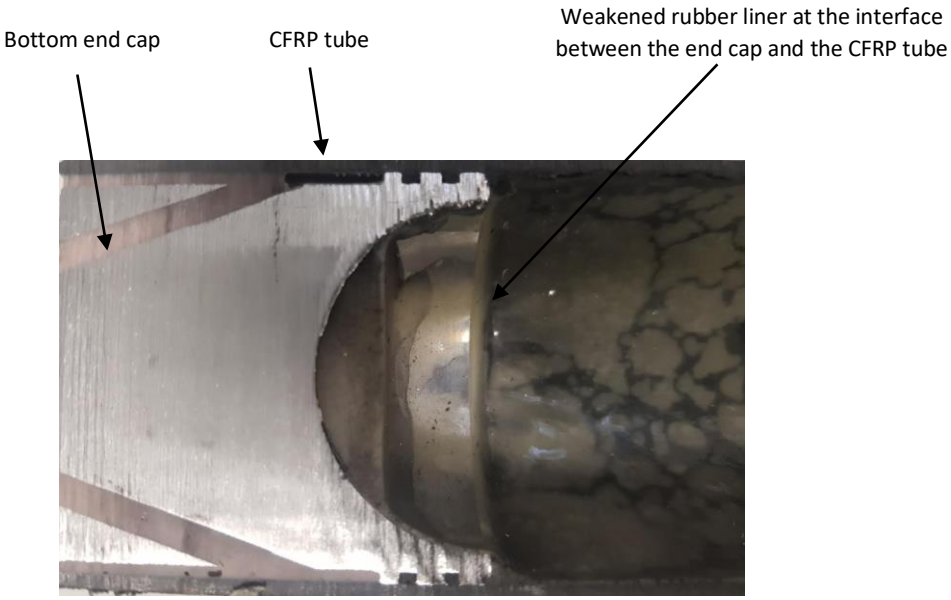

Figure 5.89: Photograph showing the region near the bottom end cap in greater detail

This weakening of the rubber liner could have caused it to be porous which likely allowed more air molecules to escape through. It should be noted that the weakening of the rubber liner was not observed in a similar 2 mm CFRP pressure vessel that was proof tested with water (see Figure 5.86).

5.6.2 Discussion of the results

The use of soapy water allowed for the identification the source of the leaking. In all the test runs, the sources of leaking were at the ends of each vessel past the adhesive layer as shown in Figure 5.87. No bubbling was observed from the CFRP tube section between the two end caps. This does not mean that there was no leaking emanating from the CFRP tubes of each vessel as leaking may have been taking place at a sufficiently slow rate that no discernible bubbling could be observed.

The portion of the rubber liner on the interface between the end cap and the CFRP tube appeared thinner and weakened. The cause of this may have been some of air that did not escape through the gap between the end cap and the CFRP tube but remained and likely peeled off the rubber liner from the tube wall before forming trapped bubbles underneath it as shown in Figure 5.88. As the vessel was being pressurized, more trapped air seemed to build up and then proceeded to peel off the liner from the CFRP tube wall in several locations to form those bubbles or trapped air pockets. The trapped air pockets appeared to have stretched the rubber liner in those locations thereby weakening it. The tensile strength of the VytaFlex 60 series rubber is approximately 6 MPa which is less than half of the design pressures for the two vessels tested (14.7 MPa and 18.2 MPa). Therefore, it was probable that the exposed rubber liner was stretched beyond its elastic limit. The bubbles were more concentrated near the interface between the CFRP tube and the end cap where bubbling was observed (see Figure 5.88). This suggested that at that the interface was the most likely location where most of the air escaped past the rubber liner. This was reasonable to assume as it was established that the CFRP tube expanded (although slightly) more in the hoop direction than the end cap which would have exposed that interface as shown in Figure 5.90.

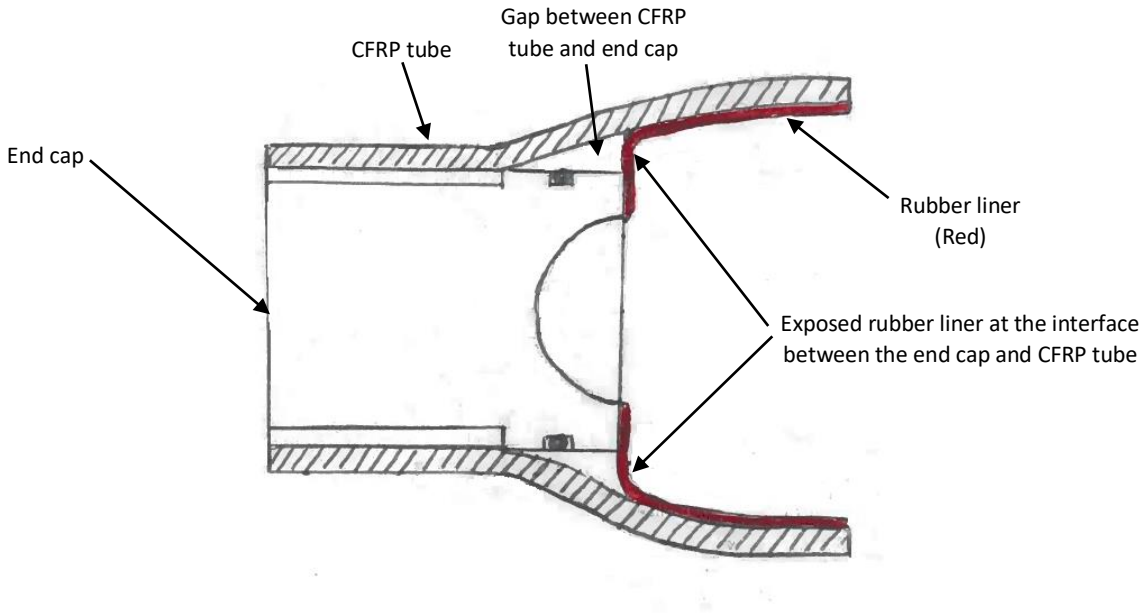

Figure 5.90: Schematic illustrating what likely occurred at the interface between the end cap and CFRP tube during the long-term gas leak test

The stretching effect likely weakened or split the rubber liner sufficiently to let the pressurised air to escape. The incompressible nature of water may have protected the rubber liner once water had leaked through the liner (into the gap shown in Figure 5.90) during the hydraulic proof tests by preventing further damage. This may explain why no leaks were detected during the proof tests. Alternatively, because some of the air managed to bypass the two O-rings and the adhesive layer to the outside, it suggested the two O-rings were also ineffective in sealing the vessel.

It was observed that for each vessel's second leak test run, the average leak rates were significantly higher (see Table 5.28). This trend was the same for all four vessels tested although the average leak rate values varied considerably. Therefore, it was possible that the portion of the rubber liner could have been further weakened after pressurization during the second test runs. It was possible that the holes/gaps in the rubber liner could have been enlarged as a result.

According to a report by Bigelow [129], the maximum acceptable leakage rate for a 350 bar hydrogen pressure vessel is 0.025 g/hour/kg of Hydrogen gas. Considering the lower design pressures of the two types of vessels and their volumes while assuming that hydrogen is an ideal gas, the maximum acceptable leakage rate was determined to be approximately 0.00455 bar/hour for both vessels (see Appendix D for detailed calculations). However, the average leak rates were at least 50 times higher than this value. Furthermore, air which has many larger molecule gases than hydrogen (e.g. oxygen and carbon dioxide). It was therefore reasonable to assume that if a small molecule gas like hydrogen or helium gas was used, the average leak rates would be higher. It could then be reasonably concluded that the rubber liner was ineffective as the primary sealant in preventing leakage of air out of the vessels.

5.7 Analysis of CFRP pressure vessel design based on experimental results

This section describes the process that was followed in critically analysing the experimental results in relation to the how the CFRP pressure vessel was designed. The second objective would also be to relate the design assumptions with the actual behaviour of the CFRP pressure vessel observed through various tests.

5.7.1 CFRP material properties

The CLT based calculations used the initial material stiffness and strength property values of the CFRP tube that were determined from the tensile tests in section 5.1. This section aims to describe how those initial property values were updated using the hydrostatic burst test data.

5.7.1.1 Stiffness properties

First set of CFRP vessels

The CLT based calculations in section 3.1.3 used the initial material stiffness property values (E_1 and E_2) from the tensile test data. The strain values that were measured during the hydrostatic burst test for the first set of vessels allowed for those initial estimated stiffness properties to be compared with. Therefore, the elastic moduli values were adjusted such that the CLT based equations would give strain values similar to what was given by the best fit lines for the longitudinal and hoop directions (from Figure 5.76 and Figure 5.77 respectively). This step was performed for both the first and second set of CFRP pressure vessels. The elastic moduli values that were found to give the same average deformation response in the hoop and longitudinal direction as the first set of 4 mm CFRP tubes are shown in Table 5.29.

Table 5.29: First set of the updated stiffness property values for the CFRP tube

Property	**Symbol**	**Initial Estimate Values**	**Updated Values**
Longitudinal Elastic Modulus	E_1	109 GPa	140 GPa
Transverse Elastic Modulus	E_2	6 GPa	9 GPa

These updated longitudinal and transverse elastic moduli were higher than the initial estimates. This shows that the initial stiffness values were conservative. Therefore, the first set of three 4 mm CFRP pressure vessels were stiffer than designed in both orientations i.e. in the fibre direction and in the direction transverse to the fibres. The first set of 4 mm CFRP tubes used in the hydrostatic burst test were constructed using a standard industrial automated filament winding process. This meant that manufacturing inconsistencies and errors should have been kept to a minimum. However, this data that was used to update the stiffness values was derived from only three CFRP pressure vessel specimens. To improve the data, strain measurements were taken from the second set of tested CFRP vessels.

Second set of CFRP vessels

The linear portions of the strain vs applied internal pressure graphs for the second set of 2 mm and 4 mm CFRP vessels using Figure 5.82 to Figure 5. were used in determining the second set of updated stiffness values for the CFRP tube's material. This information is shown in Table 5.30 where it is compared with the first set of updated stiffness values.

Table 5.30: Second set of updated stiffness property values of the CFRP tubes

Property	**Symbol**	**First Set of Updated Values**	**Second Set of Updated Values**
Longitudinal Elastic Modulus	E_1	140 GPa	130.2 GPa
Transverse Elastic Modulus	E_2	9 GPa	10 GPa

There were small differences in the two elastic moduli values between the first and second update likely because the CFRP tubes were derived from different tubes. This may have been partially responsible for the slight variation in the values. For the linear portion of the strain responses of the

vessels, these updated stiffness properties as well as the CLT calculations could be used to predict the behaviour of any CFRP tube with different fibre winding angles, wall thicknesses, etc for the same type of CFRP material, laminate structure and manufacturing process.

5.7.1.2 Strength properties

The second set of 2 mm CFRP pressure vessels were the only vessels that experienced failure of the CFRP tube section during the burst tests. Therefore, they provided the only set of results that could be used to determine the actual strength property values that would update the initial estimated values from the tensile tests. Because, the UTS for the direction transverse to the fibres was suggested as the most conservative value in the design chapter, it was the property that was primarily adjusted until the predicted burst pressures for the Tsai-Hill and Tsai-Wu failure theories were approximately equal to 330 bar. The burst pressure of 330 bar was chosen because it was the minimum burst pressure observed for all 2 mm pressure vessels from Table 5.23 The burst pressures were calculated again using the failure theories' equations and the local stresses calculated using the CLT equations to give the new predicted burst failure pressures as shown in Table 5.31.

Table 5.31: Second predictions of burst pressures for the 2 mm CFRP vessels using updated strength properties

Failure theory	**Predicted Burst Pressure [bar]**	**Actual Burst Pressure [bar]**
Maximum Stress	415	330
Maximum Strain	820	
Tsai-Hill	324	
Tsai-Wu	346	

The updated strength properties that resulted in these new set of predicted pressures are shown in Table 5.32 and were compared with the initial strength property values from the tensile tests:

Table 5.32: Updated strength property values based on the 2 mm CFRP vessel's burst test compared to the initial values from the tensile tests

Property	**Symbol**	**Initial values [MPa]**	**Updated values [MPa]**
Ultimate Tensile Strength in the 0^{O} direction	$\sigma_{1\text{-uts}}$	1357	1650
Ultimate Tensile Strength in the 90^{O} direction	$\sigma_{2\text{-uts}}$	14.8	50

In both loading directions, the initial strength property values proved to be lower especially in the direction transverse to the fibres where the updated value of the UTS was more than three times the initial value. The updated values were also found to be similar to the values for typical standard CFRP composites with similar constituent materials e.g. 1500–2000 MPa for $\sigma_{1\text{-uts}}$ and 50–65 MPa for $\sigma_{2\text{-uts}}$ according to the sources [3-4, 81, 95].

Although none of the 4 mm CFRP tubes burst, their predicted burst pressures could now be estimated using these updated strength values. It was assumed that the 2 mm CFRP tubes had essentially the same strength properties as the 4 mm CFRP tubes as they were manufactured using the same process, type of fibres and epoxy resin at the same time. Using the updated strength properties, the predicted burst pressures for the 4 mm CFRP tubes are listed in Table 5.33.

Table 5.33: Predicted burst pressures for the 2 mm CFRP vessels using the updated strength properties	
Failure theory	**Predicted Burst Pressure [bar]**
Maximum Stress	606
Maximum Strain	1150
Tsai-Hill	584
Tsai-Wu	624

With the exception of the Maximum Strain failure theory prediction, the other three failure theories predicted a burst failure pressure in the range between 584 bar and 624 bar for the 4 mm CFRP tube. Thus, considering burst failure of the CFRP tube section, the maximum design pressure for the 4 mm CFRP pressure vessel would be between 259 bar and 277 bar. Alternatively, the longitudinal strain vs pressure graph for the second set of 4 mm of CFRP pressure vessels suggested that the 4 mm tubes started sustaining damage at approximately 250 bar. Therefore, to obtain a maximum design pressure of 250 bar, this corresponds to a burst pressure of approximately 563 bar for the 4 mm CFRP pressure vessel which was reasonably close to and consistent with the predictions of the three failure theories.

5.7.2 End cap design

The end cap was designed mainly to close off the ends of the CFRP tube and form a closed pressure vessel. To bind them to the two ends of the internal wall of the CFRP tube required an adhesive (SpaBond 340 LV) and it had to be sufficiently strong in shear to be able to resist the load due to the pressure. To determine the actual shear strength of the adhesive, end cap adhesive shear tests were performed. All three end cap adhesive shear tests (section 5.2) indicated that shear failure only occurred at the interface between the end cap and the adhesive layer. This was not observed in two of the hydrostatic burst tests where the pressure vessels experienced shear failure and delamination on the interface between the adhesive layer and the CFRP tube.

For the end cap adhesive shear tests, the adhesive layer was loaded to cause pure shear which led to failure at the interface between the end cap and the adhesive layer. However, for the burst tests, the adhesive layer experienced multiple loads including expansion of the CFRP tube in the hoop direction in addition to the shearing force due to the internal pressure. In the hoop direction, the CFRP tube expanded more than the end cap. This subjected the adhesive layer to a tensile load which is what eventually caused some CFRP delamination as illustrated by Figure 5.79. Initially during the design phase, it was assumed that because the CFRP tube was significantly stiffer than the aluminium end cap, the end cap would always be “pressed up” against the internal wall of the CFRP tube because of the hemispherical dome.

5.7.3 Rubber liner

In the hydraulic proof tests, no leaking of water was observed for both the 2 mm and 4 mm CFRP pressure vessels for a period of approximately 24 hours. Therefore, this meant that the rubber liner was successful as the primary seal in preventing water from leaking to the outside of the vessel(s). However, for the long-term gas leak tests, all four vessels tested showed signs of leaking meaning the rubber lining was unable to prevent pressurized air from leaking to the outside of the vessel. The rubber liner showed signs of weakening at the gap/interface between the end cap and the CFRP tube as it was thinner which probably made it possible for more air to escape through. The differential expansion of the end cap and the CFRP tube was identified as the likely location where most of the air escaped through the liner. The second test runs may have exacerbated the damage on the rubber

liner resulting in the drastic increase in leak rates of (from Table 5.28). Therefore, the rubber liner was likely only suited for an incompressible fluid like water rather than a compressible fluid such as air.

5.8 Optimisation of the filament winding angle

In the design chapter, the optimal filament winding angle was determined by using the Maximum Stress failure theory for laminated composites. Some of the reasons it was the chosen failure theory was because it was a simple method to apply. Because the initial estimate of the strength property value transverse to the fibres was very low, it was assumed that it was probably the most likely mode of failure for the CFRP pressure vessel. The optimum filament winding angle that would result in the highest failure strength for the CFRP tube was 52° based on the Maximum Stress failure theory.

Alternative failure theories including Tsai-Hill and Tsai-Wu failure theories are deemed as more accurate in predicting the burst failure pressure of the CFRP tube section of the pressure vessel according to several literature sources [3, 106]. After determining the validated strength property values from the burst test results, the Tsai-Hill and Tsai-Wu failure theories were then used to determine the optimum filament winding angle for the CFRP pressure vessel by plotting a graph of the anticipated burst pressure against the winding angle as shown in Figure 5.91. The Maximum Stress and Strain failure theories were also plotted to provide a comparison. Since the burst failures of the CFRP tube section was observed to occur on the 2 mm thin pressure vessels, the graph in Figure 5.91 is based on those results. The optimum winding angle differed according to each of the failure theories though they were all in agreement that the optimal winding angle lay between 50° and 55°. The Maximum Strain failure theory predicted an optimal winding angle of 51°. The predicted burst pressure with this method is almost 1000 bar. This was considered unreasonable and disagreed with the observed burst pressures in the range 330-380 bar for the 2 mm thin vessels. To a lesser extent, the Maximum Stress failure theory was also insufficiently conservative in burst pressure predictions though it also predicted an optimal winding angle of approximately 52°.

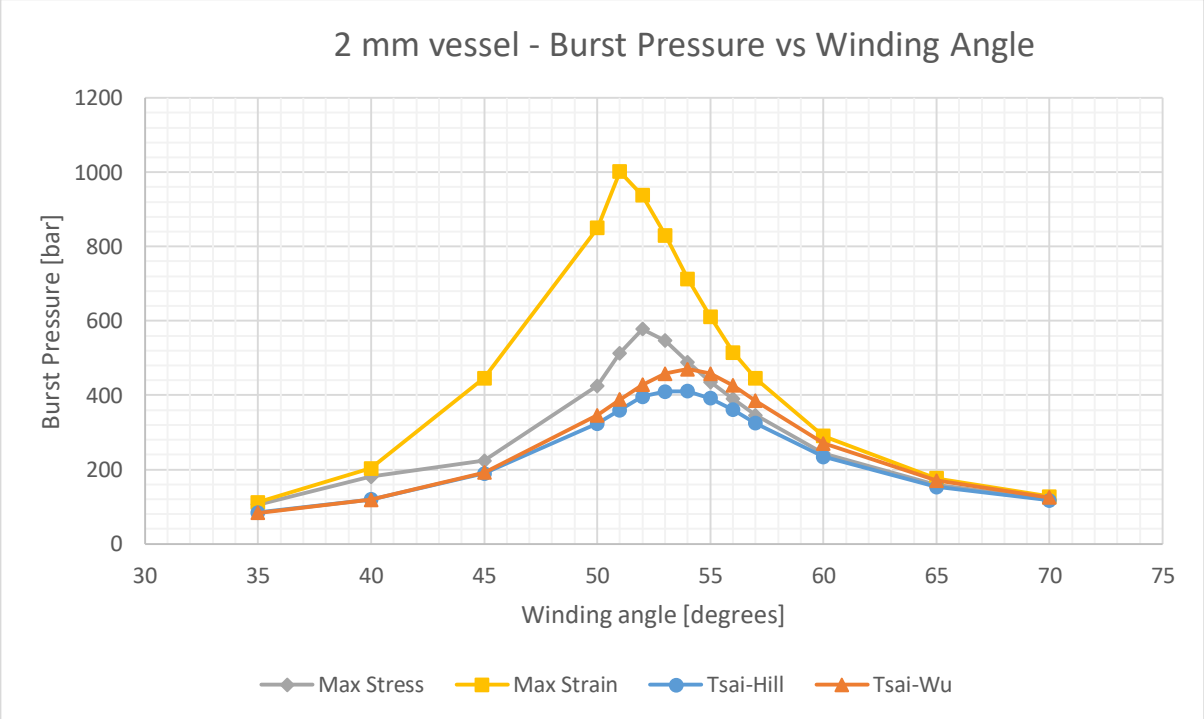

Figure 5.91: Graph comparing the expected burst pressures for various filament winding angles using the four failure theories for the 2 mm pressure vessel

The Tsai-Hill and Tsai-Wu failure theories were closely matched as they predicted optimal angles in the narrow band between 53° and 54° with the respective predicted burst pressures being also within 15% of each other. The optimal winding angle results are summarised in Table 5.34.

Table 5.34: Optimal winding angles for the different failure theories based on the 2 mm thin pressure vessels

Failure theory	**Optimal winding angle**	**Predicted Peak Burst Pressures [bar]**
Maximum Stress	52°	578
Maximum Strain	51°	1002
Tsai-Hill	53°-54°	411
Tsai-Wu	54°	470

Based on the predictions of the latter two failure theories, any winding angle from 53° to 55°, should result in the highest possible burst pressures. According to Shultz et al [106], the Tsai-Hill predicts an optimal winding angle of 52.5° while the Maximum Stress and Strain failure theories both predicted optimal winding angle of 50.5°. These angles were in close agreement with those from Table 5.34.

The predicted peak burst pressures are ideal but more often than not, cannot be matched accurately in practice. As with most manufacturing processes, there is an associated tolerance value that specifies the upper and lower bounds within which the desired (property) values is acceptable. The filament winding process used to manufacture the cylindrical CFRP tubes is no different. According to the curve for the Maximum Stress failure theory in Figure 5.91, an accuracy of approximately ±1° is required for the predicted burst pressures to be at least 88% of the peak value. For the Maximum Strain theory, the accuracy would also have to be ±1° if the burst pressure is to be within 15% of the peak pressure. However, an accuracy of approximately ±2° is required for the predicted burst pressures to be at least 90% of the peak value when it comes to curves for the Tsai-Hill and Tsai-Wu failure theories. The latter two failure theories require less accuracy for the winding angle while still resulting in a predicted pressure within 10% of the peak value. This is reasonable and more feasible for an automated filament winding process. Again, supporting the use of the Tsai-Wu and Tsai-Hill failure theories as preferred methods for calculating winding angles and burst pressures.

5.9 Cost of the novel CFRP pressure vessel

The costs incurred in purchasing the raw materials essential for the manufacture of the 2mm CFRP pressure vessels in comparison with Type IV 350 and 700 bar storage vessels are detailed in Appendix E.

5.10 Summary of the results and discussion

The tensile tests were performed and produced in-plane tensile property values that were significantly lower than the expected theoretical property values (i.e. from micromechanics) of the CFRP material in both the 0° and 90° loading directions. In addition, these property values were also very low compared to reported values from literature. The reasons for this were traced back to the manufacturing method of the CFRP tensile test specimens. These low in-plane tensile property values were still used in the initial design of the CFRP tube as it was reasoned that they would give a conservative design.

The three end cap adhesive shear tests all indicated mean shear strength values less than half of the manufacturer's reported data for SpaBond 340 LV. Visual inspection of the adhesive layer post-testing showed void formation in the first test. The second test's mean shear strength value was

approximately 15.7% higher than that of the first test. This improvement was attributed to the absence of voids in the adhesive layer of the second test specimens. This meant the use of angled holes which allowed for the direct injection of the adhesive into the bond area were a success. However, there was a drop in the mean shear strength of about 10% from the second to the third test. This result proved that knurling did not necessarily result in an increase in the bond shear strength between the end cap and adhesive layer. However, the standard deviation as a percentage of the mean is the lowest in the third test. From all tests, it was observed that shear failure occurred on the adhesive layer to Aluminium end cap interface indicating that it was the limiting case.

The hydrostatic burst test was essential in determining the failure pressures of a pressure vessels and the deformation behaviour of the CFRP tubes. There were three 4mm CFRP pressure vessels in the first set and all failed at pressures in the range 136-220 bar due to either leakage or shear failure of the adhesive bond. Therefore, none of these three vessels failed on the CFRP tube section. The second set of vessels had five 2 mm and another five 4 mm CFRP pressure vessels all with end caps based on the third design. The five 2 mm vessels predominantly failed due to bursting of the CFRP tube at a mean pressure of 352 bar which was significantly higher than the predicted burst pressures from the failure theories. This proved that the mechanical property values from the ASTM tensile tests were too low. The other five 4 mm vessels failed principally due to shear failure on the adhesive layer to end cap interface at a mean pressure of 429 bar. Therefore, this mean failure pressure value was indicative of the pressure at which the bond on the adhesive layer to end cap interface would fail. This translated to an applied shear stress value of 12.8 MPa which was consistent with the mean shear strength value of 13.3 MPa from the third shear test. It was also established that the 4 mm CFRP tubes would not fail at a mean pressure below 429 bar.

The results on the deformation behaviour of the 4 mm CFRP tubes from the first set of pressure vessels showed a linear relationship between strain and applied pressure for both the hoop and longitudinal directions. However, the strain measurements from the second set of CFRP pressure vessels showed an initially linear relationship between the pressure and both types of strains until a certain pressure value was reached. Beyond this pressure, the relationship became non-linear which translated to a decrease in stiffness of the CFRP tubes. The start of the non-linear behaviour was possibly because the CFRP tubes has started to sustain damage. The pressure at which the damage commenced was approximately 160 bar for the 2 mm CFRP tubes and about 250 bar for the 4 mm CFRP tubes. The maximum working pressures (determined from the failure pressure values) for the 2 mm and 4 mm CFRP pressure vessels were lower than the pressures at which the damage commenced in the tubes i.e. 147 bar and 182 bar respectively. This suggested it was safe to operate both 2 mm and 4 mm CFRP pressure vessels at these working pressures.

For the hydraulic proof tests, new 2 mm and 4 mm CFRP pressure vessels were constructed. Both types of vessels managed to retain pressure for just over 24 hours without failure, leakage or any visible permanent deformation. This meant the rubber liner and the end caps were able to sufficiently seal the pressure vessels thereby preventing leakage.

Long-term leak tests were performed at the respective maximum working pressures of the two types of vessels. Leaking was observed in all vessels that were tested as there was a decrease in the pressure over time. The occurrence of bubbling of soapy water determined that the end caps were the source of the leak. Leaking was only possible if the air had passed through the rubber liner first before also passing the two O-rings as well as between the adhesive layer the CFRP tube before escaping the vessel. The observed average leak rates were at least 50 times higher than the maximum acceptable leak rate for a typical 350 bar hydrogen gas storage pressure vessel. Air has many larger molecule gases than hydrogen. Therefore, it was reasonable to conclude that the observed average leak rates

would even be higher if a small molecule gas like hydrogen gas was used. To that end, the rubber liner as well as the O-rings were ineffective in preventing leakage of air out of the pressure vessels.

The results of the hydrostatic burst tests allowed for the validation of the in-plane property values determined from the ASTM tensile tests. The strain measurements were essential in updating the in-plane tensile stiffness property values i.e. E_1 and E_2. Furthermore, the burst pressure values (from the 2 mm CFRP pressure vessels) were essential for updating the in-plane tensile strength values i.e. $\sigma_{1\text{-}uts}$ and $\sigma_{2\text{-}uts}$. The updated in-plane tensile stiffness and strength property values proved that the values from the tensile tests were too low.

6. Conclusions and recommendations

6.1 Conclusions

This research work initially set out to investigate the feasibility and suitability of the novel, low-cost CFRP pressure vessel concept for storing high pressure hydrogen gas for HFC applications. This involved designing, manufacturing and assembling the components that made up the pressure vessel. The CFRP pressure vessels were tested using various pressure tests to assess their strength, reliability and leak-tightness. Based on the results of these tests presented and discussed in the previous chapter, the CFRP pressure vessel design was determined to not be feasible for gas storage with the main issues being the end cap design and the rubber liner used. However, other important conclusions were drawn from the various tests performed. For instance, the hydrostatic burst tests provided an innovative, convenient and quick means to determine some of the material properties of the CFRP material without needing to perform comprehensive material characterisation tests which are costly and time-consuming. The hydrostatic burst tests also provided crucial information with regards to the deformation behaviour of the CFRP tubes. This information would be helpful in designing similar filament wound CFRP tubes to be used in other applications. Other conclusions that were drawn include the following:

6.1.1 End cap

- The end caps were designed under the assumption they would deform more than the CFRP tube in the hoop direction because of the hemispherical dome geometry and thin walls. However, the CFRP tubes expanded more in the hoop direction as noted from the hydrostatic burst tests (see Figure 5.16). This was what most likely caused the two observed cases of failure due to delamination at the adhesive layer to CFRP tube wall interface as resulted in a tensile load on the adhesive layer which then pulled off a layer of the internal wall of the CFRP tube. Therefore, it was likely the case that the aluminium end cap was stiffer than initially hoped. Alternatively, it could also have been that the end cap was too thick in the sections close to the hemispherical dome where the pressure acted such that the end cap's deformation in the hoop direction was not enough to cause it to be pressed up against the CFRP tube internal wall.
- The use of a double O-ring design in the end caps for the second set of CFRP pressure vessels resulted in no water leaks during burst and proof tests while the use of one O-ring resulted in one vessel experiencing leaks for the first set of vessels. This proved that the use of two O-rings was more effective than using one O-ring.
- The mean shear strength of the SpaBond 340 LV adhesive layer interface with the end cap was established to be approximately 13 MPa during burst testing and 13.3 MPa during the third end cap adhesive test. The second adhesive application method and knurling were proven to give good and consistent results.
- The shear failure at the end cap to adhesive layer interface was manifested as a gradual movement of the end cap because of the pressure. This is considered safer from a design point of view as it does not result in the end cap shooting out as a projectile.

6.1.2 CFRP tube

- The deformation behaviour for the CFRP tube sections of the pressure vessel was initially linear until a certain pressure before sustaining some damage which manifested itself as a decrease in stiffness. The decrease in stiffness occurred earlier in the longitudinal direction

than in the hoop because the CFRP tubes were less stiff in the longitudinal direction. The linear strain response for the 2 mm and 4 mm CFRP tubes was observed until about 150 bar and 250 bar respectively. Therefore, those pressures represented the upper limit for design pressures that the 2 mm and 4 mm CFRP pressure vessels could be operated at without the onset of damage to the CFRP tubes.

- The 2 mm CFRP tubes burst at a mean pressure of 357 bar. The 4 mm CFRP tubes could not be caused to burst but it was established that they will not burst at a pressure below 450 bar. However, the revised burst pressure calculations suggest that the 4 mm CFRP tubes would fail at pressures between 584 bar and 624 bar based on the Tsai-Hill and Tsai-Wu failure theories.
- The optimal filament winding angle for maximizing this CFRP pressure vessel design's strength was determined to be approximately $53^{o}\pm1^{o}$ using the Tsai-Hill and Tsai-Wu failure theories.

6.1.3 Rubber liner

- The method for applying the rubber liner took at least 16 hours for a single layer with a thickness of between 0.20-0.25 mm primarily because of the curing time of the rubber. Four layers of the rubber liner needed at least 3 days to apply and cure. This process was therefore not commercially viable for mass producing similar CFRP pressure vessels as it takes too long.
- The thin rubber liner was proven to be water-tight as there were no leaks observed during proof tests of both the 2 mm and 4 mm CFRP pressure vessels in single tests for a period of approximately 24 hours.
- The thin rubber liner was however not air-tight as there were leaks that were observed during the long-term gas leak tests. Air contains some gas molecules considerably larger than smaller molecule gases like hydrogen. Therefore, it is reasonable to conclude that if the same rubber liner (i.e. VytaFlex 60 series) was used when leak testing with hydrogen gas, the leak rates would even be higher.
- The VytaFlex 60 series rubber liner was used to prevent the air-water mixture pressurised and maintained at 100 bar in the Ascension III water rocket for a duration of ten minutes before launch. This was a short-term application of the CFRP pressure vessel. In comparison, the air leak tests were performed for up to 72 hours and they proved that the CFRP pressure vessel concept with the rubber liner could not retain pressure suitably over that long period.

6.2 Recommendations

Although the CFRP pressure vessel design was determined to not be feasible for gas storage, certain areas were identified that could be addressed in future works as highlighted in this section. The following recommendations are made for future work pertaining to this research work:

6.2.1 End cap design

To ensure that the end cap deforms at a rate at similar (or higher) than that of the CFRP tubes in the hoop direction, the following options can be explored:

- Use of a less stiff material for the end caps that would deform significantly more than Aluminium 6082-T6 or the CFRP tube material for the same applied load. However, that material should be able to sustain the load due to the internal pressure without deforming permanently or fracturing. The material also should be inexpensive, easy to machine, readily available and offer good chemical resistance. Examples of such materials could include PEEK (polyetheretherketone), PBT (polybutylene terephthalate) and Nylon [130].

- Alternatively continuing the use of aluminium for the end caps but alter the design of the end cap such that it will have thinner sections on the end with the hemispherical dome. These thinner sections would deform more in the hoop direction for the same applied load as before. Analytical solutions and Finite Element Analysis (FEA) can be used to ensure that this proposed end cap design will not yield or fracture.

6.2.2 CFRP tube

- The pressure at which the 4 mm CFRP tubes would fail was not determined because the shear failure of the adhesive layer occurred first. The burst pressure was predicted to be between 584 bar and 624 bar. However, the 4 mm CFRP tubes will need to be hydrostatically burst tested until the tube fails. This would likely require the end caps to have a sufficiently large bond shear area and such that they will fail at pressures beyond at least 700 bar. New CFRP tubes should be manufactured and tested to confirm this.
- It was predicted the optimal filament winding angle that would maximize the burst pressure was in the range 51^{o}-54^{o} using the four failure theories. To confirm that hypothesis, CFRP tubes with winding angles of 50^{o}, 51^{o}, 52^{o}, 53^{o}, 54^{o} and 55^{o} should be made into pressure vessels and be hydrostatically burst tested to failure.

6.2.3 Rubber liner

- The VytaFlex 60 series rubber lining failed to hinder the escape of pressurized air at the respective design pressures of the 2 mm and 4 mm CFRP pressure vessels. Research into the permeability of that rubber lining will need to be conducted independently to establish the leak rate of air and possibly hydrogen gas over a given period of time as no such information was readily provided by the manufacturer [115].
- Using an alternative rubber liner with suitably low permeability rates, similar or lower mass density and faster curing times than VytaFlex 60 series rubber. An example is Butyl rubber which is easy to glue and ideal for applications where seals are required to be impermeable to gases [131-132].

7. References

[1] S. Swan, “Water rocket world record attempt - Engineering Project Report,” University of Cape Town, Cape Town, 2015.

[2] A. G. Malan, “UCT Water Rocket World Record Documentary,” 2016. [Online]. Available: https://youtu.be/K8WP9QCa2co. [Accessed: 12-May-2017].

[3] A. K. Kaw, *Mechanics of Composite Materials*, 1st ed. United States of America: CRC Press LLC, 2006.

[4] D. Hull, *An introduction to composite materials*, 1st ed. Cambridge University Press, 1981.

[5] S. G. Swan and A. G. Malan, “Proposed PCT Patent Application,” P3127PC00, 2015.

[6] “Fuel Cells Information, Facts, and Technology.” [Online]. Available: https://www.nationalgeographic.com/environment/global-warming/fuel-cells/. [Accessed: 16-Oct-2018].

[7] “Hydrogen Fuel Cell Vehicles | Center for Climate and Energy Solutions.” [Online]. Available: https://www.c2es.org/technology/factsheet/HydrogenFuelCellVehicles#_edn11. [Accessed: 09-Aug-2017].

[8] “Fuel Cell Systems | Department of Energy.” [Online]. Available: https://www.energy.gov/eere/fuelcells/fuel-cell-systems. [Accessed: 08-Mar-2018].

[9] J. Garche and J. Ludwig, “Applications of Fuel Cell Technology : Status and Perspectives,” *Electrochem. Soc. Interface*, pp. 39–43, 2015.

[10] M. Alkin, *ASME Boiler and Pressure Vessel Code - Section X - Fiber-Reinforced Plastic Pressure Vessels*. New York: The American Society of Mechanical Engineers, 2015.

[11] Department of Labour-South Africa, “Pressure Equipment Standard - 17 July 2009.” 2009.

[12] “Fuel Cells | Hydrogenics.” [Online]. Available: http://www.hydrogenics.com/technology-resources/hydrogen-technology/fuel-cells/. [Accessed: 08-Mar-2018].

[13] “Fuel Cells | Department of Energy.” [Online]. Available: https://www.energy.gov/eere/fuelcells/fuel-cells. [Accessed: 08-Mar-2018].

[14] R. K. Ahluwalia, T. Q. Hua, and J. K. Peng, “On-board and Off-board performance of hydrogen storage options for light-duty vehicles,” *Int. J. Hydrogen Energy*, vol. 37, no. 3, pp. 2891–2910, 2012.

[15] D. Mori and K. Hirose, “Recent challenges of hydrogen storage technologies for fuel cell vehicles,” *Int. J. Hydrogen Energy*, vol. 34, no. 10, pp. 4569–4574, 2009.

[16] H. T. Hwang and A. Varma, “Hydrogen storage for fuel cell vehicles,” *Curr. Opin. Chem. Eng.*, vol. 5, pp. 42–48, 2014.

[17] “Hydrogen Storage | Department of Energy.” [Online]. Available: https://energy.gov/eere/fuelcells/hydrogen-storage. [Accessed: 27-Jul-2017].

[18] “FCT - Fuel Cell Applications - Stationary.” [Online]. Available: http://www.fuelcelltoday.com/applications/stationary. [Accessed: 17-Mar-2018].

[19] “FCT - Fuel Cell Applications - Portable.” [Online]. Available: http://www.fuelcelltoday.com/applications/portable. [Accessed: 17-Mar-2018].

[20] “FCT - Fuel Cell Applications - Transport.” [Online]. Available: http://www.fuelcelltoday.com/applications/transport. [Accessed: 17-Mar-2018].

[21] S. W. Jorgensen, “Hydrogen storage tanks for vehicles: Recent progress and current status,” *Curr. Opin. Solid State Mater. Sci.*, vol. 15, no. 2, pp. 39–43, 2011.

[22] M. R. Gardiner and A. Burke, “Comparison of hydrogen storage technologies: A focus on energy required for hydrogen input,” *ACS Div. Fuel Chem. Prepr.*, vol. 47, no. 2, pp. 794–795, 2002.

[23] D. J. Durbin and C. Malardier-Jugroot, “Review of hydrogen storage techniques for on board vehicle applications,” *Int. J. Hydrogen Energy*, vol. 38, no. 34, pp. 14595–14617, 2013.

[24] H. Barthelemy, “Hydrogen Storage - Recent improvements and industrial prospectives,” *Proc. Int. Conf. Hydrog. Safety, Sept. 11-13*, pp. 1–19, 2013.

[25] N. L. Garland, D. C. Papageorgopoulos, and J. M. Stanford, “Hydrogen and fuel cell technology: Progress, challenges, and future directions,” *Energy Procedia*, vol. 28, pp. 2–11, 2012.

[26] H. Barthelemy, M. Weber, and F. Barbier, “Hydrogen storage: Recent improvements and industrial perspectives,” *Int. J. Hydrogen Energy*, vol. 42, no. 11, pp. 7254–7262, 2017.

[27] A. Kalanidhi, “Boil-off in long-term stored liquid hydrogen,” *Int. J. Hydrogen Energy*, vol. 13, no. 5, pp. 311–313, Jan. 1988.

[28] A. Zuttel, “Materials for hydrogen storage,” *Mater. Today*, vol. 6, no. 9, pp. 24–33, 2003.

[29] S. Satyapal, C. Read, G. Ordaz, N. Stetson, G. Thomas, and J. Petrovic, “Office of Hydrogen, Fuel Cells and Infrastructure Technologies 2 DOE (on assignment); retired, Sandia National Laboratory,” 2007.

[30] “Glossary | Publications and Other Information | BTSC.” [Online]. Available: https://brownfieldstsc.org/glossary.cfm?q=1. [Accessed: 14-Mar-2018].

[31] “Adsorption, Absorption and Desorption - What’s the Difference? Chromatography Today.” [Online]. Available: https://www.chromatographytoday.com/news/hplc-uhplc/31/breaking-news/adsorption-absorption-and-desorption-what39s-the-difference/31397. [Accessed: 07-Feb-2019].

[32] L. Schlapbach, L. Schlapbach, and A. Züttel, “Hydrogen-storage materials for mobile applications,” vol. 414, no. May 2016, pp. 353–358, 2001.

[33] K. L. Lim, H. Kazemian, Z. Yaakob, and W. R. W. Daud, “Solid-state Materials and Methods for Hydrogen Storage: A Critical Review,” *Chem. Eng. Technol.*, vol. 33, no. 2, pp. 213–226, Feb. 2010.

[34] “Hydride | chemical compound | Britannica.com.” [Online]. Available: https://www.britannica.com/science/hydride. [Accessed: 14-Mar-2018].

[35] “DOE Technical Targets for Onboard Hydrogen Storage for Light-Duty Vehicles | Department of Energy.” [Online]. Available: https://www.energy.gov/eere/fuelcells/doe-technical-targets-onboard-hydrogen-storage-light-duty-vehicles. [Accessed: 24-Mar-2018].

[36] “Honda’s Hydrogen Fuel Cell Clarity Comes Loaded With Perks | WIRED.” [Online]. Available: https://www.wired.com/2017/04/honda-will-nearly-anything-get-hydrogen-car/. [Accessed: 16-Feb-2018].

[37] “Hydrogen Fuel Cell Car | Tucson Fuel Cell | Hyundai USA.” [Online]. Available: https://www.hyundaiusa.com/tucsonfuelcell/index.aspx. [Accessed: 16-Feb-2018].

[38] “Hydrogen Fuel Cell Car | Toyota Mirai.” [Online]. Available: https://ssl.toyota.com/mirai/fcv.html. [Accessed: 16-Feb-2018].

[39] K. Law, “Cost Analyses of Hydrogen Storage Materials and On- Board Systems Timeline Barriers Budget,” Cupertino, 2011.

[40] “Pressure vessel definition and meaning | Collins English Dictionary.” [Online]. Available: https://www.collinsdictionary.com/dictionary/english/pressure-vessel. [Accessed: 16-Oct-2018].

[41] “Pressure measurement: Compressible vs. incompressible media.” [Online]. Available: https://campaign.stssensors.com/blog/pressure-measurement-compressible-media. [Accessed: 28-Jan-2019].

[42] “Compressible Fluid - an overview | ScienceDirect Topics.” [Online]. Available: https://www.sciencedirect.com/topics/engineering/compressible-fluid. [Accessed: 28-Jan-2019].

[43] “Safety and Health Topics | Pressure Vessels | Occupational Safety and Health Administration.” [Online]. Available: https://www.osha.gov/SLTC/pressurevessels/index.html. [Accessed: 16-Oct-2018].

[44] J. Darlaston and J. Wintle, “Safety factors in the design and use of pressure equipment,” *Eng. Fail. Anal.*, vol. 14, no. 3, pp. 471–480, 2007.

[45] “Tips for Pressure Vessel Design.” [Online]. Available: https://www.buckeyefabricating.com/post/tips-for-pressure-vessel-design. [Accessed: 16-Oct-2018].

[46] “The 3 Most Common Types of Pressure Vessels.” [Online]. Available: https://www.buckeyefabricating.com/post/the-3-most-common-types-of-pressure-vessels. [Accessed: 29-Jan-2018].

[47] “Types of Pressure Vessels.” [Online]. Available: http://www.oakleysteel.co.uk/types-of-pressure-vessels. [Accessed: 09-Apr-2018].

[48] “Pressure Vessels, Spherical Pressure vessels (Pressure Spheres), Cylindrical Pressure Vessels.” [Online]. Available: http://www.wermac.org/equipment/pressurevessel.html. [Accessed: 24-May-2017].

[49] M. J. Thattil and C. Pany, “Design and Analysis of Pressure Vessel with Hemispherical and Flat Circular End,” vol. 7, no. 5, pp. 12458–12469, 2017.

[50] R. J. Brogan, “HEAT EXCHANGERS,” *A-to-Z Guide to Thermodynamics, Heat and Mass Transfer, and Fluids Engineering*. Begellhouse, 2011.

[51] “What is a Process Vessel? - Definition from Corrosionpedia.” [Online]. Available: https://www.corrosionpedia.com/definition/1769/process-vessel. [Accessed: 09-Apr-2018].

[52] M. T. Altinbalik and S. İsencik, “Comparative Design and Cost Analysis of Cylindrical Storage Tanks with Different Head Types by Using COMPRESS,” pp. 1–8, 2016.

[53] S. Lawate and B. B. Deshmukh, “Analysis of Heads of Pressure Vessel,” *Int. J. Innov. Res. Sci. Eng. Technol.*, vol. 4, no. 2, pp. 759–765, 2015.

[54] “Comparison Between Head Types: Hemi, SE, F&D and Flat – Pressure Vessel Engineering.” [Online]. Available: https://pveng.com/home/asme-code-design/comparison-between-head-types-hemi-se-fd-and-flat/. [Accessed: 14-May-2018].

[55] “ASME Boiler and Pressure Vessel Code,” 2017. [Online]. Available: https://www.asme.org/wwwasmeorg/media/ResourceFiles/Shop/Standards/New Releases/ASME-BPVC-Brochure-webview.pdf. [Accessed: 16-Oct-2018].

[56] European Parliament and Council, “Directive 2014/68/EU of the European Parliament and of the Council of 15 May 2014,” *Off. J. Eur. Union*, vol. 93, no. 765, pp. 164–259, 2014.

[57] European Parliament and Council, “Directive 2010/35/EU of the European Parliament and of the Council of 16 June 2010 on transportable pressure equipment,” *Off. J. Eur. Union*, vol. 2010, no. May, 2010.

[58] European Parliament and Council, “Directive 2009/105/EC of The European Parliament and of the Council of 16 September 2009 relating to simple pressure vessels,” *Off. J. Eur. Union*, no. 1025, pp. 1–25, 2013.

[59] C. Lower and S. Park, *CODAP 2010 Sivision 1 & 2: Code for Construction of unfired pressure vessels*, vol. 44, no. 0. Paris: SNCT Publications, 2012.

[60] Canadian Standards Association, “B51-09 Boiler, pressure vessel, and pressure piping code,” 2009.

[61] SABS, *SANS 347 : 2012 - South African National Standard - Categorization and conformity assessment criteria for all pressure equipment*, 2nd ed., no. 014. SABS Standards Division, 2012.

[62] “Pressure vessel tank types : CompositesWorld.” [Online]. Available: https://www.compositesworld.com/articles/pressure-vessel-tank-types. [Accessed: 09-Apr-2018].

[63] “Hydrogen storage | Innovation for Sustainable Energy | Washington State University.” [Online]. Available: https://hub.wsu.edu/ise/design/hydrogen-storage/. [Accessed: 17-Oct-2018].

[64] B. D. James, J. M. Huya-kouadio, and D. A. Desantis, “Final Report : Hydrogen Storage System Cost Analysis,” *Doe Osti*, no. September, 2016.

[65] “Physical Hydrogen Storage | Department of Energy.” [Online]. Available: https://www.energy.gov/eere/fuelcells/physical-hydrogen-storage. [Accessed: 17-Oct-2018].

[66] H. Barthelemy, “Hydrogen Storage – Industrial Prospectives,” pp. 1–14.

[67] “Destructive Testing (DT) - Inspecta.” [Online]. Available: https://www.inspecta.com/en/Our-Services/Testing/Destructive-Testing/. [Accessed: 17-Oct-2018].

[68] H. Division, “Pressure Test Procedures,” 2015. [Online]. Available: http://www-group.slac.stanford.edu/esh/eshmanual/references/pressureProcedTest.pdf.

[69] “Modern Techniques for Inspecting HighPressure Vessels.” [Online]. Available: https://www.asme.org/engineering-topics/articles/pressure-vessels/modern-techniques-for-inspecting-high-pressure. [Accessed: 12-Apr-2018].

[70] “Non Destructive Testing - Pressure Testing is a non-destructive test performed to ensure the integrity of the pressure shell on new pressure equipment.” [Online]. Available: http://www.wermac.org/others/ndt_pressure_testing.html. [Accessed: 17-Oct-2018].

[71] “Proof Pressure Testing - Maximator Test.” [Online]. Available: https://maximator-test.com/high-pressure-testing/proof-pressure-testing/. [Accessed: 16-Jul-2018].

[72] M. E. E. Joints, “Proof-Pressure Test and Leak Detection Test.” [Online]. Available: http://www.macoga.com/documents/products/metal-expansion-joints/proof-pressure-test-leak-detection-test.pdf.

[73] “Pressure Testing.” [Online]. Available: http://www.e-labsinc.com/pressure-testing.shtml. [Accessed: 17-Oct-2018].

[74] “Lecture 15-Stresses within a Pressure Vessel.” [Online]. Available: http://www.nptel.ac.in/courses/112107146/lects & picts/image/lect15/lecture15.htm. [Accessed: 25-Jan-2018].

[75] “Stress in Thick-Walled Cylinders - or Tubes.” [Online]. Available: https://www.engineeringtoolbox.com/stress-thick-walled-tube-d_949.html. [Accessed: 25-Jan-2018].

[76] R. C. Stephens and E. J. Hearn, “Mechanics of Materials 2,” 3rd ed., London: Butterworth-Heinemann, 1997.

[77] E. J. Hearn, “Mechanics of Materials 1,” 1st ed., Butterworth-Heinemann, 1970, pp. 198–214.

[78] R. M. Jones, *Mechanics of Composite Materials*, Second. Philadelphia: Taylor & Francis, 1999.

[79] I. Olofin and R. Liu, “The Application of Carbon Fibre Reinforced Polymer (CFRP) Cables in Civil Engineering Structures,” vol. 2, no. 7, pp. 1–5, 2015.

[80] “Carbon Fiber - Sit Back, It’s Time For A Lesson in Composites.” [Online]. Available: https://www.turnology.com/tech-stories/carbon-fiber-a-lesson-in-composites/. [Accessed: 11-Oct-2018].

[81] “Mechanical Properties of Carbon Fibre Composite Materials.” [Online]. Available: http://www.performance-composites.com/carbonfibre/mechanicalproperties_2.asp. [Accessed: 04-Jul-2017].

[82] “Carbon Fiber Properties.” [Online]. Available: https://www.christinedemerchant.com/carboncharacteristics.html. [Accessed: 09-Jan-2018].

[83] “Composite materials guide: Reinforcements - Fabric Types | NetComposites.” [Online]. Available: https://netcomposites.com/guide-tools/guide/reinforcements/fabric-types/. [Accessed: 06-Nov-2018].

[84] “Composite materials guide: Reinforcements - Unidirectional Fabric | NetComposites.” [Online]. Available: https://netcomposites.com/guide-tools/guide/reinforcements/unidirectional-fabric/. [Accessed: 07-Nov-2018].

[85] “Composite materials guide: Reinforcements - Woven Fabrics | NetComposites.” [Online]. Available: https://netcomposites.com/guide-tools/guide/reinforcements/woven-fabrics/. [Accessed: 07-Nov-2018].

[86] “Carbon fiber all patterns explained. Carbon.ee Blog.” [Online]. Available: https://www.carbon.ee/en/n/carbon-fiber-all-patterns-explained. [Accessed: 11-Oct-2018].

[87] P. R. Velmurugan, “Composite Materials-Manufacturing Techniques (Dept. of Aerospace Eng),” Madras.

[88] “Composites Manufacturing Processes | CompositesLab.” [Online]. Available:

http://compositeslab.com/composites-manufacturing-processes/. [Accessed: 17-Jan-2018].

[89] “Composite materials guide: Manufacturing - Filament Winding | NetComposites Now.” [Online]. Available: http://netcomposites.com/guide-tools/guide/manufacturing/filament-winding/. [Accessed: 22-Jun-2017].

[90] “Filament Winding - F - NetComposites.” [Online]. Available: https://netcomposites.com/guide-tools/glossary/f/filament-winding/. [Accessed: 08-Nov-2018].

[91] I. M. Daniel and O. Ishai, *Engineering Mechanics of Composite Materials*, 2nd ed. New York: Oxfor University Press, 2006.

[92] “Dry Winding - D - NetComposites.” [Online]. Available: https://netcomposites.com/guide-tools/glossary/d/dry-winding/. [Accessed: 08-Nov-2018].

[93] “Wet Winding - W - NetComposites.” [Online]. Available: https://netcomposites.com/guide-tools/glossary/w/wet-winding/. [Accessed: 08-Nov-2018].

[94] “HOW ARE FRP/GRP PIPE FILAMENT WINDING MACHINE WORKING? - Hebei Maple FRP Industry Co.,Ltd.” [Online]. Available: http://www.frpmachining.com/faqs/frpgrp-pipe-filament-winding-machine. [Accessed: 17-Jan-2018].

[95] V. V. Vasiliev and E. V. Morozov, *Advanced Mechanics of Composite Materials*, Third. Lomdon: Elsevier, 2013.

[96] ASTM, “Standard Guide for Testing Polymer Matrix Composite Materials 1,” *Annu. B. ASTM Stand.*, pp. 1–22, 2012.

[97] A. Wube Dametew, “Design and Empirical Analysis of Selected Machine Elements from Composite Materials is Better to Use,” 2017.

[98] C. T. Sun, B. J. Quinn, and J. Tao, “Comparative evaluation of failure analysis methods for composite laminates,” *U.S. Dep. Transp.*, no. May, p. 133, 1996.

[99] C. W. Bert, “Classical Lamination Theory,” in *Manual on Experimental Methods for Mechanical Testing of Composites*, Dordrecht: Springer Netherlands, 1989, pp. 11–16.

[100] S. T. Peters, *Composite filament winding*. ASM International, 2011.

[101] “Multi Axis Filament Winding.” [Online]. Available: http://ccp-gransden.com/index.php/multi-axis-filament-winding. [Accessed: 09-Oct-2018].

[102] Aerontech, “Epoxy AR600 +AH2336 Hardener -Technical data sheet,” 2010. [Online]. Available: https://www.aerontec.co.za/ar600-epoxy-resin-expands-range/. [Accessed: 15-Feb-2018].

[103] M. J. Hinton, A. S. Kaddour, and P. D. Soden, *Failure Criteria in Fibre-Reinforced-Polymer Composites*. 2004.

[104] N. Tiwari, “Introduction to Composite Materials and Structures - Lecture 28 - Failure of Unidirectional Composites,” Madras.

[105] “Stress in Thin-Walled Tubes or Cylinders.” [Online]. Available: https://www.engineeringtoolbox.com/stress-thin-walled-tube-d_948.html. [Accessed: 24-May-2018].

[106] M. Shultz and L. V Smith, “Optimal fiber orientation for fiber reinforced pressure vessels,” in *2004 SEM Annual Conference and Exposition of Experimental and Applied Mechanics*, 2004,

pp. 1–7.

[107] “Thermal - Thermal Expansion | Characteristics of Fine Ceramics | FINE CERAMICS WORLD - All About Advanced Ceramics -.” [Online]. Available: https://global.kyocera.com/fcworld/charact/heat/thermaexpan.html. [Accessed: 09-Oct-2018].

[108] Gurit, “Spabond 340LV Epoxy Adhesive System - Technical Data Sheet.” [Online]. Available: www.gurit.com.

[109] “Granta’s CES EduPack 2017.” [Online]. Available: http://www.grantadesign.com/education/edupack/edupack2017.htm. [Accessed: 10-Sep-2018].

[110] “Aluminium Alloy - Commercial Alloy - 6082 - T6~T651 Plate.” [Online]. Available: http://www.aalco.co.uk/datasheets/Aluminium-Alloy_6082-T6~T651_148.ashx. [Accessed: 23-Apr-2018].

[111] Epoxy Technology Incorporated, “Bonding to Aluminum,” 2013. [Online]. Available: www.epotek.com.

[112] “Poisson’s ratio.” [Online]. Available: https://www.engineeringtoolbox.com/poissons-ratio-d_1224.html. [Accessed: 15-Aug-2018].

[113] G. Fernlund, J. Wells, L. Fahrang, J. Kay, and A. Poursartip, “Causes and remedies for porosity in composite manufacturing,” *IOP Conf. Ser. Mater. Sci. Eng.*, vol. 139, p. 012002, 2016.

[114] K. Ishiguro, S. S. Sangari, and J. Seferis, “Microcrack initiation mechanism of CFRP under the thermal cycle,” *Int. SAMPE Symp. Exhib.*, vol. 51, 2006.

[115] S. Inc., “VytaFlex Series Liquid Urethane Rubbers,” 2015. [Online]. Available: www.smooth-on.com. [Accessed: 06-Oct-2018].

[116] “Pressure Vessels - processdesign.” [Online]. Available: https://processdesign.mccormick.northwestern.edu/index.php/Pressure_Vessels. [Accessed: 16-Jan-2019].

[117] “AMT Composites.” [Online]. Available: https://www.amtcomposites.co.za/. [Accessed: 25-Jan-2019].

[118] T. Tenax, “Tenax HTS carbon fiber product datasheet,” 2011. [Online]. Available: https://www.tohotenax.com/. [Accessed: 30-May-2017].

[119] “Aerontec | Composite Materials, Flowcrete, Fibreglass, Epoxy Systems.” [Online]. Available: https://www.aerontec.co.za/. [Accessed: 25-Jan-2019].

[120] ASTM International, “ASTM D3039/D3039M - Standard Test Method for Tensile Properties of Polymer Matrix Composites,” *Annual Book of ASTM Standards*. ASTM International, West Conshohocken, PA, pp. 1–13, 2014.

[121] “Strain Gauges: Types, What It Is & How It Works | Omega.” [Online]. Available: https://www.omega.com/prodinfo/strain-gauges.html. [Accessed: 07-Feb-2019].

[122] “Measuring Strain with Strain Gages - National Instruments.” [Online]. Available: http://www.ni.com/white-paper/3642/en/. [Accessed: 24-Jul-2017].

[123] “Mechanics eBook: Strain Gages and Strain Rosette.” [Online]. Available: https://www.ecourses.ou.edu/cgi-

bin/ebook.cgi?doc=&topic=me&chap_sec=08.3&page=theory. [Accessed: 11-Aug-2017].

[124] “Strain Gauges-Rosettes.” [Online]. Available: http://www.continuummechanics.org/straingauges.html. [Accessed: 20-Jul-2017].

[125] Vishay Micro-Measurements, “Strain Gage Selection: Criteria, Procedures, Recommendations Strain Gages and Instruments MICRO-MEASUREMENTS,” 2017. [Online]. Available: http://www.vishaypg.com/docs/11055/tn505.pdf.

[126] “Strain Gage: Length.” [Online]. Available: http://www.efunda.com/designstandards/sensors/strain_gages/strain_gage_selection_length.cfm. [Accessed: 21-Jun-2018].

[127] “Coefficients of Linear Thermal Expansion.” [Online]. Available: https://www.engineeringtoolbox.com/linear-expansion-coefficients-d_95.html. [Accessed: 25-Jun-2018].

[128] I. Measurements Group, “P-3500 Portable Strain Indicator - User Guide,” 1992. [Online]. Available: http://www.groupes.polymtl.ca/mec6405/Instruments Spec/Vishay_P3500.pdf. [Accessed: 12-Oct-2018].

[129] Bigelow Erik, “Conformable Hydrogen Storage Coil Reservoir,” 2015.

[130] “Strong, Stiff, Hard Plastic Sheets | Curbell Plastics.” [Online]. Available: https://www.curbellplastics.com/Research-Solutions/Applications/Strong-and-Stiff. [Accessed: 21-Jan-2019].

[131] “Heat-resistant and gas-impermeable rubber sheets - Teknikum.” [Online]. Available: https://www.teknikum.com/en/heat-resistant-and-gas-impermeable-rubber-sheets/. [Accessed: 21-Jan-2019].

[132] “Highly Gas Impermeable Elastomeric Rubber-Rubber Blend Nano Composites | Gandhian Young Technological Innovation Award.” [Online]. Available: http://gyti.techpedia.in/project-detail/highly-gas-impermeable-elastomeric-rubber-rubber-blend-nano-composites/802. [Accessed: 21-Jan-2019].

[133] K. Law, J. Rosenfeld, V. Han, M. Chan, H. Chiang, and J. Leonard, “U.S. Department of Energy Hydrogen Storage Cost Analysis,” 2013.

Appendices

Appendix A: CFRP tubes

Appendix B: Detailed end cap drawings

Appendix C: Leak rate calculation

Appendix D: Material and product data sheets

Appendix E: Detailed costs associated with the novel CFRP pressure vessels and the Type IV pressure vessels

Appendix A: CFRP tubes

1. Stress calculations

Introduction

These calculations were perfromed using PTC MathCAD Express software. The CFRP tube stress and strain calculations begin with defining the material properties as well as the dimensions of the tube. The hoop and longitudinal stresses (i.e. global stresses) are then evaluated using the Cylinder Theories given by EJ Hearn [76]. The rest of the calculations are based on the Classical Lamination Theory and can be found in section 2.3.4.2 and the steps taken are derived from the summary given on page 39.

Material properties and vessel dimensions

Pressure $p_o := 350\ bar$

Inner diameter $D_i := 50\ mm$

Thickness of vessel $t := 4\ mm$

Outer diameter $D_o := D_i + 2 \cdot t = 58\ mm$

Winding angle $\alpha_1 := 50\ °$

$\alpha_2 := -\alpha_1$

Laminae thickness $t_l := 0.25\ mm$

Number of laminae $n_l := \frac{t}{t_l} = 16$

Laminate thickness $h := t = 4\ mm$

Longitudinal modulus $E_1 := 109\ GPa$

Transverse modulus $E_2 := 6\ GPa$

In-plane shear modulus $G_{12} := 5\ GPa$

Major Poisson's ratio $v_{12} := 0.30$

Minor Poisson's ratio $v_{21} := \frac{E_2 \cdot v_{12}}{E_1} = 0.017$

Applied stresses on the pressure vessel

Inner radius $R_1 := \frac{D_i}{2} = 25\ mm$

Outer radius $R_2 := \frac{D_o}{2} = 29\ mm$ $K := \frac{R_2}{R_1} = 1.16$

Lame's constants $A := \frac{p_o \cdot {R_1}^2}{\left({R_2}^2 - {R_1}^2\right)}$

$B := \frac{p_o \cdot {R_1}^2 \cdot {R_2}^2}{\left({R_2}^2 - {R_1}^2\right)}$

Stresses evaluated at: $r := R_1 = 0.025\ m$

Hoop stress $\sigma_H := \frac{p_o \cdot \left(\left(\frac{R_2}{r}\right)^2 + 1\right)}{K^2 - 1} = 237.546\ MPa$

Longitudinal stress $\sigma_L := \frac{p_o \cdot {R_1}^2}{{R_2}^2 - {R_1}^2} = 101.273\ MPa$

Global stresses on the laminate $\begin{bmatrix} \sigma_x \\ \sigma_y \\ \tau_{xy} \end{bmatrix} := \begin{bmatrix} \sigma_L \\ \sigma_H \\ 0\ MPa \end{bmatrix}$

Transformation Matrices

Transformational matrix $T := \begin{bmatrix} \cos(\alpha)^2 & \sin(\alpha)^2 & 2\cdot\sin(\alpha)\cdot\cos(\alpha) \\ \sin(\alpha)^2 & \cos(\alpha)^2 & -(2\cdot\sin(\alpha)\cdot\cos(\alpha)) \\ -\sin(\alpha)\cdot\cos(\alpha) & \sin(\alpha)\cdot\cos(\alpha) & \cos(\alpha)^2 - \sin(\alpha)^2 \end{bmatrix}$

For laminae with $50°$ fibre winding angle $T_1 = \begin{bmatrix} 0.413 & 0.587 & 0.985 \\ 0.587 & 0.413 & -0.985 \\ -0.492 & 0.492 & -0.174 \end{bmatrix}$

For laminae with $-50°$ fibre winding angle $T_2 = \begin{bmatrix} 0.413 & 0.587 & -0.985 \\ 0.587 & 0.413 & 0.985 \\ 0.492 & -0.492 & -0.174 \end{bmatrix}$

Reduced Stiffness Matrix

$Q_{11} := \frac{E_1}{1 - v_{12}\cdot v_{21}}$ $\quad Q_{12} := \frac{v_{12}\cdot E_2}{1 - v_{12}\cdot v_{21}}$ $\quad Q_{16} := 0\ GPa$

$Q_{66} := G_{12}$ $\quad Q_{26} := 0\ GPa$

$Q_{22} := \frac{E_2}{1 - v_{12}\cdot v_{21}}$

$Q := \begin{bmatrix} Q_{11} & Q_{12} & Q_{16} \\ Q_{12} & Q_{22} & Q_{26} \\ Q_{16} & Q_{26} & Q_{66} \end{bmatrix} = \begin{bmatrix} 109.543 & 1.809 & 0 \\ 1.809 & 6.03 & 0 \\ 0 & 0 & 5 \end{bmatrix} GPa$

Transformed Reduced Stiffness Matrix

$m := \cos(\alpha_1)$ $\quad n := \sin(\alpha_1)$

$Q_{11}` := Q_{11}\cdot m^4 + 2\cdot(Q_{12} + 2\ Q_{66})\cdot n^2\cdot m^2 + Q_{22}\cdot n^4$

$Q_{12}` := (Q_{11} + Q_{22} - 4\cdot Q_{66})\cdot m^2\cdot n^2 + Q_{12}\cdot(n^4 + m^4)$

$Q_{22}` := Q_{11}\cdot n^4 + 2\cdot(Q_{12} + 2\ Q_{66})\cdot n^2\cdot m^2 + Q_{22}\cdot m^4$

$Q_{16}` := (Q_{11} - Q_{12} - 2\cdot Q_{66})\cdot m^3\cdot n + (Q_{12} - Q_{22} + 2\cdot Q_{66})\cdot m\cdot n^3$

$Q_{26}` := (Q_{11} - Q_{12} - 2\cdot Q_{66})\cdot m\cdot n^3 + (Q_{12} - Q_{22} + 2\cdot Q_{66})\cdot m^3\cdot n$

$Q_{66}` := (Q_{11} + Q_{22} - 2\cdot Q_{12} - 2\cdot Q_{66})\cdot m^2\cdot n^2 + Q_{66}\cdot(n^4 + m^4)$

For laminae with $50°$ fibre winding angle

$$Q`_1 := \begin{bmatrix} Q_{11}` & Q_{12}` & Q_{16}` \\ Q_{12}` & Q_{22}` & Q_{26}` \\ Q_{16}` & Q_{26}` & Q_{66}` \end{bmatrix} = \begin{bmatrix} 26.5 & 24.1 & 21.55 \\ 24.1 & 44.48 & 29.42 \\ 21.55 & 29.42 & 27.3 \end{bmatrix} \ GPa$$

For laminae with $-50°$ fibre winding angle

$$Q`_2 = \begin{bmatrix} 26.5 & 24.1 & -21.55 \\ 24.1 & 44.48 & -29.42 \\ -21.55 & -29.42 & 27.3 \end{bmatrix} \ GPa$$

Calculations of strains of each lamina in the laminate

Z-position of the bottom surface of the laminate

$$z_0 := \frac{-h}{2} = -2 \ mm$$

$$\text{ORIGIN} := 0$$

Z-positions for the top and bottom surfaces of each lamina

$$p := \left(z_0 + l \cdot t_l\right) = \begin{matrix} 0 \\ 1 \\ 2 \\ 3 \\ 4 \\ 5 \\ 6 \\ 7 \\ 8 \\ 9 \\ 10 \\ 11 \\ \vdots \\ 16 \end{matrix} \begin{bmatrix} -2 \\ -1.75 \\ -1.5 \\ -1.25 \\ -1 \\ -0.75 \\ -0.5 \\ -0.25 \\ 0 \\ 0.25 \\ 0.5 \\ 0.75 \\ \vdots \end{bmatrix} \ mm$$

The extensional stiffness matrix

$$A = \begin{bmatrix} 0.106 & 0.096 & 0 \\ 0.096 & 0.178 & 0 \\ 0 & 0 & 0.109 \end{bmatrix} \ GPa \cdot m$$

The coupling stiffness matrix

$$B = \begin{bmatrix} 0 & 0 & 0 \\ 0 & 0 & 0 \\ 0 & 0 & 0 \end{bmatrix} \ Pa \cdot m^2$$

The bending stiffness matrix

$$D = \begin{bmatrix} 0.141 & 0.129 & 0.022 \\ 0.129 & 0.237 & 0.029 \\ 0.022 & 0.029 & 0.146 \end{bmatrix} \ kPa \cdot m^3$$

The resultant forces on the laminate per unit length

$$N_x := \int_{\frac{-h}{2}}^{\frac{h}{2}} \sigma_x \, dz = \left(4.051 \cdot 10^5\right) \ N \cdot m^{-1}$$

$$N_y := \int_{\frac{-h}{2}}^{\frac{h}{2}} \sigma_y \, dz = \left(9.502 \cdot 10^5\right) \ N \cdot m^{-1}$$

$$N_{xy} := \int_{\frac{-h}{2}}^{\frac{h}{2}} \tau_{xy} \, dz = 0 \ N \cdot m^{-1}$$

The resultant moments on the laminate per unit length

$$M_x := \int_{\frac{-h}{2}}^{\frac{h}{2}} \sigma_x \cdot z \, dz = 0 \ N$$

$$M_y := \int_{\frac{-h}{2}}^{\frac{h}{2}} \sigma_y \cdot z \, dz = 0 \ N$$

$$M_{xy} := \int_{\frac{-h}{2}}^{\frac{h}{2}} \tau_{xy} \cdot z \, dz = 0 \ N$$

Mid-plane strains

$$\begin{bmatrix} \varepsilon`_x \\ \varepsilon`_y \\ \gamma`_{xy} \end{bmatrix} := \begin{bmatrix} A_{0,0} & A_{0,1} & A_{0,2} \\ A_{1,0} & A_{1,1} & A_{1,2} \\ A_{2,0} & A_{2,1} & A_{2,2} \end{bmatrix}^{-1} \cdot \begin{bmatrix} N_x \\ N_y \\ N_{xy} \end{bmatrix} = \begin{bmatrix} -0.0020433 \\ 0.0064481 \\ 0 \end{bmatrix}$$

Mid-plane curvatures

$$\begin{bmatrix} \kappa`_x \\ \kappa`_y \\ \kappa`_{xy} \end{bmatrix} := \begin{bmatrix} D_{0,0} & D_{0,1} & D_{0,2} \\ D_{1,0} & D_{1,1} & D_{1,2} \\ D_{2,0} & D_{2,1} & D_{2,2} \end{bmatrix}^{-1} \cdot \begin{bmatrix} M_x \\ M_y \\ M_{xy} \end{bmatrix} = \begin{bmatrix} 0 \\ 0 \\ 0 \end{bmatrix} \frac{1}{m}$$

Global strains for all laminae

$$\begin{bmatrix} \varepsilon_x \\ \varepsilon_y \\ \gamma_{xy} \end{bmatrix} := \begin{bmatrix} \varepsilon`_x \\ \varepsilon`_y \\ \gamma`_{xy} \end{bmatrix} + p_0 \cdot \begin{bmatrix} \kappa`_x \\ \kappa`_y \\ \kappa`_{xy} \end{bmatrix} = \begin{bmatrix} -2.04327 \cdot 10^{-3} \\ 6.44806 \cdot 10^{-3} \\ -87.31476 \cdot 10^{-36} \end{bmatrix}$$

Global Stresses

For laminae with $50°$ fibre winding angle

$$\begin{bmatrix} \sigma_x \\ \sigma_y \\ \tau_{xy} \end{bmatrix} := Q`_1 \cdot \begin{bmatrix} \varepsilon_x \\ \varepsilon_y \\ \gamma_{xy} \end{bmatrix} = \begin{bmatrix} 101.273 \\ 237.546 \\ 145.638 \end{bmatrix} MPa$$

For laminae with $-50°$ fibre winding angle

$$\begin{bmatrix} \sigma_{x\_2} \\ \sigma_{y\_2} \\ \tau_{xy\_2} \end{bmatrix} := Q`_2 \cdot \begin{bmatrix} \varepsilon_x \\ \varepsilon_y \\ \gamma_{xy} \end{bmatrix} = \begin{bmatrix} 101.273 \\ 237.546 \\ -145.638 \end{bmatrix} MPa$$

Local Strains and Stresses

For laminae with $50°$ fibre winding angle

$$\begin{bmatrix}\varepsilon_1\\ \varepsilon_2\\ \gamma_{12}\end{bmatrix} := T_1 \cdot \begin{bmatrix}\varepsilon_x\\ \varepsilon_y\\ \gamma_{xy}\end{bmatrix} = \begin{bmatrix}0.0029396\\ 0.0014651\\ 0.0041812\end{bmatrix}$$

$$\begin{bmatrix}\sigma_1\\ \sigma_2\\ \tau_{12}\end{bmatrix} := T_1 \cdot \begin{bmatrix}\sigma_x\\ \sigma_y\\ \tau_{xy}\end{bmatrix} = \begin{bmatrix}324.667\\ 14.152\\ 41.812\end{bmatrix} \textit{MPa}$$

For laminae with $-50°$ fibre winding angle

$$\begin{bmatrix}\varepsilon_1\\ \varepsilon_2\\ \gamma_{12}\end{bmatrix} := T_2 \cdot \begin{bmatrix}\varepsilon_x\\ \varepsilon_y\\ \gamma_{xy}\end{bmatrix} = \begin{bmatrix}0.00294\\ 0.00147\\ -0.00418\end{bmatrix}$$

$$\begin{bmatrix}\sigma_1\\ \sigma_2\\ \tau_{12}\end{bmatrix} := T_2 \cdot \begin{bmatrix}\sigma_{x\_2}\\ \sigma_{y\_2}\\ \tau_{xy\_2}\end{bmatrix} = \begin{bmatrix}324.667\\ 14.152\\ -41.812\end{bmatrix} \textit{MPa}$$

2. Strain measurements

2.1 First set of CFRP pressure vessels

Vessel 1		
Pressure Reading [bar]	Strain readings	
	0° [με]	90° [με]
20	-80	62
28	-145	98
36	-218	159
68	-536	377
96	-795	543
116	-973	657
124	-1007	683
130	-1092	740
162	-1400	934

Vessel 2		
Pressure Reading [bar]	Strain readings	
	0° [με]	90° [με]
22	-106	90
42	-233	199
46	-273	231
90	-595	500
100	-693	578
114	-796	662
136	-942	771

Vessel 3		
Pressure Reading [bar]	Strain readings	
	0° [με]	90° [με]
22	-165	93
36	-313	183
55	-501	297
80	-755	453
99	-930	558
118	-1102	657
138	-1300	777
158	-1493	901
172	-1592	967
176	-1643	1015
198	-1898	1152
218	-2089	1256
220	-	-

2.2 Second set of CFRP pressure vessels

2.2.1 CFRP tubes – 2 mm

Vessel 1		
Pressure readings [bar]	Strain readings	
	0° [με]	90° [με]
0	0	0
28	-223	1509
47	-434	2378
78	-1231	3568
118	-1707	5054
140	-2105	6080
172	-2612	7439
200	-3156	8640
220	-3880	9876
235	-4220	10488
260	-5300	11970
286	-5930	13365
302	-6680	14427
320	-7790	15412
330	-7850	16070

Vessel 2		
Pressure readings [bar]	Strain readings	
	0° [με]	90° [με]
0	0	0
32	-227	110
56	-490	2120
78	-877	3335
100	-1275	4426
118	-1615	5256
138	-2120	6372
158	-2754	7600
180	-3400	8858
200	-4054	10150
222	-4879	11450
240	-5559	12700
260	-6334	13855
282	-7055	15300
304	-7990	16700
322	-8823	18029
340	-9639	19330
360	-	-

Vessel 3		
Pressure readings [bar]	Strain readings	
	0° [με]	90° [με]
0	0	0
22	-140	538
32	-350	1340
48	-596	2144
72	-970	3220
98	-1524	4520
116	-2000	5540
138	-2664	6700
160	-3360	7940
180	-4000	9155
200	-5000	10474
220	-6060	12018
244	-7000	13400
260	-8440	14750
284	-9650	16500
300	-10500	17770
325	-12000	19200
340	-13400	20710
362	-14500	22172
365	-15500	23634
380	-16567	25096

Vessel 4		
Pressure readings [bar]	Strain readings	
	0° [με]	90° [με]
0	0	0
22	-138	493
44	-470	1580
68	-873	2765
96	-1375	4012
132	-2200	5718
148	-2700	6675
168	-3365	7791
196	-4270	9392
224	-5450	11120
254	-6700	13100
272	-7700	14370
302	-9300	16500
324	-10840	18560
350	-12100	20260

Vessel 5		
Pressure readings [bar]	Strain readings	
	0° [με]	90° [με]
0	0	0
22	-208	765
46	-552	1965
64	-860	2898
88	-1325	4115
102	-1661	4890
118	-2052	5714
126	-2330	6158
148	-3020	7601
194	-4800	10560
220	-5980	12450
238	-6780	14065
258	-7950	15265
280	-9200	16900
320	-11397	18245
330	-	-

2.2.2 CFRP tubes – 4 mm

Vessel 1		
Pressure readings [bar]	Strain readings	
	0° [με]	90° [με]
0	0	0
20	-40	99
33	-157	380
54	-270	652
78	-419	1005
94	-530	1250
118	-675	1576
142	-835	1923
160	-962	2176
180	-1108	2470
202	-1285	2813
224	-1470	3152
242	-1640	3447
266	-1850	3803
284	-2020	4095
304	-2260	4478
322	-2436	4783
340	-2635	5080
360	-2900	5470
384	-3180	5883
410	-3483	6327
425	-	-

Vessel 2		
Pressure readings [bar]	Strain readings	
	0° [με]	90° [με]
0	0	0
6	-24	76
46	-153	556
64	-235	797
98	-375	1237
118	-480	1237
146	-644	1490
174	-769	1925
200	-912	2270
220	-1113	2605
254	-1319	2890
275	-1460	3382
304	-1629	3705
320	-1799	4145
346	-1968	4450
370	-2138	4870
400	-2307	5250
420	-2477	5630
430	-	-

Vessel 3		
Pressure readings [bar]	Strain readings	
	0° [με]	90° [με]
0	0	0
22	-32	102
42	-164	500
62	-260	813
81	-350	1160
108	-496	1573
136	-661	1953
168	-850	2417
202	-1090	2910
232	-1348	3384
250	-1500	3870
276	-1730	4245
306	-2015	4802
324	-2216	5145
340	-2410	5513
360	-2611	5914
380	-2840	6400
420	-3326	7015
450	-3641	7544

Vessel 4		
Pressure readings [bar]	Strain readings	
	0° [με]	90° [με]
0	0	0
24	-70	232
45	-153	505
68	-244	698
92	-351	944
123	-496	1450
130	-543	1487
154	-661	1782
186	-858	2226
204	-975	2512
230	-1147	2939
258	-1327	3167
280	-1509	3560
300	-1684	3909
312	-1812	4070
330	-1988	4384
344	-2132	4596
359	-2284	4833.5
374	-2436	5071
389	-2588	5308.5
404	-2740	5546
419	-2892	5783.5
430	-3044	6021

Vessel 5		
Pressure readings [bar]	Strain readings	
	0° [με]	90° [με]
0	0	0
0	0	0
30	-90	297
38	-119	392
60	-196	661
85	-292	983
104	-359	1193
124	-440	1443
144	-525	1689
170	-643	2026
202	-803	2450
224	-912	2702
248	-1052	3040
266	-1158	3286
282	-1266	3494
302	-1415	3798
320	-1529	4004
328	-1591	4100
350	-1746	4420
382	-1880	4760
388	-2048	5000
410	-2190	5110

Appendix B: Detailed End Cap Drawings

1.1 First end cap design

First End Cap Design

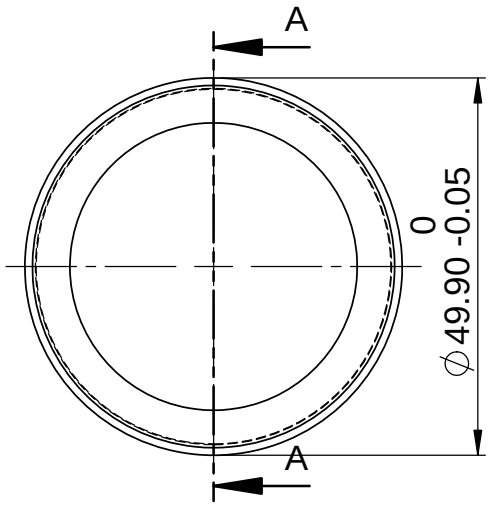

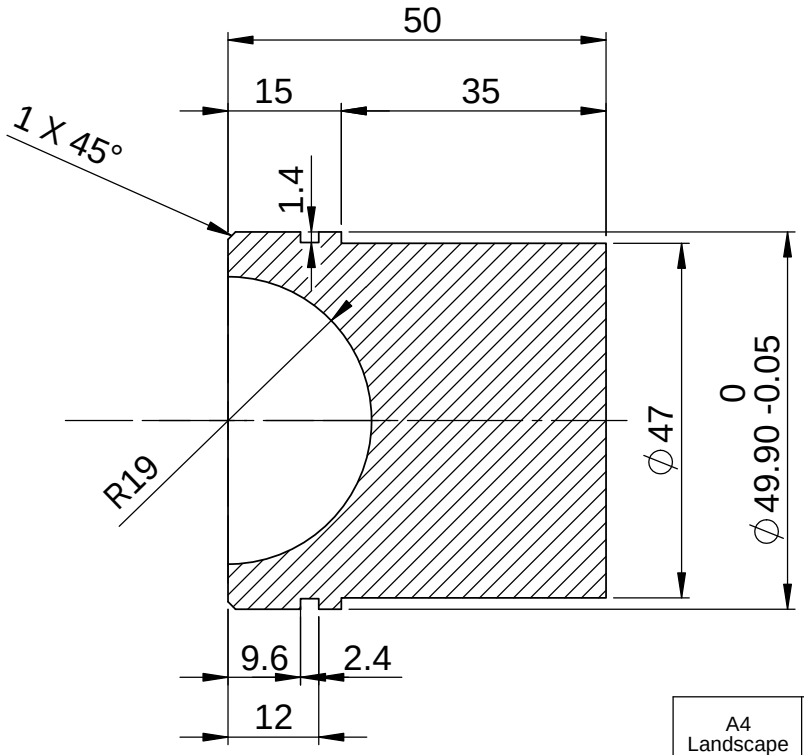

SECTION A-A

A4 Landscape	University of Cape Town Department of Mechanical Engineering				
	Title: End Cap-1				
Quantity: 10	Part Finish 3.2	Date: 2018/12/05	Scale: 1:1	Sheet1	of 1
Material: Aluminium 6083	Drawn By: Nyasha Mawire (MWRNYA002)			Drawing Number 1	

First End Cap Design

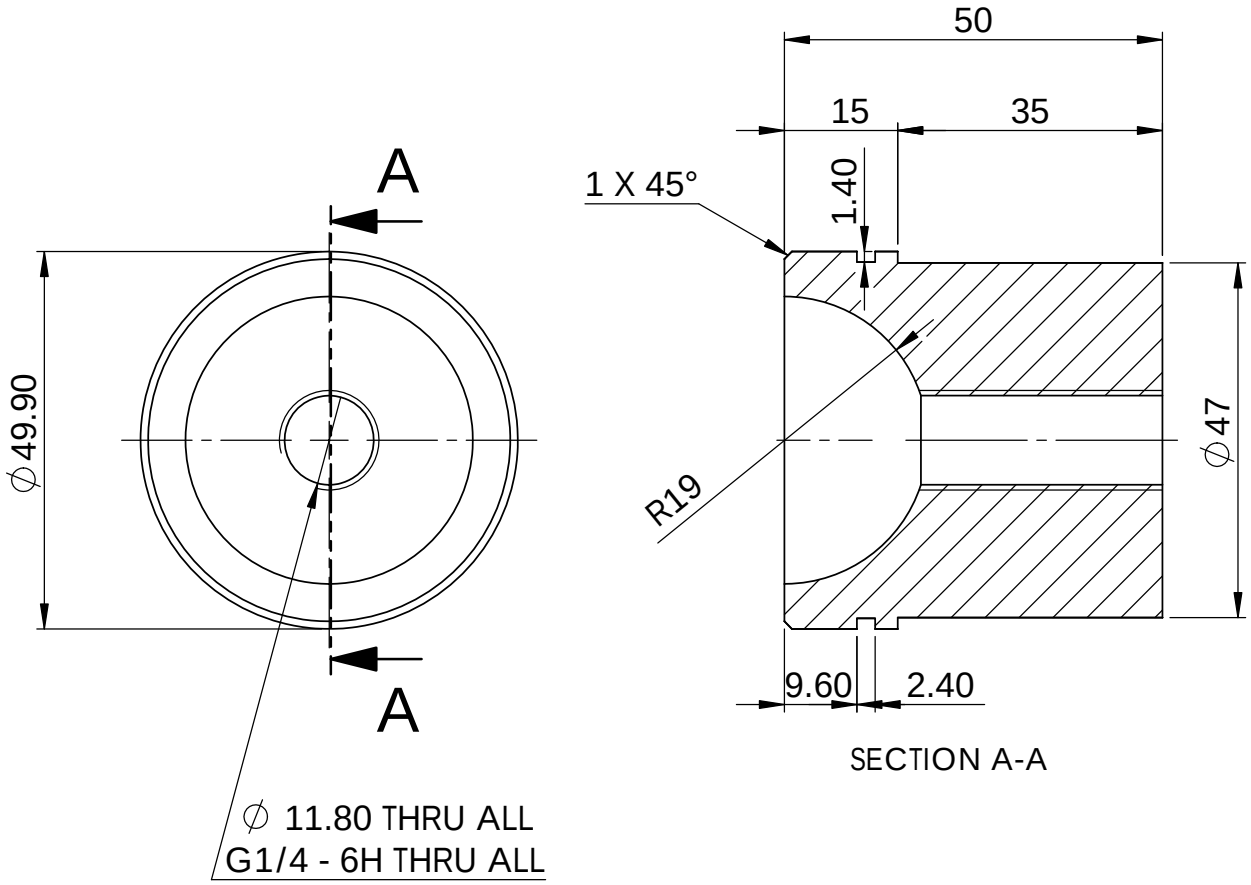

A4 Landscape	University of Cape Town Department of Mechanical Engineering				
	Title: End Cap-1-threaded				
Quantity: 5	Part Finish	Date: 2018/12/05	Scale: 1:1	Sheet1	of 1
Material: Aluminium 6083	Drawn By: Nyasha Mawire (MWRNYA002)			Drawing Number 3	

1.2 Second end cap design

Second End Cap Design

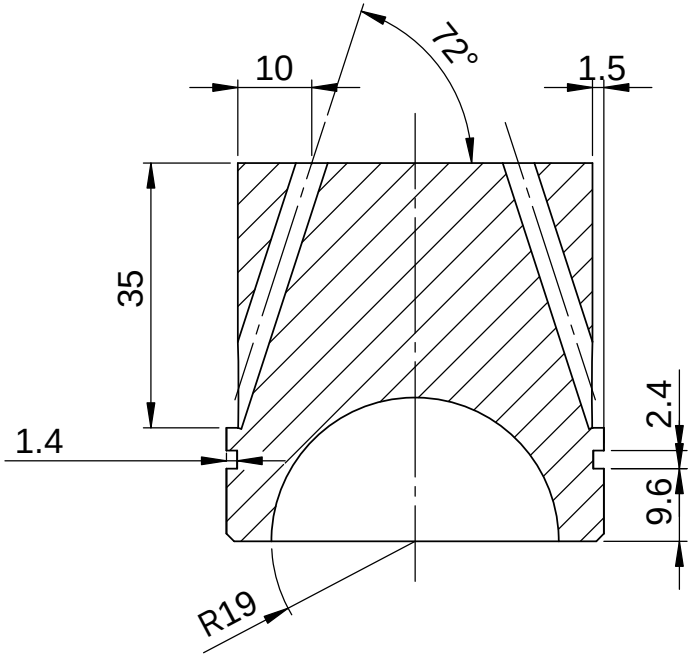

SECTION A-A

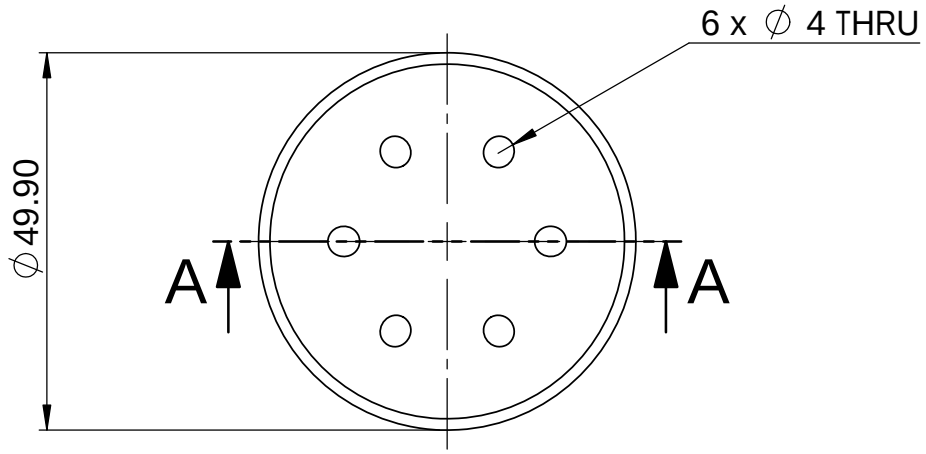

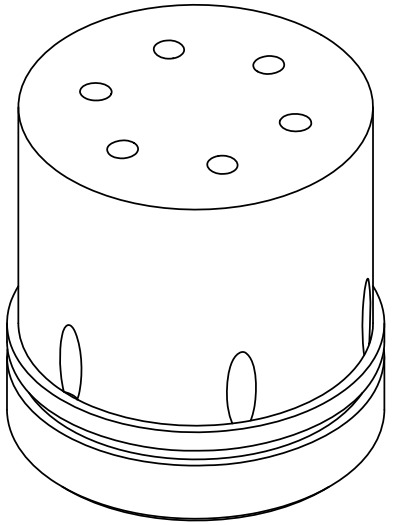

Note

1. All chamfers are 1 mm high at 45 degrees

A4 Landscape	University of Cape Town Department of Mechanical Engineering				
	Title: End Cap-2-Angled Holes				
Quantity: 2	Part Finish	Date: 2018/12/05	Scale: 1:1	Sheet1	of 1
Material: Aluminium 6083	Drawn By: Nyasha Mawire (MWRNYA002)			Drawing Number 1	

Second End Cap Design

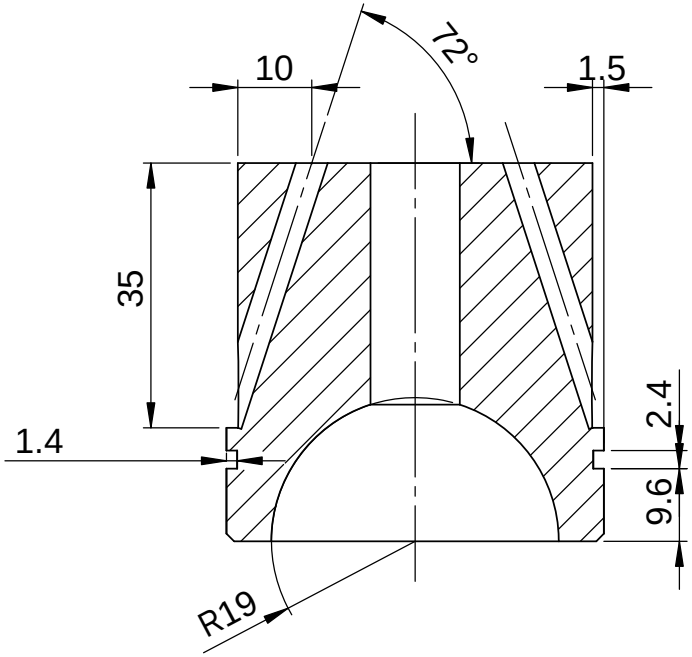

SECTION A-A

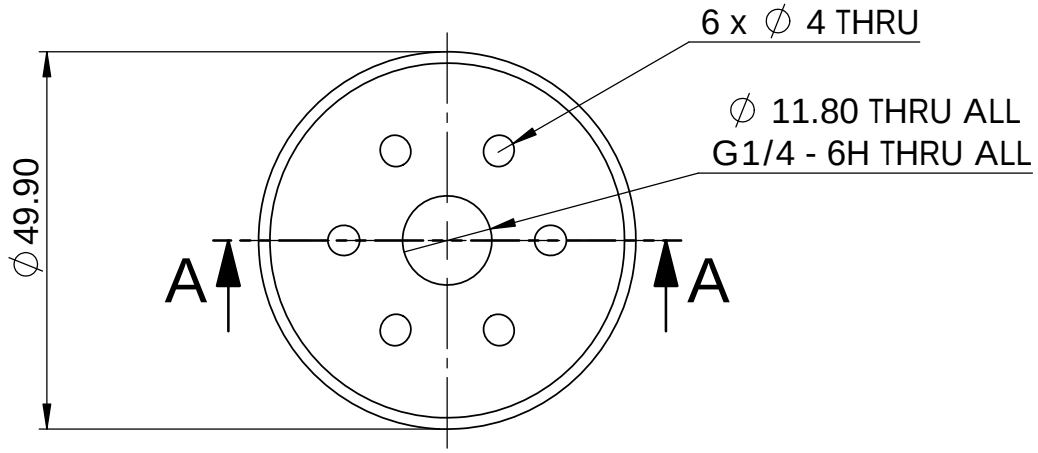

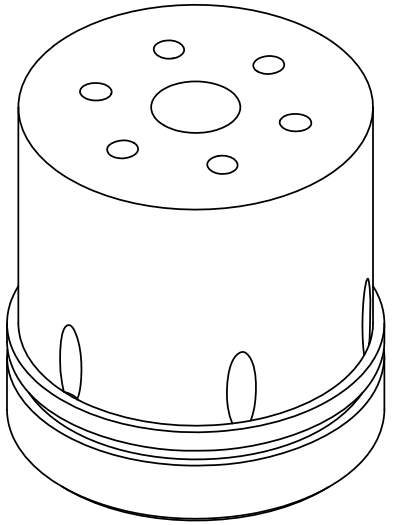

Note

1. All chamfers are 1 mm high at 45 degrees

A4 Landscape	University of Cape Town Department of Mechanical Engineering				
	Title: End Cap-2-Angled Holes				
Quantity: 2	Part Finish	Date: 2018/12/05	Scale: 1:1	Sheet1	of 1
Material: Aluminium 6083	Drawn By: Nyasha Mawire (MWRNYA002)			Drawing Number 1	

1.3 Third end cap design

Appendix C: Leak rate calculations

Third End Cap Design

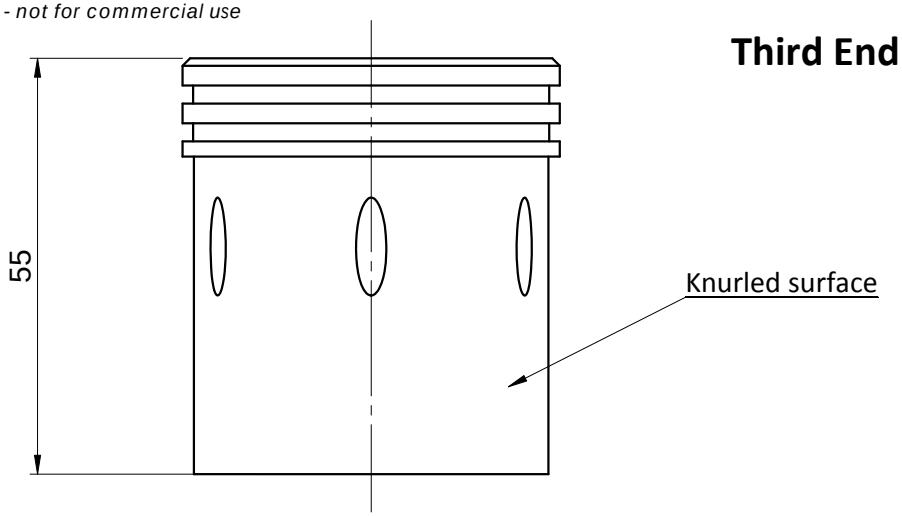

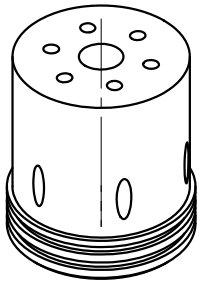

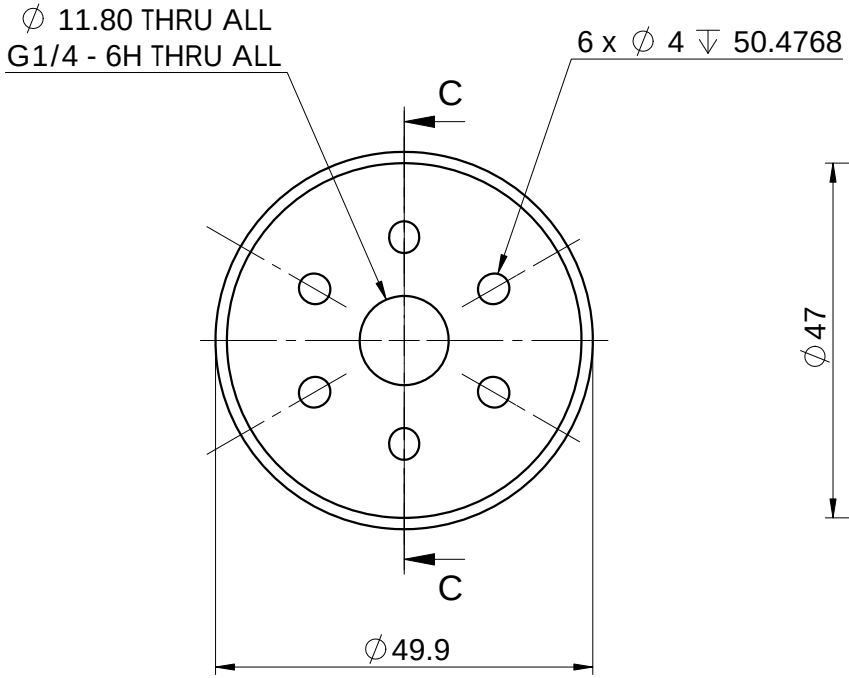

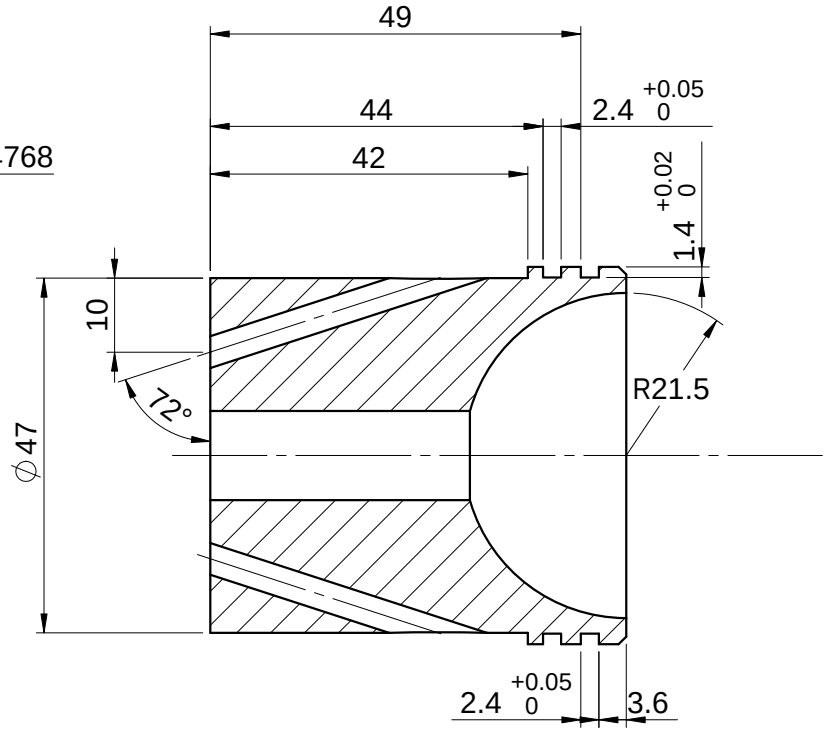

SECTION C-C

Scale: 1:1 on A4	University of Cape Town Department of Mechanical Engineering			
Drawn By: Nyasha Mawire	All un-toleranced dimensions to adhere to ISO 2768-m	Title: Third End Cap Design-Threaded		
Checked :	Material : AA 6083	Drawing Number : MWRNYA002-004	Rev. : A	Sheet : 1 of 1

Third End Cap Design

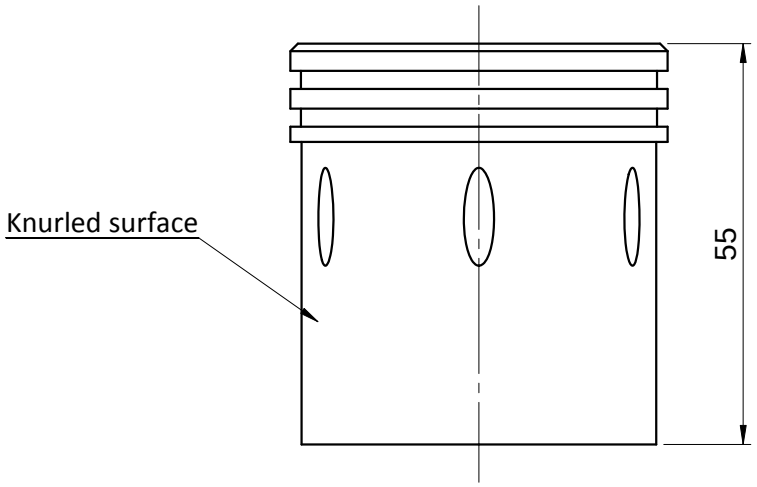

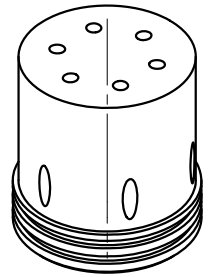

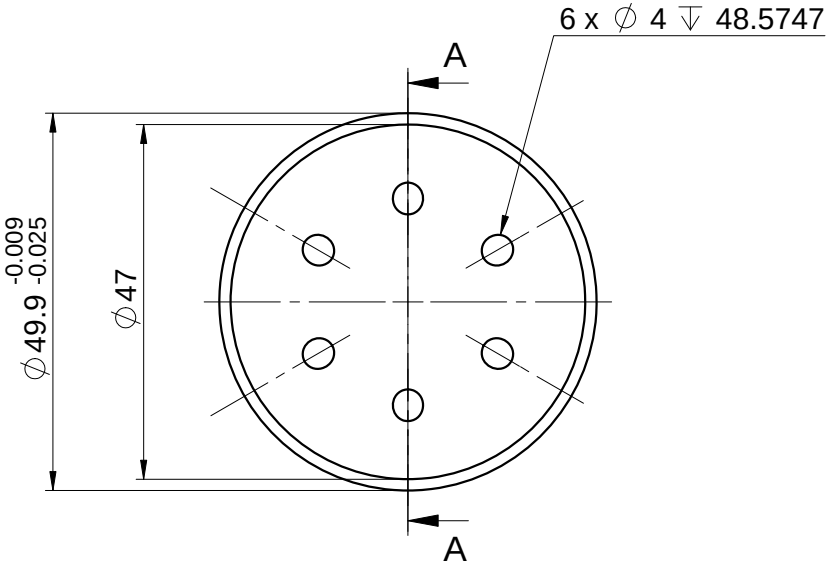

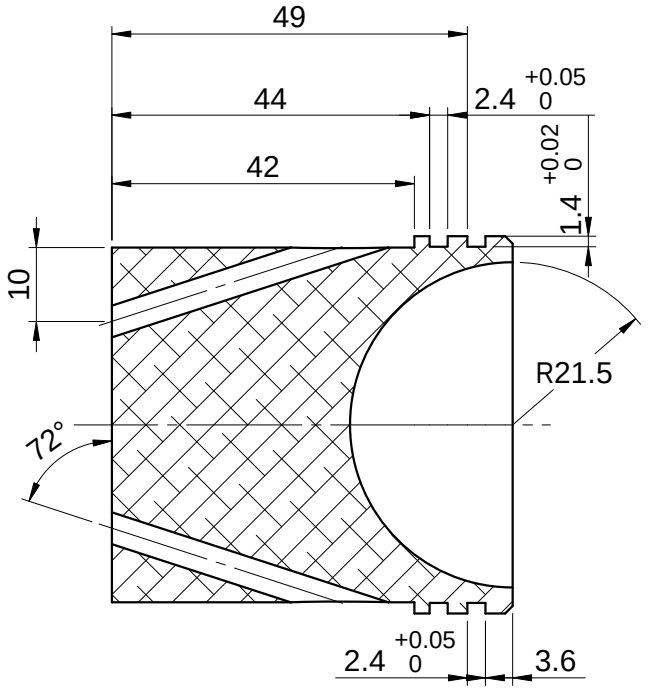

SECTION A-A

Scale: 1:1 on A4	University of Cape Town Department of Mechanical Engineering			
Drawn By: Nyasha Mawire	All un-toleranced dimensions to adhere to ISO 2768-m	Title: Third End Cap Design		
Checked :	Material : AA 6083	Drawing Number : MWRNYA002-003	Rev. : A	Sheet : 1 of 1

Appendix D: Material and product data sheets

TohoTenax

TEIJIN

Delivery programme and characteristics for Tenax® HTS filament yarn

Brand name		**Tenax®**	**Tenax®**	**Tenax®**
Production site		**E**	**E**	**E**
Fiber family & tensile properties		**HTS40**	**HTS40**	**HTS45**
Sizing properties		F13	F13	E23
Number of filaments		12K	24K	12K
Nominal linear density [1]	[tex]	800	1600	800tex
Twist	[t/m]	0/10Z	0/5Z	0
Running length per kg	[m/kg]	1250	625	1250
Package weight, net	[kg]	2 • 4 • 6	2 • 4 • 6 • 8	2 • 4 • 6

1) ohne Präparationsauftrag

Tensile Properties (typical values)

Tensile strength	[MPa]	4300	4300	4500
Tensile modulus	[GPa]	240	240	240

Characteristics (typical values)

Filament diameter	[µm]	7
Density	[g/cm^3]	1,77
Elongation at break	[%]	1,8
Specific heat capacity	[J/kgK]	710
Thermal conductivity	[W/mK]	10
Coefficient of thermal expansion [	[10^{-6}/K]	-0,1
Specific electrical resistance	[Ω cm]	1,6 x 10^{-3}

Sizing properties for fiber family HTS

HTS is a classic Tenax® high performance carbon fiber. The high tenacity (HT) fibers provide excellent mechanical laminate properties.

E23 = Type with ca. 1,3 % sizing based on epoxy resin
F13 = Type with ca. 1,0 % sizing based on polyurethane

Please contact our sales team any time for choosing the right type. The stated numbers are typical values. For design purposes please request fiber specification.

Please note the application (aerospace or industry & sports) on your order.

The export or transfer of carbon fibers can be subject to authorization, depending on end-use and final destination.

Toho Tenax Europe GmbH Kasinostraße 19-21 42103 Wuppertal, Deutschland Tel.: +49 202 32 - 2339 Fax: +49 202 32 - 2360 www.tohotenax-eu.com sales@tohotenax-eu.com
(04/2011)

Technical data sheet

Issued June 2010

Resin System for Composites

Epoxy Resin AR 600 with Hardener AH 2336
(Requires heat cure for full properties)

Introduction

Epoxy resin AR 600 with hardener AH 2336 is a high performance epoxy resin system for performance composite parts designed for wet lay-up, vacuum bagging, tooling / moulds, filament winding and resin-infusion. AR 600 is a low viscosity epoxy resin produced from bisphenol A/F and epichlorohydrin, and contains a proportion of E10P (glycidyl ester of neodecanoic acid) as a reactive diluent; AH 2336 is a unmodified cycloaliphatic polyamine hardener system. This system provides a unique combination of good mechanical properties and thermal properties. It is especially useful in high performance composite parts where fibre to resin ratio's are important.

Features

> Low viscosity, good, fast wet-out
> Good mechanical properties
> Good thermal and heat deflection temperatures
> Long pot-life

Suggested Uses

> Advanced composite structures
> Tooling / moulds
> Filament winding / pultrusion
> Resin transfer molding

Typical Properties

AR 600 (Epoxy Resin)

Property	Test Method	Unit	Value
Density at 23°C	SMS 1347	kg/L	1,14
Flashpoint	ASTM D93	°C	141
Viscosity at 23°C	ASTM D445	Pa.s	0,7 – 1,1
Epoxy group content	SMS 2026	mmol/kg	5280
EEW		g	180 – 195
Colour	ASTM D1209	Pt-Co	200 max

AH 2336 (Hardener)

Property	Test Method	Unit	Value
Density at 23°C	SMS 1347	kg/L	0.96
Flashpoint	ASTM D93	°C	194
Viscosity at 23°C	D-150F	mPa.s	70 - 100
AHEW		g/g	52,5
Amine value		mgKOH/g	526

Formulas

Material	Pounds	Kilograms
AR 600	10 lbs	1,0 kg
AH 2336	2,8 lbs	280 g

Ratio 100 : 28 parts by weight

Typical Cured State Properties

The physical properties of neat resin castings made with AR 600 with AH 2336 are given below. As these tests were done in a controlled environment, and it is suggested that appropriate tests are carried out for your own application and end use.

Mix ratio	
By weight	**100 : 28**
Glass transition (Tg)	
By Rheometrics, °C	182
By HDT, °C	180
Tensile strength	
At 23 °C, Mpa	73 - 81
Tensile modulus	
At 23 °C, MPa	2500 - 2600
Tensile elongation	
At 23 °C, %	5,5

Composite Fabrication

Pot-life @ 23°C (128g) 200 – 400 mins

Curing – The curing cycle will depend on part size and thickness, method of heat application, and end properties required.
Additional post curing is achieved by heating the composite structure up to the desired post-cure temperature. Temperature increase should be between 1,5 to 2,0°C per minute for best results, and to prevent thermal shock.

Typical Cure and Post Cure Schedule –
2 hours at 60°C + 3 hours at 80°C + 4 hours at 120°C + 2 to 6 hours at 160°C.

Cooling down should also be slow, and should be left until room temperature is reached.

Product Precautions

Uncured epoxies are toxic and may cause skin irritation. It is strongly recommended to use gloves and safety glasses when working with epoxies. If gloves are not available, use a suitable barrier cream. In the event of skin contact, wipe off epoxy or hardener with paper towel and wash skin well with soap and water. Do not use solvents to wash epoxies off skin.

Product Storage

Resin and hardeners should be stored in conditions so that moisture is excluded, preferably in the original containers kept tightly closed. Under these normal storage conditions the storage life should be at least one year.

Disclaimer

These are starting point formulations and are not proven for use in the user's particular application but are simply meant to demonstrate the efficacy of the products and to assist in the development of the user's own formulations. It is the user's responsibility to fully test and qualify the formulation, along with the ingredients, methods, applications, cure and post-cure cycles, or equipment identified herein, by the user's knowledgeable formulator or scientist, and to determine the appropriate use conditions and legal restrictions, prior to use of any information.

ALL WARRANTIES OF ANY KIND ARE EXPRESSLY EXCLUDED AND DISCLAIMED, WITHOUT LIMITATION, NO REPRESENTATION IS MADE AND NO WARRANTY, EXPRESS OR IMPLIED, IS EXTENDED WITH RESPECT TO THE ACCURACY, REPRODUCIBILITY, COMPLETENESS, OR USEFULNESS OF THE INFORMATION TO MEET YOUR REQUIREMENTS, OR WITH RESPECT TO THE TITLE OR MERCHANTIBILITY OF THE INFORMATION PROVIDED, OR THE FITNESS OF THE INFORMATION PROVIDED FOR A PARTICULAR PURPOSE, OR THAT THE USE OF THE INFORMATION IS FREE FROM INFRINGEMENT OF ANY PATENT OR ANY OTHER INTELLECTUAL PROPERTY RIGHT, AND EACH OF THESE ARE THE SOLE AND EXCLUSIVE RESPONSIBILITY OF THE USER. USE OF THE INFORMATION AND PRODUCTS IS AT YOUR OWN RISK.

AERONTEC cc
PO Box 683, Howard Place, 7450
Tel : 021-671 2114
info@aerontec.co.za

Spabond 340LV

EPOXY ADHESIVE SYSTEM

- **High strength and toughness industrial adhesive**
- **Excellent gap filling properties**
- **Designed for cartridge and mixing machine dispense**
- **Three hardener speeds give a range of working times / clamp times**
- **Low exotherm and shrinkage**
- **Temperature performance up to 80°C**
- **Resin & hardener are pigmented to give a visual indication of mix quality**

INTRODUCTION

Spabond 340LV is a high performance adhesive designed for bonding large structures such as yacht hulls and wind turbine blades. It is a cost-effective system with good thermal and mechanical properties.

The components are pigmented to give a visual indication of mix quality, which is a useful feature when mixing by hand or with a machine. The system has a simple 2:1 mix ratio by weight and volume.

Spabond 340LV is available in cartridges, pails and 200 litre drums for machine mixing/dispense.

INSTRUCTIONS FOR USE

The product is optimised for use at 15 - 25°C. At lower temperatures the components thicken and may eventually become unworkable. To ensure accurate mixing and good workability pre-warm the resin & hardener as well as the surfaces to be bonded before use.

Surface Preparation

Before using the product ensure that surfaces to be bonded are clean, dry and dust-free. Prepare all surfaces by abrading with medium grit paper or other suitable abrasive, remove dust then wipe with acetone or Gurit Fast Epoxy Solvent (Solvent A).

Metals usually require a chemical pre-treatment to create the best bond. Please contact Gurit for a Guide to Surface Preparation and Pre-treatments.

Ensure that polyester or vinylester laminates are fully cured before bonding, then prepare as above. When bonding epoxy laminates, the use of a suitable Peel Ply as the last stage in their manufacture is recommended, otherwise prepare as above. Trials may be required to test Peel Ply suitability.

For ferrocement, etch with 5% solution of hydrochloric acid, wash with fresh water, then dry.

For all timber, sand with abrasive paper across grain. Degrease oily timber with a fast evaporating solvent (e.g. Gurit Fast Epoxy Solvent). For resinous or gummy timber, etch with 2% caustic soda solution, wash off with fresh water and dry.

Mixing & Handling

The Spabond 340 components are supplied pigmented in the following colours:

Resin	-	yellow
Fast Hardener	-	red
Standard	-	mauve
Slow Hardener	-	purple
Extra Slow Hardener	-	blue

Spabond 340 resin should be combined with any one Spabond 340 hardener in the following mix ratio:

Spabond 340LV resin		Spabond 340 hardener
100	:	50 (by weight and volume)

Mix thoroughly for at least one minute, paying particular attention to the sides and bottom of the mixing vessel, to ensure no streaks remain. Once fully mixed the adhesive should have a uniform colour. Use from pot quickly to maximise resin working life.

Cartridge Use

If dispensing product from twin cartridges with a mixing / dispensing head , please discard the first mix head length of resin and hardener components, prior to applying adhesive to the job, in order to ensure thorough mixing of the system. We recommend the use of a new mix head for each application, particularly where the time between each application approaches the pot life.

PROPERTIES

Component Properties

	Resin	Fast	Standard	Slow	Extra Slow
Mix Ratio (by weight)	100	50	50	50	50
Mix Ratio (by volume)	100	50	50	50	50
Viscosity @ 15°C (cP)	49000	59100	-	45000	44700
Viscosity @ 20°C (cP)	29000	38400	-	37920	36600
Viscosity @ 25°C (cP)	21000	25800	313000	30790	22400
Viscosity @ 30°C (cP)	13000	17100	-	23640	17500
Shelf Life (months)	24	24	24	24	24
Colour	yellow	red	mauve	purple	blue
Mixed Colour	-	pink	cream	grey	green
Component Dens. (g/cm³)	1.1	1.1	1.1	1.1	1.1
Mixed Density (g/cm³)	1.1	1.1	1.1	1.1	1.1
Hazard Definition	Please refer to SDS				

PROPERTIES (CONT'D)

Working Properties

	Resin/Fast Hardener				Resin/Standard Hardener				Resin/Slow Hardener				Resin/Extra Slow Hardener			
	15°C	20°C	25°C	30°C	15°C	20°C	25°C	30°C	15°C	20°C	25°C	30°C	15°C	20°C	25°C	30°C
Initial Mixed Viscosity (cP)	43500	27600	19000	12500	-	-	25500	-	42000	27000	20000	10000	48000	34000	21000	14300
†Pot Life - 500g mix in air (hrs:mins)	0:20	0:16	0:12	0:10	-	00:30	-	-	01:00	00:45	00:34	00:26	3:10	2:20	1:40	1:15
***†Clamp Time (hrs:mins)**	5:12	3:50	2:50	2:05	-	9:15	-	-	23:00	17:40	13:30	10:20	33:50	24:00	14:50	10:30
Sag Resistance (mm)	TBA	20	20	TBA	-	20	-	-	TBA	20	20	TBA	TBA	20	20	TBA

Cured System Properties

	Room Temp. Cure (28 days @ 21°C)				Cured 24 hours @ 21°C +16 hours @ 50°C				Cured 5 hrs @ 70°C			
	Fast	Standard	Slow	Ex. Slow	Fast	Standard	Slow	Ex. Slow	Fast	Standard	Slow	Ex. Slow
Tg DMTA (Peak Tanδ(°C)	65.8	TBC	60.0	60.9	74.1	84.8	81.7	76.3	80.8	TBC	79.7	77.4
Tg Ult - DMTA (°C)	92.4	TBC	80.5	86.4	92.4	76.5	80.5	86.4	92.4	TBC	80.5	86.4
Tg2 - DSC (°C)	55.0	TBC	52.8	54.2	71.8	74.1	67.4	63.7	72.3	TBC	69.1	66.5
Tg1 - DMTA (°C)	54.9	TBC	50.4	51.5	63.3	74.1	67.5	65.1	69.2	TBC	68.5	67.1
Cured Density (g/cm³)	TBA				TBA	1.16	TBA		1.12	TBC	1.11	1.09
Linear Shrinkage (%)	TBA				TBA				1.92	TBC	1.91	1.94
Cleavage Strength (kN)	10.7	TBC	11.1	10.7	11.0	10.3	11.9	12.0	10.6	TBC	11.7	11.0
Shear Strength on Steel (MPa)	24.9	TBC	27.0	30.7	28.0	32.5	31.0	32.2	33.3	TBC	34.5	33.4
Shear Strength Wet Retention (%)	70.5	TBC	75.6	80.2	TBA				TBA			

Notes: For an explanation of test methods used see 'Formulated Products Technical Characteristics'.

All figures quoted are indicative of the properties of the product concerned. Some batch to batch variation may occur.

† All times are measured from when resin and hardener are first mixed together.

*Clamp time data shows the time taken to achieve a 2000N bond strength. This figure allows comparison of cure speed with other adhesive products of the Spabond range. However, because of the unusual cure development of this product at 15 - 30°C, the time to reach a safe handling strength should be extended by approximately 50%. Alternatively, an elevated temperature posture should be applied before handling.

WORKING PROPERTIES

Clamp Time

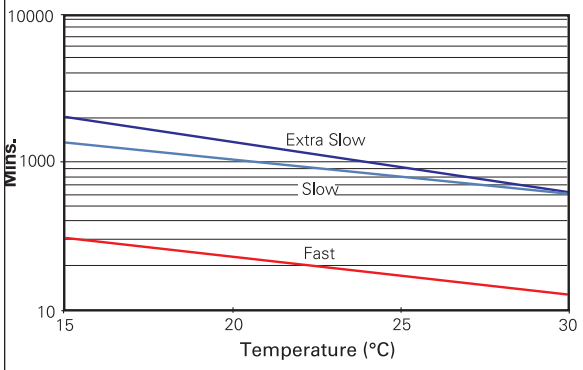

MECHANICAL PROPERTIES

Glass Transition Temperature

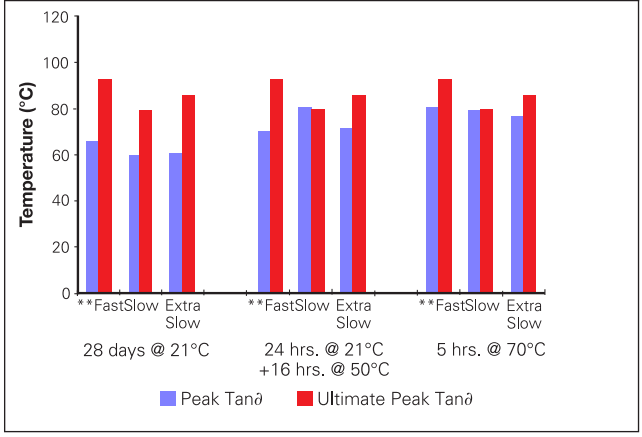

Cleavage Strength

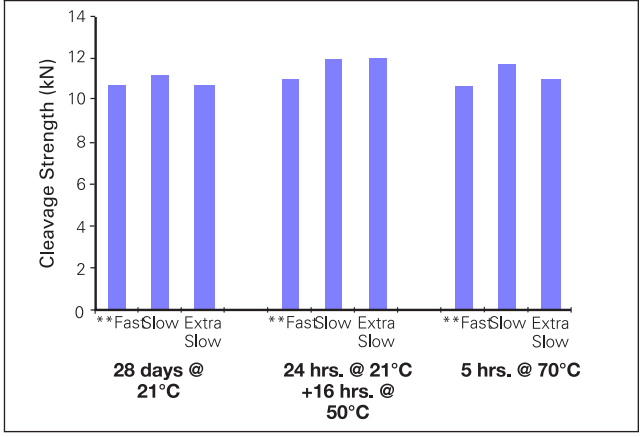

Shear Strength on Shotblasted Steel

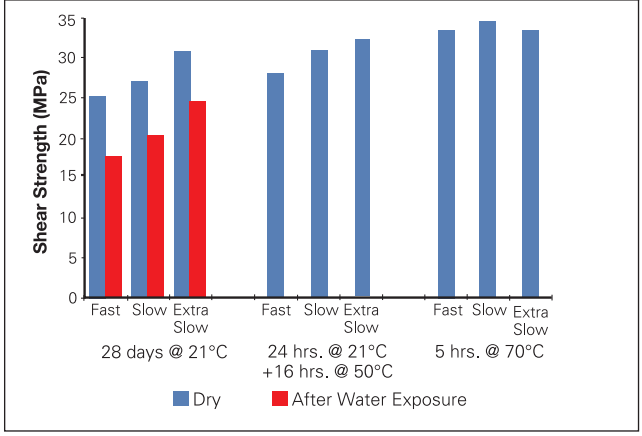

HEALTH AND SAFETY

The following points must be considered:

1. Skin contact must be avoided by wearing protective gloves. Gurit recommends the use of disposable nitrile gloves for most applications. The use of barrier creams is not recommended, but to preserve skin condition a moisturising cream should be used after washing.

2. Overalls or other protective clothing should be worn when mixing, laminating or sanding. Contaminated work clothes should be thoroughly cleaned before re-use.

3. Eye protection should be worn if there is a risk of resin, hardener, solvent or dust entering the eyes. If this occurs flush the eye with water for 15 minutes, holding the eyelid open, and seek medical attention.

4. Ensure adequate ventilation in work areas. Respiratory protection should be worn if there is insufficient ventilation. Solvent vapours should not be inhaled as they can cause dizziness, headaches, loss of consciousness and can have long term health effects.

5. If the skin becomes contaminated, then the area must be immediately cleansed. The use of resin-removing cleansers is recommended. To finish, wash with soap and warm water. The use of solvents on the skin to remove resins etc must be avoided.

Washing should be part of routine practice:

- before eating or drinking
- before smoking
- before using the lavatory
- after finishing work

6. The inhalation of sanding dust should be avoided and if it settles on the skin then it should be washed off. After more extensive sanding operations a shower/bath and hair wash is advised.

Gurit produces a separate full Safety Data Sheet for all hazardous products. Please ensure that you have the correct SDS to hand for the materials you are using before commencing work. A more detailed guide for the safe use of Gurit resin systems is also available from Gurit, and can be found at www.gurit.com

APPLICABLE RISK & SAFETY PHRASES

Please refer to product SDS for up to date information specific to this product.

TRANSPORT & STORAGE

The resin and hardeners should be kept in securely closed containers during transport and storage. Any accidental spillage should be soaked up with sand, sawdust, cotton waste or any other absorbent material. The area should then be washed clean (see appropriate Safety Data Sheet).

Adequate long term storage conditions will result in a shelf life of two years for both the resin and hardeners. Storage should be in a warm dry place out of direct sunlight and protected from frost. The storage temperature should be kept constant between 10°C and 25°C, cyclic fluctuations in temperature can cause crystallization. Containers should be firmly closed. Hardeners, in particular, will suffer serious degradation if left exposed to air.

For more information on crystallization please refer to the Adhesives section on the Gurit website. (www.gurit.com)

NOTICE

All advice, instruction or recommendation is given in good faith but Gurit AG (the company) only warrants that advice in writing is given with reasonable skill and care. No further duty or responsibility is accepted by the Company. All advice is given subject to the terms and conditions of sale (the Conditions) which are available on request from the Company or may be viewed at the Company's Website: http://www.gurit.com/terms-and-conditions.aspx

The Company strongly recommends that Customers make test panels and conduct appropriate testing of any goods or materials supplied by the Company to ensure that they are suitable for the Customer's planned application. Such testing should include testing under conditions as close as possible to those to which the final component may be subjected. The Company specifically excludes any warranty of fitness for purpose of the goods other than as set out in writing by the Company. The Company reserves the right to change specifications and prices without notice and Customers should satisfy themselves that information relied on by the Customer is that which is currently published by the Company on its website. Any queries may be addressed to the Technical Services Department.

Gurit are continuously reviewing and updating literature. Please ensure that you have the current version, by contacting Gurit Marketing Communications or your sales contact and quoting the revision number in the bottom right-hand corner of this page.

E gurit@gurit.com
W www.gurit.com

VytaFlex® Series

Liquid Urethane Rubbers

www.smooth-on.com

PRODUCT OVERVIEW

Using Smooth-On's exclusive "V-Polymer®" technology, **VytaFlex®** urethane rubbers offer superior physical and performance properties for casting concrete. **VytaFlex®** urethanes are available in 10A, 20A, 30A, 40A, 50A and 60A Shore hardness's and feature convenient one-to-one by volume mix ratios.

Vacuum degassing is not necessary and **VytaFlex®** rubbers cure with negligible shrinkage to a durable rubber that will last in production.

VytaFlex® mold rubbers work especially well for casting pigmented / colored concrete. Molds made with VytaFlex® Series urethanes will render accurate and uniform colored castings.

TECHNICAL OVERVIEW

	A:B Mix Ratio by Volume	A:B Mix Ratio by Weight	Mixed Viscosity (ASTM D-2393)	Specific Gravity (g/cc) (ASTM D-1475)	Specific Volume (cu. in./lb.)	Color	Shore A Hardness (ASTM D-2240)	Tensile Strength (ASTM D-412)	100% Modulus (ASTM D-412)	Elongation at Break % (ASTM D-412)	Die C Tear Strength (ASTM D-624)
VytaFlex® 10	1:1 pbv	1:1 pbw	3,100 cps	1.00	27.9	Off-White	10A	200 psi	25	1,000%	38 pli
VytaFlex® 20	1:1 pbv	1:1 pbw	1,000 cps	1.00	27.7	Clear Amber	20A	200 psi	50	1,000%	60 pli
VytaFlex® 30	1:1 pbv	1:1 pbw	1,800 cps	1.02	27.3	Off-White	30A	500 psi	65	1,000%	78 pli
VytaFlex® 40	1:1 pbv	1:1 pbw	2,000 cps	1.03	26.9	Off-White	40A	522 psi	100	660%	82 pli
VytaFlex® 50	1:1 pbv	1:1 pbw	2,000 cps	1.04	26.7	Off-White	50A	588 psi	215	400%	102 pli
VytaFlex® 60	1:1 pbv	1:1 pbw	2,000 cps	1.04	26.6	Off-White	60A	880 psi	300	480%	136 pli

***Pot Life:**

VytaFlex® 10, 20, 30, 40: 30 minutes

VytaFlex® 50, 60: 60 minutes

***Cure Time:**

VytaFlex® 20, 30, 40, 50, 60: Overnight/16 hours

VytaFlex® 10: 24 hours

Shrinkage: < .001 in./in.

*All values measured after 7 days at 73°F/23°C

PROCESSING RECOMMENDATIONS

START BY PREPARING YOUR MODEL...

Preparation - Store and use at room temperature (73°F/23°C). These products have a limited shelf life and should be used as soon as possible. Environmental humidity should be as low as possible. Good ventilation (room size) is essential. Wear safety glasses, long sleeves and rubber gloves to minimize contamination risk.

Some Materials Must Be Sealed - Urethanes are adhesive. To prevent adhesion between the rubber and model surface, models made of porous materials (gypsum plasters, concrete, wood, stone, etc.) must be sealed prior to applying a release agent. SuperSeal® (available from Smooth-On) or One Step® are fast drying sealers suitable for sealing porous surfaces without interfering with surface detail. Sonite Wax®or high-grade shellac is suitable for rough contours. A high quality Shellac is suitable for sealing modeling clays that contain sulfur or moisture (water based). Thermoplastics (polystyrene) must also be sealed with shellac or PVA. **In all cases,** the sealing agent should be applied and allowed to completely dry prior to applying a release agent.

Non-Porous Surfaces - Metal, glass, hard plastics, sulfur free clays, etc. require only a release agent.

IMPORTANT: Shelf life of product is reduced after opening. Remaining product should be used as soon as possible. Immediately replacing the lids on both containers after dispensing product will help prolong the shelf life of the unused product. **XTEND-IT® Dry Gas Blanket** (available from Smooth-On) will significantly prolong the shelf life of unused liquid urethane products.

Safety First!

The Material Safety Data Sheet (MSDS) for this or any Smooth-On product should be read prior to use and is available upon request from Smooth-On. All Smooth-On products are safe to use if directions are read and followed carefully.

Be careful.

Part A is a TDI prepolymer. Vapors, which can be significant if material is heated or sprayed, cause lung damage and sensitization. Use only with adequate ventilation. Contact with skin and eyes may cause severe irritation. Flush eyes with water for 15 minutes and seek immediate medical attention. Remove from skin with waterless hand cleaner followed by soap and water Prepolymers contain trace amounts of TDI which, if ingested, must be considered a potential carcinogen. Refer to MSDS .

Part B is irritating to the eyes and skin. If contaminated, flush eyes with water for 15 minutes and seek immediate medical attention. Remove from skin with soap and water. When mixing with Part A follow precautions for handling isocyanates.

Important: The information contained in this bulletin is considered accurate. However, no warranty is expressed or implied regarding the accuracy of the data, the results to be obtained from the use thereof, or that any such use will not infringe upon a patent. User shall determine the suitability of the product for the intended application and assume all risk and liability whatsoever in connection therewith.

Applying A Release Agent - A release agent is necessary to facilitate demolding when casting into or over most surfaces. Use a release agent made specifically for mold making (Universal® Mold Release available from Smooth-On). A liberal coat of release agent should be applied onto all surfaces that will contact the rubber.

IMPORTANT: To ensure thorough coverage, lightly brush the release agent with a soft brush over all surfaces of the model. Follow with a light mist coating and let the release agent dry for 30 minutes. Because no two applications are quite the same, a small test application to determine suitability for your project is recommended if performance of this material is in question.

MEASURING & MIXING...

Liquid urethanes are **moisture sensitive** and will absorb atmospheric moisture. Mixing tools and containers should be clean and made of metal or plastic. Materials should be stored and used in a warm environment (73°F/23°C).

IMPORTANT: Pre Mix the Part B before using. After dispensing equal amounts of Parts A and B into mixing container, mix thoroughly for at least 3 minutes making sure that you scrape the sides and bottom of the mixing container several times.

If Mixing Large Quantities (16 lbs./7 kgs. or more) at one time, use a mechanical mixer (i.e. Squirrel Mixer or equal) for 3 minutes followed by careful hand mixing for one minute as directed above. Then, pour entire quantity into a new, clean mixing container and do it all over again.

Although this product is formulated to minimize air bubbles in your the cured rubber, vacuum degassing prior to pouring rubber will further reduce entrapped air.

POURING, CURING & PERFORMANCE...

For best results, pour your mixture in a single spot at the lowest point of the containment field. Let the rubber seek its level up and over the model. **A uniform flow will help minimize entrapped air.** The liquid rubber should level off at least 1/2" (1.3 cm) over the highest point of the model surface.

Curing - Allow rubber to cure a minimum of 16 – 24 hours at room temperature (73°F/23°C) before demolding. VytaFlex® 10 should cure for at least 24 hours before demolding. Cure time can be reduced with mild heat or by adding Smooth-On "Kick-It®" Cure Accelerator. Do not cure rubber where temperature is less than 65°F/18°C.

Post Curing - Optional . . . Following an overnight cure, heating the rubber to 150°F (65°C) for 4 to 8 hours will increase physical properties and performance.

Using The Mold - If using as a mold material, a release agent should be applied to the mold before each casting. **In & Out® II Concrete Release Concentrate** (available from Smooth-On) is recommended for releasing concrete.

Performance & Storage - Fully cured rubber is tough, durable and will perform if properly used and stored. The physical life of the rubber depends on how you use it.

SMOOTH-ON SINCE 1895

Call Us Anytime With Questions About Your Application

Toll-free: **(800) 762-0744** Fax: **(610) 252-6200**

The new **www.smooth-on.com** is loaded with information about mold making, casting and more.

Appendix E: Detailed costs associated with the novel CFRP pressure vessels and Type IV pressure vessels

The costs incurred in purchasing the raw materials essential for the manufacture of the 2mm and 4 mm CFRP pressure vessels are listed in the table below. In comparison, the costs associated

Table E1: Costs of the 2 mm CFRP pressure vessel compared to Type IV pressure vessels

	Novel 2 mm pressure vessel	**Type IV 350 bar pressure vessel** [133]	**Type IV 700 bar pressure vessel** [133]
Physical dimensions			
Internal diameter	50 mm	-	-
Wall thickness	2 mm	-	-
Length	1 m	-	-
Volume	2 litres	258 litres	149 litres
Materials required			
Mass of carbon fibre tow required	300 g	55 kg	69 kg
Mass of epoxy resin required	150 g	23 kg	29 kg
Rubber liner	20g	-	-
Costs of the materials			
Carbon fibre tow per kg	R775/kg	R401/kg*	R401/kg*
Epoxy resin per kg	R272/kg	R100/kg*	R100/kg*
Rubber liner (VytaFlex 60) per kg	R179/kg	-	-
End caps (material and machining included)	R110	-	-
Mass of H_2 stored (kg)	**0.03**	**5.6**	**5.6**
Total cost (R)	**R390**	**R36043***	**R40113***
Normalised cost (R/kg of H_2)	**R13,000**	**R6,436**	**R7,163**

*These values were quoted initially US dollars as of 2005 [133] before being converted into the SA Rand value and then inflated to match the value as of 2018. These values also roughly include the effect of inflation since the year 2015.

It should be noted that the total cost from the table above does not include the filament winding manufacturing or labour costs for any of the three pressure vessels.

It can be seen from the table above that the Type IV pressure vessels have a normalised cost approximately half of the cost of the 2 mm CFRP pressure vessel. This significant difference in cost is due to the significantly dissimilar costs of the carbon fibres and epoxy resins used for the two types of vessels. The costs of the carbon fibre as well as the epoxy resin used for the Type IV pressure vessels are slightly higher than half of the costs pertaining to the 2 mm CFRP pressure vessel. Secondly, the costs associated with the Type IV pressure vessel are given factoring in a production volume of 500,000

units which is advantageous in lowering the costs significantly as those materials can be bought in large/bulk quantities at significant discounts [14], [64]. Thirdly, the cost of the carbon fibre used in the construction of the novel 2 mm pressure vessel is higher because it was imported. This means that import duty and shipping costs are also factored into the purchase price. Therefore, it is likely that the normalised cost of the 2 mm CFRP pressure vessel may be very similar or better to that of the Type IV pressure vessels if there were large production volumes and if the same carbon fibre and resin from the Type IV vessel were used.